



Design and synthesis of photoactivatable myristic acid analogues for UNC119 cargo interactions and target identification of autophagy inhibitors

DISSERTATION

zur Erlangung des akademischen Grades eines
Doktors der Naturwissenschaften (Dr. rer. nat.)
der Fakultät für Chemie und Chemische Biologie
der Technischen Universität Dortmund

vorgelegt von

M. Sc. Nadine Kaiser

aus Sundern-Hagen/

Nordrhein-Westfalen

Dortmund 2019

Die vorliegende Arbeit entstand im Zeitraum von September 2015 bis Januar 2019 unter der Anleitung von Prof. Dr. Dr. h.c. Herbert Waldmann an der Fakultät für Chemie und Chemische Biologie der Technischen Universität Dortmund und dem Max-Planck-Institut für molekulare Physiologie Dortmund.

1. Gutachter: Prof. Dr. Dr. h.c. Herbert Waldmann
2. Gutachter: Prof. Dr. Daniel Summerer

Results presented in this thesis contributed to the following publications:

T. Mejuch, G. Garivet, W. Hofer, N. Kaiser, E. K. Fansa, C. Ehrt, O. Koch, M. Baumann, S. Ziegler, A. Wittinghofer, H. Waldmann, “Small-Molecule Inhibition of the UNC119–Cargo Interaction”, *Angew. Chem. Int. Ed.* **2017**, *56*, 6181-6186

N. Kaiser, T. Mejuch, R. Fedoryshchak, P. Janning, E. W. Tate, H. Waldmann, „Photoactivatable Myristic Acid Probes for UNC119-Cargo Interactions”, *ChemBioChem*, **2019**, *20*, 134-139

G. Garivet, W. Hofer, A. Konitsiotis, C. Klein, N. Kaiser, T. Mejuch, E. Fansa, A. Wittinghofer, P. I. H. Bastiaens, H. Waldmann, *Cell Chem. Biol.* (*Manuscript accepted*), **2019**

Für Tom und meine Familie

ACKNOWLEDGEMENTS

First and above all, I'm grateful to Prof. Dr. Herbert Waldmann, for giving me the opportunity to work on these interesting and challenging projects in such an excellent scientific environment. I highly appreciated the freedom to work independently and would like to thank him for his constant input, patient guidance and everything I have learned.

I would like to express my gratitude to Prof. Dr. Daniel Summerer for being my second examiner.

My deepest gratitude goes to Dr. Tom Mejuch for being an incredible mentor and friend. I would like to thank him for his excellent guidance, the endless scientific discussions and his constructive ideas. He gave me unconditioned support and continuous encouragement. His enthusiasm and passion for science are inspiring.

I am deeply grateful to Luca Laraia for his outstanding guidance and great support in the autophagy project. Even after leaving the MPI and becoming a group leader himself he would always find time to discuss scientific questions.

A special thanks goes to Dr. Petra Janning for the endless scientific discussions and sharing her MS-knowledge. With her constructive suggestions and professional expertise, she helped me to pursue my projects.

I'm grateful to the UNC119- and autophagy-team for working with them on such interesting and challenging projects. Special thanks goes to Dr. Eyad Fansa for his scientific input and help with the UNC119 protein crystallization. Furthermore, I would like to thank Dr. Daniel Foley for synthesis of the Autoquin derivatives and the fruitful scientific discussion. I would also like to thank Christine Nowak for expression of the UNC119 proteins and Alicia Dammers for her work on the autophagy project.

I would like to express my gratitude to Prof. Dr. Edward Tate for giving me the opportunity to shortly join his group, his scientific suggestions and the fruitful collaboration. A special thanks also goes to Dr. Roman Fedoryshchak for his support with the transferase assay and the

constructive comments. I would also like to thank the whole group for the warm welcome and the great time.

I gratefully acknowledge Dr. Sonja Sievers, Dr. Axel Pahl, Dr. Claude Ostermann, and the rest of the COMAS performing the screens of my compounds and answering my scientific questions regarding their assays. My thanks go to the MS-team, especially to Dr. Petra Janning, Andreas Brockmeyer and Malte Metz for processing and analyzing my samples. I would also like to thank Jens Warmers for labeling the TPP samples. I'm grateful to the NMR and HRMS departments of the TU Dortmund. Furthermore, I gratefully acknowledge the administration and facility management, as well as the IT department of the MPI. A special thanks goes to Brigitte Rose, Irina Shmatko and Melanie Wilkesmann.

I would like to thank the whole group for the great working atmosphere, the scientific input, the summer BBQs and fun TGIFs. Especially I would like to name: Dr. H  l  ne Adihou, Annina Burhop, Andreas Christoforow, Jana Flegel, Dr. Daniel Foley, Dr. Alexandra Friese, Dr. Michael Grigalunas, Elisabeth Hennes, Luca Laraia, Dr. Nancy Martinez, Dr. Tom Mejuch, Elena Reckzeh, Tabea Schneidewind, Dr. Peter 't Hart, Julian Wilke, Michael Winzker and Stefan Zimmermann.

Ich bin meinen Eltern und meiner Schwester unendlich dankbar, f  r ihre bedingungslose Unterst  tzung und endlose Ermutigung. Ich kann nicht in Worte fassen, wie viel mir das bedeutet.

אהובי, תודה על הכל!

TABLE OF CONTENTS

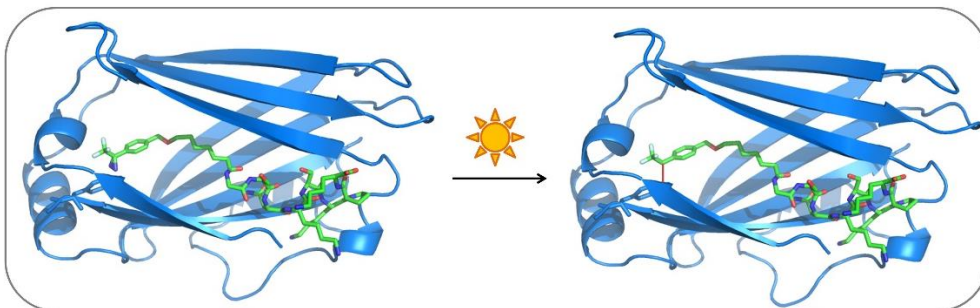
ABSTRACT	I
KURZZUSAMMENFASSUNG	IV
1. GENERAL INTRODUCTION	9
1.1. Chemical genetics approaches in chemical biology	9
1.2. Phenotypic screening	10
1.3. Target identification	11
1.3.1. Affinity enrichment.....	11
1.3.2. Labe free techniques.....	12
1.4. Target validation	15
2. DESIGN AND SYNTHESSES OF PHOTOACTIVATABLE MYRISTOYL ANALOGS FOR UNC119 CARGO INTERACTIONS	19
2.1. Introduction	19
2.1.1. Posttranslational modifications	19
2.1.2. Protein lipidation.....	20
2.1.3. The myristoyl-chaperone protein UNC119.....	22
2.1.4. Photoaffinity labelling probes	25
2.2. Motivation and goals	29
2.3. Results and discussion	31
2.3.1. Design and Syntheses of photoactivatable myristoyl analogues.....	31
2.3.2. Evaluation of Pacman-based probes.....	36
2.3.3. Mapping of the UNC119 binding pocket.....	43
2.3.4. Crystallization of photolabelled UNC119 proteins.....	46
2.3.5. Affinity enrichment of UNC119 proteins from lysate.....	50
2.3.6. Metabolic incorporation of Pacman-3.....	59
2.3.7. Thermal proteome profiling of UNC119 inhibitors.....	63
2.4. Summary and conclusion	67
3. TARGET IDENTIFICATION OF AUTOPHAGY INHIBITORS	69
3.1 Introduction	69
3.1.1. Autophagy.....	69
3.1.2. The molecular machinery of autophagy.....	70

3.1.3. Regulation of autophagy signaling.....	72
3.1.4. Autophagy in disease progression and prevention.....	75
3.1.5. Small molecule modulators of autophagy.....	76
3.1.6. Biological activity of cinchona alkaloids.....	78
3.1.7. Phenotypic screening in autophagy.....	79
3.2. Motivation and goals.....	83
3.3. Results and discussion.....	85
3.3.1. Identification of novel autophagy inhibitors by phenotypic screening.....	85
3.3.2. Oxazolidinones as autophagy inhibitors.....	87
3.3.3. Autoquin as an inhibitor of autophagy.....	95
3.3.4. Thienopyrimidines as autophagy inhibitors.....	113
3.3.5. Summary.....	129
4. EXPERIMENTAL PART.....	133
4.1 General chemical methods.....	133
4.2. Chemical synthesis.....	134
4.3. Materials for biological experiments.....	150
4.4. General biological methods.....	154
4.5. Biological methods UNC119 project.....	159
4.6. Biological methods autophagy project.....	167
5. APPENDIX.....	177
6. LIST OF ABBREVIATIONS.....	191
7. REFERENCES.....	199
Curriculum Vitae.....	211
Eidesstattliche Erklärung/ Affidavit.....	213

ABSTRACT

UNC119 is a chaperone protein, which regulates the trafficking of myristoylated proteins between cellular membranes. Even though these chaperones were extensively studied in the past two decades, only few of their interaction partners are known to date. Transient interactions and low affinities can hamper the identification of new previously unknown binding partners. Photoactivatable myristoyl analogues, which form a covalent bond upon irradiation, can serve as tools to overcome these obstacles and study protein-myristate interactions.

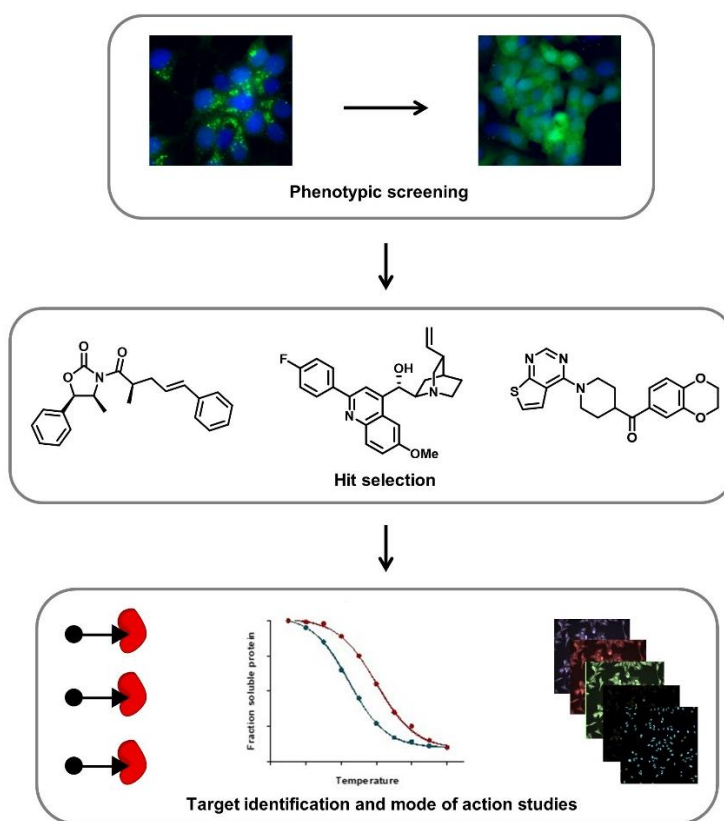
In the course of this project three different photoactivatable myristic acid analogues (Pacman 1-3) were designed and synthesized. These photoactivatable lipid analogues were attached to the short N-terminal peptide sequences, derived from myristoylated proteins Src and transducin alpha subunit Gnat1. The affinities of these probes to UNC119 proteins and photolabeling efficiencies were investigated. Pacman-1 and -2 based probes did not covalently label UNC119A and UNC119B. Pacman-3-Src established a covalent crosslink selectively with UNC119B protein, not labelling UNC119A. Pacman-3-Gnat covalently labelled both UNC119 proteins.



The photocrosslinking site of Pacman-3 probes was characterized within the hydrophobic pocket of UNC119. The myristate analogues binding mode is similar to the native myristate moiety. Co-crystallization of covalently labelled UNC119 proteins with Pacman probes was unsuccessful. Affinity enrichment of UNC119A and UNC119B from lysate by immobilized Pacman-peptide demonstrated specific interaction of the probe with UNC119 chaperones in a complex protein mixture. Substrate recognition of Pacman-3 by *N*-myristoyl transferase (NMT) enzymes from different organisms was investigated. Pacman-3 was not incorporated into a peptide substrate by human NMT. Remarkably, NMT derived from the protozoan parasite *Leishmania* and *Trypanosoma* recognized Pacman-3 as a substrate. Conclusively, Pacman-3 can serve as a valuable tool to investigate the role of UNC119 protein in these

parasites, to identify novel myristoyl-interaction partners and shed light on the myristoylome of different organisms.

Autophagy is an essential biological process for the regulation of cellular homeostasis and energy supply. Furthermore, this catabolic mechanism is involved in various severe disorders, such as cancer and neurodegenerative diseases. Modulators of autophagy are highly valuable tools, which can provide insight into the regulation of autophagic flux and unravel its role in various diseases. In order to obtain and characterize novel autophagy modulators, a medium throughput phenotypic screen was performed. Three structurally different potential inhibitors of autophagic flux were investigated in detail.



The first compound **51** was a representative of the oxazolidinone-scaffold, namely Autoxain. Autoxain inhibited starvation-induced autophagy with an IC_{50} of $2.7 \pm 1.9 \mu\text{M}$. A thermal proteome profiling experiment performed for target identification revealed a high amount of ribosomal proteins as potential interaction partners. This result indicated a similar mode of action as the oxazolidinone-based antibiotics linezolid and tedizolid. Both of these therapeutics exert their antibacterial activity by inhibition of protein biosynthesis via the ribosome. Due to a possible interaction of Autoxain with the ribosome, this potential autophagy inhibitor was not evaluated further.

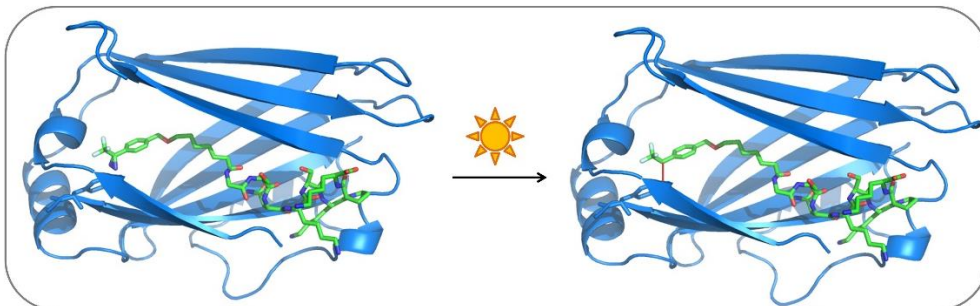
Another small molecule **52** that inhibited starvation-induced autophagy with the IC_{50} of $0.90 \pm 0.09 \mu\text{M}$ was Autoquin. Autoquin features high structural similarity to chloroquine, which suggests lysosomotropic activity. The compound has an indirect inhibitory effect on the lysosomal acid ceramidase and prevents autophagosome-lysosome fusion. Thus, Autoquin seems to interfere with correct function of the lysosome, which impairs autophagic flux. An affinity enrichment experiment identified ferrochelatase as a potential target of Autoquin. This suggested a similar mode of action to the known autophagy inhibitors salinomycin and ironomycin, which sequester Fe^{2+} in the lysosome. Autophagy plays a crucial role in maintenance of cellular iron homeostasis and novel tool compounds, which could shed light on this biological process are highly relevant.

The third potential inhibitor of autophagy **53** is Authipyrin, which inhibited starvation-induced autophagy with an IC_{50} of $0.02 \pm 0.01 \mu\text{M}$ and rapamycin-induced autophagy with an IC_{50} of $0.18 \pm 0.07 \mu\text{M}$. Authipyrin interferes with mitochondrial respiration by direct inhibition of complex I. Complex I activity is required for regular autophagic flux. Furthermore, mitophagy is frequently dysregulated in patients suffering from Parkinson's disease. However, the exact mechanism underlying this interplay remains to be elucidated. Authipyrin is a structurally novel tool compound, which can be employed to investigate this interdependency in detail.

KURZZUSAMMENFASSUNG

UNC119 ist ein Chaperon-Protein, welches den Transport myristoylierter Proteine zwischen zellulären Membranen reguliert. Obwohl dieses Chaperon in den vergangenen zwei Jahrzehnten intensiv erforscht wurde, sind bislang nur wenige Interaktionspartner bekannt. Transiente Interaktionen und geringe Affinitäten können die Identifizierung bisher unbekannter Bindungspartner erschweren. Photoaktivierbare Myristinsäureanaloga, welche bei Bestrahlung eine kovalente Bindung eingehen, können nützlich sein, um diese Herausforderungen zu überwinden und Protein-Myristat-Interaktionen zu untersuchen.

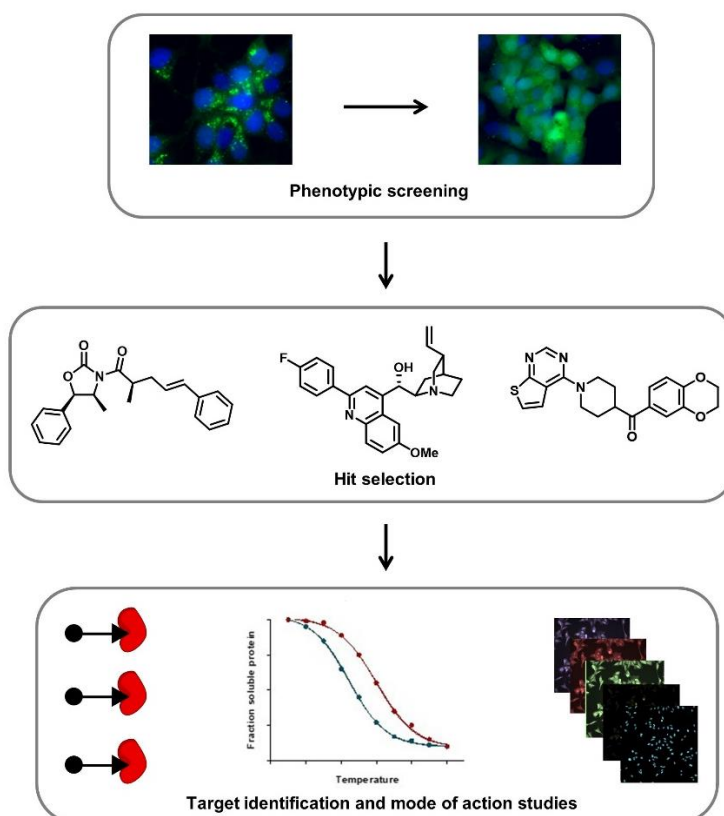
Im Verlauf dieses Projekts wurden drei verschiedene photoaktivierbare Myristatanaloga entworfen und synthetisiert. Diese photoaktivierbaren Lipidanaloga wurden an kurze N-terminale Peptidsequenzen gebunden, welche von den myristoylierten Proteinen Src und der transducin alpha Untereinheit Gnat1 abgeleitet wurden. Anschließend wurde die Affinität dieser Sonden zu UNC119 und die Effizienz der Photomarkierung untersucht. Auf Pacman-1 und -2 basierende Sonden, markierten weder UNC119A noch UNC119B. Pacman-3-Src ging selektiv eine kovalente Querverbindung mit dem UNC119B Protein ein, markierte aber nicht UNC119A. Pacman-3-Gnat markierte kovalent beide UNC119 Proteine.



Charakterisierung der Lage der Photomarkierung durch Pacman-3 innerhalb der hydrophoben Tasche zeigte, dass der Bindungsmodus des Myristinsäureanalog ähnlich zu dem der nativen Myristinsäure-Gruppe ist. Co-Kristallisation des kovalent markierten UNC119 Proteins mit der Pacman-Sonde war nicht erfolgreich. Affinitätsanreicherung von UNC119A und UNC119B aus Lysat durch immobilisiertes Pacman-Peptid zeigte eine spezifische Interaktion der Sonde mit UNC119 Chaperonen in einem komplexen Proteingemisch. Anschließend wurde die Substraterkennung von Pacman-3 durch *N*-Myristoyl Transferase (NMT) Enzyme aus unterschiedlichen Organismen untersucht. Pacman-3 wurde nicht durch die humane NMT auf das Peptidsubstrat übertragen. Bemerkenswerterweise erkannten NMTs, aus den parasitischen Protozoen *Leishmania* und *Trypanosoma*, Pacman-3 als Substrat. Daher könnte Pacman-3 als

wertvolles Hilfsmittel dienen, um die Rolle von UNC119 in diesen Parasiten zu erforschen, neue Myristoyl-Interaktionspartner zu identifizieren und das Myristoylom unterschiedlicher Organismen zu beleuchten.

Autophagie ist ein essentieller biologischer Prozess für die Regulierung der zellulären Homöostase und Energieversorgung. Dieser katabolische Mechanismus ist an verschiedenen schweren Erkrankungen, einschließlich Krebs und neurodegenerativen Krankheiten, beteiligt. Autophagie-Modulatoren sind äußerst wertvolle Hilfsmittel, welche Einsicht in die Regulierung der Autophagie verschaffen und deren Rolle in verschiedenen Krankheiten entschlüsseln können. Um neue Autophagie-Modulatoren zu finden und zu charakterisieren wurde ein Screen mit mittlerem Durchsatz durchgeführt.



Verbindung **51** ist ein Stellvertreter des Oxazolidin-Gerüsts, genannt Autoxain. Autoxain inhibiert Hunger-induzierte Autophagie mit einem IC_{50} von $2.7 \pm 1.9 \mu\text{M}$. Ein Experiment zur Erstellung des thermischen Proteom Profils (thermal proteome profiling), welches zur Target-Identifizierung diente, ergab eine hohe Anzahl ribosomaler Proteine als potentielle Interaktionspartner. Dieses Ergebnis weist auf einen ähnliches Wirkprinzip, wie das der Oxazolidin-basierten Antibiotika Linezolid und Tedizolid hin. Beide dieser Therapeutika üben ihre antibakterielle Wirkung durch die Inhibierung der Proteinbiosynthese durch das Ribosom

aus. Aufgrund der möglichen Interaktion Autoxains mit dem Ribosom wurde dieser potentielle Autophagie-Inhibitor nicht weiter evaluiert.

Substanz **52**, die durch Aushungern induzierte Autophagie mit einem IC_{50} Wert von $0.90 \pm 0.09 \mu\text{M}$ inhibierte, war Autoquin. Autoquin ist strukturell mit Chloroquine verwandt, was eine lysosomotropische Aktivität vermuten lässt. Die Verbindung hat einen direkten inhibierenden Effekt auf die lysosomale saure Ceramidase und verhindert die Fusion des Autophagosoms mit dem Lysosom, welches den Verlauf der Autophagie beeinträchtigt. Ein Experiment zur Affinitätsanreicherung identifizierte Ferrochelatase als ein potentielles Target von Autoquin. Dies weist auf ein ähnliches Wirkprinzip, wie die bekannten Autophagie-Inhibitoren Salinomycin und Ironomycin hin, welche Fe^{2+} im Lysosom anreichern. Autophagie spielt eine wesentliche Rolle in der Erhaltung der zellulären Eisen-Homöostase und neue Hilfsmittel, welche diesen biologischen Prozess aufklären können, sind hochrelevant.

Der potentielle Autophagie-Inhibitor Authipyrin **53**, inhibiert Hunger-induzierte Autophagie mit einem IC_{50} von $0.02 \pm 0.01 \mu\text{M}$ und Rapamycin-induzierte Autophagie mit einem IC_{50} von $0.18 \pm 0.07 \mu\text{M}$. Authipyrin beeinträchtigt die mitochondrielle Atmung durch die direkte Inhibierung von Komplex I. Komplex I Aktivität wird für den normalen Verlauf der Autophagie benötigt. Weiterhin weißt die Mitophagie häufig Fehlfunktionen in Patienten auf, welche unter Parkinson leiden. Allerdings ist der genaue Mechanismus, welcher dieser Erkrankung zugrunde liegt noch ungeklärt. Authipyrin ist ein strukturell neues Hilfsmittel, welches dafür verwendet werden kann diese Wechselbeziehung im Detail zu untersuchen.

1. GENERAL INTRODUCTION

1.1. Chemical genetic approaches in chemical biology

Chemical Biology describes the interdisciplinary field comprising biology, chemistry and pharmacology. In this discipline bioactive molecules are developed and employed to investigate biological questions. The selective alteration of a phenotype with chemical tool compounds is a valid strategy to study biological processes and signaling pathways. Furthermore, the function of cellular macromolecules including proteins, lipids and nucleic acids can be investigated on a mechanistic level.^{[1],[2]}

Obtaining biologically relevant compounds with a desired activity can be a challenging task, especially due to the large size of chemical space. One strategy to overcome this obstacle is biology-oriented synthesis (BIOS). Biological macromolecules and their respective ligands evolved interdependently. Thus, certain small molecule scaffolds are biologically favored. The bioactivity of these natural products is proposed to originate from the scaffold itself. BIOS employs this hypothesis by creating small molecule libraries derived from selected natural product scaffolds. By introducing different substituents and functional groups the desired bioactivity can be fine-tuned.^{[3],[4]} However, libraries based on those privileged scaffolds often feature equivalent biological activity to the parent natural products they are derived from. The fusion of two or more natural product-based fragments can serve as a gateway to novel biological functions. These novel chemical entities are referred to as pseudo natural products.^[5]

Pseudo natural product or BIOS libraries can subsequently be subjected to chemical genetic-based screening approaches, to identify compounds with a desired biological activity. In chemical genetics biological processes can be altered by small molecules instead of directly influencing the genetic code. This has the advantage that, in contrast to the conventional method, the applied changes are temporary and reversible. Moreover, chemical genetics gives access to a dose-dependent modification of the respective biological process and compound treatment can be performed at arbitrary time points during the experiment.^[6]

Two different approaches exist in chemical genetics, forward and reverse chemical genetics (Figure 1). In forward chemical genetics compounds that cause a desired change in cellular or organismal phenotype are identified. Subsequently, the biological target of the most promising hit compound has to be identified and validated.^[7] The forward chemical genetics approach can be beneficial to identify novel therapeutic targets for the pharmaceutical industry.

Furthermore, the role of a protein in a certain biological process or signaling pathway can be studied directly. In reverse chemical genetics a protein of interest is selected and screened against a compound library to determine interaction partners. Afterwards, the cellular effect and phenotypic influence of the chosen hit compound are investigated (Figure 1).^[8]

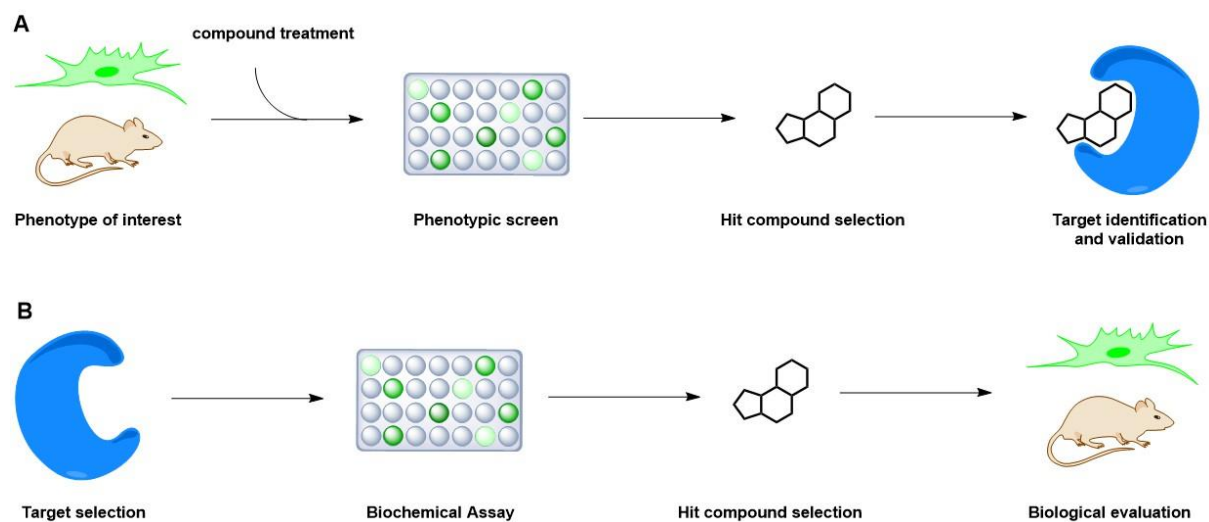


Figure 1: Schematic representation of chemical genetic approaches. **A:** Forward chemical genetics. **B:** Reverse chemical genetics.

1.2. Phenotypic screening

Phenotypic screening offers unbiased identification of bioactive substances. The screening takes place on organismal or cellular level, which should provide physiologically relevant results. Due to recent advances in technology and the development of robotic screening platforms, the efficiency of phenotypic screens has improved significantly. This makes it suitable for the analysis of chemical libraries by high throughput screening (HTS). Phenotypic screens can for instance be applied to identify disease-relevant compounds, as well as those substances that affect certain signaling pathways or influence cell viability.^[9]

In order to determine cell viability, fluorescent dyes can be employed. One such dye is propidium iodide, which interacts with nucleic acids. Propidium iodide is not membrane permeable and therefore unable to enter viable cells. However, cell death results in compromised cell membrane integrity, enabling propidium iodide to access and intercalate with the DNA of these cells. Hence, propidium iodide stains exclusively dead cells.^[10]

Furthermore, phenotypic screens are applied to investigate cellular signaling pathways. The readout can for instance be a fluorescent protein conjugate, which is expressed downstream of a certain signaling pathway.^[11] The green fluorescent protein (GFP) can be fused to proteins of interest and expressed in cells as well as *in vivo*. Optimization regarding its temperature sensitivity, stability and brightness provided the enhanced GFP (eGFP). The eGFP protein enables tracking of cellular protein dynamics and cellular visualization under minimal photobleaching.^[12] Another experimental readout is based on reporter genes (e.g. luciferase). In this technique the generation of a detectable fluorescence or luminescence signal directly correlates with pathway activity.^{[13],[14]} The main advantage of a phenotypic screen based on signaling pathways is that a bioactive compound could possibly target every component at various levels of the pathway. Thus, signaling pathway assays are especially beneficial for identification of novel targets.^[9]

1.3. Target identification

A crucial step in the development of novel bioactive compounds from phenotypic screens is target identification and validation. To understand the biological mechanism underlying the observed phenotypic changes, the molecular interaction partner of a small molecule has to be determined.^[15] There are various different methods available to achieve this. However, target identification is a time-consuming process and, depending on target and compound, some approaches are better suited than others.

1.3.1. Affinity enrichment

One of the most widely used methods for target identification is affinity enrichment. This method requires ligand immobilization on a solid support. Therefore, the bioactive compound is chemically modified with a suitable linker. The linker serves as a spacer between solid support and compound, to avoid steric hindrance. To exclude non-specific binders, an inactive compound is employed as a negative control. Subsequently, the negative and positive probes are incubated with cell lysate. The small molecules function as “bait” and enrich interaction partners from the lysate. The amount of non-specific binding partners is further reduced by several thorough washing steps. The remaining proteins are digested by proteases, which generate specific peptide fragments. These peptides can be annotated to their respective protein

of origin with the aid of databases, such as Uniprot. Subsequently, the proteins enriched by the positive and negative probes are analyzed. Only those proteins which are significantly enriched with the positive probe in comparison to the negative probe are considered as possible targets (Figure 2).

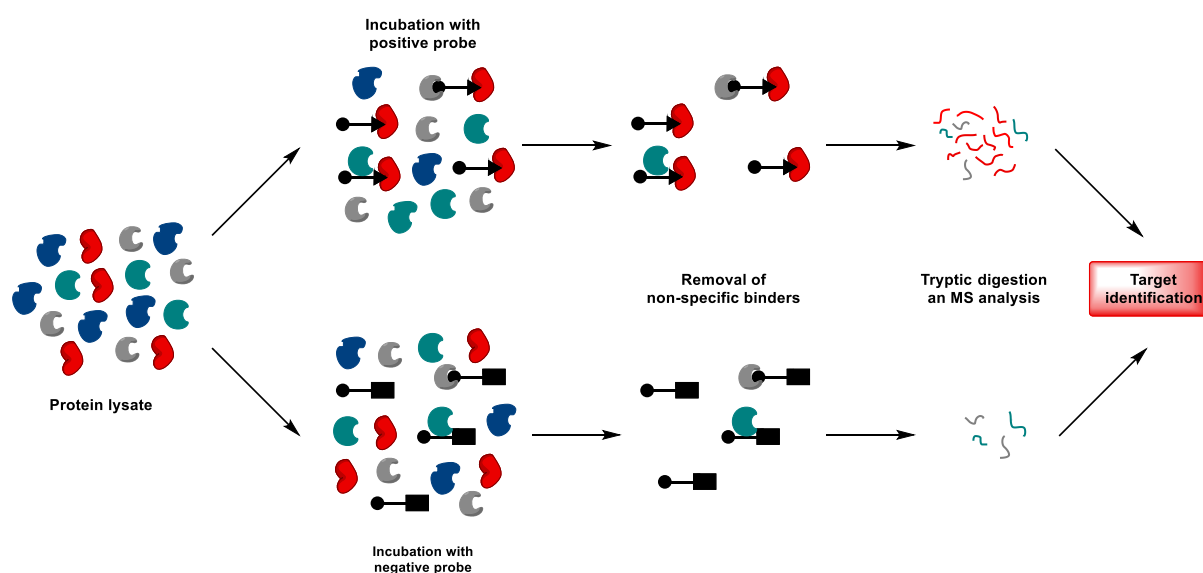


Figure 2: Schematic representation of affinity enrichment.

However, this method usually requires high affinity ligands, since low affinity interactions might not be stable during washing and result in loss of target protein.^{[16],[17]} Another disadvantage of this method is the chemical modification by the linker, which can influence the target affinity of the bioactive compound. Thus, structure activity relationship studies are helpful to determine a suitable modification point, which is not required for compound activity. In order to avoid impairment by the linker, several label free techniques were developed.

1.3.2. Label free techniques

Label free target identification methods have several advantages. One main advantage is that they do not require extensive modification of the bioactive compound. Thus, laborious structure activity relationship (SAR) studies to identify a suitable site for linker attachment can be avoided.^[18] A novel method for label free target identification is the cellular thermal shift assay (CETSA). This approach is based on the assumption that a compound can influence the thermal stability of a protein. A ligand-treated target protein should have a different melting

temperature than the control. This shift in the melting temperature can be an indication for target engagement (Figure 3). Until now the thermal shift assay was mostly performed with purified proteins. However, CETSA allows analysis of complex protein mixtures. Aliquots of compound and control treated cell lysates are subjected to incubation at various temperatures. Denaturated proteins tend to form aggregates and precipitate and can therefore be removed by ultracentrifugation. The supernatant is subsequently analyzed by immunoblotting. Thus, the soluble fraction of the protein of interest can be quantified and the shift in melting temperature determined.^[19] However, to define the correct compound concentration for the CETSA experiment might be a challenge. If the melting curve of the potential target protein is available, an isothermal dose response fingerprint (ITDRF) can be generated. With an ITDRF the effect of ligand concentration on protein stability can be determined at a constant temperature, which is typically close to the melting point.^[20]

CETSA is usually limited to analysis of only few proteins, since the detection is performed by immunoblotting. However, in combination with high-resolution mass spectrometry (HRMS) this method can also be applied in a proteome-wide manner as thermal proteome profiling (TPP). Therefore, the samples are digested by addition of trypsin protease after heat treatment. Subsequent labeling with neutron-encoded isobaric mass tagging reagents (TMT10), allows differentiation of the single temperature points (Figure 3).^[21] Thus, melting curves for all identified proteins can be generated. Addition of detergents, such as NP40, during cell lysate preparation improves the solubility of membrane proteins and increases the overall amount of detected proteins.^[22] TPP is an unbiased method and in comparison to CETSA does not necessarily require a target hypothesis. Thus, TPP can also be applied for *de novo* target identification.^[23]

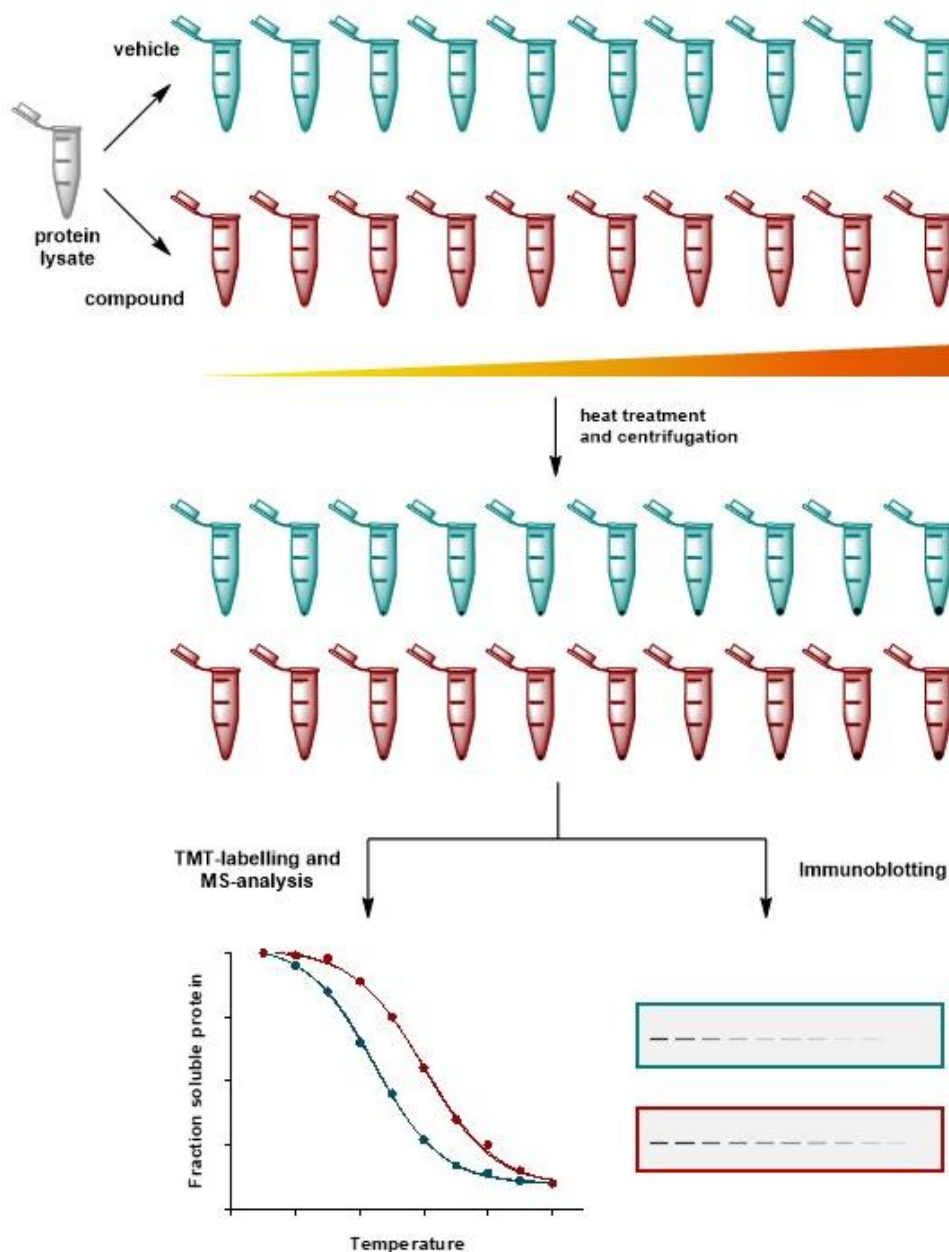


Figure 3: Schematic representation of TPP (left) and CETSA (right)

Another approach for mode of action prediction and target identification is the cell painting assay (CPA) (Figure 4). The CPA is an unbiased image-based, high-content screening approach. Standard phenotypic screening usually focuses on alteration of one specific parameter. The CPA also relies on cell morphology profiling for compound evaluation. However, in contrast to traditional image-based approaches, a large number of cellular features is investigated in parallel.^[24] In this assay five fluorescent dyes are employed, which can be detected in different channels. These fluorophores stain important cellular organelles or

components, such as the nuclei, mitochondria, the endoplasmic reticulum (ER) and the golgi apparatus. Furthermore, the cell membrane and cytoskeleton, as well as cytoplasmic RNA and nucleoli are visualized. Cell-based screening can be performed with extensive compound libraries. The readout is performed by means of high throughput fluorescence microscopy. Subsequently, hundreds of features are detected and analyzed to determine possible morphological alterations. The collectivity of these data for each compound provides a unique fingerprint.

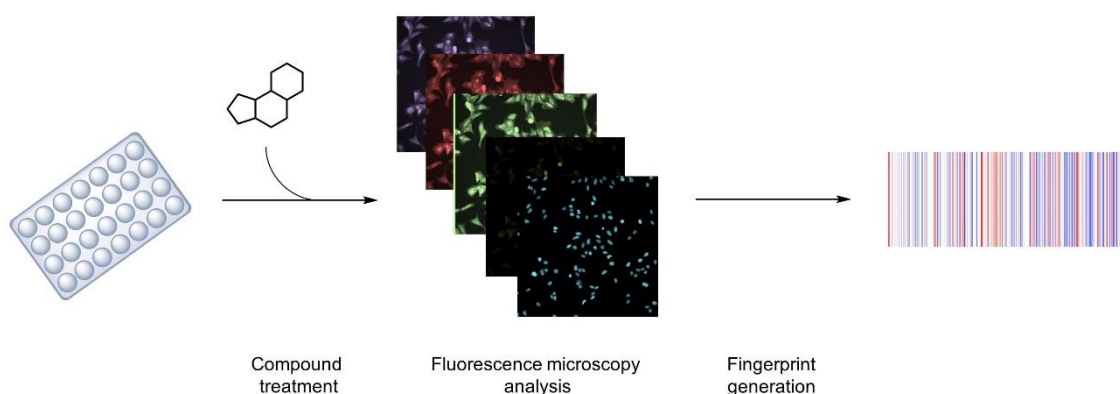


Figure 4: Representative scheme of the cell painting assay.

The fingerprint of a certain bioactive compound is compared to those of reference compounds.^[24] Similarity to a reference compound might indicate the molecular target. Furthermore, the analyzed compound could have a similar mode of action or affect the same signaling pathway. Thus, for efficient and reliable data evaluation, CPA requires numerous reference compounds. These references should be biologically and structurally diverse molecules with known target or mode of action.

1.4. Target validation

Target validation forms the final step in the forward chemical genetics approach. Therefore, target engagement has to be demonstrated. Furthermore, a connection between the observed phenotype and the potential target should be established. Often target identification yields not a single, but several different targets. Initially, the involvement of these possible targets in the

investigated biological process is researched, to prioritize certain candidates. Subsequently, suitable validation methods are chosen.

If target identification included affinity enrichment, a competitive pulldown is often the method of choice for validation. Here, protein lysates are incubated with an excess of the unmodified active compound prior to protein enrichment. The compound should interact with the target protein and thus interfere with binding of the immobilized small molecule. Those proteins, which are detected during affinity enrichment, but not in the competition assay can be regarded as targets.^[25] A method for target validation that requires compound modification with a fluorophore is fluorescence polarization (FP). In the FP assay, a protein-ligand mixture is excited with polarized light. Due to molecular rotation the light depolarizes in a rate proportional to the size of the labeled species. While small molecules depolarize quickly, the depolarization rate for macromolecules is higher. Thus, protein-ligand interaction will result in significant decrease of the depolarization rate.^[26]

Furthermore, target interaction can also be shown in a label free manner by previously mentioned CETSA method. After establishment of a target hypothesis, thermal protein stability can be detected by immunoblotting with a specific antibody. While CETSA is temperature dependent the ITDRF can show target engagement in a dose-dependent manner at a constant temperature.^[27] Another method to determine the influence of a ligand on protein stability is differential scanning fluorimetry (DSF). Upon unfolding of a protein hydrophobic domains are exposed. For DSF a dye is employed, which is quenched in aqueous environment and becomes highly fluorescent in non-polar surroundings. Thus, protein denaturation is characterized by a significant increase in fluorescence intensity.^[28] Further biophysical assays to show ligand target interaction are isothermal titration calorimetry (ITC) and circular dichroism (CD).^{[29].[30]}

Since protein-ligand interaction is not sufficient for alteration of protein function, additional assays are required for target validation. Provided that the potential target is an enzyme, the possible alteration of catalytic activity could be studied. If inhibitors for the respective target are already known, they can also be analyzed to determine whether they cause similar changes in phenotype. Moreover, knock-down experiments based on RNA interference are often utilized in attempts to phenocopy the effect of the bioactive species of interest.^[25]

In order to gain structural information of a protein-ligand complex on a molecular level, X-ray crystallography is a powerful tool. However, even if crystallization conditions for the purified protein are known, co-crystallization of small molecule and a protein represents a major

challenge. Different factors that can influence co-crystallization include protein and ligand concentration, temperature and the use of additives. Thus, crystallization of a protein ligand complex is a time-consuming endeavor and requires extensive optimization.^{[31],[32]}

Bioactive compounds with thoroughly validated targets are invaluable tool compounds for the investigation of signaling pathways and biological processes. Furthermore, the discovery of novel targets and the elucidation of their biological function is of utmost importance for the discovery of novel therapeutic targets and the development of efficient pharmaceuticals for clinical application.

2. DESIGN AND SYNTHESIS OF PHOTOACTIVATABLE MYRISTIC ACID ANALOGUES FOR UNC119 CARGO INTERACTIONS

2.1. Introduction

An essential component of numerous biological processes is the specific interaction of diverse proteins. These protein-protein interactions (PPI) can be characterized according to their complex stability. While some interactions are only transient, other proteins require permanent complex formation to obtain their native structure.^[33] The protein surfaces involved in PPI interactions are complementary and often highly hydrophobic. Thus, the main driving force that underlies the interaction is the reduction of the non-polar surface area.^[34]

The collectivity of all PPIs in an organism is referred to as the interactome. A protein network that represents a certain cluster of these interactions can be visualized in an interaction map. Most cellular processes and the resulting phenotypes are characterized by those complex PPI networks. Thus, elucidation of the interactome is highly important to fully understand relevant genotype-phenotype connections and the respective biological processes on a system wide level.^[35] The interaction maps that arise therefrom can also assist in prediction of possible protein function and drug targets for novel therapeutics.^[36] However, PPIs are often highly dynamic, which creates further challenges in the prediction and establishment of the respective maps.

2.1.1. Posttranslational modifications

The complexity of an organism is not only determined by its genome, but predominantly by the proteome. The diversity of the proteome is on one hand regulated by alternative splicing during gene expression and processing. The second influencing factor is posttranslational modifications (PTM) (Figure 5).^[37] Even though the name implicates that the PTM occurs after translation, the modification can also take place co-translationally. Those modifications describe the proteolytic cleavage or covalent attachment of a functional group or macromolecule to one or more amino acids of a protein. This highly dynamic process can be reversible as well as irreversible and alters the functionality of the respective protein. PTMs can change the active state and localization of a protein and regulate its turnover and interaction with other proteins.^[38] To date more than 300 different physiological PTMs were identified with approximately 5% of the eukaryotic proteome designated to the implementation of these

modifications.^{[39],[40]} The five most common PTMs are acylation, alkylation, phosphorylation, glycosylation and oxidation. The possible combination of various PTMs give rise to a severe increase in proteome heterogeneity.^[39] Furthermore, PTMs facilitate a quick reaction to changes in external and internal cellular conditions. Recognition and interpretation of these modifications is performed by specific interaction domains.^[41]

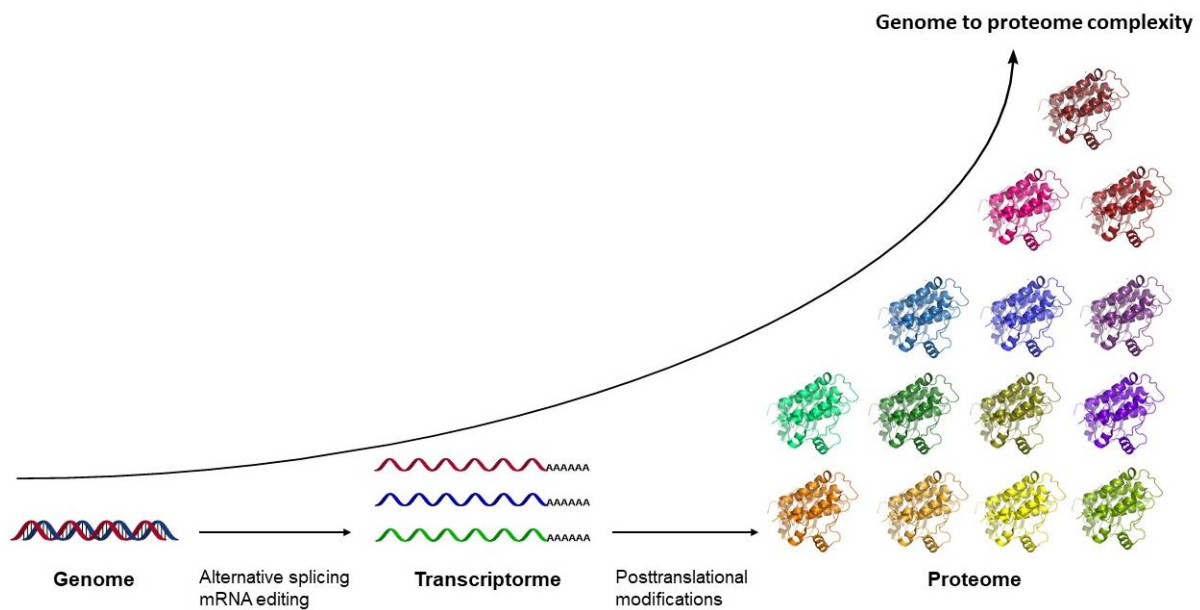


Figure 5: Exponential increase of complexity from genome to proteome due to RNA processing and posttranslational modifications.

A modification that regulates the cellular localization of a protein is lipidation, which describes the covalent attachment of a lipid moiety to an amino acid side chain or the C- or N-terminus. The hydrophobic lipid moiety induces membrane association of the respective proteins and is often crucial for biologic function. Lipidation is of central importance in cellular trafficking and signaling, as well as protein-protein and protein-lipid interactions.^[42]

2.1.2. Protein lipidation

Isoprenylation (*S*-prenylation) and acylation (*S*-palmitoylation and *N*-myristoylation) are the most thoroughly researched lipid modifications (Figure 6). During the process of *S*-prenylation a C15 farnesyl or C20 geranylgeranyl moiety is attached to a cysteine residue in proximity of the C-terminus. The consensus sequence for prenylation is referred to as the CaaX box, in

which C represents a cysteine and A is an aliphatic amino acid, while X can be any amino acid. However, the nature of X influences the substrate specificity.^[42] If serine, methionine, glutamine or alanine are in X position farnesylation occurs, while leucine results in geranylgeranylation. The lipid moiety is attached to the side chain of cysteine through thioether formation followed by subsequent cleavage of the three C-terminal residues (aaX) by the Ras converting enzyme 1. Finally, the resulting C-terminal cysteine residue is methylated by the isoprenylcysteine methyltransferase.^[43] However, not all isoprenylated proteins feature a CaaX box, especially double prenylated proteins are characterized by a CC- or CXC-motif. Only in case of the CXC-motif, the C-terminal cysteine is methylated.^[44]

During *S*-palmitoylation a cysteine side chain is modified by reaction with the C16 palmitate. The attachment is catalyzed by the palmitoyl-transferase through formation of a labile thioester. In contrast to the other two mentioned lipid modifications, *S*-palmitoylation is reversible, which creates a “switch-like” system.^{[45],[46]} To date, no distinct consensus sequence was identified for palmitoylation.^{[47],[48]} The modification can occur independently or in combination with other lipid PTM, including prenylation and *N*-myristoylation.^[49]

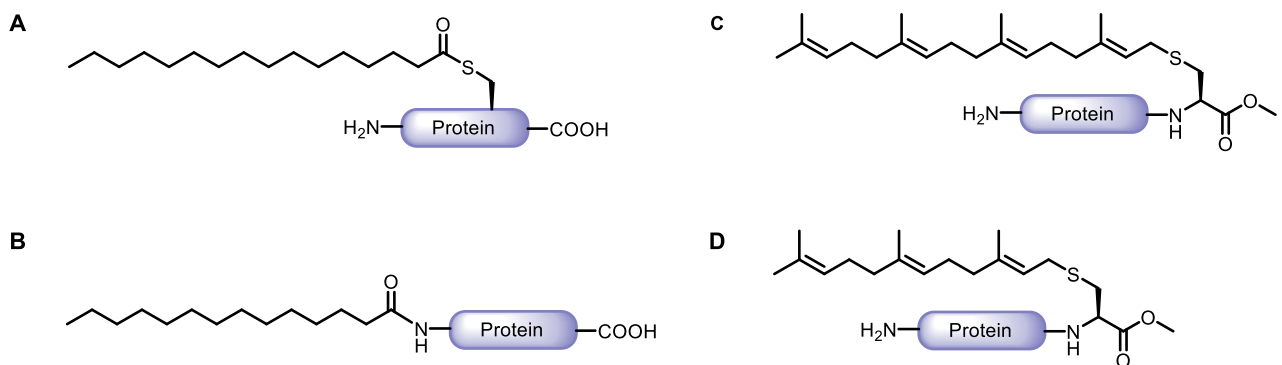


Figure 6: The four most studied lipid modifications. **A:** *S*-Palmitoylation; **B:** *N*-Myristoylation; **C:** *S*-Geranylgeranylation; **D:** *S*-Farnesylation.

N-Myristoylation describes the covalent attachment of C14 saturated fatty acid to the N-terminal glycine of a protein (Figure 5).^[50] This lipidation usually occurs co-translationally.^[51] Myristoylation is found almost exclusively in eukaryotes and viruses. This modification plays also an essential role in parasite viability.^[52] Attachment of the myristate moiety is catalyzed by the *N*-myristoyl transferase (NMT). Initially, myristoyl-CoA binds to NMT, which initiates a conformational change and creates a binding-site for the peptide moiety. Subsequently,

transfer of the myristate onto the peptide substrate is catalyzed and the respective product released.^[53] The consensus sequence for myristoylation is Met-Gly-X-X-X-Ser/Thr. Initially, the initiator methionine is removed prior to lipidation by the methionine amino peptidase. The now N-terminal glycine is essential for myristoylation and cannot be substituted by any other residue. While the subsequent three amino acids are variable, serine or threonine in 6 position and arginine or lysine in 7/8 position are favored.^[54]

Most myristoylated proteins are localized at cellular membranes, where the lipid moiety promotes reversible membrane attachment. However, insertion of the myristate chain into the lipid bilayer is often not sufficient for stable localization. Thus, a second signal might be required to reinforce the membrane interaction. Such a signal could be a polybasic stretch on the protein surface that binds to the negatively charged phospholipids of the membrane.^[54] Also a second lipid modification or the interaction with other membrane proteins would increase overall membrane affinity.^[55] Another proposed mechanism to regulate membrane binding is the myristoyl switch. Ligand binding can induce a conformational change, which sequesters the myristate within an intramolecular hydrophobic pocket of the protein. This mechanism triggers protein release from the membrane.^[56] Furthermore, a myristoyl switch facilitates cytosolic trafficking of lipidated proteins. Due to the presence of the lipid moiety myristoylated proteins are hardly soluble. However, inside the hydrophobic pocket the myristate moiety is concealed from the hydrophilic environment of the cytoplasm. Overall solubility of the protein is increased significantly, which enables trafficking through the cytosol.^[57] Proteins that lack a myristoyl switch require the assistance of a chaperone protein to cross the cytosol. One such chaperone of myristoylated proteins is uncoordinated 119 (UNC119).

2.1.3. The myristoyl-chaperone protein UNC119

UNC119 is a lipid-binding protein that regulates the transport of myristoylated proteins between different cellular membranes.^[58] This chaperone protein was first identified in *C. elegans*, due to the fact that a mutated form caused severe abnormalities in chemosensation, feeding behavior and locomotion.^[59] Following this discovery, ubiquitous expression of UNC119 was described in various different organisms including animals and plants. UNC119 proteins share significant sequence similarity with PDE δ , which is a farnesyl-binding protein. In vertebrates, two different homologues of UNC119 are expressed, termed UNC119A and UNC119B with a respective size of 240 and 251 amino acids.^[60] The two homologues exhibit

a sequence homology of about 55%.^[61] Highest similarity occurs in the C-terminal region, while the N-terminal tail deviates. UNC119A was only recently co-crystalized with a myristoylated nephrocystin-3 (NPHP3) peptide (Figure 7).^[62]

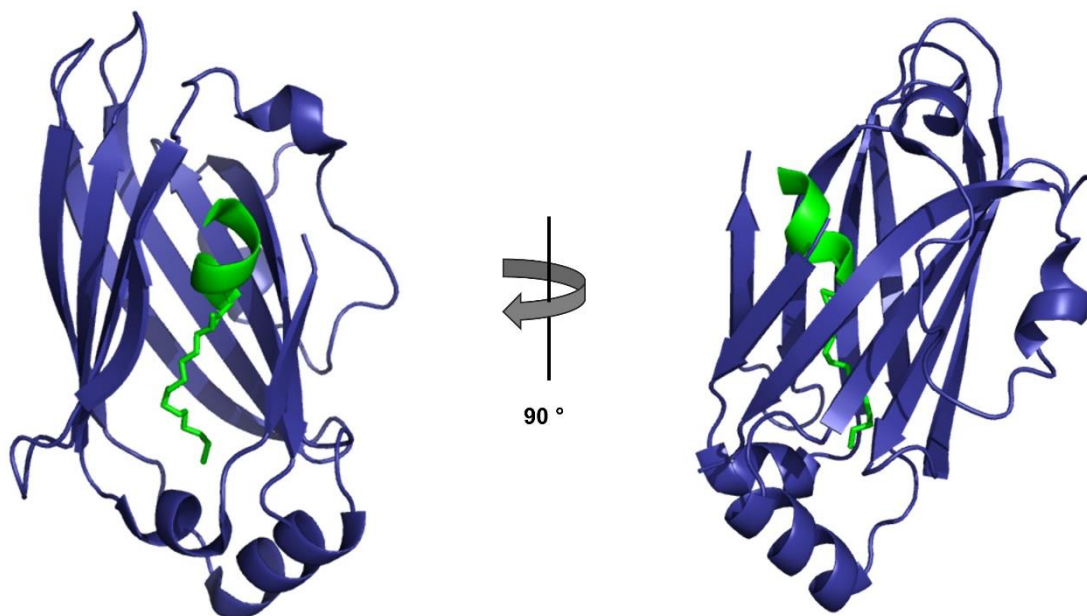


Figure 7: Co-crystal structure of UNC119A and myristoylated NPHP3 subunit (PDB code: 5L7K).

An immunoglobulin-like β -sandwich fold dominates the structure of this chaperone protein, which creates a hydrophobic cavity. The lipid chain can insert into this binding pocket together with the first N-terminal amino acids. The amino acids in +2 and +3 position, which follow the myristoylated glycine are postulated to have a great influence on cargo affinity. High affinity interaction partners have small amino acids such as glycine, alanine and serine in these positions. Cargo proteins with low affinity feature more bulky amino acids, such as phenylalanine and glutamine, which might cause minor steric clashes with the UNC119 protein residues.^[62] The hydrophobic pocket itself is characterized by 11 highly conserved phenylalanine residues. These aromatic amino acids play a key role in lipid binding, while especially the residues on the bottom of the binding site (F144, F148, and F207) have the greatest influence (Figure 8).^[63]

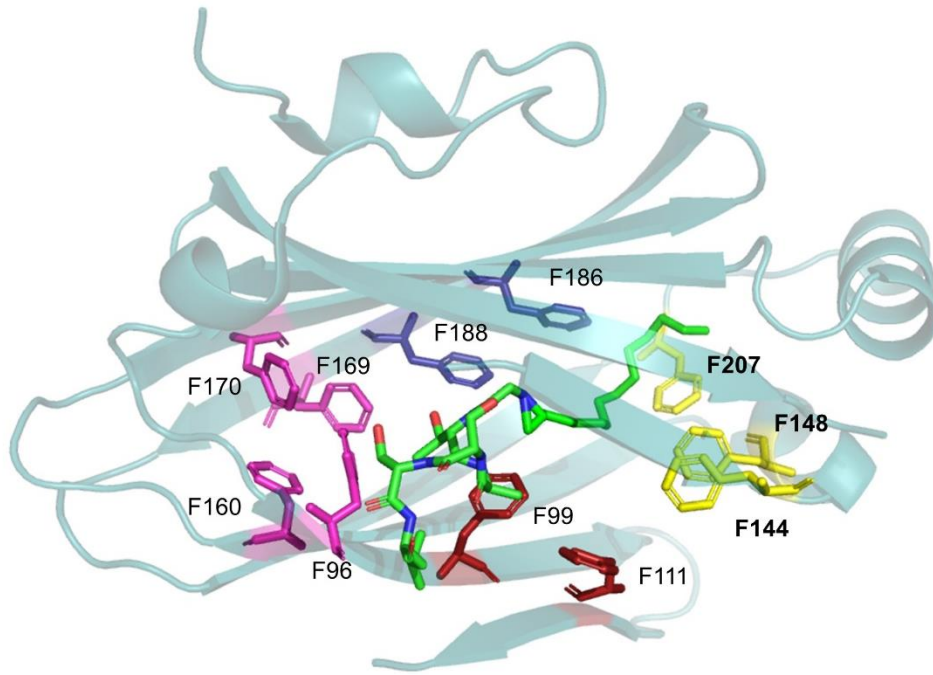


Figure 8: Highly conserved phenylalanine residues within the binding site of UNC119A. The most important residues (F207, F148, and F144) for binding of myristoylated proteins are highlighted in bold. Adaptation from Wright et al.^[63]

Myristoylated cargo can be allosterically released by the small GTPases Arf-like proteins 2 and 3 (Arl2 and Arl3). However, only Arl3 is able to unload high affinity interaction partners. While myristoylated cargo proteins with high affinity are located in the cilia, those with low affinity reside in the cytoplasm. Thus, Arl2 and Arl3 seem to regulate the sorting of myristoylated proteins between cilia and cytoplasm.^{[61],[62]} UNC119 is predominantly expressed in synaptic regions and the retinal photoreceptor inner segments. For this reason, human UNC119A is also referred to as human retina gene 4 (HRG4). In the retina the UNC119 protein is responsible for translocation of the guanine nucleotide binding protein (G protein) subunit alpha transducin 1 and 2 (Gnat1 and Gnat2) from the inner to the outer segment as part of the light-adaption mechanism.^{[58],[64]} Furthermore, UNC119 is required for trafficking of NPHP3 to the ciliary membrane. NPHP3 is essential for correct function and development of the cilia.^[63] The UNC119 protein also interacts with and controls plasma membrane localization of the proto-oncogene Src family kinases (SFK).^{[65],[66]} Bastiaens et al. reported the UNC119-mediated dynamics of the spatial Src cycle. The chaperone protein solubilizes Src from the cytoplasm and transports it by diffusion to the recycling endosome (RE). Arl2 and Arl3 are localized close to the RE and unload Src from UNC119, where the kinase binds to the RE membrane and those

membranes in close proximity. While Src is strongly interacting with RE due to its polybasic stretch, palmitoylatable SFKs are located at the Golgi. The kinases are subsequently relocated through vesicular transport to the plasma membrane, which restores their signaling activity.^[66] Furthermore, UNC119 trafficking of the SFK lymphocyte-specific protein tyrosine kinase (Lck) strongly contributes to initiation of T-cell receptor (TCR) antigen signaling and formation of the immune synapse. However, UNC119 does not only interact with SFKs through the lipid moiety. It was also postulated that the UNC119 protein can bind to Src homology 2 and 3 (SH2 and SH3) domains.^[67] This interaction causes SFK activation, which is crucial for TCR signaling.^[68] Furthermore, apparent SFKs play a crucial role in tumor development and progression.^[69] Mutation of UNC119 is known to be involved in different diseases, including the retinopathy cone-rod dystrophy and the immunodeficiency idiopathic CD4 lymphocytopenia.^{[70],[71]} Thus, the UNC119 protein would be an attractive target for drug development. Recently, Squarunkin A the first small molecule inhibitor of this chaperone protein was developed. Squarunkin A prevents activation of Src kinase by UNC119.^[72] In a subsequent study, another UNC119 inhibitor was shown to interfere with Src localization to the plasma membrane.^[73]

2.1.4. Photoaffinity labelling probes

The identification of different binding partners and the further characterization of a protein-protein-interaction is crucial for the detailed understanding of its biological function. However, the investigation of PPIs is challenging. Often the binding sites are difficult to identify, since they cover a large surface area of the protein and the interaction itself is usually highly dynamic.^[74] Photoaffinity probes can assist to overcome this problem. These ligands feature a photoactivatable group, which can establish a covalent bond upon irradiation. Initially, probe and protein of interest are incubated and form an affinity-based, non-covalent interaction. Subsequent irradiation with UV light transforms the photoactivatable group into a highly reactive intermediate, which creates a covalent bond. The covalent crosslink stabilizes transient interactions and allows identification of low affinity binding partners. Therefore, photoactivatable probes are highly valuable tools to investigate protein-protein and protein-ligand interactions.^{[75],[76]}

The three most frequently employed photoactivatable groups are the benzophenone, the aryl azide and the diazirine (Figure 9). To be suitable for incorporation in a photocrosslinking probe,

the photophore has to fulfil several criteria. First it should be fairly stable at ambient light, even though these compounds are activated through UV-radiation. Otherwise synthesis and handling of photophores under normal working conditions would be rather challenging. Furthermore, the photochemistry should be distinct, to ensure reproducible generation of a single covalent bond. Therefore, the reactive species should be able to insert into C-H bonds, as well as nucleophilic X-H bonds. The life time of the photoactivated state has to be appropriate. Thus, the reactive moiety has to react before dissociation of the protein-ligand complex. However, the lifetime should also be sufficient for covalent bond formation with a suitable interaction partner in a close proximity.^[77]

Aryl azides consist of a phenyl moiety that features a linear azide. These photophores are advantageous due to their small size, which prevents steric clashes and should not affect the interaction of interest. Aryl azides are converted to the excited state at wavelength of around 250 nm. The average absorption wavelength of most proteins is below 300 nm. Thus, molecular macromolecules could potentially be damaged and non-specific covalent protein-DNA crosslinks might occur. Upon irradiation aryl azides generate nitrenes under release of molecular nitrogen. However, rearrangement of aryl-nitrenes into less reactive species by ring expansion reduces overall reactivity (Figure 9).^[78]

Photolysis of benzophenones generates a reactive biradical with high crosslinking efficiency (Figure 8). They are advantageous due to their inertness towards solvents and simple synthesis. However, benzophenones are relatively bulky photophores, which can interfere with the desired protein-ligand interaction. They are activated at wavelength above 350 nm, thus the risk of affecting cellular macromolecules is minor. Another drawback is the long irradiation time benzophenones require, which causes increased non-specific labeling.^[79]

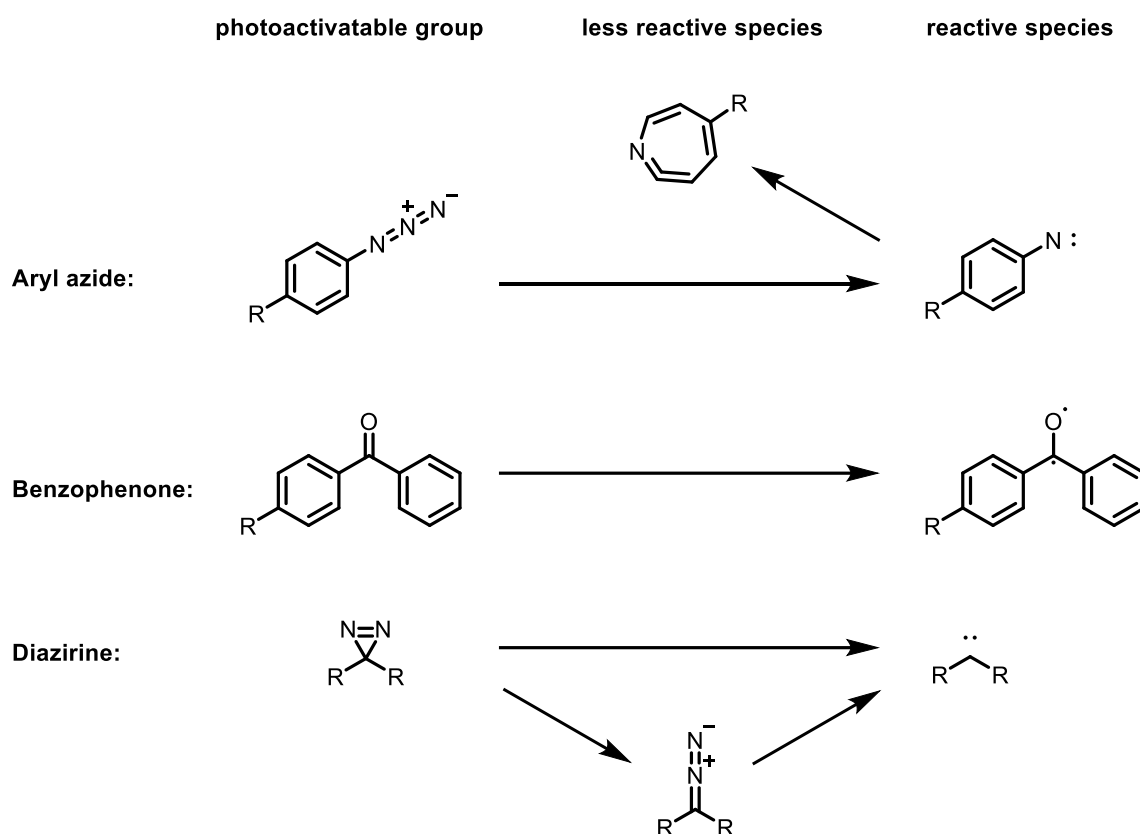


Figure 9: The three most frequently used photophores aryl azide, benzophenone and diazirine.

Since the photophore might affect the features of a bioactive compound, alteration of the biomolecule should be minor. In order to mimic the original compound, photoactivatable groups of small size are beneficial. The least bulky of the mentioned photophores is the diazirine. Upon irradiation the diazirine is converted into a highly reactive carbene species, which has a relatively short lifetime. Thus, the resulting carbene quickly reacts with an interaction partner in close proximity or is quenched by buffer components, which reduces unspecific labelling. The carbene can insert into C-H and heteroatom-H bonds to rapidly create a covalent bond.^[80] Furthermore, diazirines are activated at >350 nm. Thereby, damage of cellular macromolecules is prevented.^[77] One drawback of diazirines is the possibility of diazo isomerization through photolysis, which reduces the photo-crosslinking efficiency (Figure 8). However, a trifluoromethyl group in α -position to the diazirine can prevent undesired isomerization.^[81]

2.2. Motivation and goals

N-Myristoylation plays a key role in regulation of cellular signaling and protein activation and myristoylation is involved in various severe disorders. Furthermore, the myristoyl moiety contributes to protein-protein and protein-lipid interactions and dictates localization and reversible membrane attachment of the lipidated protein. Due to their hydrophobic nature myristoylated proteins preferably locate at cellular membranes. The UNC119 chaperone protein facilitates trafficking of myristoylated proteins through the cytosol. UNC119 proteins have a well-defined hydrophobic pocket for insertion of the myristoyl chain of its binding partner. However, short-lived interactions and low affinities can cause great difficulties in identification of new binding partners. **Photoactivatable myristoyl analogues** (Pacman) forming a covalent bond upon irradiation, can serve as tools to overcome these obstacles.

For this purpose, several diazirine based analogues of myristic acid should be designed and synthesized (Figure 10). Subsequently, the probes should be evaluated for their affinity to UNC119 and their ability to establish a covalent bond with the chaperone protein. To obtain structural information, identification of the cross-linking site and co-crystallization of Pacman probes with UNC119 protein should be attempted. The interaction of the myristoyl analogues with UNC119 in a complex mixture of proteins should be confirmed by affinity enrichment. Moreover, the probes should be screened in a fluorescence-based assay to investigate substrate recognition by NMT. Finally, metabolic labeling should be performed followed by affinity enrichment of new interaction partners of UNC119 chaperone protein. The identification of previously unknown UNC119 binding partners would provide valuable insight into the biological role of the chaperone protein and its involvement in various disorders.

2.3. Results and discussion

2.3.1. Design and Synthesis of photoactivatable myristic acid analogues

The myristate moiety is a C14 saturated fatty acid and the photoactivatable group should be incorporated into the backbone of this lipid chain. The diazirine group was chosen as the photoactivatable moiety, since it has several advantageous characteristics (as described in the Introduction). The small size of the diazirine should allow insertion of the myristic acid analogue into the hydrophobic binding pocket of UNC119 proteins without creating steric hindrance. Potentially, the diazirine moiety can be installed at various positions along the aliphatic chain. The photoactivatable moiety was installed at the end of the alkyl chain to target one of the residues inside the hydrophobic pocket of UNC119 proteins. This should ensure a stable covalent crosslink between UNC119 protein and its interaction partner. Three potential analogues were envisioned (Figure 10). The first two analogues contain a more reactive aliphatic diazirine moiety, which keeps the structural perturbation to a minimum. Analogue 3 is based on an aryl diazirine with a trifluoromethyl group. Even though the aromatic diazirine is relatively bulky in comparison to alkyldiazirines, it brings several advantages. The aromatic ring and the trifluoro group prevent isomerization to the less reactive linear diazo-species and stabilize the formed carbene.^[82]

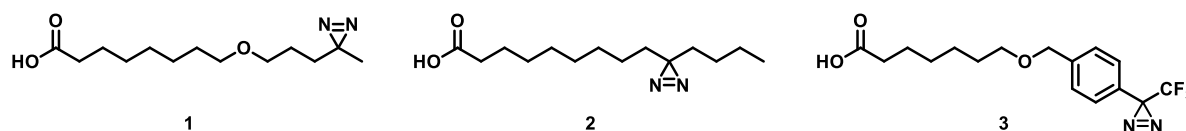


Figure 10: Diazirine based photoactivatable analogues of myristic acid Pacman 1-3.

2.3.1.1. Synthesis of Pacman-1

Pacman-1 analogue **1** was synthesized from two building blocks, 1,8-octanediol **6** and 4-hydroxybutan-2-one **4** (Figure 11). Initially, the keto group of 4-hydroxybutan-2-one **4** was transformed into the diazirine **5** in two steps following a published procedure.^[83] First, the diaziridine moiety was formed by the reaction of the ketone with liquified ammonia and hydroxylamine-*O*-sulfonic acid. Subsequently, the diaziridine moiety was oxidized to the corresponding diazirine using iodine as an oxidant and triethylamine as a base. In parallel, 1,8-octanediol **6** was monoprotected with *tert*-butyldimethylsilyl chloride (TBDMSCl) and

equipped with a leaving group, introduced by substitution of the remaining alcohol with methanesulfonylchloride. Consequently, the diazirinated alcohol **5** was deprotonated with potassium hydride in dioxane under reflux and reacted with the methanesulfonate **8**. The silyl protecting group of the alcohol was removed with tetrabutylammonium fluoride (TBAF). The alcohol **10** was oxidized to furnish the desired carboxylic acid to obtain Pacman-1 analogue in overall 15% yield.

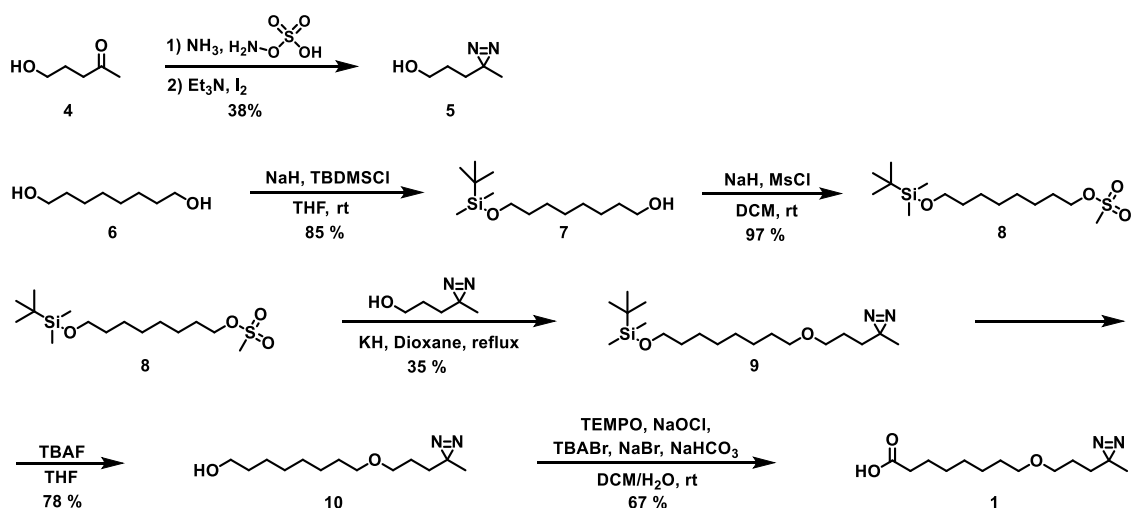


Figure 11: Synthesis of Pacman-1 **1** from 4-hydroxybutan-2-one **4** and 1,8-octanediol **6**.

2.3.1.2. Synthesis of Pacman-2

In order to synthesize Pacman-2 **2**, the respective Grignard reagent was prepared from 1-bromobutane **11** and magnesium (Figure 12). Subsequently, n-butyl magnesium bromide **12** was reacted with methyl 10-undecanoate **13** to obtain the respective alcohol **14** that was oxidized to the corresponding ketone **15** using the Dess-Martin periodinane reagent. The methyl ester **15** was cleaved with lithium hydroxide in dioxane under reflux. The ketone **16** was converted to the corresponding diazirine **2** using 7 N ammonia in methanol, followed by oxidation with iodine and triethylamine, providing the desired Pacman-2 **2** in 10% overall yield.

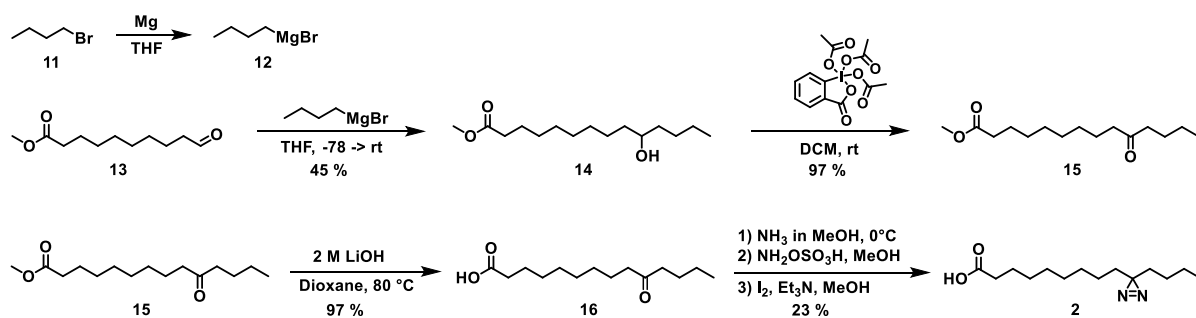


Figure 12: Synthesis of Pacman-2 **2** from 1-bromobutane **11** and 10-undecanoate **13**.

2.3.1.3. Synthesis of Pacman-3

The photo-activatable myristoyl analogue Pacman-3 **3** is based on a trifluoromethylphenyldiazirine (Figure 13). Initially, commercially available 1,7-heptanediol **17** was reacted with TBDMSCl to obtain a monoprotected alcohol **18**. The alcohol **18** reacted with the diazirinated benzyl bromide. Subsequently, the silyl protecting group was removed with TBAF and the alcohol **20** was oxidized to the corresponding carboxylic acid **3**. The overall yield over four synthetic steps was 13%.

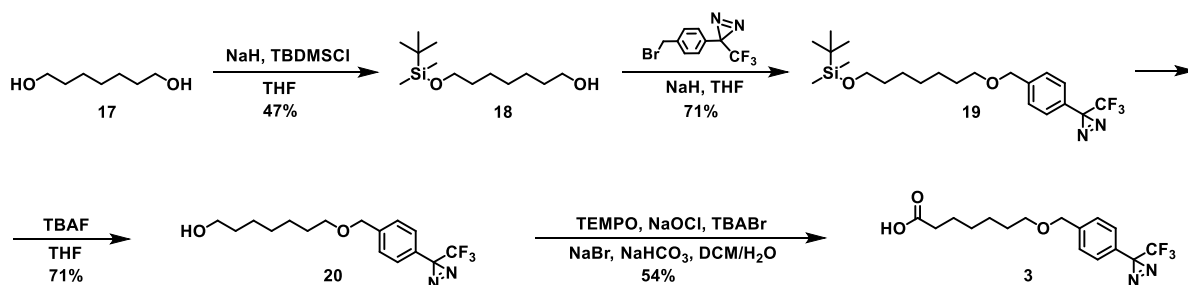


Figure 13: Synthesis of Pacman-3 **3** from a commercially available aromatic trifluoro-diazirine and 1,7-heptanediol **17**.

In order to improve the efficiency of the synthesis, the synthetic route was optimized by directly reacting the excess of 1,7-heptanediol **17** with the diazirine building block (Figure 14). The desired monosubstituted alcohol **20** was the predominant product of the reaction (66% yield) with only traces of the double substituted site product being formed. Thus, the unnecessary protection and deprotection steps were omitted from the synthetic sequence, which reduced the number of steps and increased the synthesis efficiency. Thus, the Pacman-3 analogue is readily accessible in two steps with overall yield of 44%.

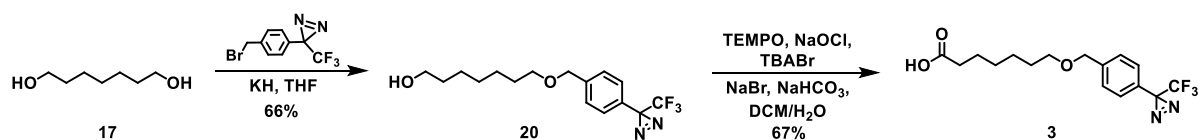


Figure 14: Optimized synthesis route for Pacman-3.

2.3.1.4. Synthesis of Pacman-based peptide probes

Pacman-based peptide probes were prepared for the photocrosslinking experiments with UNC119 proteins (Figure 15). To this end, short N-terminal peptide sequences were chosen, based on known UNC119 interaction partners. The first peptide was derived from the Src protein, since previous work in our group showed the interaction of myristoylated Src peptide with UNC119A.^[65] Furthermore, a transducin alpha subunit Gnat1-based probe was synthesized. This protein is known to be a high affinity binding partner of UNC119 proteins.^[62] The crystal structure of transducin alpha peptide with UNC119 has demonstrated that only the first six N-terminal amino acids insert along with the lipid chain into the hydrophobic pocket of UNC119.^[58] Based on our previous work, peptide sequences of nine (Gnat) and eight (Src) amino acids were selected for the photocrosslinking experiments (Figure 15). The peptide fragments were synthesized by microwave-assisted solid phase peptide synthesis (SPPS) using fluorenylmethoxycarbonyl (Fmoc)-protected amino acids, O-(1H-6-chlorobenzotriazole-1-yl)-1,1,3,3-tetramethyluronium hexafluorophosphate (HCTU) as a coupling reagent and *N,N*-diisopropylethylamine (DIPEA) as the base. The Fmoc groups were cleaved with a 20% solution of piperidine in dimethylformamide (DMF) prior to the coupling step. Subsequently, Pacman analogues were coupled to the N-terminus of the corresponding peptide to obtain the respective photoactivatable probes.

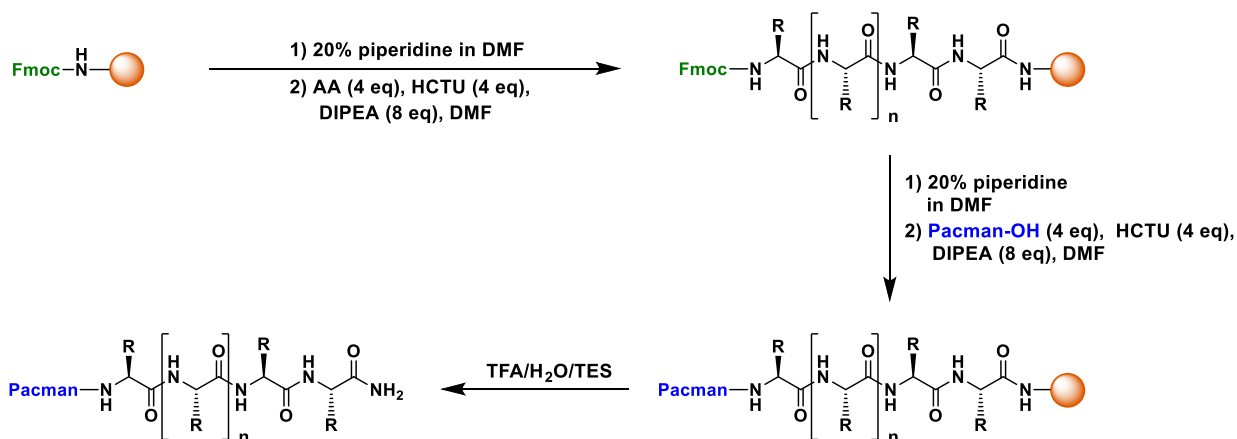


Figure 15: General synthesis of lipidated peptide probes.

The affinity of the photoactivatable probes towards UNC119A and UNC119B was determined by fluorescence polarization measurements. For this purpose, fluorescein isothiocyanate (FITC) was coupled to the C-terminal lysine residue of the respective Pacman-probes (Figure 16). As only the first six amino acids insert into the hydrophobic pocket, labeling with the fluorophore at this position should not interfere with binding to UNC119. To achieve this goal, the C-terminal lysine was protected with the 4-methyltrityl (Mtt) protecting group. The Mtt moiety can be removed under mild acidic conditions without affecting other protecting groups. Initially, Mtt-removal was attempted with a mixture of TFA/TIS/DCM (1:2:97). However, an unwanted partial removal of the Boc-protecting groups of other lysine residues was observed under these conditions. This resulted in unselective labeling of several lysine residues with FITC. The lysine deprotection was afterwards carried out with HFIP/DCM (1:4), which caused selective cleavage of the Mtt-group. The remaining protecting groups were not affected. Subsequently, the FITC moiety was attached to the free amino group of the C-terminal lysine side chain in the presence of DIPEA.

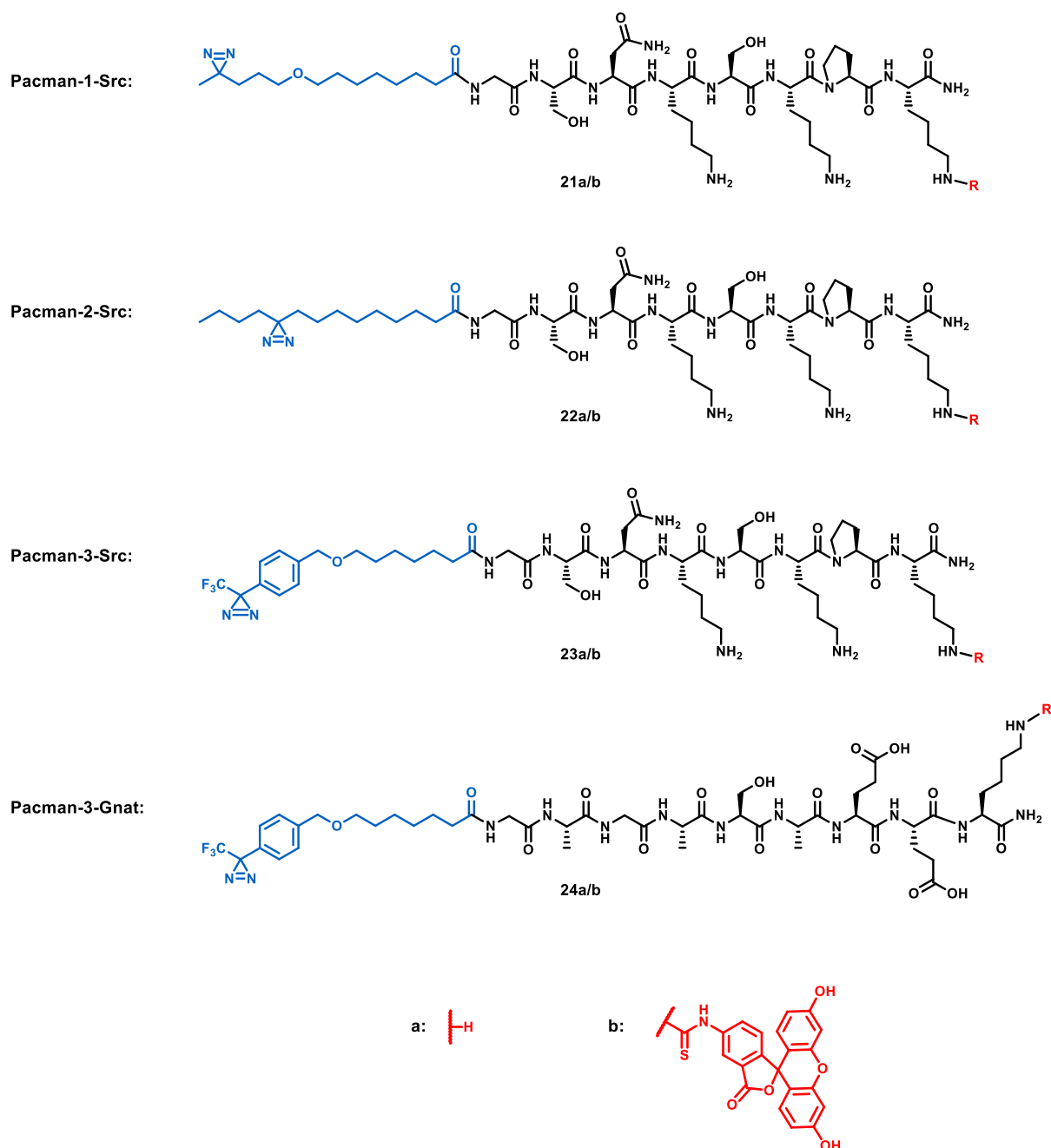


Figure 16: Structures of Pacman-Src probes for photocrosslinking (a) and fluorescence polarization measurement (b) with UNC119 proteins.

2.3.2. Evaluation of Pacman-based probes

2.3.2.1. Determination of the affinity of Pacman-based probes for UNC119 proteins

Since modification of the myristic acid can alter the interaction of the fatty acid with UNC119 proteins, the affinity of Pacman-substituted probes to UNC119A and UNC119B was determined by means of a FP assay. Therefore, FITC labeled Pacman-Src probes **21b** to **24b**

were prepared. In this assay, the fluorescent probes are incubated with increasing amounts of UNC119 protein in a buffer and irradiated with linear polarized light (Figure 17). Fluorescence polarization is sensitive to changes in molecular weight. Small fluorescent compounds show a high degree of free rotation in solution, which results in quick depolarization of the emitted light. If the fluorophore binds to a species with much higher molecular weight, like a protein, this results in reduction of the rotational speed and consequently depolarization is slowed down.^[26]

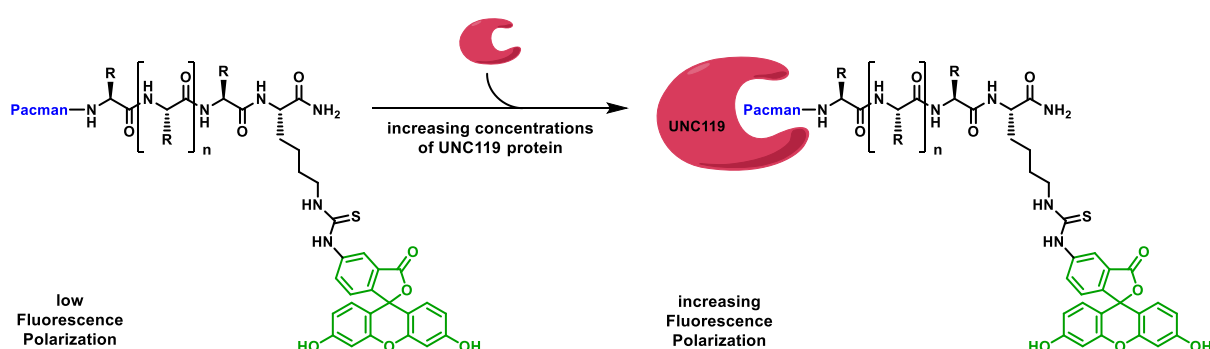


Figure 17: Fluorescence Polarization Assay with FITC labelled Pacman probes and increasing concentration of UNC119 protein.

As a reference value the affinity of a myristoyl-Src peptide (Myr-Src) to both UNC119 proteins was determined (Figure 18A). Myr-Src has an affinity of 150 nM to UNC119A and 80 nM to UNC119B.^[65] The affinities of Pacman-2-Src **22b** to UNC119A and UNC119B are comparable to those of Myr-Src with 40 nM and 60 nM respectively (Figure 18C). In contrast, Pacman-3-Src **23b** (Figure 18C) and Pacman-1-Src **21b** (Figure 18B) show a significant drop in affinity, which is most likely caused by the bulky aromatic ring of Pacman-3 and the oxygen in the backbone of Pacman-1. While the affinity of Pacman-3-Src **23b** is 2.3 μ M for UNC119A and 1.3 μ M for UNC119B, Pacman-1-Src **21b** has an affinity of 1.4 μ M for UNC119A.

Also for Pacman-3-Gnat **24b**, affinities to UNC119 proteins were determined (Figure 18D). The probe showed high affinity to UNC119A and UNC119B with 40 nM and 130 nM respectively. To investigate whether Pacman-3 probes also interact with other lipid binding chaperones, affinities of Pacman-3-Gnat **24b** and Pacman-3-Src **23b** to PDE δ were determined (Figure 18C and 18D). Both probes did not interact with the farnesyl binding protein PDE δ and, thus, are specific for the UNC119 chaperone protein.

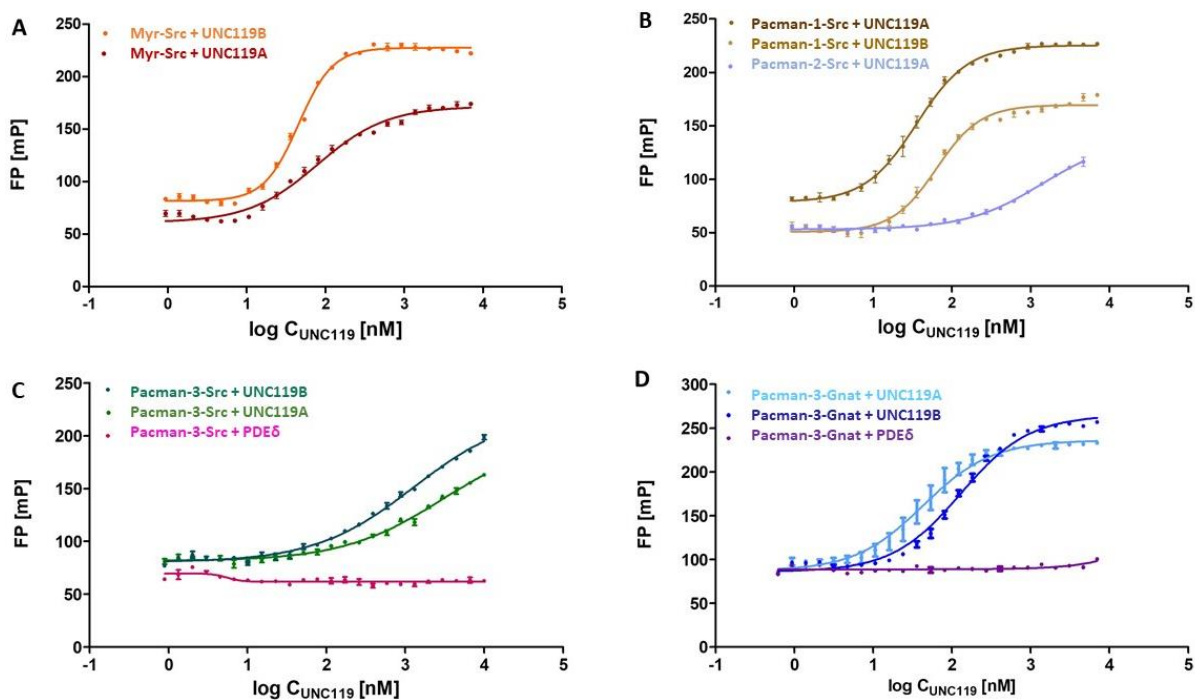


Figure 18: Affinities of Pacman based probes to UNC119 and PDE δ proteins. **A:** Affinity of Myr-Src to UNC119A and UNC119B. **B:** Affinities of Pacman-1-Sr **21b** to UNC119A and UNC119B and Pacman-2-Src **22b** to UNC119A. **C:** Affinities of Pacman-3-Src **23b** to UNC119A, UNC119B and PDE δ . **D:** Affinities of Pacman-3-Gnat **24b** to UNC119A, UNC119B and PDE δ .

2.3.2.2. Covalent labeling of UNC119 proteins by photoactivatable probes

In order to confirm photo-activation and covalent bond formation between Pacman peptides and UNC119 proteins, a mass spectrometry-based readout was chosen (Figure 19). Following incubation of probe and protein, covalent bond formation was initiated by irradiation at 365 nm. The carbene moiety, created upon irradiation, is highly reactive and is expected to insert into C-H and X-H bonds (where X is a heteroatom) of the adjacent moieties, thus forming a covalent bond with the residues of UNC119 proteins.^[84] Outside of the binding pocket, photo-activated probes are short-lived species. They are immediately quenched by water molecules in the reaction buffer. Fast hydrolysis of the carbene prevents unspecific bond formation with outer parts of the protein. When the photoactivated probe is present inside the hydrophobic pocket of the protein, a covalent bond between the probe and the protein is formed. The process can be monitored using mass spectrometry by following adduct formation of the UNC119 protein with the Pacman probe. This adduct has the molecular mass of the protein plus the probe minus 28 mass units due to the loss of two diazirine nitrogen atoms. For the detection of

covalent bond formation, matrix assisted laser desorption ionization spectrometry (MALDI) with time of flight (TOF) detection mode was chosen. Since this method can only detect high affinity interactions and covalent complexes, MALDI is suitable for confirmation of covalent bond formation between Pacman-probes and UNC119 proteins.

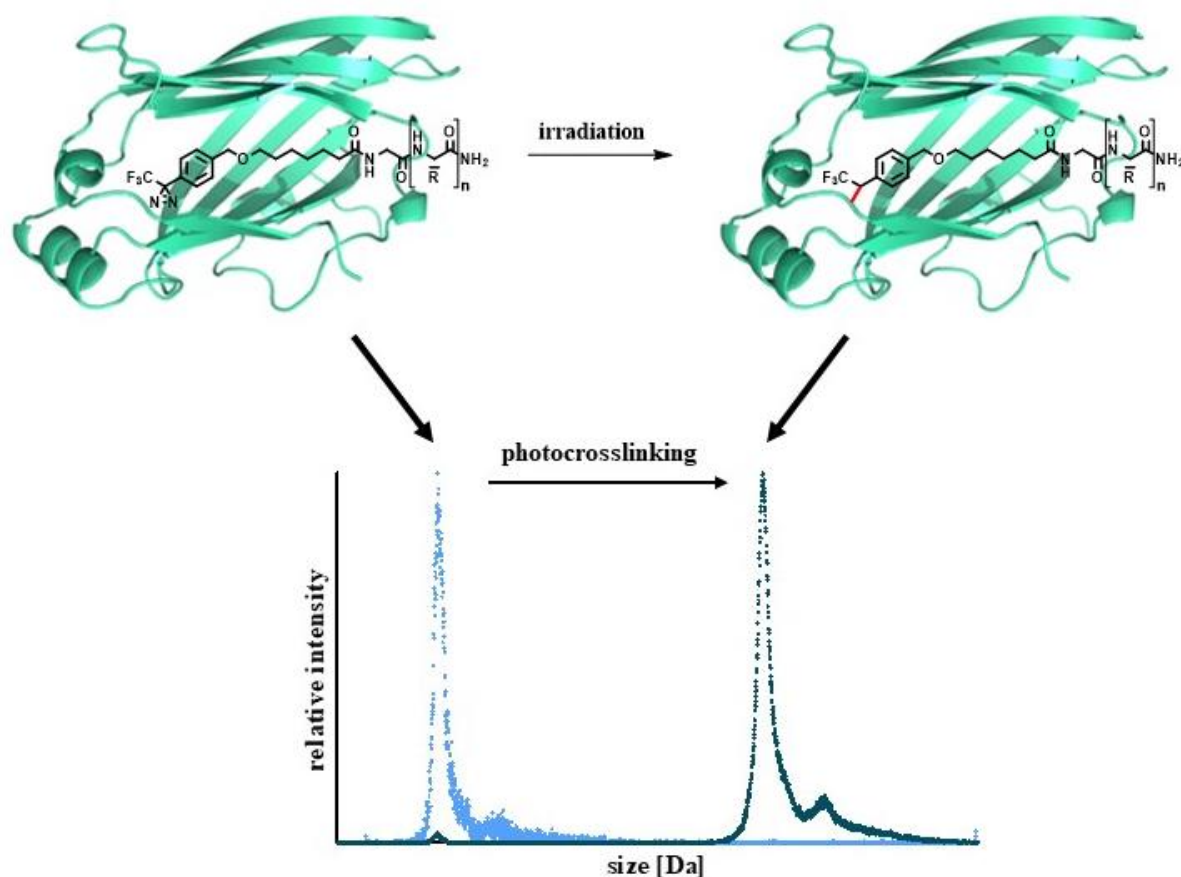


Figure 19: Photocrosslinking of Pacman-probes and UNC119 protein upon irradiation results in increased molecular weight detectible by MALDI spectrometry.

To perform the photocrosslinking experiments a 1:4 mixture of protein and the peptide probe in PBS buffer was prepared. Detergent as component of the buffer was avoided, since previous experiments indicated interaction of detergents with the UNC119 hydrophobic pocket. The concentration of the protein was adjusted to 50 μM and of the Pacman probes to 200 μM . The resulting mixture was added to a glass vial and irradiated at 365 nm. Initially, photoactivation was performed for 1 h. During the irradiation several aliquots were taken at 0 min, 5 min and 60 min and stored in darkness on ice, to prevent further photo-activation by ambient light.

Subsequently, the samples were measured by MALDI-TOF mass spectrometric analysis. For Pacman-1-Src **21a** and Pacman-2-Src only the unchanged mass of UNC119A or UNC119B was detected (Figure 20). No mass corresponding to the protein featuring the covalent modification was observed. The results indicated that Pacman-1-Src **21a** and Pacman-2-Src **22a** were not able to establish a covalent interaction with neither UNC119A nor UNC119B.

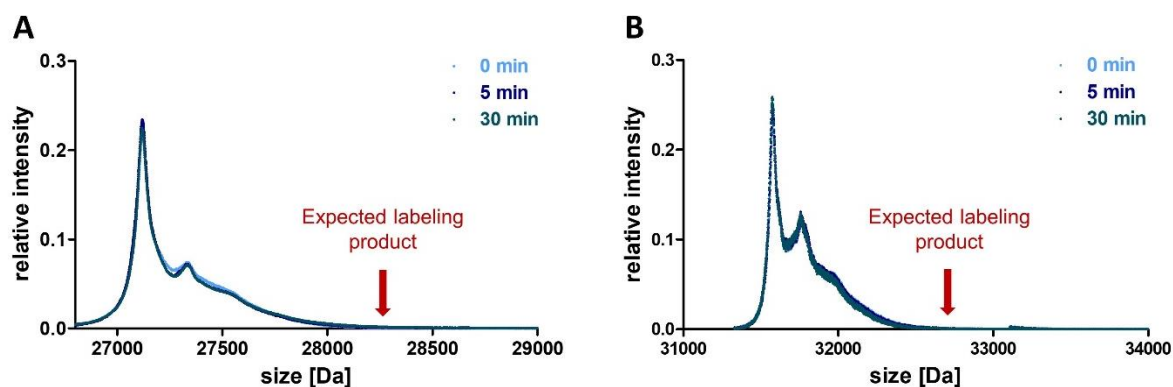


Figure 20: Labeling of UNC119 protein with Pacman-1-Src **21a** and Pacman-2-Src **22a**. **A:** Pacman-1-Src and Pacman-2-Src do not label UNC119A (representative spectrum). **B:** Pacman-1-Src and Pacman-2-Src do not label UNC119B (representative spectrum).

In order to understand why no photolabeling occurred, the results of the MALDI mass spectrometry measurements were examined. The mass of the protein remained unchanged, so the masses representing the peptide probe and possible derivatives were analyzed (Figure 21). The peak with the mass of 1081 Da represents the diazirinated Src peptide probe **22a** before the irradiation. Upon irradiation, the mass of 1081 Da disappeared and two new peaks with the masses of 1053 Da and 1075 Da appeared. The mass of 1053 Da can be attributed to the loss of the diazirine under formation of a double bond. The mass of 1075 Da represents the sodium adduct of this double bond containing side product.

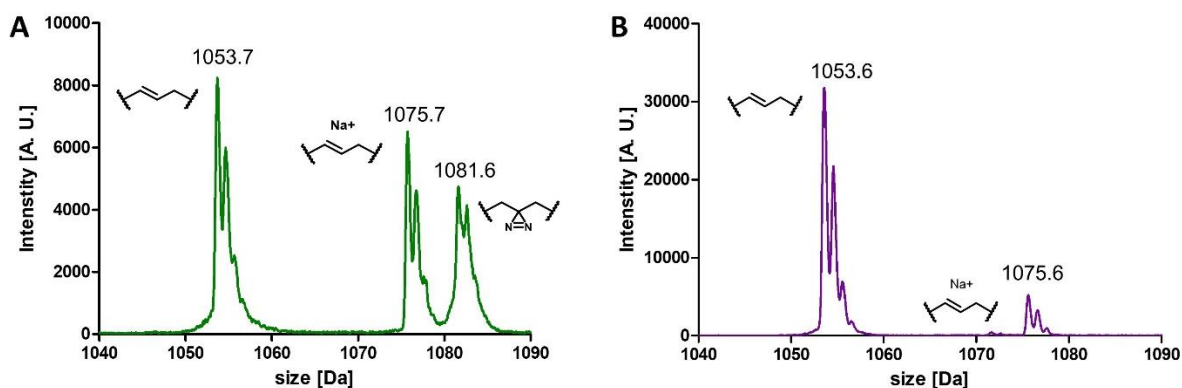


Figure 21: MALDI spectrum of Pacman-2-Src **22a**. **A:** Pacman-2-Src without irradiation. **B:** Pacman-2-Src after 30 min irradiation at 365 nm.

Alkyl diazirines are highly reactive. The formed carbene species have very short life time and can be quenched by water molecules. Furthermore, a 1,2-hydrogen migration might occur, which results in double bond formation.^[85] In case of Pacman-2-Src **22a**, the alkene formation seemed to be favored. The affinity determined by the FP assay indicates an interaction between Pacman-2-Src **22b** and UNC119 proteins. Thus, the probe seems to insert into the hydrophobic pocket of the chaperone protein. However, upon activation the alkyl diazirine seems to form a double bond instead of labeling the protein. This could be explained by the absence of a suitable moiety in close proximity that the carbene can react with. According to these results the alkyl diazirines Pacman-1 and Pacman-2 are unsuitable for covalent labeling of UNC119 proteins. While Pacman-1-Src **21a** and Pacman-2-Src **22a** labeled neither of the UNC119 proteins, Pacman-3-Src **23a** labeled only UNC119B, but not UNC119A (Figure 22 and 23).

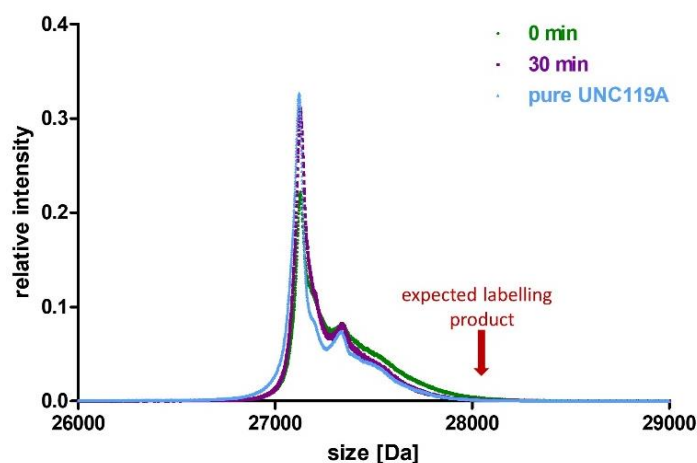


Figure 22: Labeling of UNC119A protein with Pacman-3-Src **23a**.

The labeling efficiency of Pacman-3-Src **23a** for UNC119B reached 25 % after 45 min of irradiation (Figure 23A). In order to maximize the labeling efficiency, the amount of photoactivatable probe was increased from 4 equivalents to 10 equivalents. However, the amount of covalently bound UNC119B protein increased only slightly to 35%. Due to the potential short life-time of the diazirine probe upon irradiation, the labelling was performed in several cycles. Hence, the equilibrium between bound and unbound probe is reestablished during each cycle, while the covalently labeled protein is effectively removed from the equilibrium. The amount of probe added during each cycle was reduced to 3 equivalents and irradiation time for each step was adjusted to 20 min. This approach increases the amount of covalently labeled UNC119B after four cycles to 80 % (Figure 23).

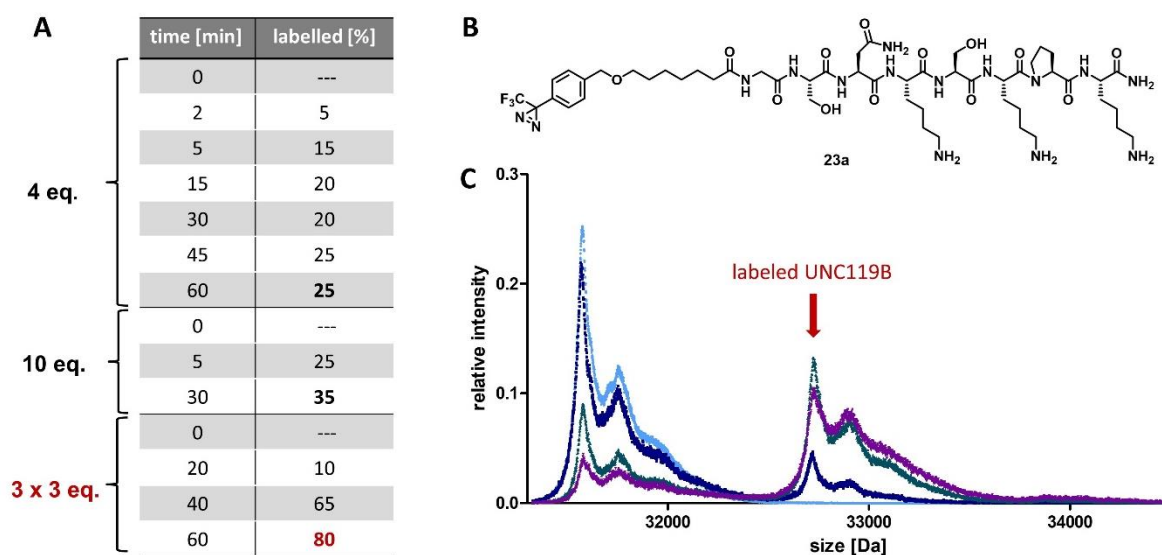


Figure 23: Labelling of UNC119B with Pacman-3-Src **23a**. **A:** Labelling efficiencies with various equivalents of Pacman-3-Src at different time points. **B:** Structure of Pacman-3-Src **23a**. **C:** MALDI spectrum of labeled UNC119B with 3x3 eq. of the probe after 0 min (light blue), 20 min (dark blue), 40 min (green) and 60 min (purple).

Based on this results Pacman-3 was chosen for further evaluation, since it was the only analogue featuring sufficient labeling efficiency. Subsequently, also Gnat1-based probe **24a** was evaluated (Figure 24). Since Gnat1 is a known high affinity interaction partner of UNC119 proteins higher photolabeling efficiency were expected for this probe. With the Pacman-3-Gnat probe **24a** photo-crosslinking experiments were performed under the optimized conditions described above. In total, two cycles were sufficient to obtain a labeling of UNC119A with

95% efficiency and UNC119B with 99% efficiency. The variations in photocrosslinking efficiency can be explained by differences in the peptide sequence affecting the interaction with UNC119 protein.

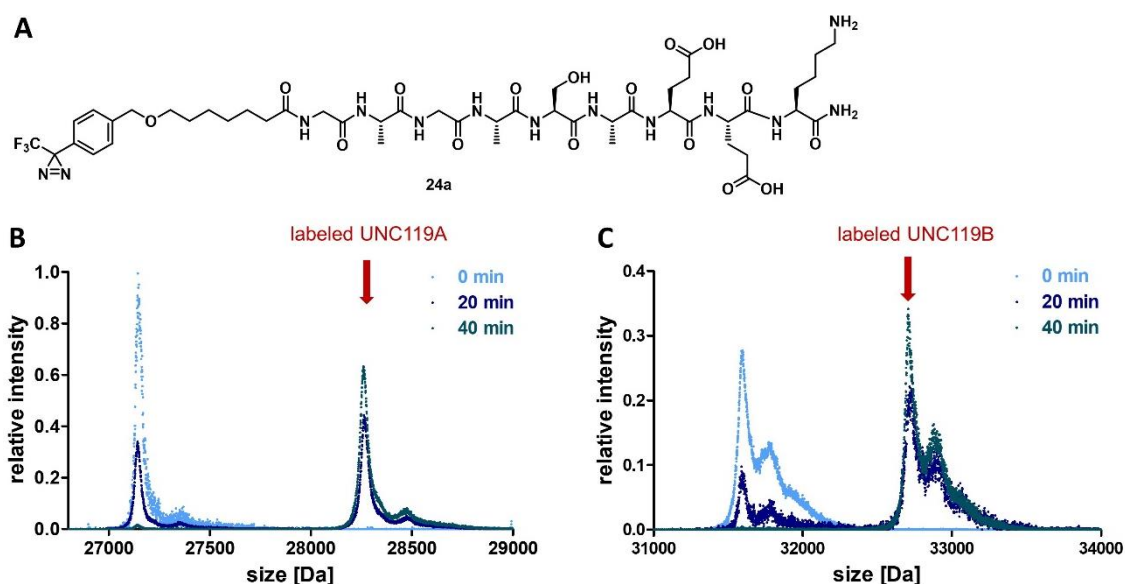


Figure 24: Labelling of UNC119 proteins with Pacman-3-Gnat **24a**. **A:** Structure of Pacman-3-Gnat **24a**. **B:** MALDI spectrum of labeled UNC119A with 2x3 eq. of probe after 0 min (light blue), 20 min (dark blue) and 40 min (green). **C:** MALDI spectrum of labeled UNC119B with 2x3 eq. of probe after 0 min (light blue), 20 min (dark blue) and 40 min (green).

In contrast to Pacman-3-Src **23a**, which labelled only the UNC119B isoform, Pacman-3-Gnat **24a** labelled both UNC119 proteins. The selectivity of Pacman-3-Src **23a** for UNC119B does not seem to be caused by a difference in affinity. Even though, the affinity of Pacman-3-Src **23a** is significantly lower than that of myristoylated Src, Pacman-3-Src **23a** shows similar affinity for UNC119A and UNC119B proteins.

2.3.3. Mapping of the UNC119 binding pocket

In order to gain structural insight into the interactions and the difference in labelling efficiency, the covalent binding site was localized. To this end, UNC119 proteins were covalently labeled with either Pacman-3-Src **23a** or Pacman-3-Gnat **24a**. Subsequently, a tryptic digestion was

performed and the samples were analyzed by tandem MS/MS. The respective unlabeled UNC119 protein was used as a control.

The results confirmed that Pacman-3-Src **23a** is selective for UNC119B, since no indication for covalent modification was found in the UNC119A sample. The modification in UNC119B was located on Tyr-247 (T247) or in the proximity thereof (Figure 25). As expected, in case of Pacman-3-Gnat **24a**, both UNC119A and B were labelled. Only UNC119A was crystallized, but not UNC119B. However, both proteins have high sequence similarity, especially within the C-terminal region forming the hydrophobic binding cavity. Thus, a sequence alignment of UNC119A and UNC119B was performed (Figure 25).

```

UNC119A      MKVKKGGGGAGTATESAPGPSGQSVAPIQPPA-----EESGSESEPDAGPGP
UNC119B      ---MSGSNPKAAAAASAAGPGGLVAGKEEKKKAGGGVLNRLKARRQAPHHAADDGVGAAV

UNC119A      RPPGLQRKQPIGPEDVLGLQRITGDYLCSPENIYKIDFVRFKIRDMSGTVLFEIKKPP
UNC119B      TEQELLALDITRPEHVLRLSRVTENYLCKPEDNIYSIDFTRFKIRDLETGTVLFEIAKPC

UNC119A      VSERLPINRR---DLDPNAGRFVRYQFTPAFLRLRQVGATVEFTVGDKPVNNFRMIERHY
UNC119B      VSDQEEDEEEGGGDVDISAGRFVRYQFTPAFLRLRTVGATVEFTVGDKPVSNFRMIERHY

UNC119A      FRNQLLKSFDHFHFGFCIPSSKNTCEHIYDFPPLSEELISEMIRHPYETQSDSFYFVDDRLL
UNC119B      FREHLLKNFDFDFGFCIPSSRNTCEHIYEFFQLSEDVLRMLIENPYETRSDSFYFVDNKL

UNC119A      VMHNKADYSYSGTP
UNC119B      IMHNKADYA247NGGQ

```

Figure 25: Sequence alignment of UNC119A and UNC119B. Grey: Identical amino acids; Red: residue covalently labeled by Pacman-3-Src **23a** (T247).

Sequence alignment revealed that the covalently labeled T247 corresponds to T236 in UNC119A (Figure 25). Examination of the UNC119A crystal structure showed that this tyrosine is located at the bottom of the hydrophobic pocket. Labelling at this residue confirms that Pacman-3 modified peptide **24a** inserts into the hydrophobic pocket prior to activation and rules out complex formation due to unspecific interactions. No crystal structure of UNC119B with or without the lipidated cargo was reported. Therefore, in order to get insight into the interactions and the binding mode of the lipidated probes **23a** and **24a**, a model of UNC119B based on the crystal structure of UNC119A in complex with the myristoylated NPHP3 peptide (PDB: 5L7K) was created using Swiss Model (Figure 26).^[86]

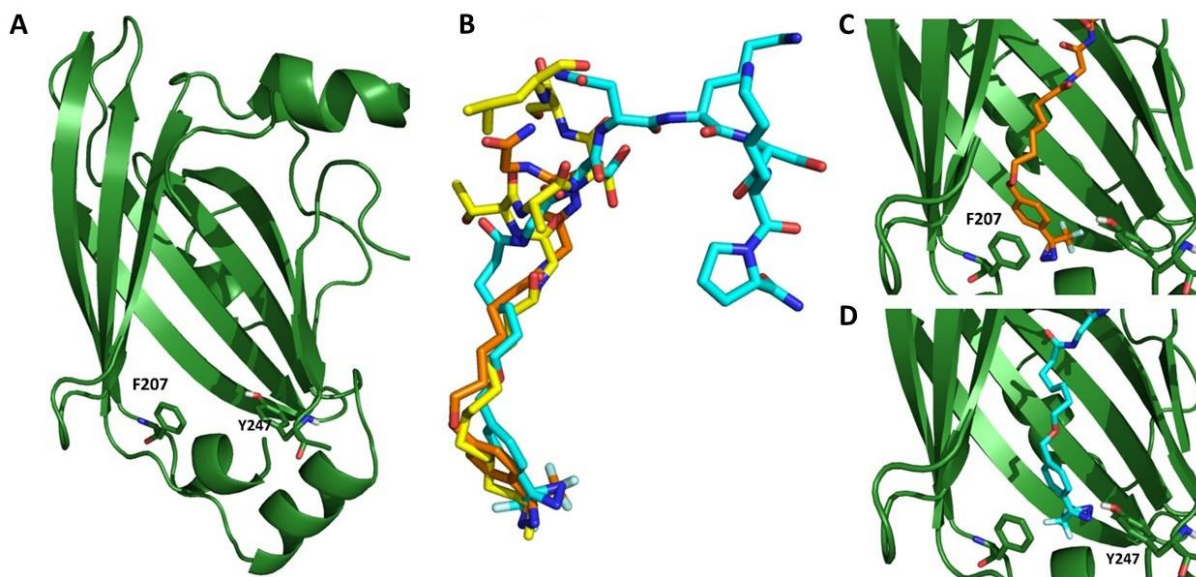


Figure 26: Covalent labelling of UNC119 proteins with Pacman-3-Gnat **24a** and Pacman-3-Src **23a**. **A:** Model of UNC119B protein with the photocrosslinking sites Phe-207 and Tyr-247 (sticks). **B:** Overlay of the myristoylated NPHP3 peptide (PDB: 5L7K, yellow), Pacman-3-Gnat (orange) and Pacman-3-Src (cyan). **C:** Pacman-3-Gnat inside the binding cavity of UNC119B with the diazirine oriented towards Phe-207. **D:** Pacman-3-Src inside the binding cavity of UNC119B with the diazirine oriented towards Tyr-247. (adopted from Kaiser et al.)^[87]

Pacman-3-Gnat **24a**, covalently modified UNC119A as well as UNC119B (Figure 27). Again, an aromatic amino acid was labeled. For UNC119A it was Phe-196 (F196) and for UNC119B Phe-207 (F209). Sequence alignment of both proteins revealed that the amino acid sequences are homologous. This finding suggests a similar binding mode of Pacman-3-Gnat **24a** for UNC119A and UNC119B. F196 is also localized on the bottom of the binding pocket.

```

UNC119A      MKVKKGGGGAGTATE SAPGFSGQSVAPIQPPA-----EESGSESEPDAGPGP
UNC119B      ---MSGSNPKAAAAASAAGPGLVAGKEEKKKAGGGVLNRLKARRQAPHHAADDGVGAAY

UNC119A      RGPPLQRKQPIGPEDVVLGLQRITGDYLCSP EENIYKIDFVRFKIRDMDSGTVLFEIKKPP
UNC119B      TEQEL LALDTIRPEHVLRLSRVTENYLCKPEDNIYSIDFTRFKIRDLETGTVLFEIAKPC

UNC119A      VSERLPINRR---DLDPNAGR FVRYQFTPAFLRLRQVGATVEFTVGDKPVNNFRMIERHY
UNC119B      VSDQEEDEEEGGGDVDISAGR FVRYQFTPAFLRLRTVGATVEFTVGDKPVS NFRMIERHY

UNC119A      FRNQLLKS FDFHFGFCIPSSKNTCEHIYD PPLSEELTSEMIRHPYETQSDSFYFVDDRL
UNC119B      FREHLLKN FDFDFGFCIPSSRNTCEHIYE PQLSEDVIRLMIENPYETRSDSFYFVDNKL

UNC119A      VMHNKADYSYSGTP
UNC119B      IMHNKADYAYNGGQ

```

Figure 27: Sequence alignment of UNC119A and UNC119B. Grey: Identical amino acids; Red: residues covalently labeled by Pacman-3-Gnat **24a** (F196 and F209).

2.3.4. Crystallization of photolabelled UNC119 proteins

To gain even better structural insight into the covalent interaction between Pacman-3 probes and UNC119 proteins, the co-crystallization of photocrosslinked Pacman UNC119 protein complex was attempted. Up to date only the crystal structure of UNC119A was published and not of UNC119B. Recently, UNC119A was co-crystallized with myristoylated NPHP3 peptide.^[62] In this study, a truncated version of the UNC119A protein was employed, since the flexible N-terminus of the protein might interfere with crystal formation.^[62] Following the same logic, the analogically truncated construct of UNC119B protein (termed shUNC119B, containing amino acids 42-251) was employed in the co-crystallization with the photocrosslinked Pacman-3-based probe.

For initial experiments, two Pacman-3 probes **25** and **26** with shorter peptide sequences, containing four amino acids, were chosen (Figure 28A and 28B). Longer peptide sequences might cause more flexibility, which could impair the crystallization process. One probe **25** was based on Pacman-3-Gnat **24a** and the second probe **26** on NPHP3, which were both previously co-crystallized with UNC119A.^{[62],[58]} Initially, short peptide probes shGnat and shNPHP3 were synthesized and modified with Pacman-3 as described earlier. Subsequently the efficiencies of photo-crosslinking with UNC119A and UNC119B were determined (Figure 28C and 28D).

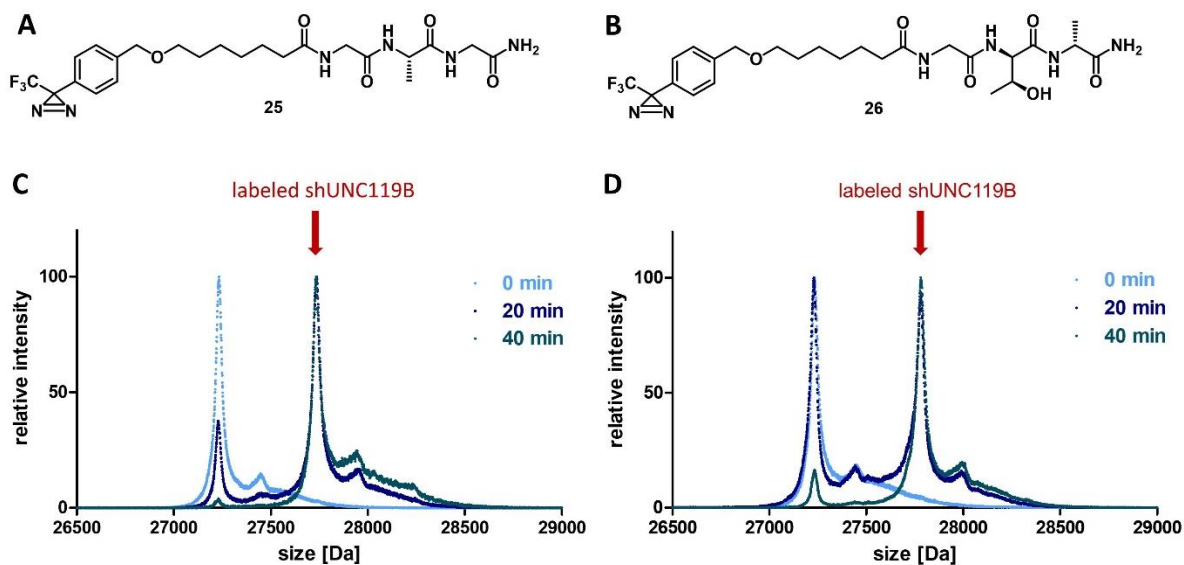


Figure 28: Photocrosslinking of shUNC119B with Pacman-3-shGnat **25** and Pacman-3-shNPHP3 **26**. **A:** Structure of Pacman-3-shGnat **25**. **B:** Structure of Pacman-3-shNPHP3 **26**. **C:** shUNC119B labeled with two times 3 equivalents of Pacman-3-shGnat **25** after 0 min, 20 min and 40 min. **D:** shUNC119B labeled with two times 3 equivalents of Pacman-3-shGnat **26** after 0 min, 20 min and 40 min.

Both Pacman-3-shGnat **25** and Pacman-3-shNPHP3 **26** probes showed excellent labelling efficiencies for full length UNC119B, as well as shUNC119B (Table 1). While Pacman-3-shGnat **25** labels both proteins quantitatively, Pacman-3-shNPHP3 **26** labels full length UNC119B quantitatively and shUNC119B up to 95%. Furthermore, Pacman-3-shNPHP3 **26** shows lower labelling efficiencies after 20 min. Hence, Pacman-3-shGnat **25** was chosen for co-crystallization with shUNC119.

Table 1: Photolabelling efficiencies of Pacman-3-shGnat **25** and Pacman-3-shNPHP3 **26** for shUNC119B and full length UNC119B including irradiation time and applied amounts of probe.

	Pacman-3-shGnat			Pacman-3-shNPHP3		
	Irradiation time [min]	Eq.	Labelling efficiency	Irradiation time [min]	Eq.	Labelling efficiency
UNC119B	0	3	0	0	3	0
	20	3	90	20	3	80
	40	6	100	40	6	100
shUNC119B	0	3	0	0	3	0
	20	3	85	20	3	55
	40	6	100	40	6	95

For co-crystallization of shUNC119B with Pacman-3-shGnat **25** the protein was incubated and irradiated twice with the probe, in order to achieve complete photo-crosslinking. Subsequently, a portion of the complex was shortly incubated with minor amounts of protease. This digestion step removes flexible sections of the protein and might promote protein crystallization. Over 500 different buffer compositions were screened, however under none of these conditions protein crystal formation was observed.

Since UNC119A was previously successfully co-crystallized with different lipidated ligands, the screening was repeated under the same conditions with shUNC119A protein. Initially, photocrosslinking experiments with Pacman-3-shGnat **25** and full length or shUNC119A were performed, resulting in 95% labelling efficiency for both proteins (Figure 29). Thus, Pacman-3-shGnat **25** was found to be suitable for the crystallization with shUNC119A.

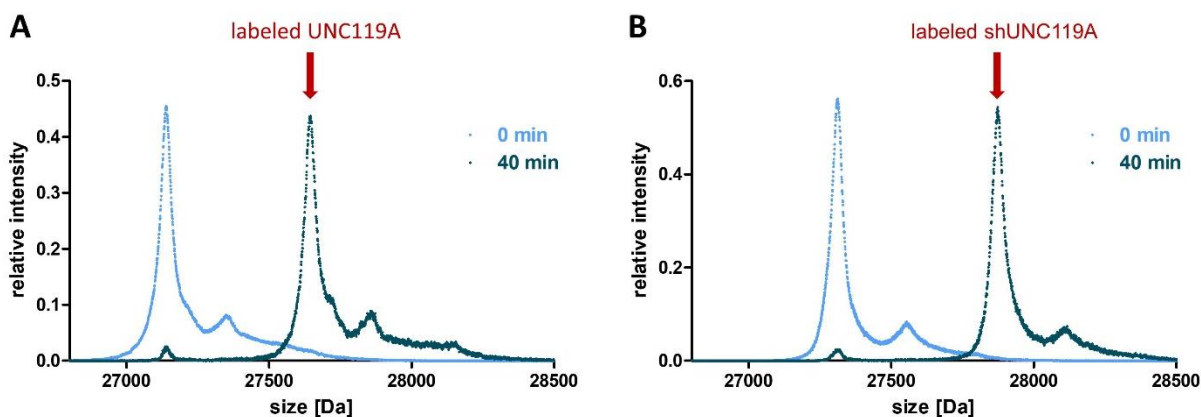


Figure 29: Photocrosslinking of full length UNC119A and shUNC119A with Pacman-3-shGnat **25**. **A:** Full length UNC119A labeled with two times 3 equivalents of Pacman-3-shGnat **25** after 0 min and 40 min. **B:** shUNC119A labeled with two times 3 equivalents of Pacman-3-shGnat **25** after 0 min and 40 min.

Screening of suitable crystallization conditions with shUNC119A revealed crystal formation after 30 min in two different buffers (Figure 30). One buffer contained 0.2 M $(\text{NH}_4)_2$ -ttrate and 20% w/v PEG3550, the other one 0.2 M KH_2PO_4 and 20% w/v PEG3550. However, the observed crystals dissolved after 8 h and could not be isolated for further analysis. The protein crystallized under no further conditions within the 90 days incubation period.

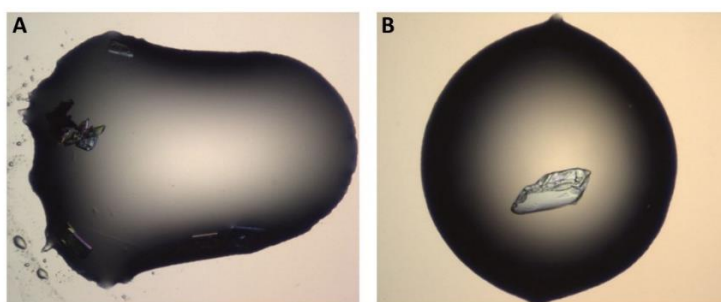


Figure 30: Images of crystals formed during screening with photocrosslinked Pacman-3-shGnat **25** and shUNC119A after 30 min. **A:** Buffer composition: 0.2 M $(\text{NH}_4)_2$ -ttrate and 20% w/v PEG3550. **B:** Buffer composition: 0.2 M KH_2PO_4 and 20% w/v PEG3550.

Optimization of screening conditions was subsequently performed with hanging drop method. Therefore, the predigested, photocrosslinked protein ligand complex was incubated with 0.1 M or 0.2 M concentration of either KH_2PO_4 or $(\text{NH}_4)_2$ -ttrate in presence of 10% to 22.5% w/v

PEG3350. However, no crystallization occurred under any of these conditions. Thus, crystallization of UNC119A or UNC119B photolabelled with Pacman-3-shGnat **25** could not be achieved. This could be caused by the different properties of the myristoyl moiety and Pacman. Consequently, Pacman might prevent formation of crystals. Later analysis of existing co-crystal structures of UNC119A with myristoylated NPHP3 or lauroylated Gnat1 revealed that the lipidated peptides are composed of six and eight amino acids respectively, which form an alpha helix (Figure 31).

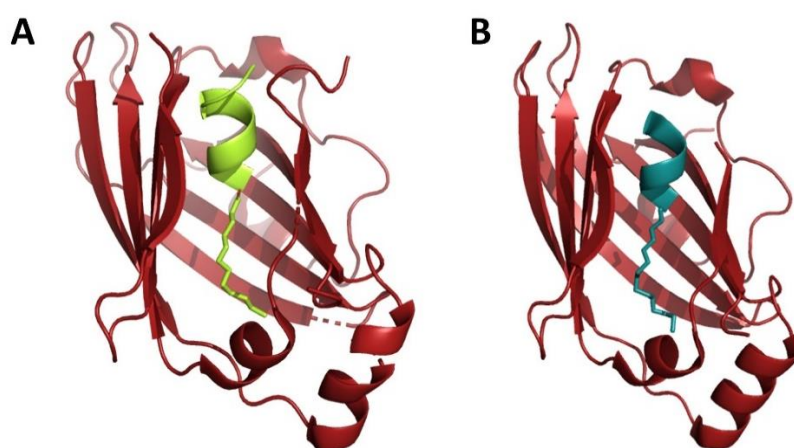


Figure 31: Alpha helix formation of both lipidated peptides co-crystallized with UNC119A. **A:** Co-crystal structure of UNC119A with lauroylated Gnat1 (PDB: 3RBQ). **B:** Co-crystal structure of UNC119A with myristoylated NPHP3 (PDB: 5L7K).

The Pacman-3-shGnat probe **25** contains only four amino acids, which might not be sufficient for formation of an alpha helix. However, the alpha helix could result in stabilization of the protein and thus be required for UNC119 crystallization. Therefore, screening for suitable crystallization conditions could be repeated with a longer Gnat peptide construct containing at least six amino acids, in order to promote possible alpha helix formation.

2.3.5. Affinity enrichment of UNC119 proteins from lysate

Since the labeling efficiency was optimized and specificity of the interaction could be confirmed, the interaction of Pacman-3 probes with UNC119 in a complex protein mixture was investigated. Therefore, an affinity enrichment experiment was chosen. The statistically

significant enrichment of a target protein from lysate with the positive Pacman-3 probe in comparison to a non-binding negative probe would indicate target engagement.

2.3.5.1. Design and synthesis of affinity enrichment probes

Initially, negative and positive affinity enrichment probes of Pacman-3-Src **23a** and Pacman-3-Gnat **24a** were prepared. As a negative control for affinity enrichment experiments the Pacman-3 moiety was substituted by an acetyl group. UNC119 proteins bind to proteins carrying the long saturated lauroyl and myristoyl fatty acid functionalities, but do not interact with proteins featuring an acetylated N-terminus. On this account, only interaction with Pacman modified probes should result in enrichment of UNC119 proteins, but not with acetylated probes. Acetylation of the N-terminal glycine was performed with acetic anhydride and DIPEA. The C-terminal lysine sidechain of both peptides, Src and Gnat, was chosen for linker attachment, since it is in sufficient distance from the Pacman moiety and interference with UNC119 protein interaction seems unlikely.

Attachment of the linker was first performed using HCTU as coupling reagent and DIPEA as base. However, the reaction did not lead to any conversion of the starting materials. Subsequently different coupling reagents were screened (Table 2). A mixture of (1-cyano-2-ethoxy-2-oxoethylideneaminoxy)dimethylamino-morpholino-carbenium hexafluorophosphate (COMU) and DIPEA, as well as a mixture of ethyl cyano(hydroxyimino)acetate (Oxyma), *N,N'*-diisopropylcarbodiimide (DIC), and DIPEA resulted in formation of various side products. The desired product was not found. Conditions involving benzotriazole-1-yl-oxy-tris-pyrrolidino-phosphonium hexafluorophosphate (PyBOP) and DIPEA gave small amounts of product. Finally, linker attachment was achieved with a reaction mixture containing COMU, Oxyma and DIPEA.

Table 2: Screened conditions for linker attachment to generate Pacman-3-based affinity enrichment probes. SM: starting material.

Reagents	Linker (eq.)	Result
HCTU (4eq.), DIPEA 8 (eq.)	4	No conversion of SM
PyBOP (3 eq.), DIPEA (6 eq.)	3	Minor product formation
COMU (3 eq.), DIPEA (6 eq.)	3	Only side reactions
Oxyma (3 eq.), DIC (3 eq.), DIPEA (6 eq.)	3	Only side reactions
COMU(4 eq.), Oxyma (4 eq.), DIPEA (8 eq.)	4	Product formation

To ensure that the positive probes are suitable for affinity enrichment and the linker does not interfere with binding to UNC119 proteins, a photolabeling experiment was performed. Both UNC119 proteins were labeled with efficiencies similar to the probes without linker. The results confirmed, that the introduction of the linker does not influence labeling efficiencies. (Figure 32).

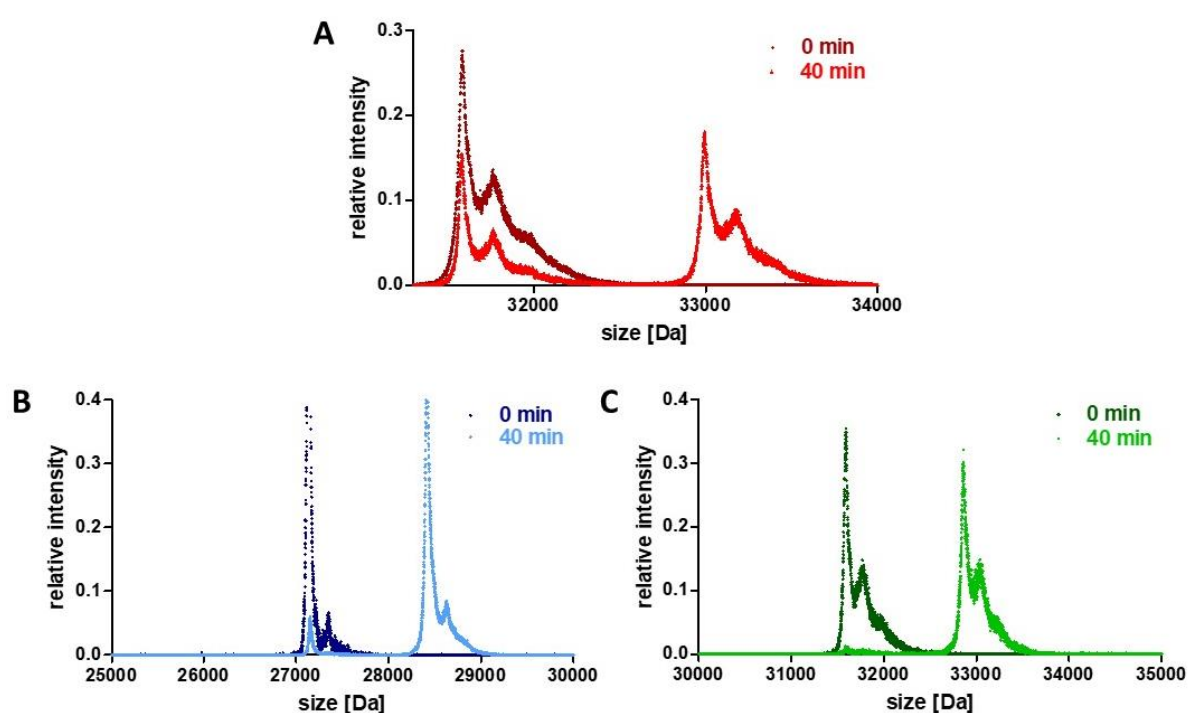


Figure 32: Photocrosslinking of UNC119 protein with affinity enrichment probes. **A:** UNC119B labeled with Pacman-3-Src positive probe **30a** after 0 min and 40 min. **B:** UNC119A labeled with two times 3 equivalents of Pacman-3-Gnat positive probe **38a** after 0 min and 40 min. **C:** UNC119B labeled with two times 3 equivalents of Pacman-3-Gnat positive probe **38a**.

2.3.5.2. Affinity enrichment with Pacman-3-Src

The established method for affinity enrichment is immobilization of probes with a free amine on NHS-coated beads. However, Src contains two additional lysine residues, apart from the C-terminal one. These lysine moieties could interact with NHS-moieties on the beads and cause unspecific immobilization of the probe. Thus, a bioorthogonal linker based on the sulfhydryl-group was chosen, which can be coupled to iodoacetyl-activated UltraLink Resin. The linker was attached to the C-terminal lysine under optimized conditions using a mixture of COMU, Oxyma and DIPEA (Figure 33).

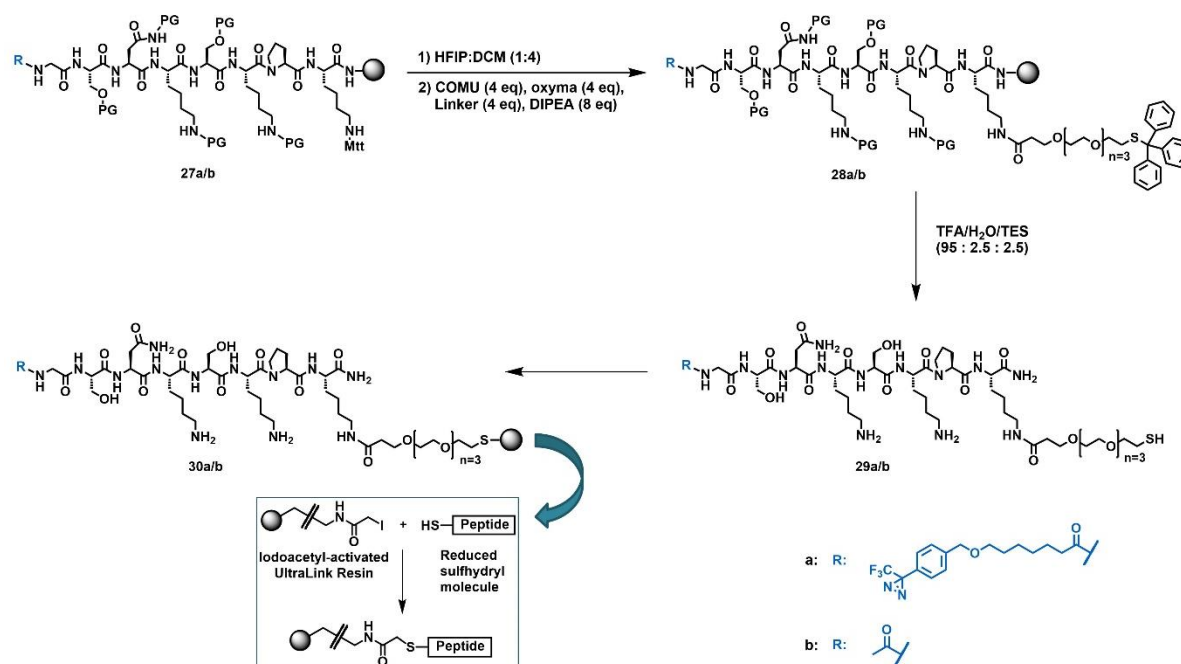


Figure 33: Synthesis and immobilization of Pacman-3-Src positive probe **30a** and the acetylated Src negative probe **30b** with a sulfhydryl linker for affinity enrichment of UNC119 proteins from lysate.

Initial mass spectrometry-based affinity enrichment was performed with Pacman-3-Src positive probe **30a** and the acetylated Src negative probe **30b** immobilized on iodoacetyl-modified beads. A wide range of proteins was isolated with the positive probe **30a** as well as the negative probe **30b**. However, neither UNC119A nor UNC119B were detected. A possible explanation for this unspecific enrichment could be insufficient saturation of the free iodoacetyl groups remaining after attachment of the probe. The capping of the unreacted iodoacetyl moieties was performed with L-cysteine. However, the free thiol groups of the amino acid

sidechain can form disulfide bridges, which prevent reaction with iodoacetyl groups of the resin. In order to reduce the disulfide bonds, tris(2-carboxyethyl)phosphine (TCEP) was added to the aqueous solution of L-cysteine. Nevertheless, the background could not be reduced and no UNC119 proteins were detected. To reduce the amount of the unspecifically bound proteins, more stringent washing conditions were applied, which should remove non-covalent binding partners. Therefore, a buffer with low pH was chosen that denatures and dissolves proteins. The interaction with the negative probe is by default non-covalent, since it does not have a diazirine group. Hence, the denaturated proteins should be washed off and overall amount of detected proteins decreases. As an additional negative control beads without probe were saturated with L-cysteine to analyze if the high amount of detected proteins is caused by the probe or by the beads themselves. The additional negative control revealed that already beads without any probe are enriched with high amounts of proteins from the lysate, which could not be eluted by more stringent washing conditions. UNC119 proteins could not be identified in any of the performed affinity enrichment experiments. Therefore, the beads are not suitable for enrichment of low abundant proteins.

Consequently, different beads were chosen for immobilization of the probe. These were dibenzocyclooctyne (DBCO) modified magnetic beads for copper-free click reactions with azides. The probes were therefore modified with another linker containing a terminal azide moiety (Figure 34). In comparison to NHS- and iodoacetyl-modified beads, copper-free click reactions are fully bioorthogonal. This enables selective ligation of the respective reaction partners in complex biomolecular mixtures and should prevent undesired reactions with components from the lysate.^[88] Quenching of the beads after probe immobilization is not required.

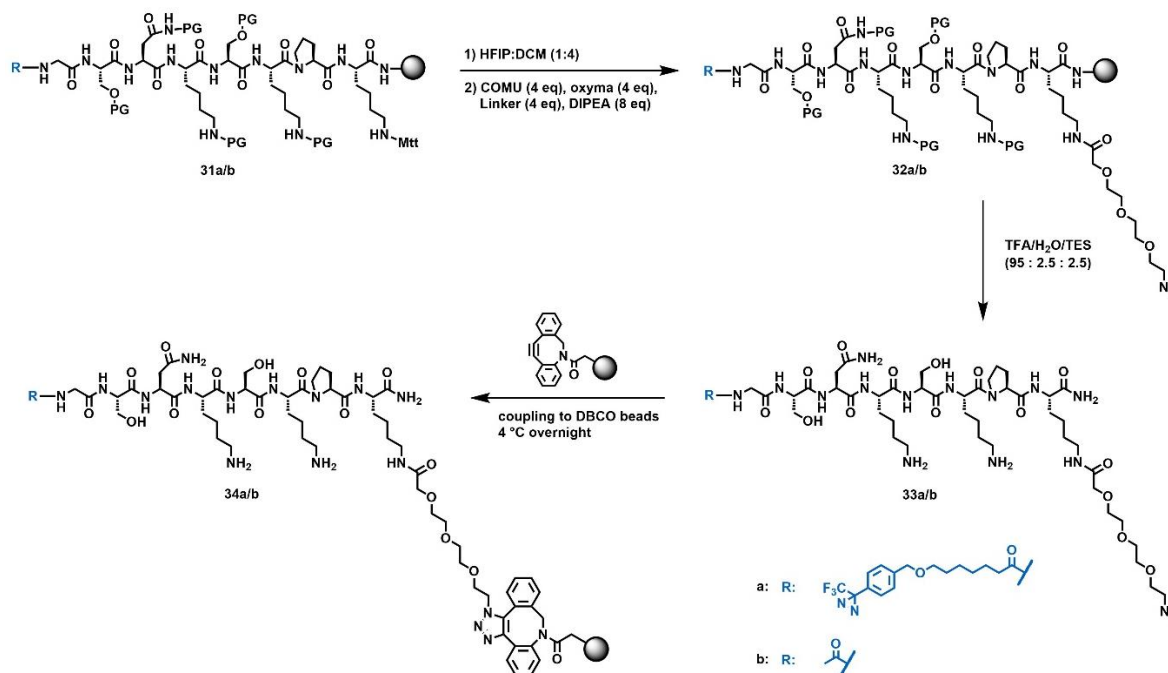


Figure 34: Synthesis and immobilization of Pacman-3-Src positive probe **34a** and the acetylated Src negative probe **34b** with a DBCO linker for affinity enrichment of UNC119 proteins from lysate.

However, also with the DBCO magnetic beads the overall amount of detected proteins was high, but neither UNC119B nor UNC119A could be identified. UNC119 proteins are of low abundance, thus it is possible that the protein binds to the positive probe, but lies below the detection limit. Therefore, the amount of resin was increased by 50 %, in order to enhance the overall amount of enriched protein. Additionally, more stringent washing conditions were applied with radioimmunoprecipitation assay (RIPA) buffer containing various detergents, leading to denaturation and solvation of non-covalently bound proteins. The beads were washed with PBS several times, in order to remove remaining detergent. However, polyethylene glycol (PEG) groups were detected, which interfere with MS measurements. Again, neither UNC119A nor UNC119B were detected. Since the loading density of the magnetic beads with 30-50 nmol DBCO-groups/mg resin is very low, agarose beads with a loading density of 10-20 μmol DBCO-groups/ml resin were used. Since RIPA buffer was not suitable, washing steps were performed with 1% SDS in PBS. However, also SDS could not be removed by subsequent washing with PBS and the samples could not be analyzed by MS measurement. For this reason, urea in PBS was used as washing buffer, which does not interfere with MS detection methods. The new conditions with DBCO agarose beads and urea washing buffer resulted in detection of UNC119B, but not UNC119A. This was expected, due to the

fact, that Pacman-3-Src only labels UNC119B and not UNC119A. However, UNC119B was also identified in the negative control samples. Subsequently, the experiment was performed with unmodified DBCO agarose beads as an additional negative control, to determine whether UNC119B interacts with the probe or binds unspecifically to the bead surface. The result showed that UNC119B protein could also be enriched with the unmodified beads. In conclusion, any optimization attempts for affinity enrichment of UNC119B with Pacman-3-Src failed. The interaction of Pacman-3-Src with UNC119B could not be demonstrated in lysate. This could be due to the low affinity of the probe for UNC119 combined with very low expression levels of the protein in cells. Since Pacman-3-Gnat has higher photolabeling efficiency, affinity enrichment of UNC119 proteins from lysates was subsequently attempted with this probe.

2.3.5.3. Affinity enrichment with Pacman-3-Gnat

For immobilization of Pacman-3-Gnat **24a** 12-(9-fluorenyl-methyloxycarbonylamino)-4,7,10-trioxa-dodecanoic acid was chosen as the linker (Figure 35). The amine group of the linker is bioorthogonal to the side chains of the peptide. Thus, the peptide does not contain any amino groups that could result in linker independent immobilization. The linker was attached to the C-terminal lysine under optimized conditions using a mixture of COMU, Oxyma and DIPEA, followed by deprotection of the amine on the linker. Finally, the peptide was fully deprotected and released from the resin.

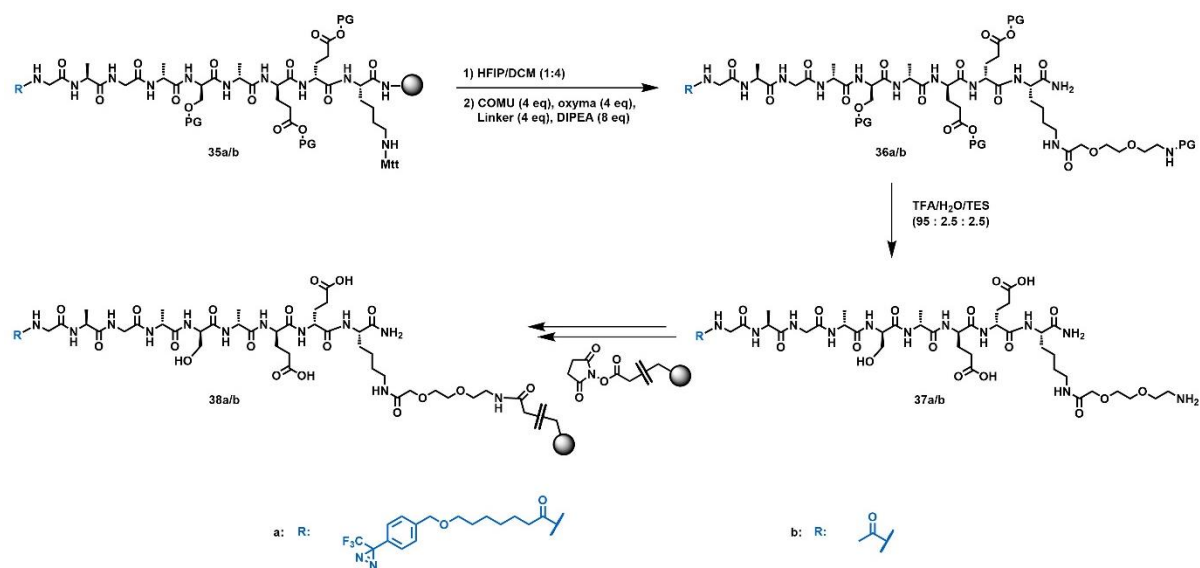


Figure 35: Synthesis and immobilization of Pacman-3-Gnat positive probe **38a** and the acetylated Gnat negative probe **38b** for affinity enrichment of UNC119 proteins from lysate.

For affinity enrichment the positive probe **38a** and negative probe **38b** were immobilized on NHS-modified magnetic beads. Initially, the experiment was performed with 1 mg of total protein per sample, but neither UNC119A nor UNC119B were enriched with Pacman-3-Gnat. Since UNC119 is only marginally expressed in cells the amount of enriched protein could be below the detection limit. Therefore, the total protein amount was increased to 2.5 mg per sample. This resulted in identification and specific enrichment of UNC119A with Pacman-3-Gnat **38a** in comparison to acetylated Gnat **38b**. However, UNC119B could not be identified. A possible reason might be that high abundant proteins saturated the beads and prevented full enrichment of UNC119 proteins. Subsequently, also the amount of beads and affinity enrichment probe was increased from 25 μ l beads and 10 μ M probe to 100 μ l beads and 60 μ M probe in coupling buffer, in order to enrich higher amounts of protein from the lysate. This resulted in statistically significant enrichment of UNC119A and UNC119B with the positive probe **38a** in comparison to the negative probe **38b**. The affinity enrichment was performed twice as triplicate. Only those proteins were considered as hits which were significantly enriched in both replicates. A total of sixteen different proteins, including UNC119A and UNC119B were identified (Table 3).

Table 3: List of proteins significantly enriched in both affinity enrichment experiments with Pacman-3-Gnat **38a** in comparison to acetylated Gnat **38b**. UNC119 proteins (green), fatty acid binding proteins (blue), RZZ complex (purple), presumably false positive hits (red), miscellaneous (black).

Hits found in both pulldowns	Gene names
Protein unc-119 homolog A	UNC119A
Protein unc-119 homolog B	UNC119B
Carnitine O-palmitoyltransferase 2, mitochondrial	CPT2
Delta(3,5)-Delta(2,4)-dienoyl-CoA isomerase, mitochondrial	ECH1
Enoyl-CoA delta isomerase 2, mitochondrial	ECI2
Peroxisomal multifunctional enzyme type 2	HSD17B4
Hydroxysteroid dehydrogenase-like protein 2	HSDL2
Methylmalonyl-CoA mutase, mitochondrial	MUT
Sterol carrier protein-2	SCP2
Kinetochore-associated protein 1	KNTC1
Protein zwilch homolog	ZWILCH
Centromere/kinetochore protein zw10 homolog	ZW10
Importin-5	IPO5
[Pyruvate dehydrogenase (acetyl-transferring)] kinase isozyme 1	PDK1
Mevalonate kinase	MVK
Fascin	FSCN1

A large number of the identified hits either bind lipids or interact generally with hydrophobic moieties. Four of these proteins, encoded by the genes CPT2, ECH1, ECI2 and HSD17B4, are involved in fatty acid beta-oxidation, a pathway regulating fatty acid degradation for cellular energy production. Another hit protein, the sterol carrier protein-2 (SCP2), was first known to bind cholesterol and mediate transport across the membrane. However, SCP2 is an unspecific lipid-transfer protein and binds also to fatty acids.^[89] The function of the hit protein hydroxysteroid dehydrogenase-like protein 2 is still mostly unknown, but since it is localized in peroxisomes also for this protein a role in fatty acid metabolism was postulated.^[90] The methylmalonyl-CoA mutase is involved in degradation of certain amino acids and odd-chain fatty acids.^[91] All these hits suggest that Pacman-3 is recognized as a fatty acid inside cells,

even though it is slightly altered with the aromatic ring and the diazirine moiety attached to the lipid chain.

The kinetochore-associated protein 1, protein zwilch homolog and centromere/kinetochore protein zw10 homolog are further hits from the affinity enrichment experiment. These three proteins form together the RZZ-complex playing a vital role in the spindle assembly checkpoint. The kinetochore-associated protein 1 has a lipid-binding site and is known to interact with the farnesylated protein spindly.^[92] Two more hits are kinases, the [pyruvate dehydrogenase (acetyl-transferring)] kinase isozyme 1 and the mevalonate kinase. Another enriched protein is fascin, which has an actin binding activity. For these proteins, no direct explanation for binding of Pacman-3-Gnat can be found.

Importin-5 is a frequent hit in affinity-enrichment experiments. Importins recognize and bind to the nuclear localization sequence (NLS) of proteins and subsequently transport these into the nucleus.^[93] Various proteins possess a NLS. Thus, importins are often false positive due to possible indirect enrichment by binding to a hit protein. Conclusively, this experiment demonstrates that Pacman-3-Gnat can interact with UNC119 proteins in a complex mixture of proteins and is recognized as a substrate also under competition with native myristoylated proteins. Furthermore, Pacman-3-Gnat is recognized as a fatty acid by several more cellular proteins. This is a first indication that the probe is suitable for experiments on cellular level.

2.3.6. Metabolic incorporation of Pacman-3

The Pacman-3 analogue should also be suitable for metabolic incorporation by cells. One critical step during metabolic incorporation is the recognition of Pacman-3 **3** by *N*-Myristoyl-transferase protein as a substrate. NMT proteins recognize the Coenzyme A (CoA) derivative of myristic acid and transfer the lipid moiety to the N-terminal glycine of the target protein followed by the release of CoA-SH. In order to investigate, whether Pacman-3 **3** is a substrate of human NMT, the Pacman-3-CoA derivative **40** was synthesized (Figure 36). Initially, Pacman-3 **3** was activated with carbodiimidazole (CDI) and subsequently CoA-SH **39** was added. The desired product should be precipitated in an aqueous solution with 20% perchloric acid. However, only minor amount of precipitate was visible and during the analysis of the solution as well as the precipitate only starting materials were detected. Afterwards, the reaction conditions were optimized and when the reaction was performed in the presence of PyBOP and DIPEA, the desired Pacman-3-CoA adduct **40** was formed in 27% yield.

Purification of the desired product **40** was performed by reverse phase HPLC with negative detection mode.

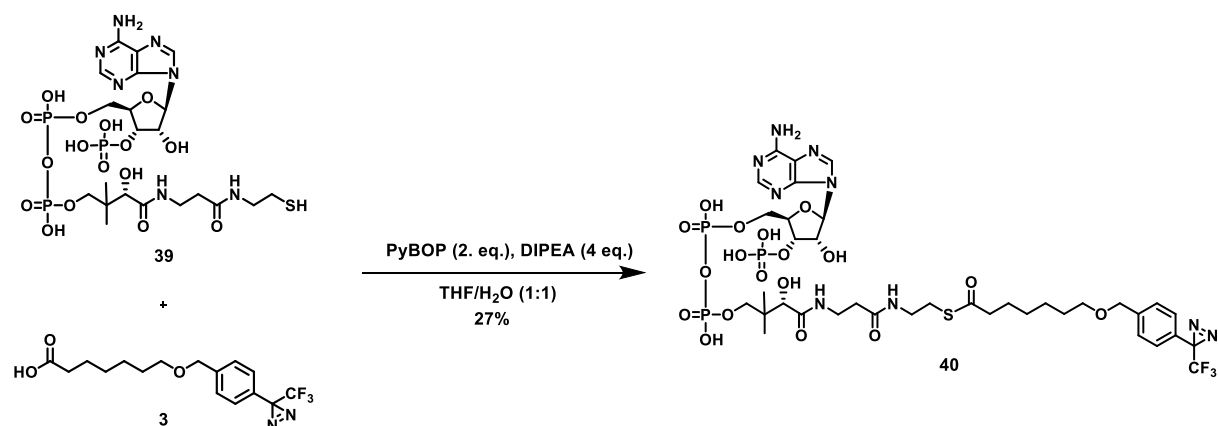


Figure 36: Synthesis of the Pacman-3-CoA derivative **40**.

The transferase assay was carried out in a collaboration with the group of Prof. Edward Tate at Imperial College London. The assay detects substrate recognition of myristate analogues by NMT enzymes (Figure 37). The assay was performed with purified NMT proteins from different species and their respective peptide substrates. During transfer of Pacman-3 **3** to the N-terminus of a peptide substrate by NMT protein, a free thiol of coenzyme A (CoA-SH) is released. The free CoA-SH can then react with 7-diethylamino-3-(4'-maleimidylphenyl)-4-methyl-coumarin (CPM). CPM by itself is only slightly fluorescent, while the CPM-CoA conjugate features strong fluorescence with an excitation maximum at 384 nm and an emission maximum at 470 nm. An increase of CPM-CoA-conjugate correlates to an increase in fluorescence intensity. Thus, the fluorescence intensity can be used as readout for the reaction rate of each NMT. Myristoyl-CoA was used as a positive control.^[94]

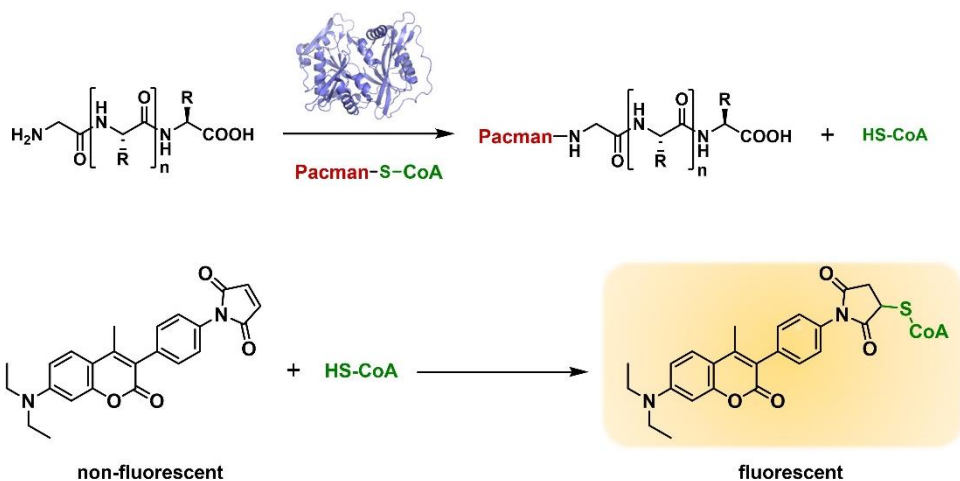


Figure 37: Transfer of Pacman-3 to N-terminus of a peptide substrate by NMT under release of HS-CoA. HS-CoA reacts with CPM to form a fluorescent adduct.

The obtained results showed that Pamcan-3-CoA **40** was not recognized as a substrate by human NMT (HsNMT). However, NMTs from different parasitic species revealed that Pacman-3-CoA **40** is a substrate for *Leishmania donovani* and *Leishmania major*, as well as *Trypanosoma brucei*, but not for *Candida albicans*, *Plasmodium vivax* and *Plasmodium falciparum*, which suggests that NMTs of these species might differ slightly in their myristoyl-CoA binding site (Figure 38).

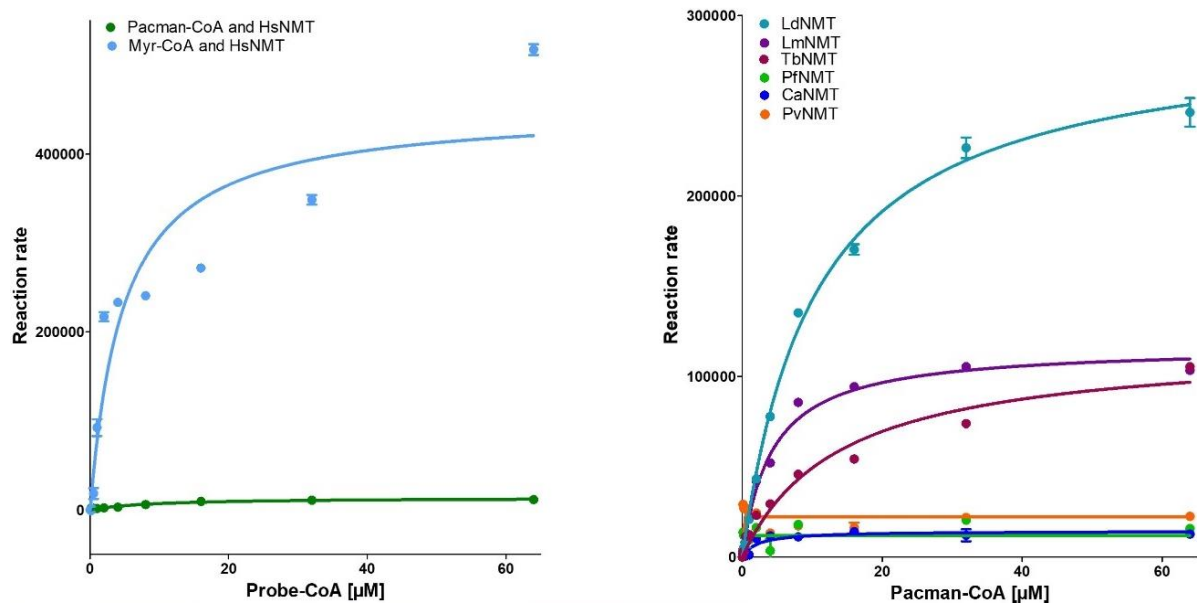


Figure 38: Incorporation of Pacman-3 by NMTs from different organisms. NMTs were incubated with substrate peptide and increasing concentrations of Pacman-3-CoA **40** in presence of CPM. Fluorescence was detected at an emission wavelength of 470 nm. Left: Incorporation of Pacman-3 (green) and myristic acid (blue) by human NMT. Right: Incorporation of Pacman-3 by LdNMT (*Leishmania donovani*, light blue), LmNMT (*Leishmania major*, purple), TbNMT (*Trypanosoma brucei*, red), PvNMT (*Plasmodium vivax*, orange), PfNMT (*Plasmodium falciparum*, green) and CaNMT (*Candida albicans*, blue).^[87]

The protozoan parasites *Trypanosoma brucei*, *Leishmania major* and *Leishmania donovani* are responsible for various diseases, including sleeping sickness and different types of leishmaniasis. Only recently the involvement of UNC119 in parasite motility and morphology of *T. brucei* was discovered.^[95] Knockdown of TbUNC119, together with its interaction partner TbUNC119BP resulted in reduced motility, morphological alterations and cellular apoptosis. Parasite motility is a key factor in mammalian host pathogenesis. Thus, it is crucial to investigate the role of TbUNC119 in this process and to identify unknown cargo proteins, for which Pacman-3 **3** can be a valuable tool. Furthermore, Pacman-3 **3** could be applied for analyzing the myristoylome of the mentioned parasitic kinetoplastids *Trypanosoma* and *Leishmania* also inside human host cells. Since HsNMT does not recognize Pacman-3-CoA **40** the probe should only be incorporated by the parasite NMT. Hence possible protein substrates of the parasite NMT could be identified.

2.3.7. Thermal proteome profiling of UNC119 inhibitors

Detailed knowledge of the binding of UNC119 to different myristoylated proteins including Src, led to the development of two classes of UNC119 inhibitors, based on the squaramide and benzothiazolone scaffold.^{[72],[73]} These inhibitors bind to the hydrophobic cavity and prevent the insertion of the myristoyl moiety of lipidated proteins. The binding of the two most potent inhibitors representing both scaffolds, namely Squarunkin A and GG1198, were evaluated in a TPP assay to confirm target interaction in a complex protein mixture (Figure 39).

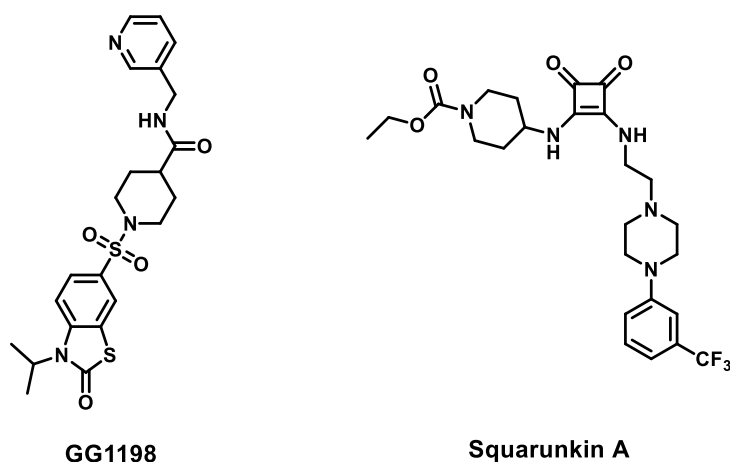


Figure 39: Structures of the UNC119 inhibitors GG1198 and Squarunkin A.

TPP is a label-free method, which in comparison to affinity enrichment does not require linker attachment (Chapter 1.3.2.). The readout is based on changes in thermal stability of a protein upon compound interaction. Therefore, cell lysates are treated with the compound or DMSO and subsequently incubated at a temperature range between 37 °C and 65 °C. The soluble fraction, obtained by centrifugation is subjected to MS/MS analysis. The measured peak intensities correspond to the amount of soluble protein for each temperature and result in a melting curve. A shift in the protein melting curve of DMSO and compound treated samples indicates a possible interaction of the compound with the respective protein.

The TPP experiment was performed with Jurkat cells. Initially, the lysis buffer contained 0.4% NP-40 alternative, a detergent, which enables solubilization of membrane proteins. Both inhibitors, Squarunkin A and GG1198, were added in a final concentration of 1 μM with 0.1% DMSO. A significant thermal shift was defined according to the following criteria: 1) the

protein is either stabilized in all the replicates or destabilized and 2) each protein shows a minimal shift of ≥ 3 °C.

Table 4: Shift in melting temperature dT_m for UNC119 proteins with 1 μ M TM-A-124 or GG1198 with or without detergent. RI-RIII: replicate I-III; av.: average

inhibitor	detergent	dT_m UNC119A [°C]				dT_m UNC119B [°C]			
		RI	RI	RII	av.	RI	RI	RII	av.
Squarunkin A	0.4% NP40	4.6	-0.9	0.7	1.5	3.0	2.9	3.5	3.2
	--	6.8	5.5	--	6.2	7.4	8.7	--	8.1
GG1198	0.4% NP40	2.4	1.6	-3.4	0.2	0.2	3.7	-5.1	-0.4
	--	0.1	3.1	1.8	1.6	5.7	0.9	6.7	4.4

Squarunkin A showed an average shift of 3.2 °C in melting temperature (dT_m) of UNC119 B. UNC119A had only an average dT_m of 1.5 °C. While UNC119B could be regarded as a possible interaction partner, UNC119A was only stabilized by more than 3 °C in one single replicate and would thus not be considered as a target (Table 4).

With inhibitor GG1198 similar result were obtained (Table 4). UNC119A had an average dT_m of 0.2 °C, caused by destabilization of -3.4 °C in one of the replicates and stabilization of 2.4 °C and 1.6 °C in the other two replicates. Comparable results were obtained for UNC119B with an average dT_m of -0.4 °C. Again, the same replicate showed a destabilization with a shift of -5.1 °C for UNC119B and in the other two replicates UNC119B was stabilized by 0.2 °C and 3.7 °C.

Previous labeling experiments with Pacman analogue and UNC119 proteins showed that detergents can interact with the lipid binding pocket and compete with the analogue for the binding site. For the lysis buffer of TPP experiments NP40 is used, featuring a polyethyleneglycol chain, which could insert into the hydrophobic pocket of UNC119. An interaction of the detergent with UNC119 could also result in destabilization or stabilization of the protein in DMSO treated samples. This would alter the difference in melting temperature between DMSO and compound treated samples unpredictively. Therefore, the TPP experiment was repeated without the addition of detergent to the lysis buffer (Table 4). When the experiment was performed with Squarunkin A the majority of shifts from one replicate differed

significantly from the other two. Thus, this replicate was not considered any further during the analysis of the results. The TPP without detergent for Squarunkin A provided an average dT_m of 6.2 °C for UNC119A, with single shifts of 6.8 °C and 5.5 °C. UNC119B showed dT_m of 7.4 °C and 8.7 °C resulting in an average dT_m of 8.1 °C (Figure 40). The respective dT_m for both UNC119 proteins met the above-mentioned criteria. Thus, the inhibitor can be considered as an interaction partner of both proteins, UNC119A and UNC119B.

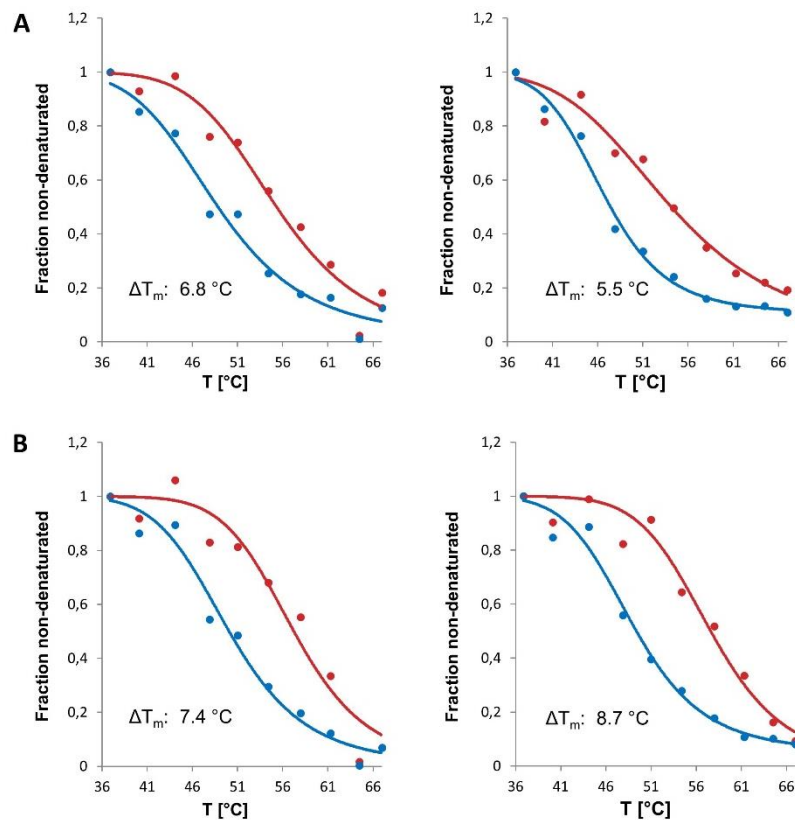


Figure 40: Thermal proteome profiling experiments with Squarunkin A. Jurkat cells were lysed with PBS, treated with 1 μ M compound (red) or DMSO (blue) and subjected to heat treatment. Thermal stability of proteins was determined by tandem MS/MS analysis. $n = 2$, each graph represents one independent experiment. **A:** Replicates of the thermal shifts of UNC119A. **B:** Replicates of the thermal shifts of UNC119B.

The TPP without detergent for the inhibitor GG1198 gave an average dT_m of 1.6 °C for UNC119A, with single dT_m of 0.1 °C, 3.1 °C, and 1.8 °C and an average dT_m of 4.4 °C for UNC119B with single dT_m of 5.7 °C, 0.9 °C and 6.7 °C (Figure 41). For this inhibitor it is more difficult to predict whether it is an interaction partner of UNC119 proteins or not. However, all

three replicates show a trend of stabilization. UNC119B is even stabilized by more than 5 °C in two of the replicates. Conclusively, Squarunkin A causes a significant stabilization of UNC119A as well as UNC119B and is therefore an interaction partner of both proteins. For GG1198 not all replicates show a significant stabilization. However, the general trend is a stabilization of both UNC119 homologs and might therefore indicate an interaction.

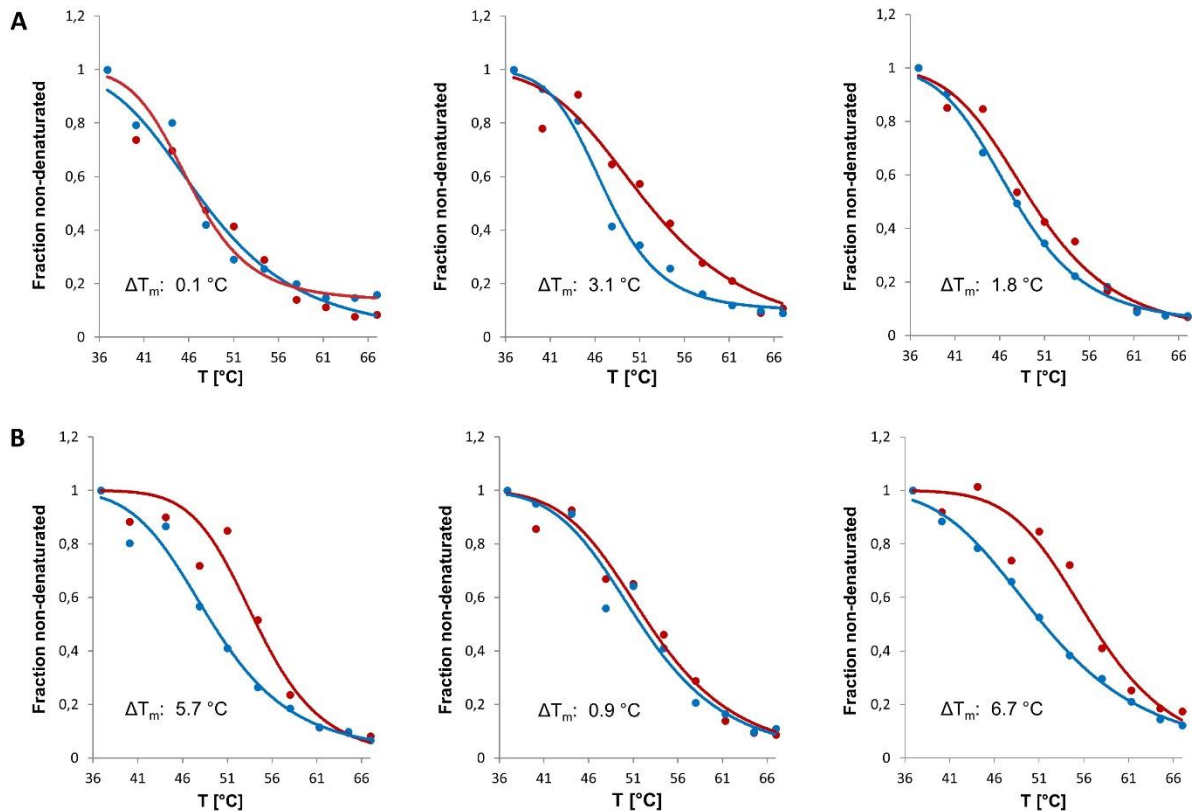


Figure 41: Thermal proteome profiling experiments with GG1198. Jurkat cells were lysed with PBS, treated with 1 μM compound (red) or DMSO (blue) and subjected to heat treatment. Thermal stability of proteins was determined by tandem MS/MS analysis. $n = 3$, each graph represents one independent experiment. **A:** Replicates of the thermal shifts of UNC119A. **B:** Replicates of the thermal shifts of UNC119B.

2.4. Summary and conclusion

N-Myristoylation plays a key role in regulation of cellular signaling and protein activation. It is involved in various severe disorders, including cancer and neurodegenerative diseases. Even though protein lipidation is intensely studied, the mechanism underlying the trafficking of myristoylated proteins between different intracellular membranes remains largely unknown. One of the chaperone proteins involved in this process is UNC119. The UNC119 protein features a hydrophobic pocket for incorporation of the lipid moiety, in order to conceal it from the hydrophilic environment of the cytoplasm. Thus, overall solubility is increased, enabling trafficking of the lipidated protein through the cytoplasm. One such cargo protein is the myristoylated non-receptor tyrosine kinase Src. Bastiaens et al. reported the UNC119-dependent spatial cycles of Src. The UNC119 chaperone protein sequesters and transports cytosolic Src to the RE. By vesicular transport the kinase is subsequently enriched at the plasma membrane, which ensures Src signaling activity. Even though at least 0.5% of the proteome is predicted to be myristoylated only few cargo proteins of UNC119 are identified to date. Photoactivatable myristate analogues forming a covalent bond upon irradiation, can serve as tools to overcome these obstacles and study protein-myristate interactions.

In the course of this project three different photoactivatable myristic acid analogues were designed and successfully synthesized (Figure 42). Two of these analogues, Pacman-1 and Pacman-2, are based on alkyl diazirines, which closely mimic the saturated lipid chain of myristic acid. The third analogue, Pacman-3, contains a more stable trifluorophenyldiazirine.

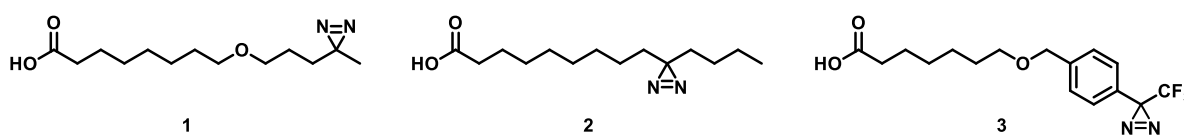


Figure 42: Diazirine-based photoactivatable analogues of myristic acid Pacman 1-3.

These photoactivatable lipid analogues were attached to the short N-terminal peptide sequence, derived from myristoylated proteins Src and transducin alpha subunit Gnat1. The affinities of these probes to UNC119 proteins were determined by means of a fluorescence polarization assay. While the alkyl diazirine-based probe Pacman-2-Src had comparable affinities to UNC119 proteins as native myristoylated Src-peptide, the affinities of Pacman-1-Src and Pacman-3-Src were significantly lower. In contrast Pacman-3-Gnat featured high affinity to UNC119A and

UNC119B. Subsequently, photocrosslinking efficiency of all Pacman-peptide probes for both UNC119 proteins was determined. The two probes featuring an aliphatic diazirine labelled neither UNC119A nor UNC119B. In contrast, Pacman-3-Src established a covalent crosslink with UNC119B protein with up to 80% labelling efficiency, but did not label UNC119A. Pacman-3-Gnat covalently labelled both UNC119 proteins with $\geq 95\%$ efficiency. Since only probes based on the myristate analogue Pacman-3, were able to covalently photolabel UNC119 proteins upon irradiation, this analogue was employed for further evaluation.

First, the photocrosslinking site within the hydrophobic pocket of UNC119 protein was located. Pacman-3-Src covalently labeled an amino acid residue in close proximity of Tyr-247 inside the hydrophobic pocket of UNC119B. Pacman-3-Gnat established a covalent crosslink close to the conserved phenylalanine residues Phe-196 of UNC119A and Phe-207 of UNC119B. Sequence alignment showed that these two residues are homologous. Conclusively, both lipid analogues seem to insert into the hydrophobic pocket of UNC119 proteins similar to the native myristate moiety. Affinity enrichment of UNC119A and UNC119B from lysate by immobilized Pacman-3-Gnat demonstrated specific interaction of the probe with UNC119 chaperones in a complex protein mixture. For the probe to be suitable for cell-base experiments, it has to be recognized as a substrate by the *N*-Myristoyltransferase. Therefore, substrate recognition of Pacman-3 by various NMTs from different organisms was investigated. Pacman-3 was not incorporated by human NMT. Remarkably, NMT enzymes derived from the protozoan parasite *Leishmania* and *Trypanosoma* recognized Pacman-3 as a substrate and transferred the myristate analogue to the N-terminus of a suitable peptide. Conclusively, Pacman-3 can serve as a valuable tool to investigate the role of UNC119 protein in these parasites, to identify novel myristoyl-interaction partners and shed light on the myristoylome of different organisms.

3. TARGET IDENTIFICATION OF AUTOPHAGY INHIBITORS

3.1 Introduction

3.1.1. Autophagy

Autophagy refers to a dynamic lysosome-dependent degradation process for cellular components, including proteins, whole organelles and pathogens. This highly conserved process is involved in clearance of protein aggregates, altered organelles and long-lived proteins to maintain cellular homeostasis. Upon starvation autophagy is induced to recycle dispensable macromolecules and organelles. Thus, cell survival is ensured by supply of essential cellular building blocks and nutrition.^[96] While the clearance of harmful and superfluous cellular components is selective, starvation-induced autophagy occurs predominantly in a non-selective manner.^[97] Furthermore, autophagy assists in adaption to environmental changes and responses to cellular stress caused by various factors.^[96]

Three major types of autophagy have been reported: chaperone-mediated autophagy (CMA), microautophagy and macroautophagy. In CMA cytosolic proteins are transported to the lysosome by chaperones, where they are degraded. These proteins are characterized by specific peptide sequences, e.g. the KERF-like motif.^[98] Microautophagy describes a catabolic mechanism, in which the cytosolic cargo is directly invaginated by lysosomal membranes.^[99] Out of the three mentioned mechanisms, macroautophagy is the most intensively studied. The main characteristic of macroautophagy is the engulfment of cellular components, which are designated for degradation by autophagosomes.^[97]

Initiation of macroautophagy (hereafter referred to as autophagy) goes along with formation of a double membrane, the phagophore or isolation membrane (Figure 43). The membrane source and composition of the phagophore is still not fully elucidated. However, recent findings suggest that ER-membrane contact sites play a major role in autophagosome nucleation.^[100] These include contact sites between the ER and mitochondria as well as at the plasma membrane and the ER.^{[101],[102]} Upon maturation and closure of the phagophore, the autophagosome is formed, which subsequently fuses with the lysosome. This causes degradation of the autophagosome content and inner membrane. Finally, lysosomal membrane permeases expose the emerging catabolites to the cytosol.^[103]

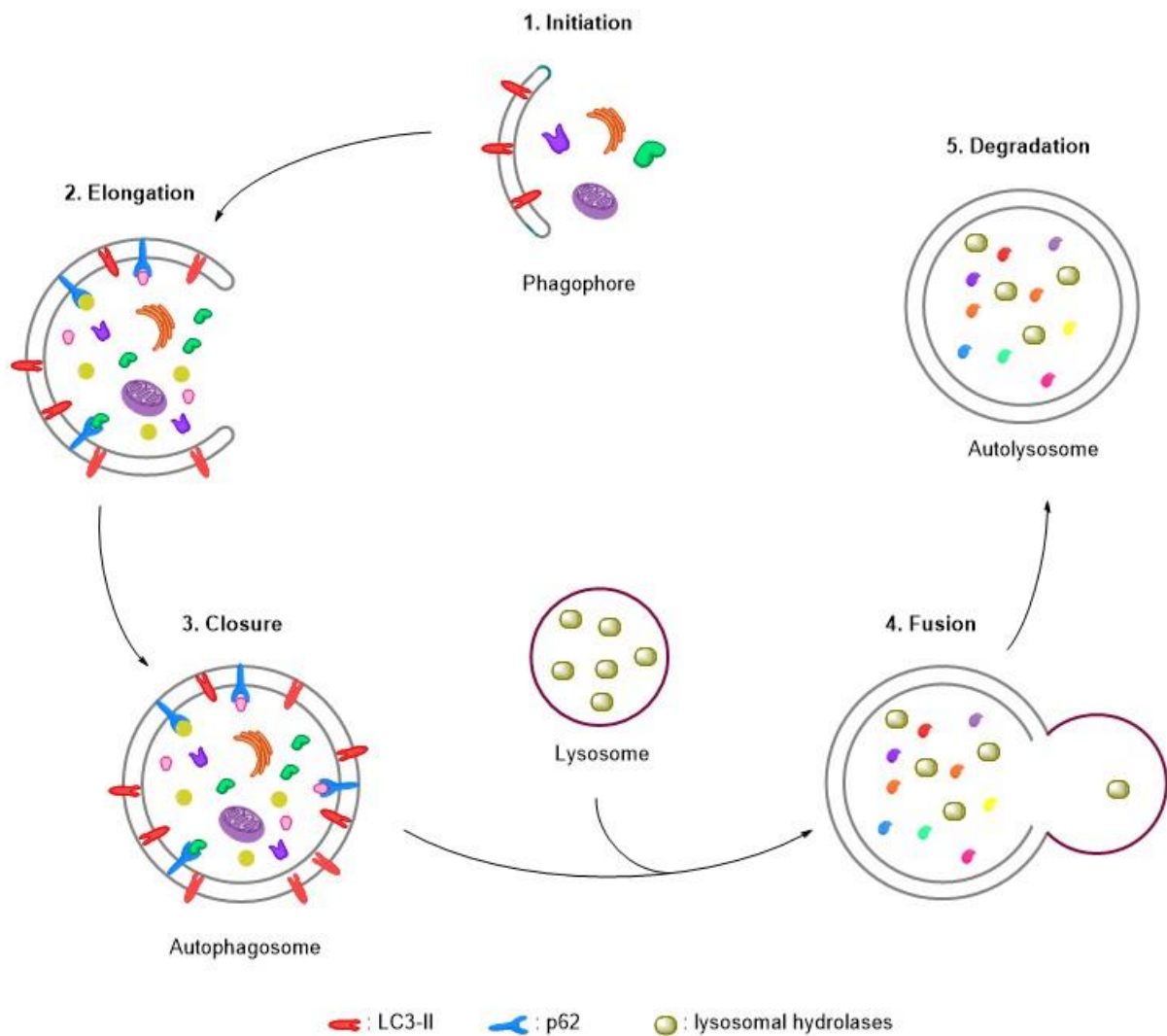


Figure 43: Schematic representation of autophagosome formation and fusion with the lysosome.

3.1.2. The molecular machinery of autophagy

Unraveling of the autophagic machinery was initiated by identification of the autophagy-related (Atg) genes.^[104] Up to date more than 30 Atgs were found in yeast, which feature various functions in autophagic signaling. Many other eukaryotic species also express orthologues of these genes.^[103]

In yeast the Atg1 protein plays a major role in autophagy initiation. The human homologs of Atg1 include the Unc51-like kinases 1 and -2 (ULK1 and ULK2), which form a complex with the focal adhesion kinase family-interacting protein of 200kD (FIP200), Atg13 and Atg101.^[105] Upstream signaling of the ULK1/2 complex is regulated by two kinases, the mammalian target of rapamycin-1 (mTORC1) and the AMP-activated protein kinase (AMPK). In its active state

mTORC phosphorylates ULK1 as well as Atg13, which inhibits the ULK1 kinase activity. Upon amino acid deprivation mTORC is inhibited and the ULK1 complex becomes activated.^[106] Subsequently, ULK1 kinase binds to Atg14L of the VPS34-Beclin1 complex. Beclin-1 gets phosphorylated by ULK1, which causes VPS34 activation.^[107] The VPS34 complex generates phosphatidylinositol 3-phosphate (PI3P), which in turn results in the recruitment of WIPI2^[108]. WIPI2 is involved in microtubule-associated protein 1 light chain (LC3) lipidation.^[109] The ubiquitin-like protein LC3 is an Atg8 family member and regulates phagophore elongation. LC3 is initially processed by Atg4 to cytoplasmic LC3-I. Further conjugation of LC3-I to phosphatidylethanolamine (PE) on the phagophore membrane is performed by the E1-like enzyme Atg7 and the E2-like enzyme Atg3. The resulting LC3-II is characteristic for the phagophore and the autophagosomal membrane. Upon autophagosome lysosome fusion LC3-II inside of the autolysosome is degraded together with the remaining cargo.^[110] The ubiquitin-like protein Atg12 is part of the Atg5-Atg12-Atg16L1 complex, which is also involved in autophagosome biogenesis. Initially, conjugation of Atg12 and Atg5 is performed by Atg7 and the E2-like enzyme Atg10. Subsequently, the Atg5-Atg-12 conjugate forms a non-covalent complex with Atg16L1. This complex is located on the phagophore, but dissociates upon autophagosome maturation (Figure 44).^{[111],[112]}

This catabolic pathway features a high degree of complexity and is involved in the response to various physiological conditions. Therefore, autophagy requires tight regulation through upstream signaling.

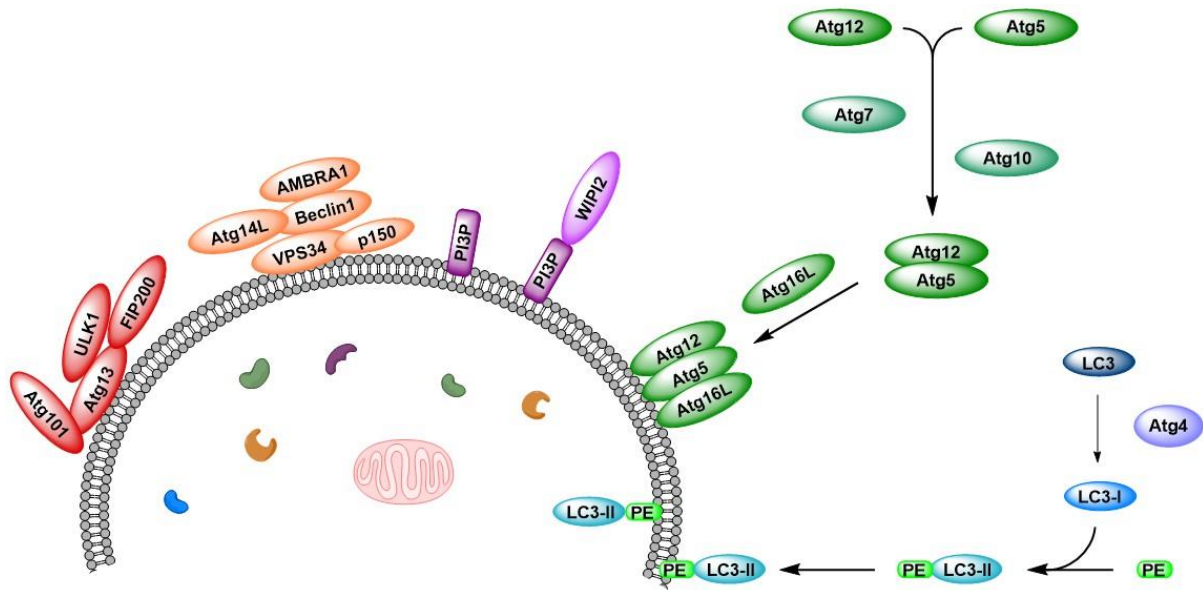


Figure 44: Representative scheme of the autophagic machinery. AMBRA1: Activating molecule in BECN1-regulated autophagy protein 1; Atg: Autophagy related protein; FIP200: Focal adhesion kinase family-interacting protein of 200kD; LC3: Microtubule-associated protein 1 light chain; PE: Phosphatidyl ethanolamine; PI3P: phosphatidylinositol 3-phosphate; ULK: Unc51-like kinase; WIPI2: WD repeat domain phosphoinositide-interacting protein 2; VPS34: Vacuolar protein sorting-associated protein 34.

3.1.3. Regulation of autophagy signaling

One of the major regulators in autophagy is the serine/threonine protein kinase mTOR, which is part of the mTOR complex 1 (mTORC1). Active mTORC1 suppresses autophagy. Different environmental conditions can induce autophagy by inhibition of mTORC1. These include amino acid starvation, growth factors and deviations in cellular energy levels.^[113] Upstream signaling of mTORC1 for nutrition deprivation is mediated by the Ras-related GTP-binding protein (Rag) GTPases. Rag GTPases detect cellular amino acid levels and retain mTORC1 in an activated state under nutrition-rich conditions to prevent autophagy.^[114] Growth factors, such as insulin, regulate autophagy through activation of the PI3KC1a pathway. Subsequently, Phosphatidylinositol-4,5-bisphosphate (PIP₂) is converted to Phosphatidylinositol (3,4,5)-trisphosphate (PIP₃), which results in translocation of the pleckstrin homology domain containing proteins phosphoinositide-dependent kinase 1 (PDK1) and Akt to the plasma membrane. Akt in turn phosphorylates the tuberous sclerosis complex (TSC), which impedes the GTPase-activating protein (GAP) activity of TSC for Rheb and causes mTORC1

activation.^[115] Furthermore, metabolic stress can cause autophagy upregulation. Cellular energy is generated by mitochondrial respiration as well as glycolysis and stored as ATP. The AMPK is a sensor of cellular ATP levels and gets phosphorylated under metabolic stress. AMPK subsequently phosphorylates TSC2, which in turn induces further phosphorylation of TSC2 by Glycogen synthase kinase 3 (GSK3).^{[116],[117]} In contrast to Akt, AMPK induces GAP activity of TSC1/2 heterodimer and thus inhibits mTORC1 (Figure 45).^[118]

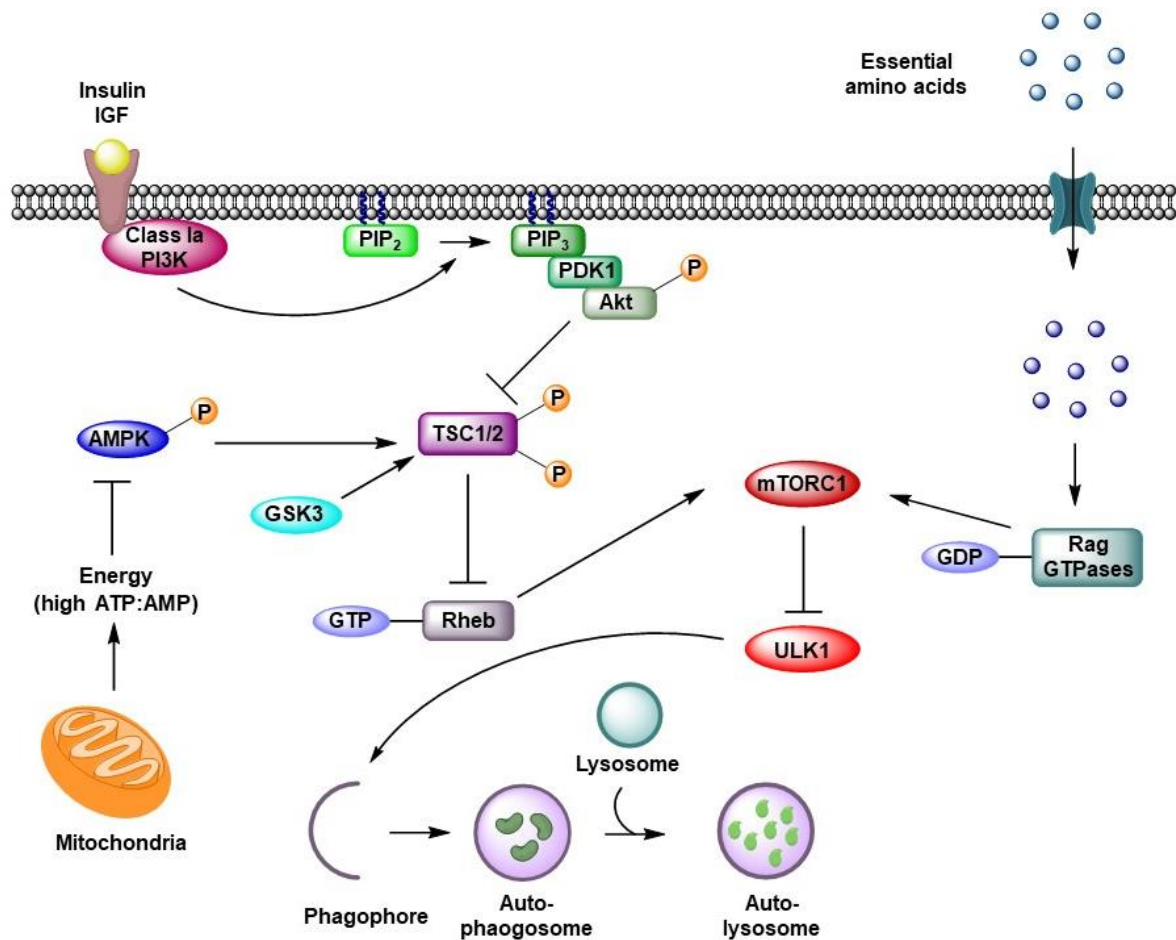


Figure 45: Schematic representation of mTOR-dependent signaling pathways in autophagy.

The macrocyclic autophagy inducer rapamycin inhibits mTORC1 and thus activates mTOR dependent autophagy. While mTOR plays an important role in autophagy, mTOR-independent regulation of the autophagic flux has also been reported, which is not affected by rapamycin.^[118] One such pathway is the Ca²⁺/calpain signaling cascade. Calpains are activated by accumulation of cytosolic Ca²⁺ and trigger cAMP generation through heterotrimeric G proteins.^[119] Subsequently the inositol dependent inhibition of autophagy is mediated

through cAMP-dependent upregulation of the Epac, Rap2B, PLC ϵ network (Figure 46).^{[120],[121],[122]}

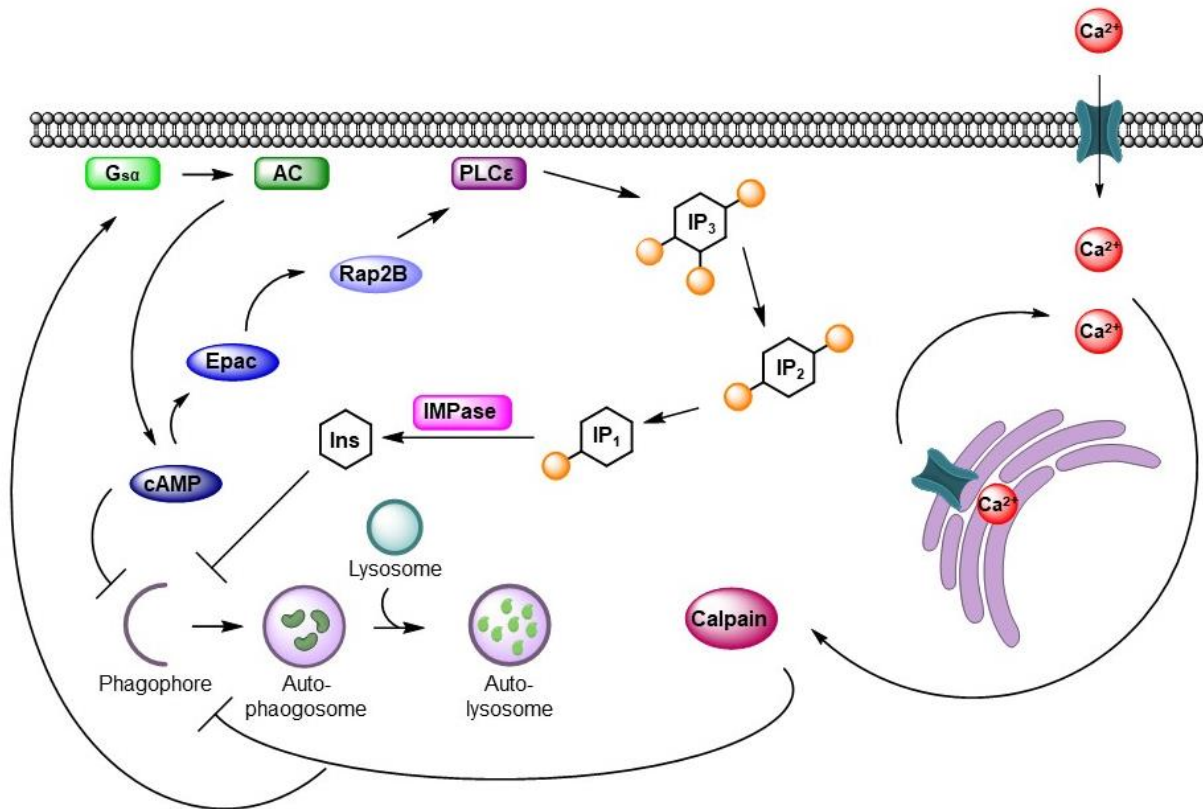


Figure 46: Schematic representation of mTOR independent signaling in autophagy. AC: Adenylyl cyclase; cAMP: cyclic adenosine monophosphate; Rap2B: Ras-related protein Rap-2B; PLC ϵ : Phospholipase C ϵ ; IP $_3$: Inositol trisphosphate; IP $_2$: Inositol bisphosphate; IP: Inositol monophosphate; IMPase: Inositol monophosphatase; Ins: Inositol.

Even though several mTOR-dependent and -independent pathways regulating this catabolic process have already been described, the signaling network remains incomplete. Thus, numerous components of this catabolic process are still to be discovered to explain crosslinks between the different signaling cascades. Since autophagy is also tightly involved in different human diseases the knowledge concerning its regulation and malfunction will significantly contribute to the development of efficient therapeutics.

3.1.4. Autophagy in disease progression and prevention

Autophagy is involved in numerous diseases including cancer, neurodegenerative disorders and pathogen infection. In seemingly contradictory findings, autophagy has been reported to be both a protective mechanism against certain diseases, but also contributive factor to pathological alterations.^[123]

Basal autophagy is of high relevance for cellular homeostasis, due to cellular protein turnover. Especially, in long-lived and non-proliferative cells, such as neurons the absence of autophagy can induce severe neurodegeneration. The loss of certain autophagic regulators, such as Atg5, can lead to the enrichment and aggregation of altered and pathogenic proteins. These aggregates are deleterious for normal cellular function and a major cause of neurodegenerative disorders.^[124] In Huntington disease, formation of protein aggregates is triggered by critical elongation of the N-terminal polyglutamine sequence of the huntingtin protein. Even though presence of mutant huntingtin induces autophagosome formation, cargo recognition is impaired. This results in cellular accumulation of pathological protein aggregates and damaged organelles.^[125] Hallmarks of Parkinson's disease are α -synuclein aggregates, while aggregation of hyperphosphorylated tau and misfolded amyloid- β are characteristic for Alzheimer's disease.^{[126],[127]} These disorders are also connected to autophagy malfunction. Thus, increasing autophagic flux might present a possible therapeutic approach for these neurodegenerative disorders.^{[127],[128]}

Autophagy is presumed to have opposite effects in cancer depending on the stage of progression. On one hand autophagy can prevent tumorigenesis. Abnormal organelles are a possible origin of oxidative stress and can cause DNA damage. Autophagy regulates the clearance of these organelles to protect the cell from deleterious genetic defects.^[129] Furthermore, oncogenic protein substrates are eliminated by autophagic degradation.^[130] However, in advanced stages of cancer, autophagy promotes tumorigenesis. Cells located at the tumor center often suffer from nutrient deprivation due to insufficient vascularization. The upregulation of autophagy ensures energy supply and survival of these cells. Furthermore, autophagy can be a protective mechanism for tumor cells, by removal of damaged organelles and proteins resulting from cancer treatment. Hence, the inhibition of autophagy presents a potential therapeutic approach to overcome autophagy based drug resistance and improve cancer treatment.^[131]

3.1.5. Small molecule modulators of autophagy

The autophagy machinery is highly complex and involved in various pathologic conditions, including neurodegenerative diseases and cancer. Thus, novel autophagy modulators are highly relevant for the development of effective therapeutics. Furthermore, these modulators are valuable tools to investigate and elucidate the mechanism underlying the autophagic machinery.

Inducers of autophagy could be beneficial therapeutics for neurodegenerative diseases (Figure 47). These disorders are characterized by the accumulation of protein aggregates and dysfunctional organelles. Elevation of cellular autophagy levels could assist in the clearance of these pathological components, which might slow down disease progression and reduce symptoms.^[132] The macrocyclic lactone rapamycin is an inducer of autophagy by inhibition of mTOR. Rapamycin has beneficial effects in a mouse model of Alzheimer's disease. The autophagy inducer reduces amyloid- β overload, diminishes cognitive defects and decelerates disease progression.^[133] Similar effects were observed with the AMPK activator resveratrol.^[134] Furthermore, the small molecules GSK621, metformin and PT1 activate AMPK, which results in inhibition of mTOR activity.^[135]

In contrast to neurodegenerative diseases, in progressive state of cancer the inhibition of autophagy could be a possible therapeutic approach (Figure 47).^[136] Such an autophagy inhibitor is wortmannin, which targets the PI3K kinase. However, wortmannin is rather unselective and also inhibits other kinases.^[137] Furthermore, several VPS34 inhibitors were reported, such as SAR405, PIK-III, VPS34-IN1 and autophinib.^{[138], [139],[140],[141]} Alteration of VPS34 activity interferes with autophagosome biogenesis.^[141] Two small molecules that impair autophagic flux are chloroquine and its derivative hydroxychloroquine. Chloroquine prevents fusion of the autophagosome with the lysosome and is an essential tool compound in autophagy research. Both hydroxychloroquine and chloroquine are FDA approved drugs.^[142] Due to synergistic effects these bioactive molecules are applied in co-treatment with several chemotherapeutics. The cinchona alkaloid chloroquine is already employed in medical treatment for centuries.^[143]

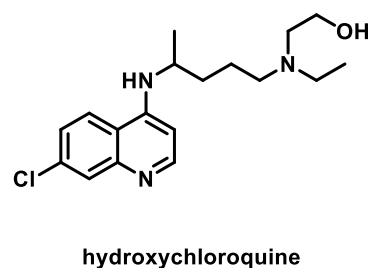
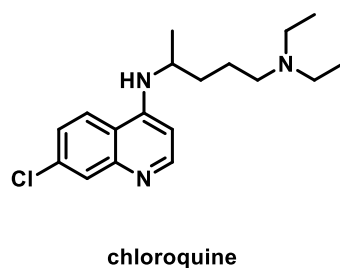
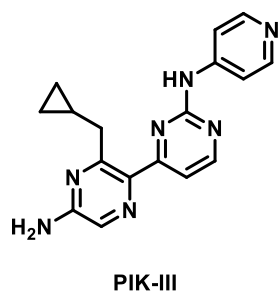
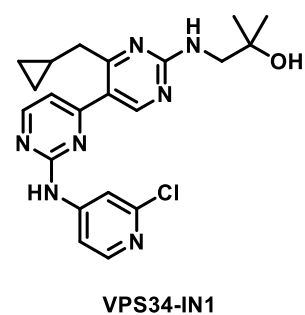
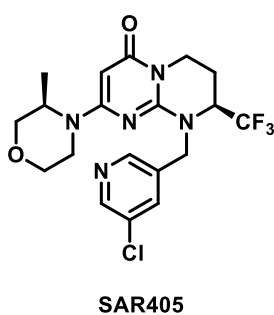
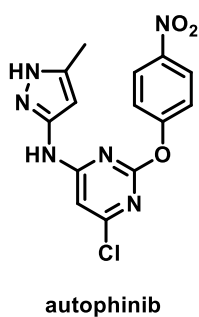
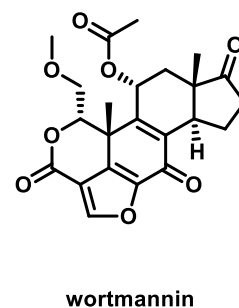
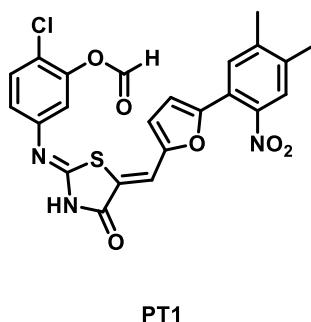
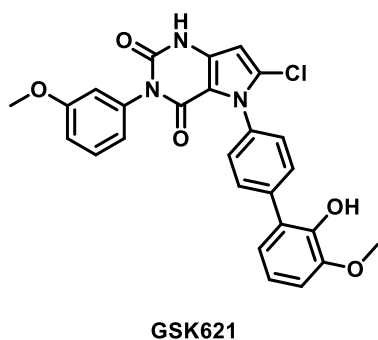
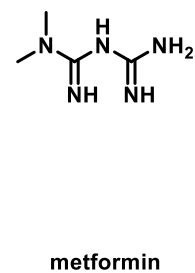
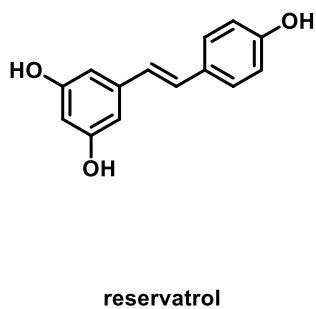
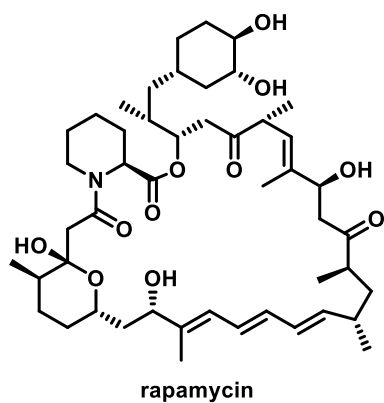


Figure 47: Structures of the autophagy activators rapamycin, resveratrol, metfonin, GSK621, PT1 and the autophagy inhibitors wortmannin, autophinib, SAR405, VPS34-IN1, PIK-III, chloroquine and hydroxychloroquine.

3.1.6. Biological activity of cinchona alkaloids

Medical properties of the cinchona bark were first discovered by South American Indians and found application for the treatment of fever. From 1640 on the bark was imported to Europe as a therapeutic agent against malaria, a disease caused by the protozoan parasite *Plasmodium*. The two cinchona alkaloids that were first isolated pure by Pelletier and Caventou in 1820 are quinine and cinchonine. The two remaining of the four major cinchona alkaloids, quinidine and cinchonidine, were isolated shortly after (Figure 48).^[143]

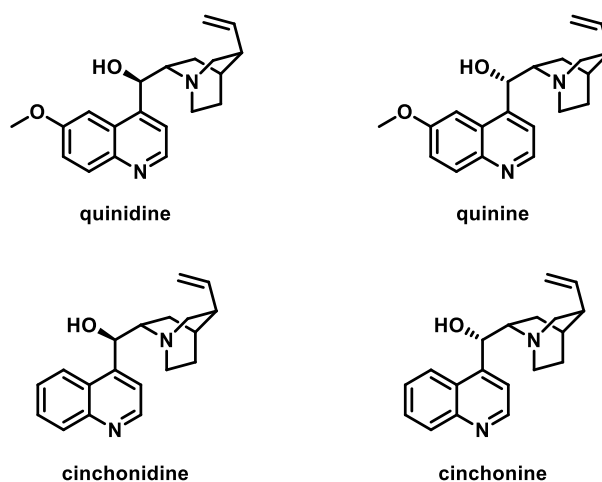


Figure 48: Structure of the four major alkaloids in cinchona bark, quinidine, quinine, cinchonidine and cinchonine.

Plasmodium causes malaria by digests of host hemoglobin in its food vacuole and thus triggers the release of iron(III) protoporphyrin IX (Fe(III)PPIX). Fe(III)PPIX is further crystalized to the non-soluble hemozoin, since the soluble, redox active form is toxic for the parasite. Quinoline-based drugs, including quinine, quinidine and chloroquine, were successfully applied in malaria therapy for centuries and potentially interfere with hemozoin formation by complexation of free Fe(III)PPIX.^{[144],[145]} Co-crystallization of quinine and quinidine with Fe(III)PPIX, demonstrated that π - π stacking of the aromatic quinolone system and protoporphyrin define the interaction. Coordination of the alkaloid moiety to the Fe(III) center and hydrogen bond formation between the nitrogen atom of the quinuclidine moiety and the Fe(III)PPIX carbonate group further increase complex stability (Figure 49). The higher anti-malarial activity of quinidine in comparison to quinine might be due to their difference in

stereochemical configuration. Recent studies suggest that the quinidine is already structurally preorganized and thus favored for complex formation with Fe(III)PPIX.^{[146],[147]}

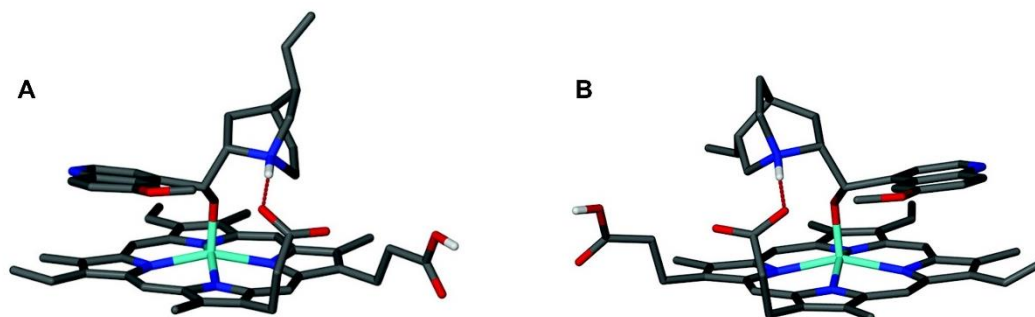


Figure 49: Co-crystal structure of Fe(III)PPIX with quinine (A) and quinidine (B).^[146]

Additional to the therapeutic effect in malaria, chloroquine also inhibits autophagosome-lysosome fusion. This results in accumulation of autophagosomes and prevents degradation of autophagosomal content.^[142] Chloroquine is a weak base and not charged at physiological pH. However, upon diffusion into the lysosome chloroquine gets protonated due to the acidic pH and is consequently unable to pass the lysosomal membrane again. This effect is referred to as lysosomotropism.^[148] Inside the lysosome chloroquine causes an increase of pH, which significantly reduces lysosomal acid hydrolase activity.^[149] However, the exact mechanism of autophagy inhibition by chloroquine still remains to be elucidated.

3.1.7. Phenotypic screening in autophagy

The discovery of novel autophagy inhibitors and identification of previously unknown components of the autophagic machinery is of utmost importance, since autophagy is involved in various severe disorders. To develop effective therapeutics, elucidating the biological machinery that underlies this catabolic process is essential. As described in paragraph 1.2 phenotypic screening is an elegant method for unbiased identification of bioactive compounds and the discovery of novel therapeutically relevant targets.

The most commonly applied phenotypic assay for detection of small molecules, which alter the autophagic process is based on the LC3 protein. As previously described, upon initiation of autophagy, cytosolic LC3-I is conjugated to PE to form LC3-II. LC3-II is localized on the outer, as well as the inner membrane of the phagophore and the autophagosome. By expression

of a GFP-LC3 fusion protein, this effect can be detected with fluorescence microscopy. While LC3-I causes a diffuse signal throughout the cytosol, LC3-II is visible as green fluorescent puncta, which represent autophagosomes. Bioactive compounds that inhibit autophagy should reverse this phenotype and thus, reduce the number of GFP-LC3 puncta per cell. On the other hand, inducers of autophagy would cause an increase of GFP-LC3 puncta (Figure 50).^{[150],[151]}

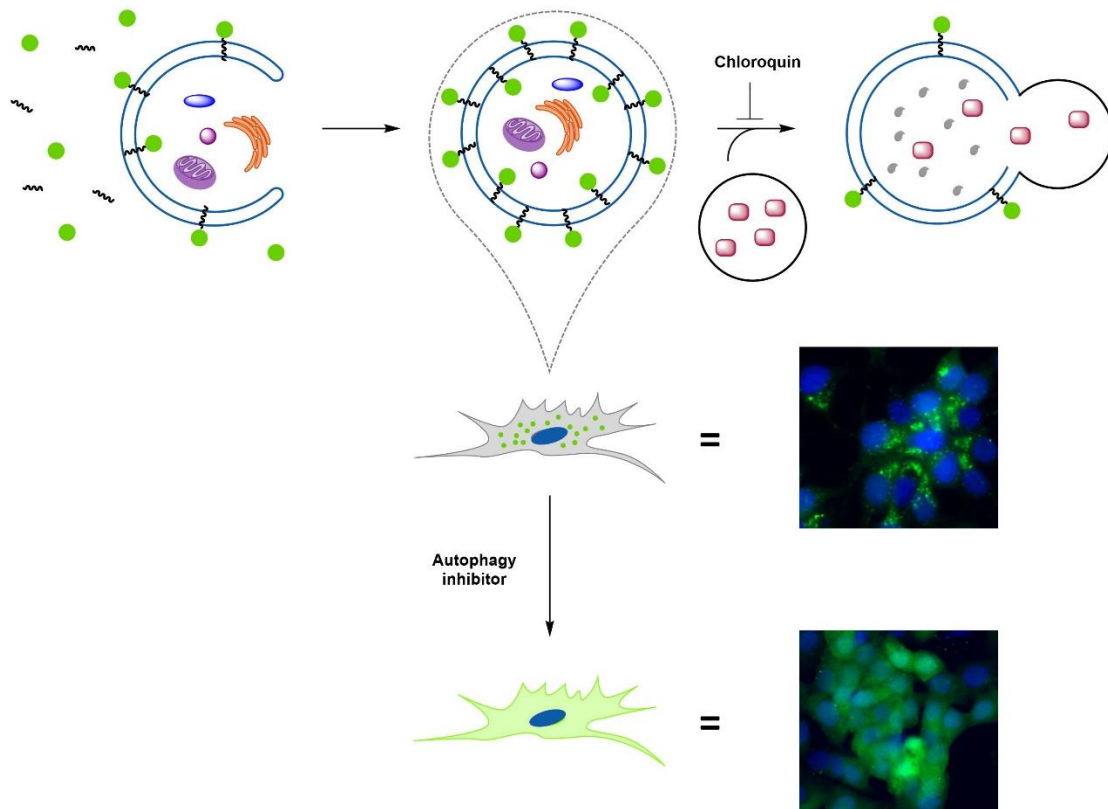


Figure 50: Schematic representation of the phenotypic autophagy assay. Amino acid starvation or the mTOR inhibitor rapamycin are applied to induce autophagy. This results in conjugation of LC3-I with PE to form LC3-II, which is relocated to the phagophore membrane. GFP-LC3-I is equally spread throughout the cytoplasm. GFP-LC3-II can be detected as fluorescent green puncta that represent the autophagosomes. To increase the overall number of puncta, chloroquine is added to prevent autophagosome lysosome fusion and the resulting LC3-II degradation. Autophagy inhibitors are characterized by the reversal of puncta formation to a diffuse fluorescence signal.

Various transgenic GFP-LC3 model organisms have been created, including mice, *Drosophila* and zebrafish.^{[152],[153],[154]} Transgenic models with tissue-specific expression of GFP-LC3 or mCherry-LC3 were applied to demonstrate the alterations in autophagosome numbers under

stress and disease relevant conditions.^{[155],[156]} Furthermore, GFP-LC3 based phenotypic high throughput screening for novel autophagy modulators, facilitates analysis of extensive small molecule libraries. After hit determination by phenotypic screening, target identification and validation are required. Therefore, compound-based deviations in protein levels of the autophagy markers LC3 and p62 are commonly analyzed by immunoblotting.^[157] Furthermore, selective toxicity under nutrition deprivation can indicate autophagy modulators.^[158] Also general target identification and validation strategies, including those mentioned in chapter 1.3. are often applied for the deconvolution of molecular targets of autophagy regulators. These techniques resulted in the discovery of selective small molecule modulators for various autophagy related targets, such as ULK1, VPS34 and mitochondrial complex I.^{[159],[141],[160]}

Thus, phenotypic screening is an unbiased approach for the identification of autophagy modulators with novel chemotypes and previously unknown components of this catabolic signaling pathway.

3.2. Motivation and goals

Autophagy is an essential biological process for the regulation of cellular homeostasis and energy supply. Furthermore, this catabolic mechanism is crucial for protection against various severe disorders, such as infections, autoimmune and neurodegenerative diseases, as well as cancer. On the contrary, mis-regulation of this mechanism can promote a variety of pathological conditions.^[161] Thus, it is of utmost importance to strive for profound knowledge of the autophagy machinery and unravel its function in disease.

The aim of this project is the identification and characterization of structurally novel autophagy inhibitors, followed by subsequent target identification. Potential modulators of the autophagic machinery were identified in a forward chemical genetic screen. Several hits with different chemotypes were chosen for further evaluation (Figure 51). Initially, the inhibitory effect on autophagic flux should be confirmed, followed by target identification and validation. Target identification was approached by several methods, including thermal proteome profiling and affinity enrichment. Subsequently, biochemical and cell-based assays were performed for validation of the established target hypothesis. Autophagy is frequently mis-regulated in numerous fatal diseases, for which no efficient treatment method was developed to date. Therefore, the discovery of previously unknown elements of the autophagic machinery is of utmost importance to expand our knowledge of this catabolic process. Furthermore, novel bioactive compounds are invaluable tools to analyze autophagy and create innovative therapeutic approaches.

3.3. Results and discussion

3.3.1. Identification of novel autophagy inhibitors by phenotypic screening

In order to identify novel autophagy inhibitors, a medium throughput phenotypic screen was performed. This screen was established at the compound management and screening center (COMAS) together with the group of Prof. Waldmann at the Max-Planck Institute of Molecular Physiology. MCF7 cells were stably transfected with a plasmid coding for an eGFP-LC3 conjugate (MCF7/LC3 cells). Upon induction of autophagy eGFP-LC3 is visible as small puncta representing the autophagosomes. An inhibitor of autophagy should at least partially reverse the phenotype to the normal state and thus decrease the number of autophagosomes per cell. As part of the autophagic flux, eGFP-LC3 is degraded in the autolysosome, which would reduce the fluorescence signal. For this purpose, chloroquine is added to the cells, an autophagosome lysosome fusion inhibitor, which prevents eGFP-LC3 degradation.^{[141],[162],[160]}

Two different conditions were chosen to induce autophagy. One method is replacement of the medium with Earle's balanced salt solution (EBSS). EBSS contains no amino acids and no serum, thus causing cell starvation, which in turn initiates autophagy.^{[157],[163]} In a second approach, cells were treated with the mTOR inhibitor rapamycin.^[164] If a compound downregulates autophagy under both conditions it is likely to act downstream of mTOR. If the inhibitor has only an effect under amino acid starvation, it is predicted to act upstream of mTOR. First, the compounds were screened at a single concentration of 10 μM . Those molecules that inhibited autophagy by $\geq 70\%$ were retested. Subsequently, confirmed hits were analyzed in dose-response to determine their IC_{50} values. A compound was considered as active if at least under one of the tested conditions the determined IC_{50} value was below 10 μM . Those inhibitors with an IC_{50} value $\leq 2\text{-}3 \mu\text{M}$ were considered for further studies.

From this screen two promising compound classes emerged, the oxazolidinones and the thienopyrimidines (Figure 51). Both scaffolds were not previously analyzed regarding their activity in autophagy. The two inhibitors with the best IC_{50} values were chosen for further evaluation. The first one is an oxazolidinone **51** (COMAS ID: 351475), which features a starvation-induced IC_{50} of $2.7 \pm 1.9 \mu\text{M}$ and was inactive under induction with rapamycin. The second compound is based on the thieno[3,2-d]pyrimidine scaffold (COMAS ID: 156381). This thienopyrimidine **53** has a starvation-induced IC_{50} of $0.63 \pm 0.15 \mu\text{M}$ and a rapamycin-

induced IC_{50} of $0.18 \pm 0.07 \mu\text{M}$. Furthermore, initial target identification for the autophagy inhibitor Autoquin **52** was performed (Figure 51). Autoquin **52** is structurally similar to the published autophagy inhibitor Oxautin-1^[162] and has a starvation-induced IC_{50} of $0.90 \pm 0.09 \mu\text{M}$. The inhibitor is inactive in rapamycin-induced autophagy and thus should be active upstream of mTOR.

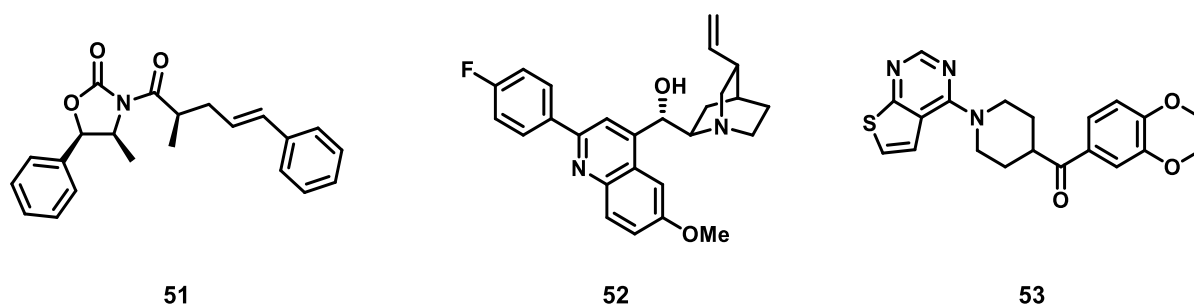


Figure 51: Structures of autophagy inhibitors **51** to **53** selected for further validation. (from left to right: 351475, Autoquin and 156381)

3.3.2. Oxazolidinones as autophagy inhibitors

The autophagy inhibitor 351475, from here on referred to as Autoxain **51**, was identified in the before mentioned phenotypic medium throughput screen and has a starvation-induced IC_{50} of $2.7 \pm 1.9 \mu\text{M}$ (Figure 52). Autoxain **51** is inactive in rapamycin-induced autophagy, which suggests that it acts upstream of mTOR. In the further course of the project, the inhibitory effect of Autoxain **51** on autophagy was validated. Therefore, the starvation dependent toxicity of Autoxain **51** was investigated as well as its influence on certain key autophagy markers.

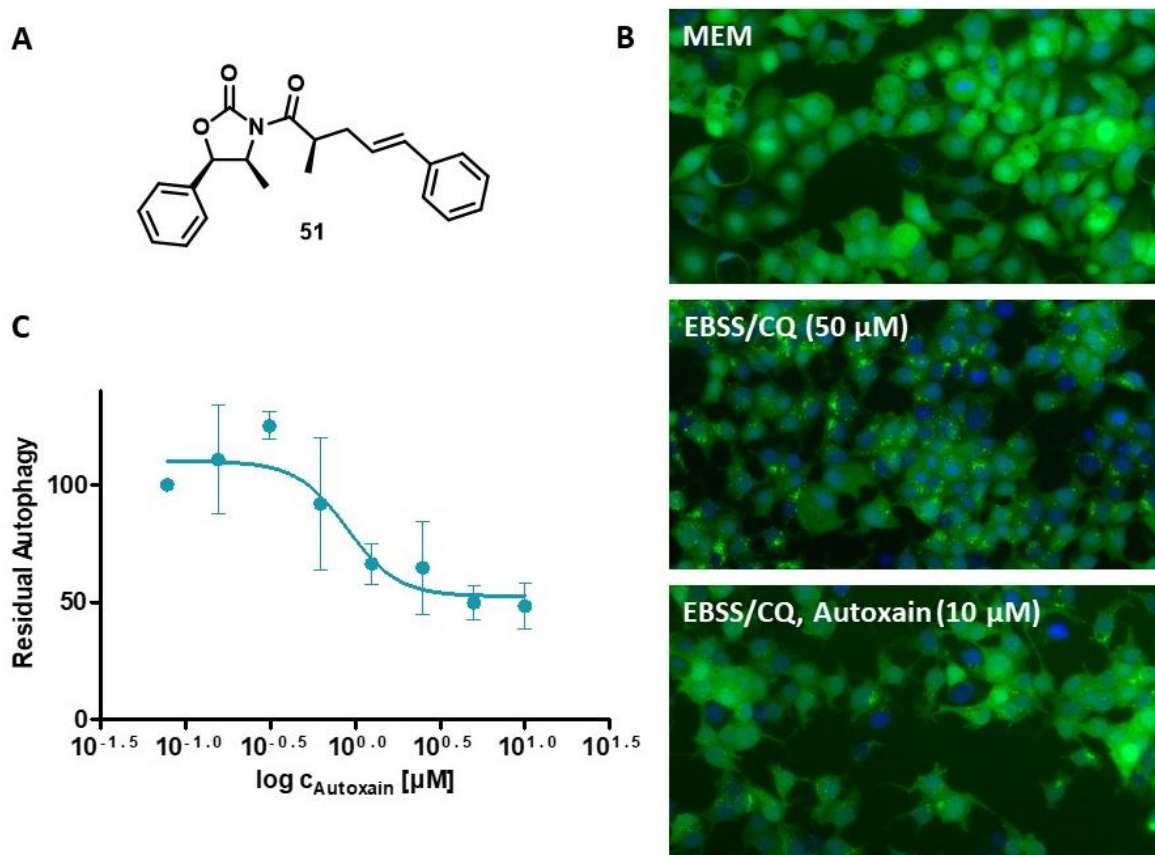


Figure 52: Autoxain **51** inhibits starvation induced autophagy. **A:** Structure of Autoxain. **B:** Phenotypic assay for the identification of autophagy inhibitors using MCF7 cells stably transfected with eGFP-LC3. Non-starved cells were treated with MEM, starved cells with EBSS and 50 μM CQ. Simultaneously decreasing concentrations of Autoxain **51** were added. After 3 h incubation, the cells were fixed with paraformaldehyde and the nuclear DNA was stained with Hoechst. **C:** Dose dependent effect of Autoxain **51** on the number of autophagosomes per cell. Representative graph shown ($n \geq 3$). MEM: Minimal Essential Medium; CQ: Chloroquine; EBSS: Earle's balanced salt solution.

3.3.2.1. Validation of Autoxain as an inhibitor of autophagy

Two important markers for monitoring autophagy are the proteins LC3 and p62. LC3 is located within the cytoplasm (LC3-I) and is lipidated upon initiation of autophagy, forming a phosphatidylethanolamine adduct (LC3-II).^[165] An inhibitor of autophagy should dose-dependently prevent the generation of LC3-II. However, the effect of Autoxain **51** is exactly opposite (Figure 53). Under starvation with 10 μM Autoxain **51** the amount of LC3-II is comparable with starved cells and higher than with 0.1 μM . The second autophagy marker p62 acts as a carrier of cellular components targeted for autophagic degradation. The p62 protein translocates to the autolysosome, where it is degraded together with its cargo. Initiation of autophagy thus results in reduced amounts of p62.^{[166],[157]} Treatment with an autophagy inhibitor should reverse this condition. Autoxain **51** has no conclusive effect on p62. The level of p62 in fed cells is significantly lower than in starved cells, which should be reversed, since p62 is degraded upon autophagy initiation. In Autoxain **51** treated fed cells the level of p62 is similar to that in starved cells with and without compound treatment. No dose-dependent significant change in p62 level can be observed. Consequently, neither the effect of Autoxain **51** on p62 nor on LC3-II is conclusive or meets the expectations.

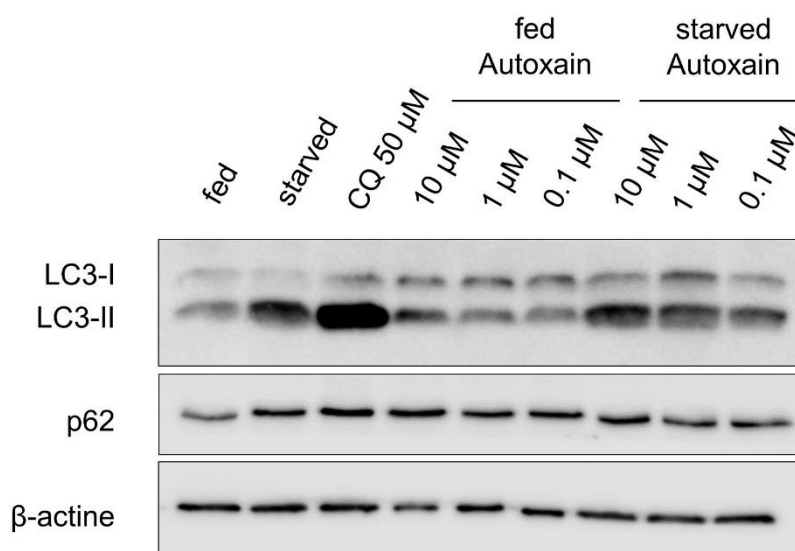


Figure 53: Dose dependent effect of Autoxain **51** on LC3-II formation and p62 degradation. Autophagy is induced by amino acid starvation. Cells are treated with decreasing amounts of Autoxain **51** or CQ as a control and lysed after 3 h. Representative blot shown (n = 3).

Subsequently, the toxicity of Autoxain **51** was investigated (Figure 54). Starved cells lack an energy source, if autophagy is suppressed. Hence, an autophagy inhibitor, which is non-toxic under normal conditions can cause selective toxicity under nutrition-deprivation. Therefore, MCF7 cells were cultivated with and without glucose and treated with decreasing amounts of Autoxain **51** for 72 h hours. Additionally, propidium iodide was used to monitor cell viability. Propidium iodide is an intercalating fluorophore not able to cross the cell membrane. Thus, this compound can only stain nucleic acids of dying cells. Cell growth and viability was observed with the microscopy-based IncuCyte® Live-Cell Analysis System.

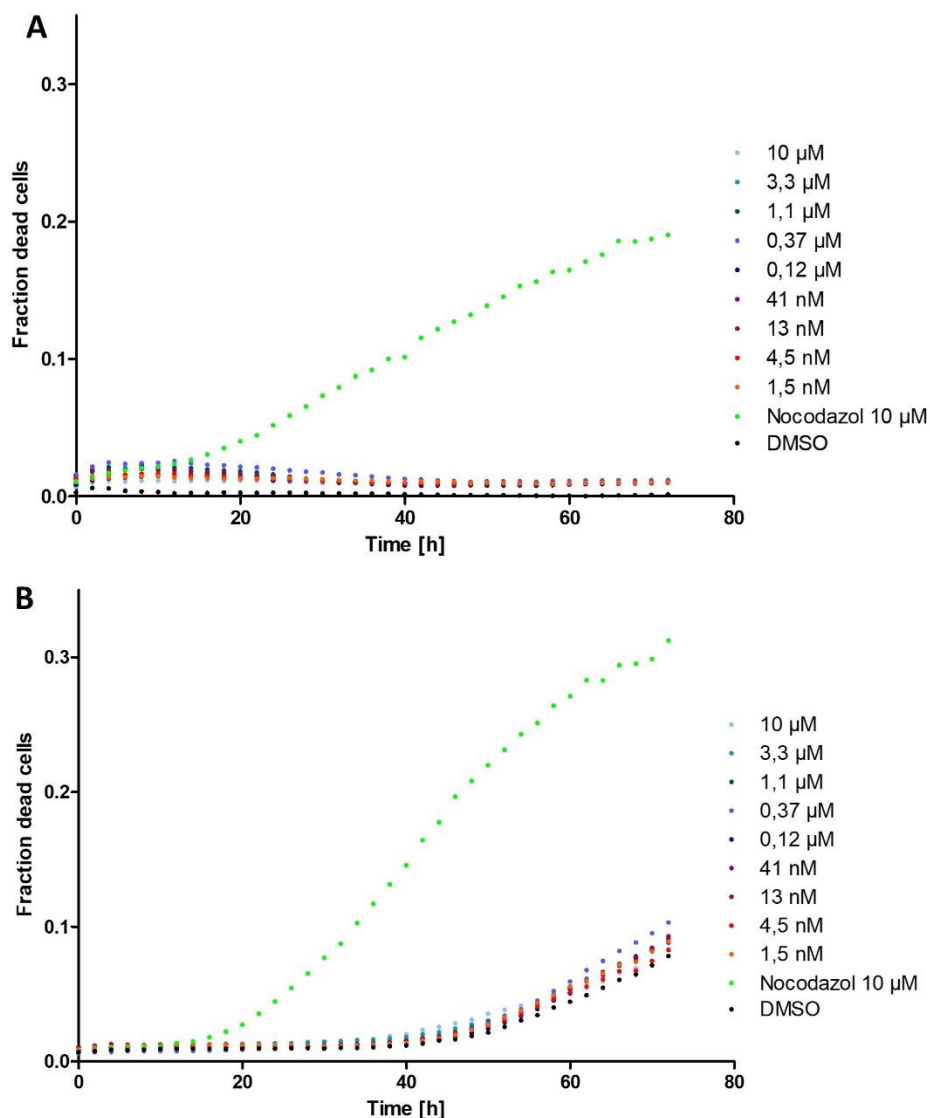


Figure 54: Viability of MCF7 cells with different concentrations of Autoxain **51**. MCF7 cells were cultivated with and without glucose and treated with Autoxain **51** over 72 h. Dying cells were stained with propidium iodide. DMSO and nocodazole were used as controls. Representative graph shown (n=3, N=3)

At concentrations of 10 μM or lower Autoxain **51** does not have an influence on cell viability, neither with nor without glucose. In non-starved cells viability did not change over 72 h, except for the nocodazole treated samples. Nocodazole was employed as a positive control and causes apoptosis by disruption of microtubule polymerization. Under nutrition deprivation Autoxain **51** treated cells behave very similar to those treated with DMSO. Cell death starts to occur after 48 h. However, the fraction of non-viable cells is below 10 % up to 72 h. This is due to nutrition deprivation, which cannot be fully compensated by autophagy. In summary, Autoxain **51** does not have an autophagy-dependent effect on cell viability.

3.3.2.2. Thermal proteome profiling

Subsequently, a TPP experiment was performed. TPP has the advantage that, in comparison to other methods for target identification, modification of the compound is not required. The readout is based on changes in protein melting temperature upon compound treatment. The interaction of a ligand with its target protein can stabilize or destabilize the respective protein. Therefore, cell lysates with and without compound are subjected to a temperature gradient. Subsequently, denaturated proteins are precipitated and the soluble fraction is analyzed by MS/MS. The amount of protein for each sample is quantified and plotted against the temperature, resulting in melting curves for each identified protein. Changes in the melting temperature of a protein by comparing compound treated and untreated samples can give indications for possible interaction partners (Chapter 1.3.2.).

Since the target of Autoxain **51** is unknown and could also be a membrane protein, MCF7/LC3 cell lysate was generated with PBS containing 0.4% NP40. NP40 is a non-ionic detergent, which improves solubilization of membrane proteins.^[22] MCF7/LC3 lysate containing 30 μM of Autoxain **51** or equivalent amounts of DMSO was subjected to heat treatment. The temperature range was 37 °C to 67 °C. Possible hits were identified according to the following criteria: 1) A protein is consistently stabilized or destabilized in all three replicates. 2) The dT_m has to be >1.5 °C in all three replicates. In total 66 proteins were identified as hits. What was striking about the results was that out of these hits 23 were ribosomal proteins (Table 5).

Table 5: List of ribosomal proteins identified as hits in a TPP experiment performed with Autoxain **51**, including gene name, protein name and dT_m [°C]. Data is shown as mean \pm SD (n = 3).

Entry	Gene name	Protein name	dT_m [°C]
1	RPL3	60S ribosomal protein L3	-4.2 \pm 1.9
2	RPL4	60S ribosomal protein L4	-4.3 \pm 0.9
3	RPLS9	40S ribosomal protein S9	-3.6 \pm 0.8
4	RPL10	60S ribosomal protein L10	-2.7 \pm 0.8
5	RPS13	40S ribosomal protein S13	-3.6 \pm 1.8
6	RPL17	60S ribosomal protein L17	-3.2 \pm 0.7
7	RPS18	40S ribosomal protein S18	-3.4 \pm 1.5
8	RPL18A	60S ribosomal protein L18a	-4.4 \pm 2.6
9	RPL19	60S ribosomal protein L19	-3.8 \pm 2.1
10	RPL21	60S ribosomal protein L21	-4.3 \pm 2.2
11	RPL35	60S ribosomal protein L35	-3.1 \pm 0.9
12	RPL35A	60S ribosomal protein L35a	-3.8 \pm 2.8
13	RPL36	60S ribosomal protein L36	-4.3 \pm 0.2
14	RPS3A	40S ribosomal protein S3a	-3.4 \pm 1.9
15	RPS6	40S ribosomal protein S6	-3.5 \pm 1.9
16	RPS14	40S ribosomal protein S14	-3.6 \pm 1.9
17	RPS24	40S ribosomal protein S24	-4.6 \pm 1.1
18	MRPS10	28S ribosomal protein S10, mitochondrial	-3.0 \pm 0.3
19	MRPS34	28S ribosomal protein S34, mitochondrial	-2.5 \pm 0.8
20	MRPS35	28S ribosomal protein S35, mitochondrial	-4.4 \pm 2.0
21	MRPS22	28S ribosomal protein S22, mitochondrial	-2.3 \pm 0.3
22	MRPL41	39S ribosomal protein L41, mitochondrial	-2.9 \pm 1.1
23	MRPL48	39S ribosomal protein L48, mitochondrial	-3.1 \pm 0.9

Literature research revealed that oxazolidinones are a novel chemical class of antibiotics that inhibit bacterial protein biosynthesis. Two oxazolidinone-based antibiotics currently on the market are linezolid **54** and tedizolid **55** (Figure 55). Linezolid **54** binds to the peptidyl-transferase center of the prokaryotic ribosome, where it blocks the A site pocket and thus interferes with protein synthesis.^[167] Oxazolidinone based antibiotics are selective for the

prokaryotic ribosome and do not interfere with eukaryotic protein biosynthesis. Nevertheless, linezolid **54** causes serious side effects during long-term treatment. It was proposed that these side effects occur due to inhibition of the mitochondrial ribosome.^{[168],[169]} In the TPP Autoxain **51** destabilized various cytosolic and mitochondrial ribosomal protein subunits. This suggests that in analogy to the oxazolidinone antibiotics, Autoxain **51** might target the ribosome. In contrast to linezolid, Autoxain **51** might not differentiate between cytosolic and mitochondrial ribosome. However, TPP only indicates possible ligand-protein interactions, which not necessarily influence enzymatic activity. Thus, Autoxain **51** could also bind to the ribosome, without having any effect on protein synthesis.

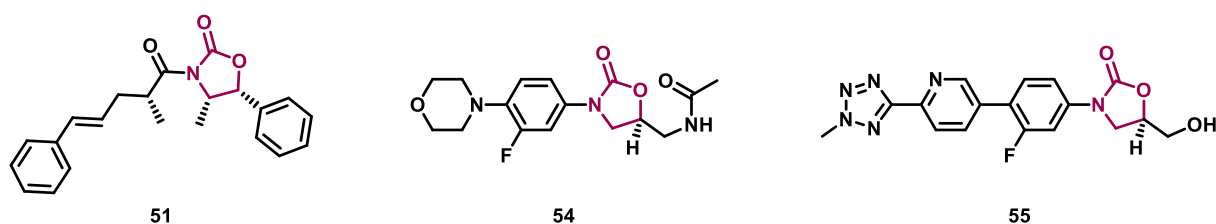


Figure 55: Structure of Autoxain **51** and the antibiotics linezolid **54** and tedizolid **55** with the oxazolidinone scaffold marked in red.

3.3.2.3. Cell painting assay

This assay was performed at COMAS

To develop a target hypothesis for Autoxain **51** a CPA was performed. The CPA is an unbiased image-based, high-content screening approach. By means of fluorescence microscopy an extensive number of cellular features can be detected and analyzed. These parameters provide a specific finger print for each compound. The fingerprint is subsequently compared to those of a reference compound library to determine possible similarities in bioactivity and mode of action.^[24] (Chapter 1.3.2) In the cell painting assay, Autoxain **51** has a maximal induction of 1%. The induction describes the fraction of parameters, which are altered by a compound. In total 579 different parameters are analyzed. In order to calculate a reliable fingerprint, which can be compared to the different finger prints of reference compounds, the induction should be $\leq 5\%$. The induction of Autoxain **51** was only 1%. Thus, no similarity to reference compounds was determined. Also the oxazolidinone-based antibiotic linezolid is part of the reference compound set. Like Autoxain **51**, linezolid **54** has an induction $\leq 5\%$. Conclusively, the

biological activity of these compounds does not cause strong alterations of the cell morphology. Thus, CPA is not suitable for mode of action studies of Autoxain **51**.

3.3.2.4. Conclusion

The oxazolidinone based compound Autoxain **51** was identified as a potential autophagy inhibitor in an in-house medium-throughput screen. However, the effect of Autoxain **51** on autophagy markers LC3 and p62 was inconclusive. Furthermore, no selective toxicity under nutrient-deprivation was observed. However, this might be due to the low potency of Autoxain **51**. A subsequent approach in target identification by means of CPA was unsuccessful, since Autoxain **51** featured an induction of only 1%. Thus, the compound is inactive and no biosimilarity to reference compounds was determined. The performed TPP experiment suggested an interaction of Autoxain **51** with the cytoplasmic and mitochondrial ribosome. Literature research revealed that oxazolidinones possess antibacterial activity. Tedizolid **55** and linezolid **54** are commercially available oxazolidinone-based antibiotics that impair prokaryotic protein biosynthesis by targeting the ribosome. Furthermore, linezolid **54** was shown to inhibit the mitochondrial ribosomes, which could be the cause for long-term side effects. Presumably, Autoxain **51** features a similar mode of action, but might not necessarily differentiate between different ribosomes. However, TPP only indicates a possible interaction. Thus, Autoxain **51** might interact with the ribosome, but does not necessarily have an influence on protein biosynthesis. Nevertheless, since Autoxain **51** could not be validated as an autophagy inhibitor and might target the ribosome, the project was not pursued further.

3.3.3. Autoquin as an inhibitor of autophagy

Synthesis of Oxautin and Autoquin compound collections was performed by Dr. Luca Laraia, Dr. Guillaume Garivet and Dr. Daniel Foley.

Screening of the compound library for structurally novel autophagy inhibitors revealed an oxazatwistane as a potential candidate. Subsequent optimization of the hit compound provided Oxautin-1 **56** as the most potent autophagy inhibitor.^[162] During the SAR studies for this compound the non-cyclized derivative, termed Autoquin **52**, was prepared. Autoquin is a cinchona alkaloid-based inhibitor with the quinidine scaffold and has a starvation-induced IC₅₀ of 0.90 ± 0.09 μM (Figure 56). The compound is inactive in rapamycin-induced autophagy. Thus, it probably acts upstream of mTOR. To improve potency, a compound collection was synthesized, which consists of 60 different derivatives. However, Autoquin **52** remained the most potent inhibitor. Therefore, the compound was chosen for target identification and mode of action studies.

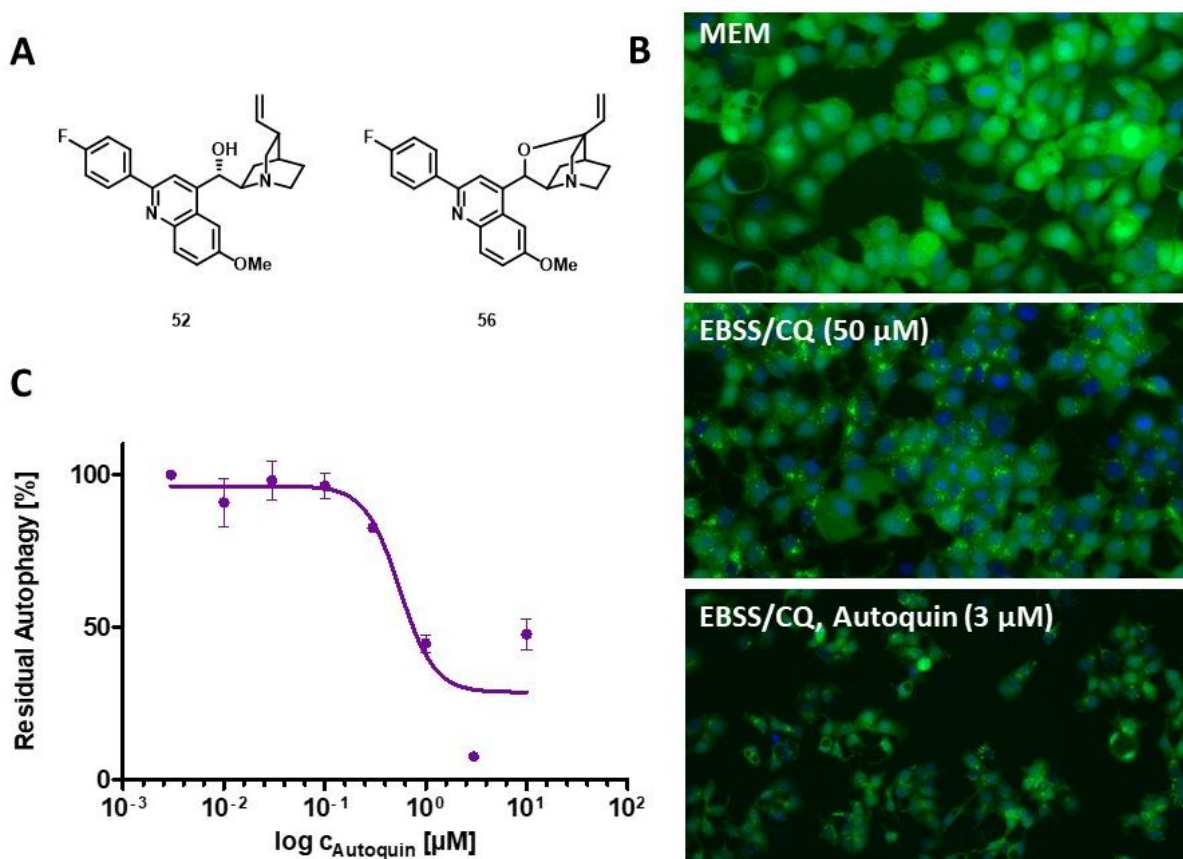


Figure 56: Autoquin **52** inhibits starvation induced autophagy. **A:** Structure of oxazatwistane based autophagy inhibitor Oxautin-1 **56** and its non-cyclized derivative Autoquin **52**. **B:** Phenotypic assay for the identification of autophagy inhibitors using MCF7 cells stably transfected with eGFP-LC3. Non-starved cells were treated with MEM, starved cells with EBSS and 50 μM CQ. Simultaneously decreasing concentrations of Autoquin **52** were added. After 3 h incubation, the cells were fixed with paraformaldehyde and the nuclear DNA was stained with Hoechst. **C:** Dose dependent effect of Autoquin **52** on the number of autophagosomes per cell. Representative graph shown (n ≥ 3); MEM: Minimal Essential Medium; CQ: Chloroquine. EBSS: Earle's balanced salt solution.

3.3.3.1. Validation of Autoquin as an autophagy inhibitor

The influence of Autoquin **52** on autophagy markers LC3 and p62 was investigated first (Figure 57). Upon initiation of autophagy LC3-II is generated and translocated to the autophagosomal membrane. Thus, downregulation of autophagy should decrease LC3-II levels. However, Autoquin **52** has exactly the opposite effect and leads to LC3-II accumulation. This effect can also be observed with chloroquine, an autophagosome lysosome fusion inhibitor.^[142] LC3-II is located on autophagosomes and is degraded upon autolysosome formation. Inhibition of autophagic flux interferes with LC3-II degradation, which causes an

increase of LC3-II in the cell. The second autophagy marker p62 transports cargo proteins, intended for autophagic degradation, to the lysosome. The p62 protein is degraded together with its cargo upon initiation of autophagy. Under starvation conditions Autoquin **52** dose-dependently prevents p62 degradation. However, under nutrition rich conditions the compound seems to induce p62 degradation at high concentrations. Thus, the effect on the autophagy marker p62 is not fully conclusive. Nevertheless, Autoquin **52** might have a similar mode of action as chloroquine and Oxautin-1 **56** and interferes with autophagosome maturation.

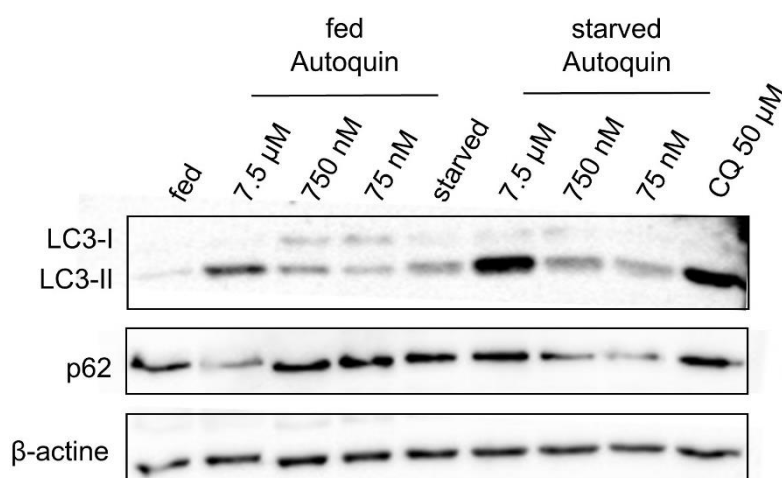


Figure 57: Effect of Autoquin **52** on LC3-II formation and p62 degradation. Autophagy is induced by amino acid starvation. Cells are treated with decreasing amounts of Autoquin **52** or CQ as a control and lysed after 3 h.

Subsequently, the toxicity of Autoquin **52** towards fed and starved cells was investigated (Figure 58). Therefore, MCF7 cells were cultivated with and without glucose and treated with decreasing amounts of Autoquin **52** over 72 h hours. Propidium iodide was added to monitor cell viability.

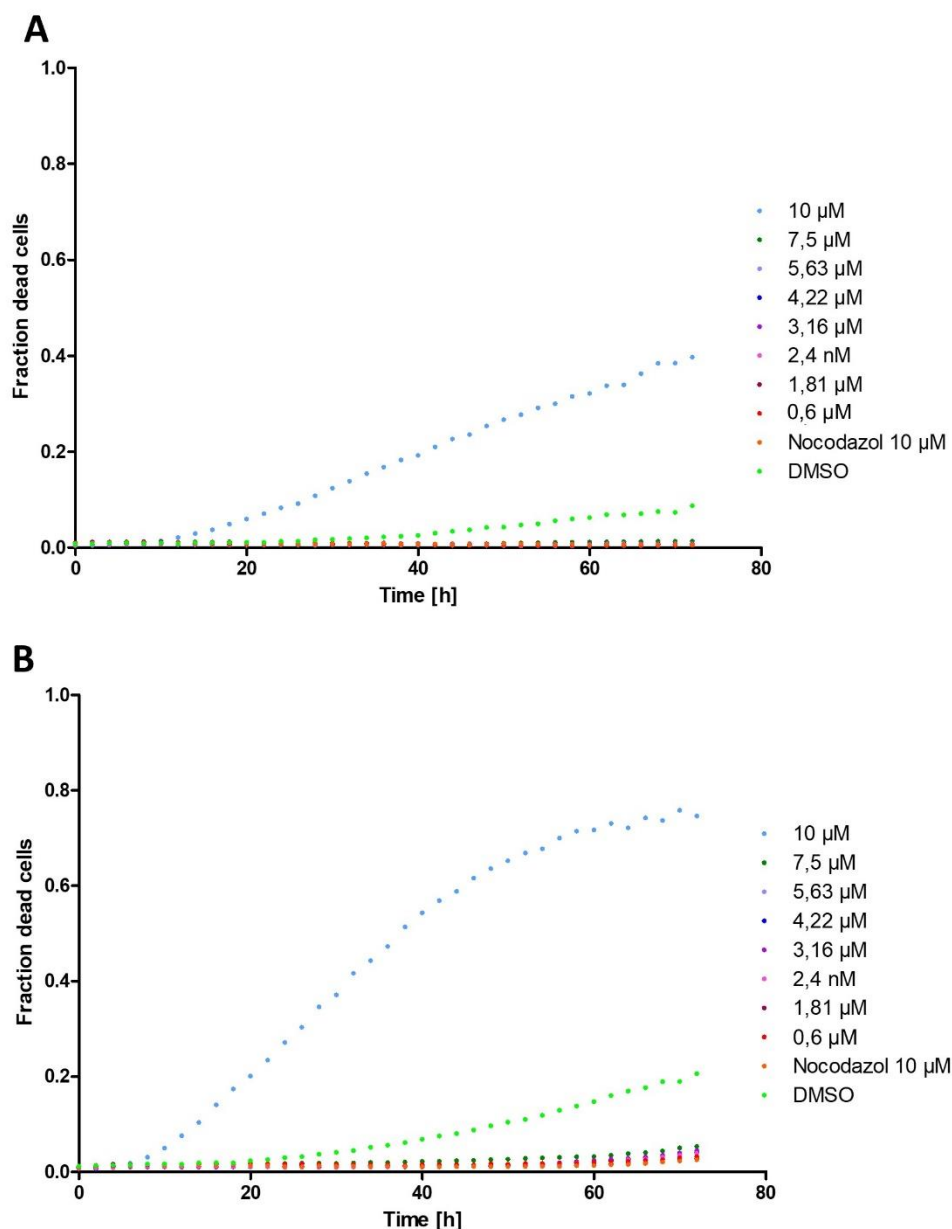


Figure 58: Viability of MCF7 cells with different concentrations of Autoquin **52**. MCF7 cells were cultivated with and without glucose and treated with Autoquin **52** over 72 h. Dying cells were stained with propidium iodide. DMSO and nocodazole were used as controls. Representative graph shown (n=3, N=3).

At concentrations of 7.5 μ M or lower Autoquin **52** does not have an influence on cell viability, neither with nor without glucose. However, at a concentration of 10 μ M Autoquin **52** causes a strong toxic response. Under normal conditions cell death is induced in about 40% of the MCF7 cells and under starved conditions in up to 70%. This also explains, why in the phenotypic autophagy assay the inhibitory effect is strongest at 3 μ M (Figure 56C).

3.3.3.2. Autoquin has lysosomotropic activity

Experiments were performed by the Arenz Lab, Humboldt Universität Berlin

Autoquin **52** has strong structural similarity with chloroquine, which has a lysosomotropic effect (Figure 59).^[170] Lysosomotropic compounds selectively accumulate inside the lysosome. This applies especially for weak bases, which are able to diffuse through cellular membranes. In the acidic environment of the lysosome these compounds become protonated. These charged species are subsequently unable to cross the membrane and are trapped inside the lysosome. This results in lysosomal accumulation.^[148]

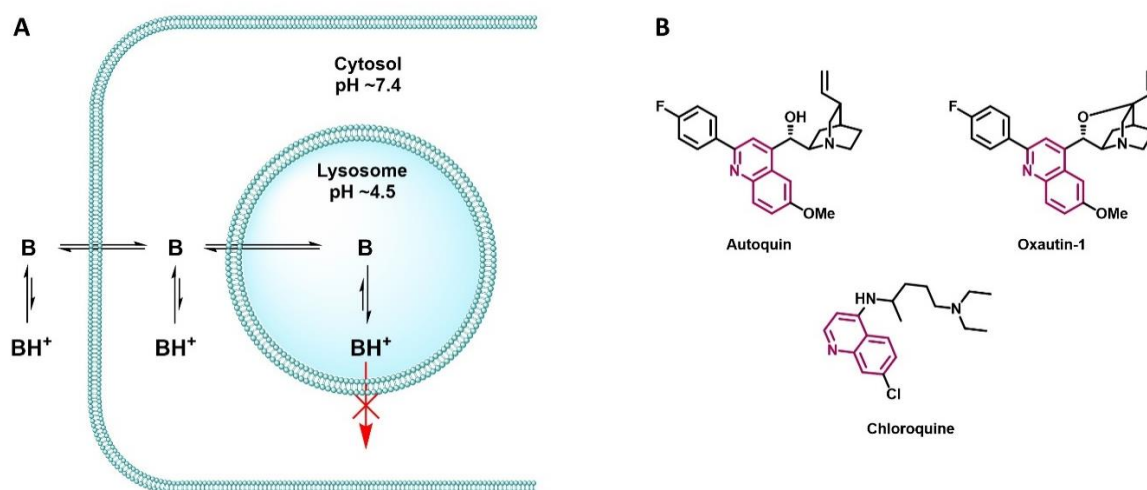


Figure 59: Lysosomotropic compounds **A:** Protonation and accumulation of weak bases in the lysosome. **B:** Structures of Autoquin **52**, Oxautin-1 **56** and chloroquine with the common quinoline scaffold marked in red.

Lysosomes play an essential role in autophagy, since they are required for autolysosome formation and subsequent autophagosomal cargo degradation.^[171] Lysosomotropic compounds typically inhibit autophagy at least in part by targeting sphingolipid hydrolases such as acid sphingomyelinase (aSM) in the lysosomes. However, they do not directly bind these hydrolases, but, when protonated sequester the negatively charged bis-monoacyl glycerol phosphate, which is required for sphingolipid hydrolase activity.^{[172],[173]} Chloroquine inhibits aSM and acid ceramidase (aCD).^[174] In order to elucidate whether Autoquin **52** has a similar mode of action, the inhibitory effect on aCM was investigated (Figure 60).

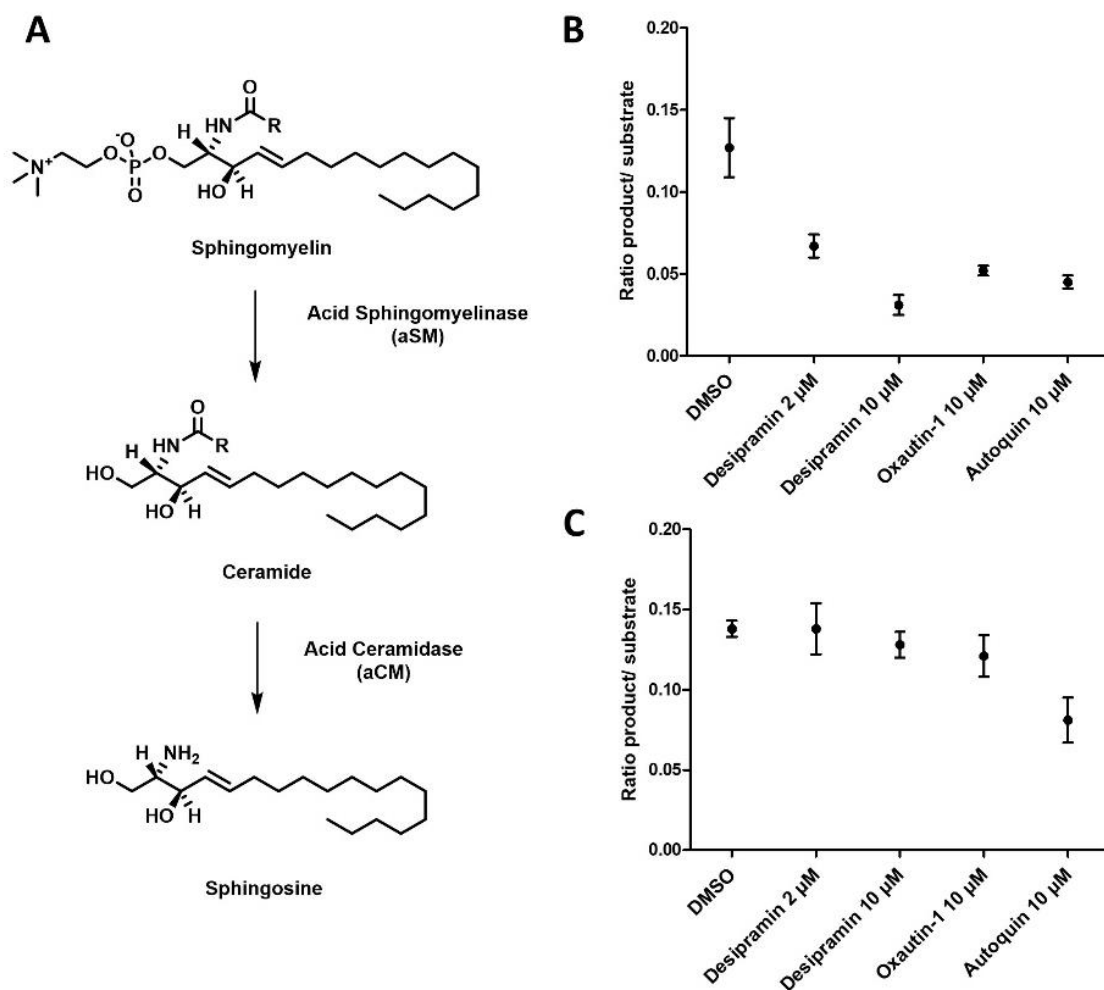


Figure 60: Autoquin **52** and Oxautin-1 **56** indirectly inhibit aCD. **A:** Conversion of sphingomyelin to ceramide and further to sphingosine by aSM and aCD. **B:** Cell based aCD assay. **C:** Cell free aCD assay.

The assay developed by the Arenz group is based on a doubly labelled fluorescent ceramide analogue. This ceramide probe is labeled with 7-nitrobenz-2-oxa-1,3-diazole (NBD) as a donor fluorophore and Nile Red as the acceptor fluorophore. Hydrolysis of the probe by aCDase caused a significant increase in NBD emission intensity, while NR emission decreases. The ceramide probe is suitable for a cell based assay with intact lysosomes, as well as in cell lysates, without a functional lysosome.^[175] The aCD assay revealed that both Autoquin **52** and Oxautin-1 **56** inhibit the aCD in a cell based, but not in a cell free setup (Figure 60B and 60C). Thus, both compounds have an indirect effect on aCD. These results support the hypothesis that Autoquin **52** interferes with lysosome function due to its lysosomotropic activity and could explain the influence of Autoquin **52** on autophagosome lysosome fusion. Sphingolipid metabolism is highly important for the regulation of autophagic flux.^[176]

3.3.3.3. Thermal proteome profiling

To obtain further information about a possible target of Autoquin **52** thermal proteome profiling was performed (Chapter 1.3.2.). MCF7/LC3 cell lysate was incubated with Autoquin **52** and subjected to heat treatment. Subsequently, denaturated proteins were precipitated by centrifugation and the soluble fraction was analyzed by tandem MS/MS. A hit was defined according to one or both of the following criteria: 1) A consistent shift of ≥ 1.5 °C for all replicates and/or 2) An increase of non-denaturated protein by more than 10% in every replicate. In total 26 hits were obtained.

Table 6: List of proteins identified as hits in TPP experiments performed with Autoquin **52**, including gene name, protein name and dT_m [°C]. Data is shown as mean \pm SD. (n = 3).

Entry	Gene name	Protein name	dT_m [°C]
1	SLC35F6	Solute carrier family 35 member F6	4.1 \pm 2.1
2	NDUFA9	NADH dehydrogenase [ubiquinone] 1 alpha subcomplex subunit 9, mitochondrial	4.1 \pm 1.8
3	TMEM128	Transmembrane protein 128	3.7 \pm 1.5
4	SNX7	Sorting nexin-7	3.3 \pm 2.4
5	RPS27L	40S ribosomal protein S27;40S ribosomal protein S27-like	3.2 \pm 1.8
6	MALSU1	Mitochondrial assembly of ribosomal large subunit protein 1	3.1 \pm 1.4
7	SLC25A1	Tricarboxylate transport protein, mitochondrial	2.9 \pm 0.4
8	SLC25A24	Calcium-binding mitochondrial carrier protein SCaMC-1	2.9 \pm 1.2
9	EXOC6B	Exocyst complex component 6B	2.9 \pm 0.9
10	GPR89A GPR89B	Golgi pH regulator A Golgi pH regulator B	2.9 \pm 1.4
11	STT3A	Dolichyl-diphosphooligosaccharide--protein glycosyltransferase subunit STT3A	2.7 \pm 0.7
12	FBL	rRNA 2-O-methyltransferase fibrillarin	2.6 \pm 0.1
13	SURF4	Surfeit locus protein 4	2.5 \pm 0.8
14	SLC25A5	ADP/ATP translocase 2;ADP/ATP translocase 2, N-terminally processed	2.4 \pm 0.3
15	PFKM	ATP-dependent 6-phosphofructokinase, muscle type	2.3 \pm 0.4
16	LARS	Leucine--tRNA ligase, cytoplasmic	2.3 \pm 0.6
17	SLC25A13	Calcium-binding mitochondrial carrier protein Aralar2	2.3 \pm 0.7
18	IDH3G	Isocitrate dehydrogenase [NAD] subunit gamma, mitochondrial;Isocitrate dehydrogenase [NAD] subunit, mitochondrial	2.3 \pm 0.6
19	RPS19	40S ribosomal protein S19	2.2 \pm 0.3
20	RPL11	60S ribosomal protein L11	2.2 \pm 0.6
21	HUS1	Checkpoint protein HUS1	2.2 \pm 0.9
22	POLR3C	DNA-directed RNA polymerase III subunit RPC3	2.2 \pm 0.4
23	NO66	Bifunctional lysine-specific demethylase and histidyl-hydroxylase NO66	2.1 \pm 0.3
24	HNRNPR	Heterogeneous nuclear ribonucleoprotein R	2.1 \pm 0.6
25	TUBA1A TUBA3C	Tubulin alpha-1A chain Tubulin alpha-3C/D chain	2.1 \pm 0.1
26	PFKL	ATP-dependent 6-phosphofructokinase, liver type	2.0 \pm 0.2

Several mitochondrial proteins were identified as potential interaction partners of Autoquin **52**. The NADH dehydrogenase [ubiquinone] 1 alpha subcomplex subunit 9, (NDUFA9) showed one of the strongest shifts in melting temperature. NDUFA9 is an essential component of the mitochondrial complex I, which is part of the electron transport chain. Disruption of NDUFA9 expression results in impairment of mitochondrial respiration.^[177] Furthermore, four different members of the solute carrier family 25 (SLC25) were stabilized by Autoquin **52**. The tricarboxylate transport protein SLC25A1 and the ADP/ATP translocase SLC25A5, as well as the two calcium-binding mitochondrial carrier proteins SLC25A24 and SLC25A13. The SLC25 protein family is also referred to as the mitochondrial carrier (MC) family, since most of its members are located in the inner mitochondrial membrane. MCs transport solutes, such as numerous metabolites and nucleotides, across the mitochondrial membrane. This protein family also has an essential influence on mitochondrial function and oxidative phosphorylation.^[178] Damaged or nonfunctional mitochondria can be selectively degraded by autophagy. This process is referred to as mitophagy. Vice versa autophagy can be regulated by mitochondria due to the generation of reactive oxygen species (ROS) and ATP.^[179] Additionally, inhibition of mitochondrial respiration impairs autophagic flux.^[180] Thus, the effect of Autoquin on mitochondrial respiration was subsequently investigated.

3.3.3.4. Mito Stress Test

The effect of Autoquin **52** on mitochondrial respiration was determined with the Seahorse XF Cell Mito Stress Test. The Seahorse XFp analyzer can detect live cell responses with two different fluorophores. One fluorophore is sensitive to changes in oxygen concentration and the other to fluctuations of the pH. The oxygen consumption rate (OCR), as well as the extracellular acidification rate (ECAR) can be determined time- and dose-dependently. The ECAR represents the anaerobic glycolysis level of the cell, responsible for the excretion of lactate. Lactate accumulation in turn results in decrease of cellular pH. Cells induce anaerobic glycolysis upon oxygen shortage. Thus, the addition of a mitochondrial respiration inhibitor to cells should cause a decrease of the OCR and an increase of the ECAR.

Initially, the basal respiration of the cell was determined (Figure 61). This represents the cells' glycolysis level and respiration rate under normal resting conditions. Subsequently, the compound of interest is added to the cells. If a molecule inhibits mitochondrial respiration, the

oxygen consumption rate should drop. The cells switch to glycolysis and the ECAR increases. The amount of oxygen required for cellular ATP production can be determined by injection of oligomycin, a complex V inhibitor. Subsequent addition of carbonyl cyanide 4-(trifluoromethoxy)phenylhydrazone (FCCP) disrupts the proton gradient. This results in increase of mitochondrial respiration to maximal capacity and reflects the cells respiration under stress. The difference between basal and maximal respiration is the spare capacity of the cells to respond to increased energetic demand. Finally, a mixture of rotenone, a complex I inhibitor, and antimycin A, a complex III inhibitor, is added to determine the lowest possible OCR. Non-mitochondrial processes cause the remaining oxygen consumption.

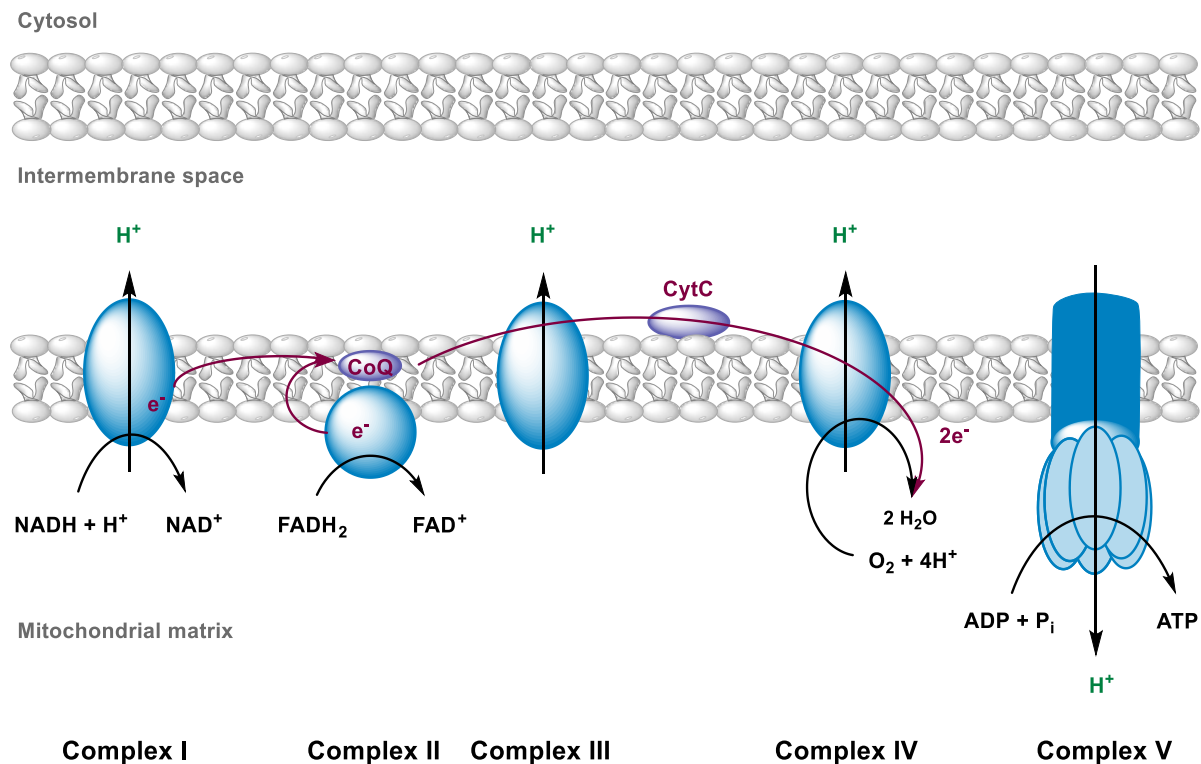


Figure 61: Representative scheme of mitochondrial respiration. Complex I (NADH-CoQ reductase) oxidizes NADH to NAD⁺ and complex II FADH₂ to FAD⁺. Complex I and complex II both transfer electrons to coenzyme Q. From coenzyme Q the electrons are passed on to complex IV via complex III and cytochrome C. Complex IV reduces molecular oxygen to water under consumption of protons. These protons are translocated into the mitochondrial matrix by complex V (ATP synthase). Complex V utilizes the proton gradient between mitochondrial matrix and intermembrane space to generate ATP from ADP and phosphate. CoQ: Coenzyme Q; CytC: Cytochrome C.

MCF7 cells were incubated with 10 μM and 1 μM Autoquin **52** and the OCR and ECAR were monitored (Figure 62). Autoquin **52** caused no significant change in the OCR and only slightly reduced the ECAR. Analysis of oxidative phosphorylation is an established method to investigate mitochondrial function. Dysfunction of mitochondria caused by a bioactive small molecule should ultimately also alter respiration.^[181] However, Autoquin **52** had no strong effect on the electron transport chain. Thus, the interaction of Autoquin **52** with mitochondrial proteins could not be confirmed by the Seahorse Mito Stress Test.

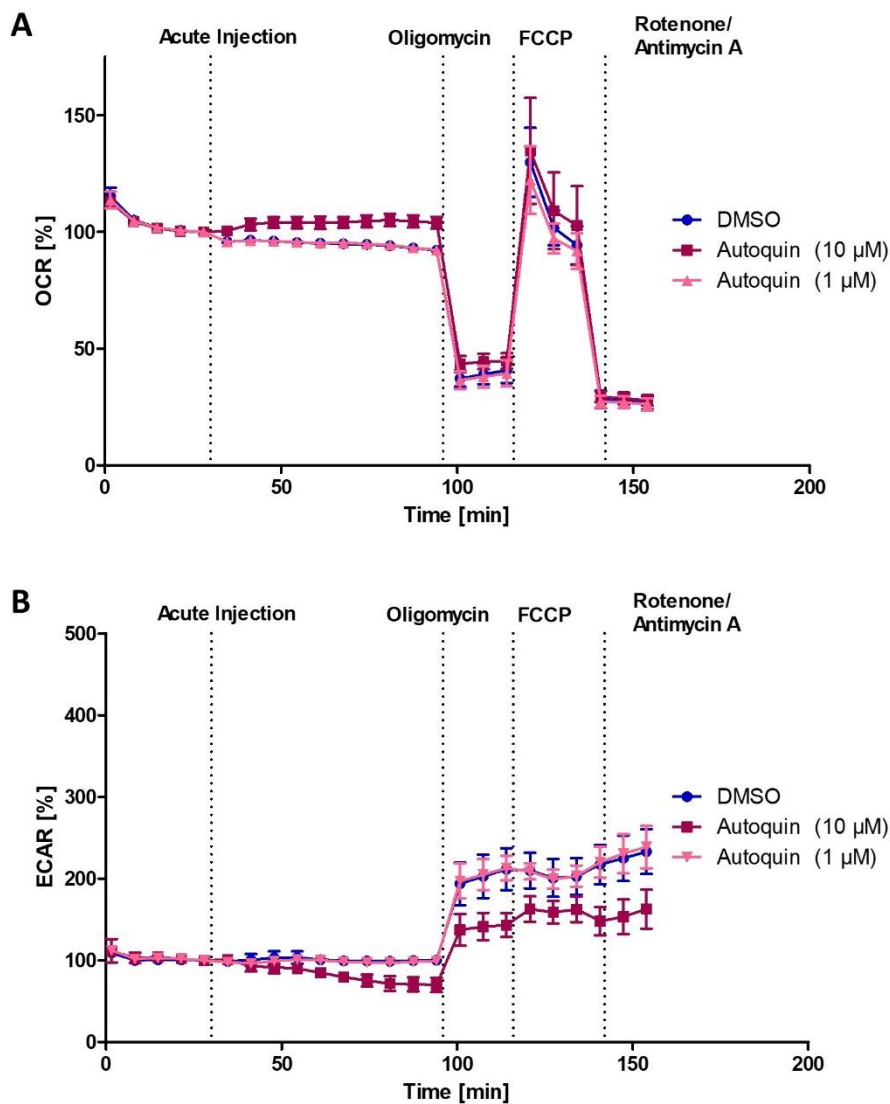


Figure 62: Influence of Autoquin on mitochondrial respiration. MCF7 cells were treated with Autoquin **52** (10 μM and 1 μM) or DMSO (0.1%) upon acute injection. Subsequently oligomycin (1 μM), FCCP (0.25 μM) and a mixture of rotenone/antimycin A (0.5 μM) were added. The OCR and ECAR were monitored over time. Data shown is mean values \pm SD (n = 3, N=2).

3.3.3.5. Affinity enrichment with Autoquin

The synthesis of the affinity enrichment probes was performed by Dr. Daniel Foley.

To gain further information about possible targets of Autoquin **52**, an affinity enrichment experiment was performed (Chapter 1.3.1.). Therefore, quinidine was chosen as the negative probe, since it was inactive in the autophagy assay. To facilitate immobilization on a solid support, the small molecules have to be modified with a suitable linker (Figure 63). Previous SAR studies showed that reduction of the double bond caused only a minor decrease in starvation-induced IC₅₀ to $1.05 \pm 0.14 \mu\text{M}$. Thus, this position was selected for linker attachment. First, a Boc-protected aminoethanethiol linker was introduced to facilitate further modification. The Boc protected precursor of the Autoquin **52** probe had an IC₅₀ of $7.9 \pm 1.96 \mu\text{M}$, while the quinidine-based precursor was inactive. Subsequently, both compounds were modified with a PEG-linker featuring a terminal amine for immobilization on solid support.

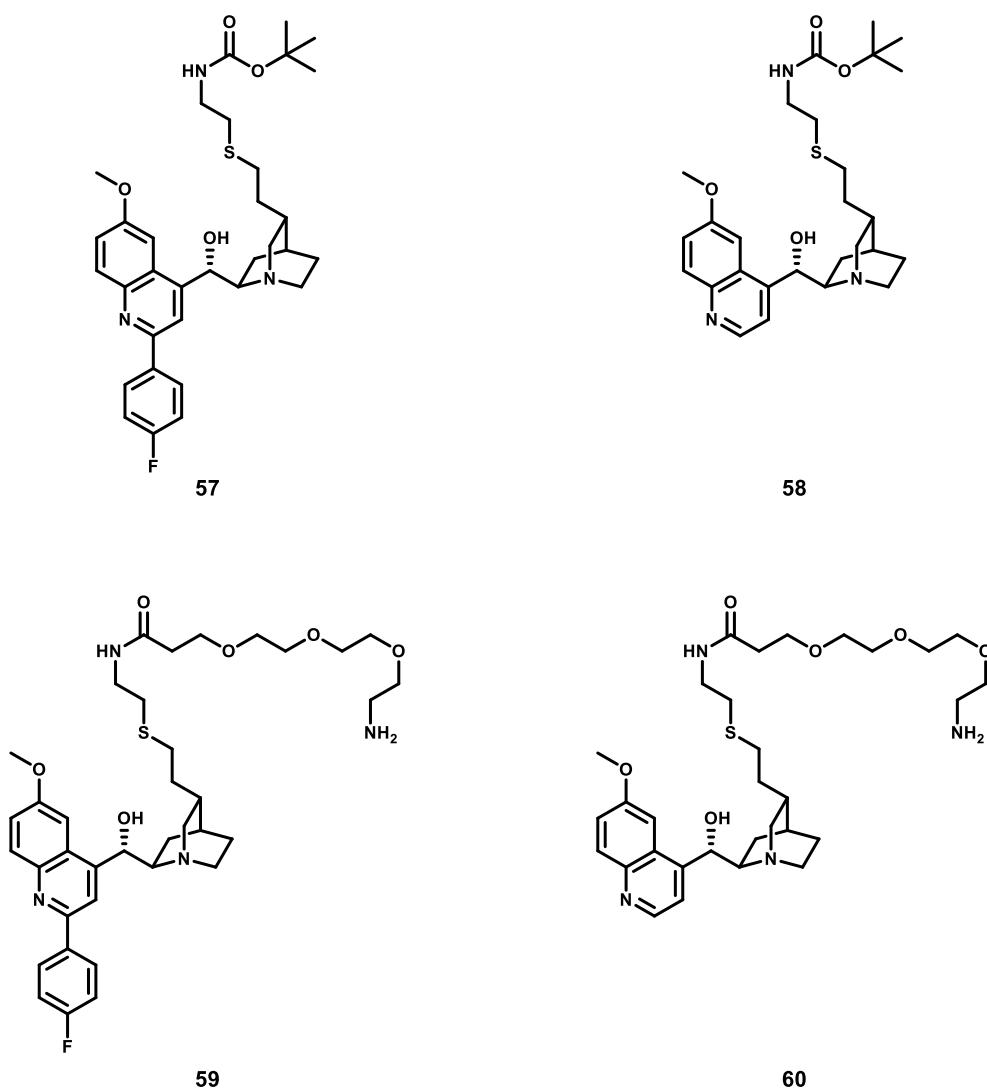


Figure 63: Structures of the Autoquin-based positive probe **59** and the quinidine-based negative probe **60** for affinity enrichment and the corresponding Boc-protected precursors **57** and **58**.

For affinity enrichment, the probes **59** and **60** were immobilized on NHS-activated beads and incubated with MCF7/LC3 lysate. Subsequently, the beads were washed to remove unbound protein, followed by digestion with the proteases trypsin and chymotrypsin. The samples were analyzed by mass spectrometry to identify bound proteins. Those proteins that were significantly enriched with the positive probe in comparison to the negative probe in all three biological replicates were considered as hits. This resulted in identification of ferrochelatase (FECH) as the only hit protein. FECH is located in mitochondria and catalyzes the insertion of iron into protoporphyrin IX (Figure 64). This represents the last step in the heme biosynthesis pathway.^[182]

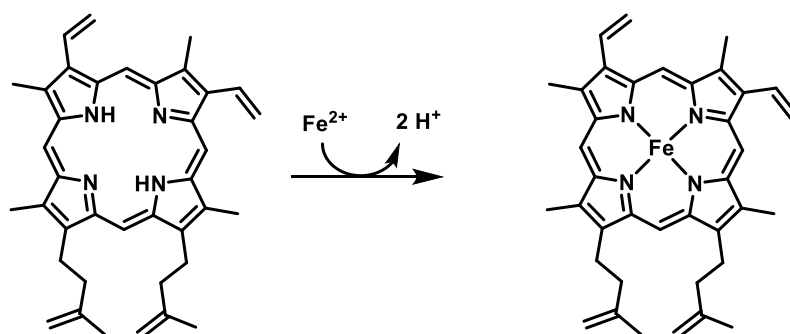


Figure 64: Insertion of iron into protoporphyrin IX by ferrochelatase.

The interaction of the positive probe with FECH was investigated by competitive affinity enrichment and subsequent immunoblotting (Figure 65). Therefore, the lysate was incubated with increasing concentrations of unlabeled compound. Subsequently, the pretreated lysate was added to the immobilized probe. However, FECH was enriched with the positive probe as well as with the negative probe. It could not be competed off in a reproducible dose-dependent fashion. Thus, no confirmation of the target hypothesis from mass spectrometry-based experiments could be obtained.

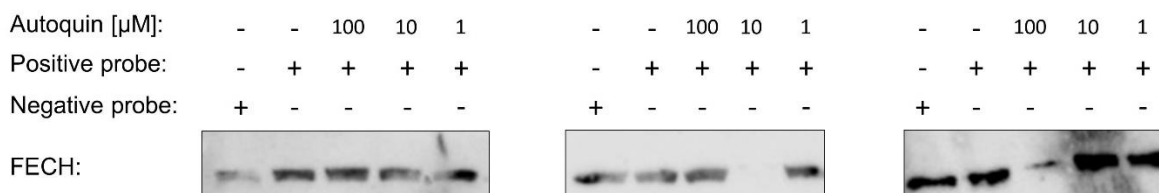


Figure 65: Competitive affinity enrichment of the positive probe **59** with increasing concentrations of Autoquin **52** in MCF7/LC3 cell lysate. Detection was performed by SDS-PAGE and subsequent immunoblotting against FECH. (Blots represent 3 independent experiments.)

3.3.3.6. Isothermal dose response fingerprint

The isothermal dose response fingerprint (ITDRF) is derived from the cellular thermal shift assay. In contrast to TPP the variable is not the temperature, but compound concentration.^[20] Cell lysate is treated with increasing concentrations of compound and DMSO is used as a reference. Subsequently, the lysate is heated to the melting point of the protein of interest, since the shift is calculated from the difference in melting temperature of treated and untreated

samples. Denatured protein is removed by ultracentrifugation and the fraction of soluble protein can be determined by immunoblotting. That allows to determine the effect of compound concentration on protein stability.

In order to analyze the effect of Autoquin **52** on the thermal stability of ferrochelatase, an ITDRF was performed (Figure 66). MCF7/LC3 cell lysate was treated with increasing concentrations of compound and the samples were heated to 56 °C. Immunoblotting revealed that Autoquin **52** had no influence on ferrochelatase stability at concentrations up to 400 μM. Thus, interaction of Autoquin **52** with ferrochelatase could also not be confirmed by ITDRF.

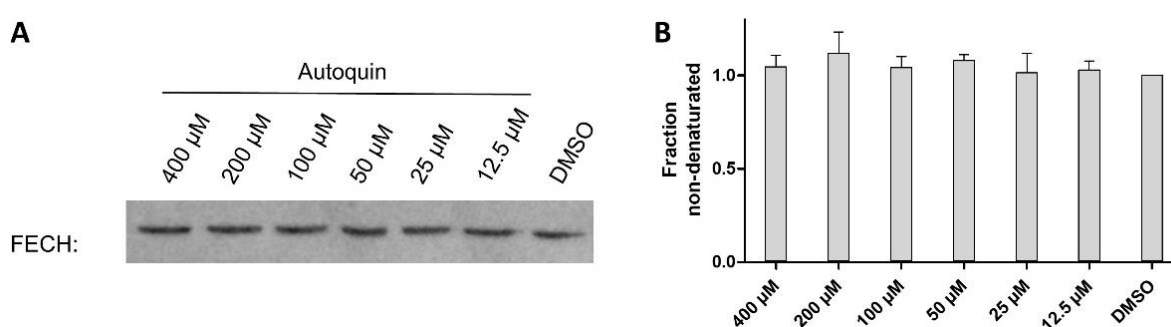


Figure 66: Autoquin **52** has no influence on thermal stability of ferrochelatase. MCF7/LC3 lysate was treated with decreasing concentrations of Autoquin **52** or DMSO (1%). All samples were heated to 56°C and subsequently centrifuged. Non-denatured fraction of ferrochelatase was detected by immunoblotting. **A:** Immunoblot of ITDRF for ferrochelatase with different concentrations of Autoquin **52**. (representative blot shown, n=3) **B:** Quantification of the immunoblots normalized to the DMSO control. Data shown is mean ± SD (n=3)

3.3.3.7. Autoquin possibly sequesters iron in lysosomes

The only hit of Autoquin **52** in affinity enrichment experiments was ferrochelatase. The human ferrochelatase is located at the inner mitochondrial membrane and forms a homodimer. The hydrophobic active sites are oriented towards the membrane and feature each a [2Fe-2S] cluster. These two clusters face towards the dimer interface.^[183] Ferrochelatase catalyzes the insertion of ferrous iron into protoporphyrin IX to form iron(III) protoporphyrin IX (Fe(III)PPIX). Protoporphyrin substrate binding initiates dynamic and conformational changes, which generates an ion channel. This channel stabilizes the active site and mediates iron uptake and insertion into protoporphyrin to produce Fe(III)PPIX.^[184] Even though ferrochelatase

could not be confirmed as an interaction partner of Autoquin **52** by competitive affinity enrichment or ITDRF, it indicated a possible mode of action for the autophagy inhibitor. The quinidine scaffold that Autoquin **52** is based on, as well as the quinidine-derived compound chloroquine feature anti-malarial activity.^[185] A possible explanation for this anti-malarial activity is complex formation of the quinidine scaffold with the ferrochelatase product Fe(III)PPIX. This results in an inhibition of hemozoin production, which is toxic for the *Plasmodium* parasite (Chapter 3.1.6.).^[186] Co-crystallization of quinidine with Fe(III)PPIX suggested several components to be critical for complex formation. The first one is an intramolecular hydrogen bond between the nitrogen atom of the quinuclidine and the Fe(III)PPIX propionate functionality. Furthermore, the alcohol coordinates the Fe(III) center of porphyrin and the whole complex is stabilized by π - π -stacking.^[146] The quinidine derivative Autoquin **52** contains all of the proposed critical structural components and could therefore also coordinate the iron center in Fe(III)PPIX. Complementary to this assumption, the group of Raphaël Rodriguez showed that the two lysosomotropic autophagy inhibitors, Salinomycin and Ironomycin, sequester iron in the lysosome. The shortage of cytosolic iron causes lysosomal degradation of ferritin. Thus, the iron content of the lysosomes is further increased, which finally results in initiation of the iron dependent cell death pathway ferroptosis.^[187] Similar to Salinomycin and Ironomycin, Autoquin **52** also affects the lysosomes and was proposed to be lysosomotropic. Furthermore, the structurally similar lysosomotropic compound chloroquine interferes with cellular iron metabolism and transporation. Thus, the compound could have a similar mode of action as Salinomycin and Ironomycin and disturb cellular iron homeostasis by sequestering iron in lysosomes. To investigate this possibility, a collaboration with the group of Raphaël Rodriguez from the Institut Curie in Paris was established.

3.3.3.8. Conclusion

Autoquin **52** is a potent autophagy inhibitor with a starvation-induced IC₅₀ of $0.90 \pm 0.09 \mu\text{M}$. The compound is inactive in rapamycin-induced autophagy and thus acts upstream of mTOR. The structural similarity to the lysosomotropic compound chloroquine suggested that Autoquin **52** has similar properties. As chloroquine, Autoquin **52** indirectly inhibits the lysosomal protein aCD and seems to cause impaired autophagosome lysosome fusion. Lysosomotropic compounds frequently interfere with sphingolipid hydrolase activity.

Sphingolipid metabolism and autophagic flux are highly interdependent. However, the exact mechanism underlying this interplay still remains to be elucidated.

Several mitochondrial proteins were identified as potential interactions partners of Autoquin **52** by means of TPP experiments. Furthermore, by affinity enrichment FECH was identified as a possible target of Autoquin **52**. However, the hit protein ferrochelatase could not be confirmed by competitive pulldown. Like some of the hits from the TPP experiments, ferrochelatase is located in the mitochondria, but no effect of Autoquin **52** on mitochondrial respiration was observed. Even though none of these mitochondrial proteins could be confirmed as a hit, ferrochelatase indicated a possible mode of action for Autoquin **52**. Autoquin **52** is based on the quinidine scaffold. Quinidine is known to complex Fe(III)PPIX, which is the product of the reaction catalyzed by ferrochelatase. In analogy to this, Autoquin **52** may also coordinate to the iron center of Fe(III)PPIX. Furthermore, Rodriguez and coworkers published the lysosomotropic autophagy inhibitors Salinomycin and Ionomycin. These compounds sequester iron in the lysosome and finally cause ferroptosis. As Salinomycin and Ionomycin, Autoquin **52** is proposed to be lysosomotropic. Furthermore, the structurally similar compound chloroquine was reported to interfere with iron metabolism and transportation. Thus, Autoquin could possess a similar mode of action as Salinomycin and Ionomycin and sequester iron in the lysosome. For this reason, a collaboration with the group Rodriguez was initiated, who will investigate this hypothesis in detail. Autophagy maintains the cellular iron balance and regulates iron recycling by degradation of iron-based proteins. However, little is known to date about the mechanism, which underlies the interplay of iron metabolism and autophagy.^[188] Thus, small molecule tool compounds to investigate this biological process are highly relevant.

3.3.4. Thienopyrimidines as autophagy inhibitors

Another bioactive compound class, which was identified by the aforementioned phenotypic screen, were the thienopyrimidines. The most potent autophagy inhibitor was a commercially available thieno[2,3-d]pyrimidine (COMAS ID: 156381), from here on referred to as Authipyrin **53** (Figure 67). Authipyrin **53** displays a starvation-induced IC_{50} of $0.02 \pm 0.01 \mu\text{M}$ and a rapamycin-induced IC_{50} of $0.18 \pm 0.07 \mu\text{M}$. Since Authipyrin **53** is active in starvation- as well as in rapamycin-induced autophagy the inhibitor is predicted to act downstream of mTOR. To validate the inhibitory effect of this thienopyrimidine on autophagy, the starvation dependent toxicity upon initiation of autophagy was investigated as well as its influence on particular key autophagy markers. Furthermore, target identification and validation of Authipyrin **53** was performed.

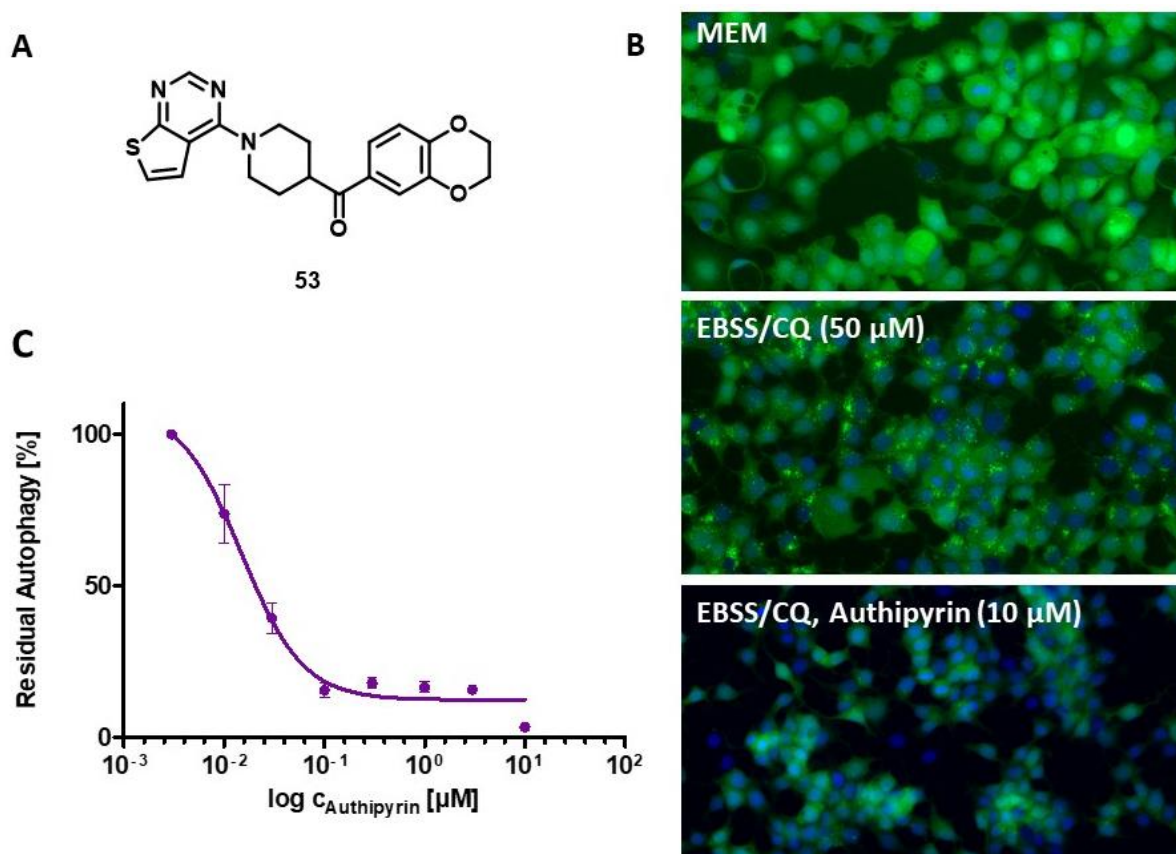


Figure 67: Authipyridin **53** inhibits starvation induced autophagy. **A:** Structure of Authipyridin **53**. **B:** Phenotypic assay for the identification of autophagy inhibitors using MCF7 cells stably transfected with eGFP-LC3. Non-starved cells were treated with MEM, starved cells with EBSS and 50 μM CQ. Simultaneously decreasing concentrations of Authipyridin **53** were added. After 3 h incubation, the cells were fixed with paraformaldehyde and the nuclear DNA was stained with Hoechst. **C:** Dose dependent effect of Authipyridin **53** on the number of autophagosomes per cell. Representative graph shown ($n \geq 3$); MEM: Minimal Essential Medium; CQ: Chloroquine; EBSS: Earle's balanced salt solution.

3.3.4.1. Validation of Authipyridin as an autophagy inhibitor

Initially, the influence of Authipyridin **53** on the autophagy markers LC3 and p62 was investigated (Figure 68). Authipyridin **53** reduced LC3-II formation compared to starved cells at concentrations of 1 μM and 100 nM. Also at 10 nM a minor decrease of LC3-II was visible in comparison to starved cells. Authipyridin **53** did not prevent p62 degradation upon starvation. Nevertheless, the effect of Authipyridin **53** on LC3 lipidation provides a first confirmation that Authipyridin **53** is a potential autophagy inhibitor.

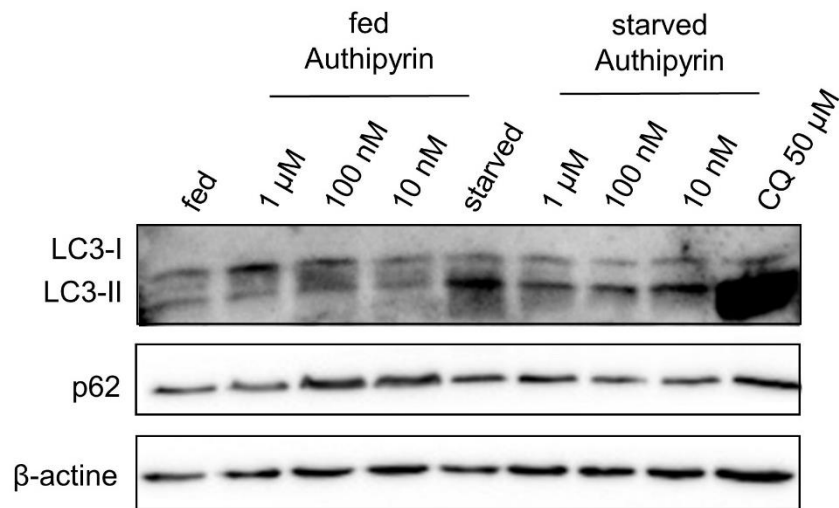


Figure 68: Effect of Authipyrin **53** on LC3 lipidation and p62 degradation. Autophagy is induced by amino acid starvation. Cells are treated with decreasing amounts of Authipyrin **53** or CQ as a control and lysed after 3 h.

In order to determine the effect of Authipyrin **53** on cell viability under fed and starved conditions a cell viability assay was performed. At concentrations of 10 μ M or lower Authipyrin **53** does not alter cell viability of non-starved cells (Figure 69A). However, under starved conditions without glucose Authipyrin **53** has a dose-dependent effect on cell viability (Figure 69B and 69C). At a concentration of 0.37 μ M and higher the inhibitor causes cell death of about 40% to 50% of the cells within 72h. These results suggest that Authipyrin **53** can induce autophagy dependent cell death under starvation, but is not toxic under nutrition rich conditions.

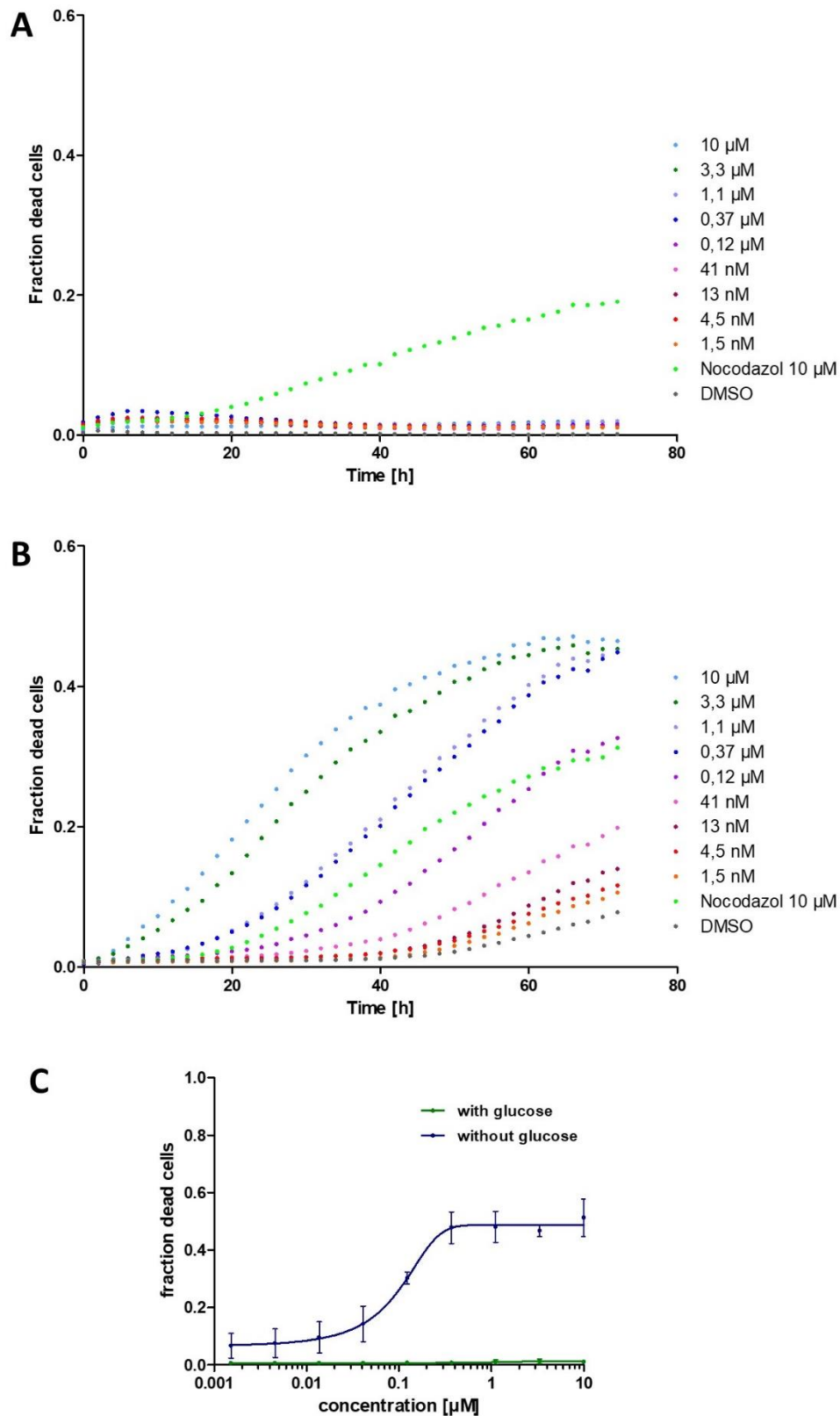


Figure 69: Viability of MCF7 cells with different concentrations of Authipyrin **53**. MCF7 cells were cultivated with (A) and without Glucose (B) and treated with Authipyrin **53** over 72 h. Dying cells were stained with propidium iodide. DMSO and Nocodazole were used as controls. Representative graph shown (n=3, N=3). C: Fraction of dead cells plotted against concentration of Authipyrin **53** after 72 h.

3.3.4.2. Devalidation of Authipyrin as a kinase inhibitor

The thienopyrimidine scaffold of Authipyrin is contained in various published kinase inhibitors.^{[189],[190],[191]} A subset of these inhibitors is also known to affect autophagy.^{[192],[193]} Thus, Authipyrin **53** could also modulate kinase activity. Authipyrin **53** was screened by SelectScreen™ (Thermo Fisher Scientific) in a full panel against 485 different kinases. The screen was performed at a single concentration of 1 μ M. The obtained screening results showed only four kinases with an inhibition higher than 50%.

Table 7: Results from SelectScreen™ Kinase profiling with Authipyrin **53**. Six kinases with the strongest inhibition at a single concentration of 1 μ M were chosen for IC₅₀ measurements. Kinases were screened against decreasing concentrations of Authipyrin **53** with the highest concentration being 1 μ M.

Kinase	Single point inhibition [%]	IC ₅₀ Inhibition [%]	IC ₅₀ [μ M]
PEAK1	83	68	0.62
ABL1 F317L	47	60	0.85
CDK11 (inactive)	70	47	>1.0
BLK	47	44	>1.0
DDR2 N456S	58	38	>1.0
GSG2 (Haspin)	51	33	>1.0

The kinase with the strongest inhibition of 85% was pseudopodium-enriched atypical kinase 1 (PEAK1). PEAK1 is a non-receptor tyrosine kinase involved in regulation of the cytoskeleton, cell migration and cancer progression.^[194] Another kinase inhibited up to 70% was the inactive form of cyclin-dependent kinase 11 (CDK11). The CDK11/cyclin C complex was only inhibited by 38%. CDKs control transcription and progression of the cell cycle. They are activated by interaction with the respective cyclin. CDK11 regulates apoptosis and cytokinesis, as well as RNA splicing.^[195] Furthermore, Authipyrin **53** modulated a mutated version of discoidin domain-containing receptor 2 (DDR2). The DDR2 protein is a collagen-induced receptor, which regulates cell proliferation and adhesion, as well as extracellular matrix remodeling.^[196] The DDR2 (N456S) mutant was inhibited up to 58%, while the wild-type DDR2 protein was inhibited only by 14% and the mutant DDR2 (T654M) by 7%. Haspin

showed 51% inhibition by Authipyryn **53** and is a serine/threonine kinase, responsible for phosphorylation of histone H3 during mitosis.

Subsequently, the six kinases with strongest alteration by Authipyryn **53** were chosen for IC₅₀ measurements. The IC₅₀ values were determined at a maximal concentration of 1 μM. These kinases include the four previously mentioned ones PEAK1, CDK11, DDR2 (N456S) and haspin. Furthermore, the B-lymphoid tyrosine kinase (BLK) and an abelson tyrosine-protein kinase 1 mutant (Abl1 F317L) were chosen. Out of these CDK11, BLK, DDR2 (N456S) and haspin had an IC₅₀ higher than 1 μM. According to calculations by SelectScreen™ Abl (F317L) was inhibited by Authipyryn **53** with an IC₅₀ of 850 nM and PEAK1 with an IC₅₀ of 620 nM. However, after inspection of the provided graphs both IC₅₀ values are probably inaccurate, since they do not reach saturation at the highest concentrations (Figure 70).

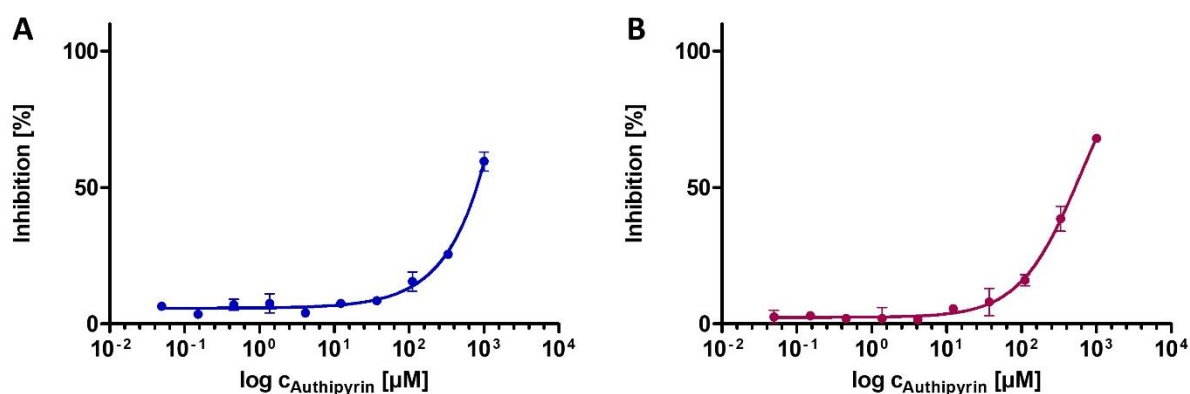


Figure 70: Determination of IC₅₀ values of Authipyryn **53** with maximum concentration of 1 μM by SelectScreen™. **A:** Inhibition measurement for PEAK1. **B:** Inhibition measurement for Abl (F317L).

The kinase panel was performed with purified protein. Thus, the IC₅₀ of a target protein responsible for autophagy inhibition should be comparable to or lower than the cellular IC₅₀. Authipyryn **53** has a cellular starvation-induced IC₅₀ of 0.02 ± 0.01 μM and a rapamycin-induced IC₅₀ of 0.18 ± 0.07 μM. However, the affinity for all six kinases is significantly weaker. Thus, the inhibitory effect of Authipyryn **53** in autophagy is most probably not caused by alteration of a kinase.

3.3.4.3. Influence on mitochondrial respiration

Damaged or nonfunctional mitochondria can be selectively degraded by autophagy. This process is referred to as mitophagy. Vice versa autophagy can be regulated by mitochondria due to the generation of ROS and ATP.^[179] Additionally, inhibition of mitochondrial respiration impairs autophagic flux.^[180] Recently a new autophagy modulator termed Aumitin **61** was reported, which downregulates autophagy by inhibition of the mitochondrial electron transport chain complex I.^[160] Alteration of autophagic flux was also previously demonstrated for the complex I inhibitor rotenone.^[197] This underlines the important interdependency between oxidative phosphorylation and the regulation of autophagic flux. The effect of Authipyrin **53** on mitochondrial oxygen consumption was investigated in detail with the Seahorse XF Mito Stress Test, which revealed that Authipyrin **53** inhibits mitochondrial respiration (Figure 71). At a concentration of 1 μM it reduces the OCR by about 75%. With a lower concentration of 0.1 μM the OCR drops by about 25%. Under both conditions the ECAR increases significantly.

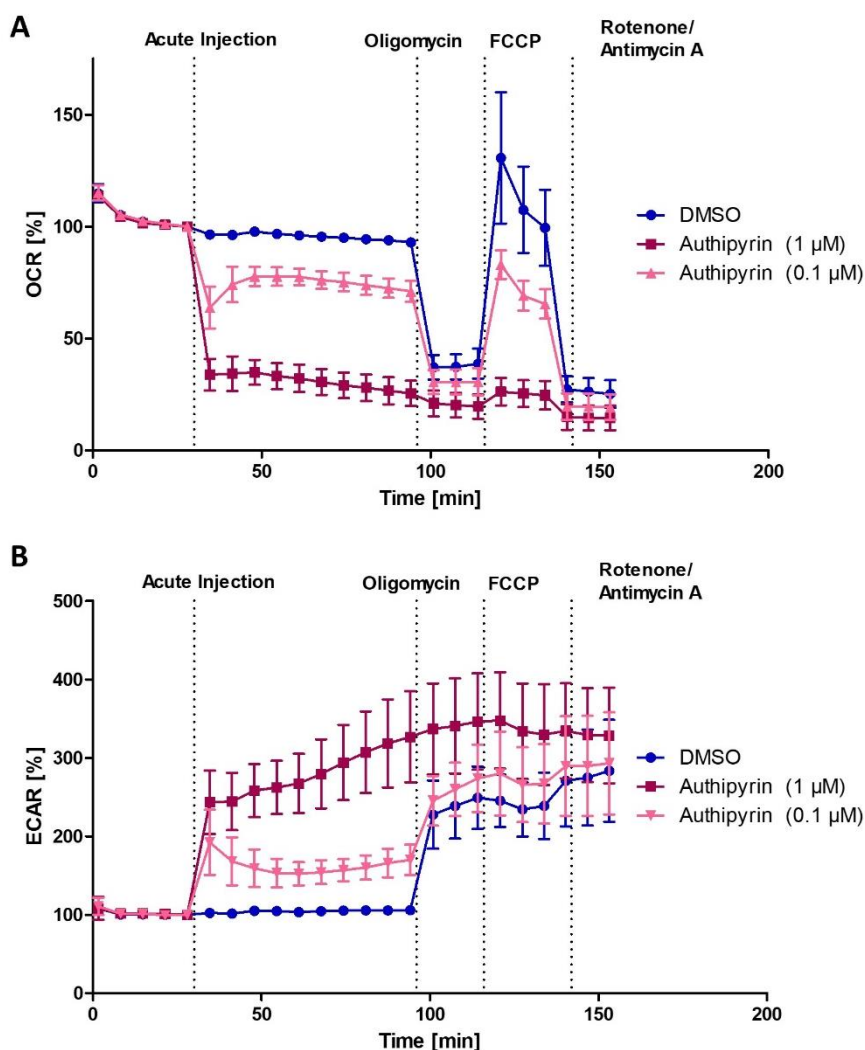


Figure 71: Influence of Authipyryn **53** on mitochondrial respiration. MCF7 cells were treated with Authipyryn **53** (1 μ M and 0.1 μ M) or DMSO upon acute injection. Subsequently, oligomycin (1 μ M), FCCP (0.25 μ M) and a mixture of rotenone/antimycin A (0.5 μ M) were added. The OCR (**A**) and ECAR (**B**) were monitored over time. Data shown is mean values \pm SD (n = 3, N=2).

Subsequently, the compounds **62** and **63** (COMAS ID: 226101 and 133633) were analyzed by Mito Stress Test. Both are based on the thienopyrimidine scaffold and not active in the phenotypic autophagy assay. None of these compounds had an influence on mitochondrial respiration (Figure 72). Thus, the inhibition of the respiratory chain by Authipyryn **53** is dependent on downregulation of autophagy.

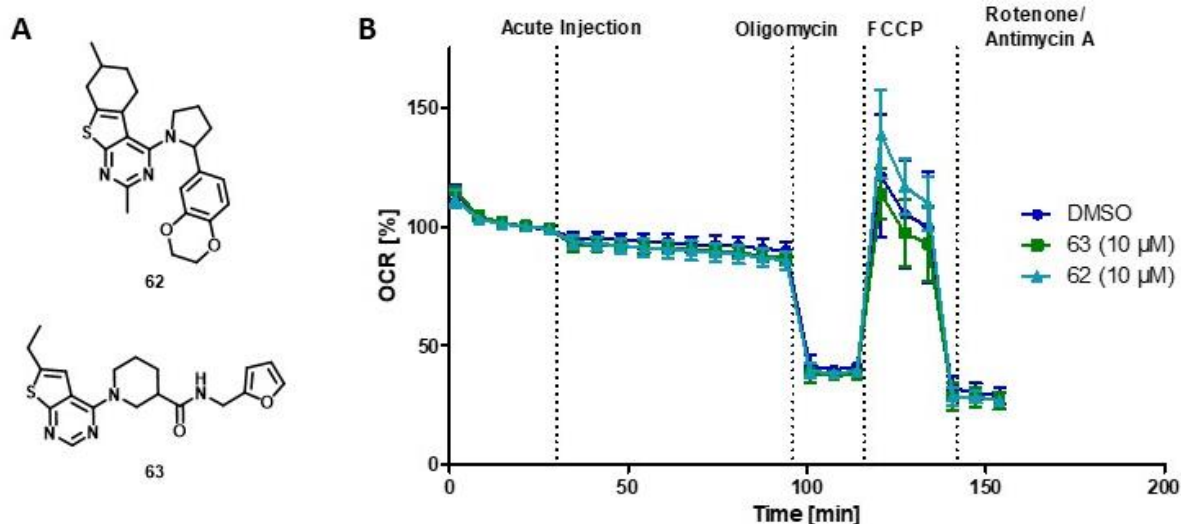


Figure 72: Influence of the thienopyrimidines **62** and **63** on mitochondrial respiration. **A:** Structure of **62** and **63**. **B:** MCF7 cells were treated with compound (10 μM) or DMSO upon acute injection. Subsequently oligomycin (1 μM), FCCP (0.25 μM) and a mixture of rotenone/antimycin A (0.5 μM) were added. The OCR was monitored over time. Data shown is mean values \pm SD ($n = 3$, $N=2$).

3.3.4.4. Investigation of individual mitochondrial complexes

Hereafter, the effect of Authipyrin **53** on the individual mitochondrial complexes I to IV was investigated in detail by semi-intact assay (Figure 73).^[198] Therefore, each complex is supplied with the respective substrates in combination with Authipyrin **53** (1 μM), a control inhibitor or DMSO (Table 8). In order to ensure delivery of the substrates to mitochondria, Seahorse XF plasma membrane permeabilizer (PMP) is added. This reagent specifically permeabilizes the plasma membrane, but has no effect on mitochondrial membranes.

Table 8: Reagents and control inhibitors required for analysis of mitochondrial complex inhibition by Authipyrin **53**. ADP (1 mM) and PMP (1 nM) were added to all complexes. TMPD: *N,N,N',N'*-Tetramethyl-*p*-phenylenediamine.

Complex	Reagents	Control Inhibitor
I	Pyruvate (10 mM), malate (1 mM)	Rotenone (1 μM)
II	Succinate (10 mM), rotenone (1 μM)	Malonate (2 mM)
III	Duroquinol (0.5 mM)	Antimycin A (30 μM)
IV	TMPD (0.5 mM), sodium ascorbate (20 mM)	Potassium cyanide (20 mM)

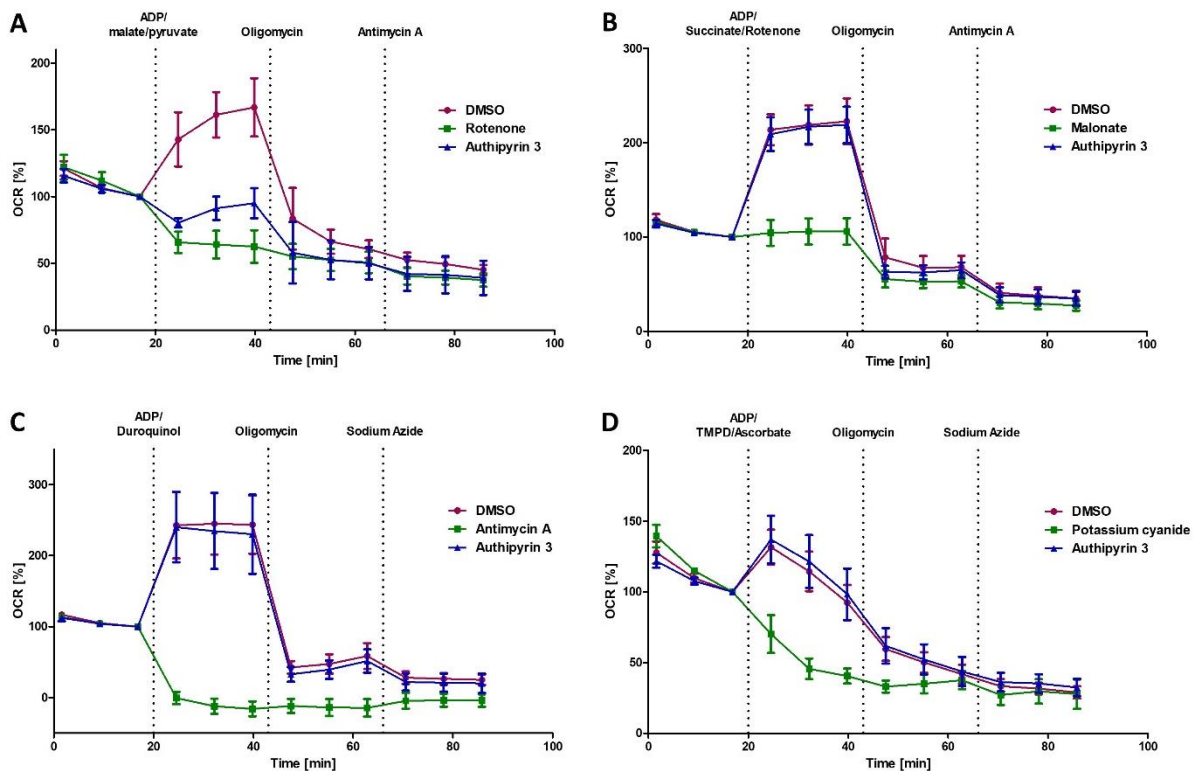


Figure 73: Semi-intact assay with Authipyryn **53**. The plasma membrane of MCF7/LC3 cells was permeabilized with PMP. Substrates for the respective complex were added together with Authipyryn **53** (1 μ M), a control inhibitor or DMSO. **A:** Effect of Authipyryn **53** on complex I with rotenone (1 μ M) as control inhibitor. **B:** Effect of Authipyryn **53** on complex II with malonate (2 mM) as control inhibitor. **C:** Effect of Authipyryn **53** on complex III with antimycin A (30 μ M) as control inhibitor. **D:** Effect of Authipyryn **53** on complex IV with potassium cyanide (20 mM) as control inhibitor. Data shown is mean values \pm SD (n = 3, N=2).

Separate investigation of each individual mitochondrial complex revealed that Authipyryn **53** had no effect on complexes II to IV (Figure 73B to 73D). While the selective inhibitors of these complexes reduced the OCR, Authipyryn **53** did not cause an alteration. However, upon simultaneous addition of Authipyryn **53** and the substrates of complex I, mitochondrial respiration was inhibited (Figure 73A). This indicates that Authipyryn **53** is a selective inhibitor of mitochondrial complex I. Aumitin **61** is a known autophagy inhibitor, which also targets mitochondrial complex I. Furthermore, previous studies proved that the complex I inhibitor rotenone downregulates autophagy, as well as complex III inhibitors antimycin A and complex V inhibitor oligomycin.^{[160],[197]} Thus, complex I can be considered as a relevant target for the effect of Authipyryn **53** on autophagy.

3.3.4.5. Thermal proteome profiling

In order to confirm complex I as a target of Authipyrimin **53**, a TPP experiment was performed. Therefore, MCF7/LC3 cell lysate was incubated with 1 μ M of Authipyrimin **53**. The samples subjected to heat treatment with a temperature gradient between 37 °C and 67 °C. Subsequently, insoluble components were removed by centrifugation and the supernatant was analyzed by mass spectrometry. A hit was defined according to one or both of the following criteria: 1) A consistent shift of ≥ 1.0 °C for all replicates and/or 2) An increase of the non-denatured protein fraction by more than 0.1 in every replicate. Evaluation of the obtained data provided 30 potential hit proteins. (Appendix) Furthermore, several subunits of complex I were identified. However, none of them fulfilled the criteria for being a hit. Two of those, the NADH dehydrogenase [ubiquinone] 1 beta subcomplex subunit 1 and 2 (NDUFB1 and NDUFB2), were stabilized in two out of three replicates (Figure 74). While NDUFB1 was twice stabilized by 5.76 °C and 3.23 °C and once destabilized by -3.50 °C, NDUFB2 showed a stabilization of 4.52 °C and 1.35 °C and a destabilization of -0.32 °C.

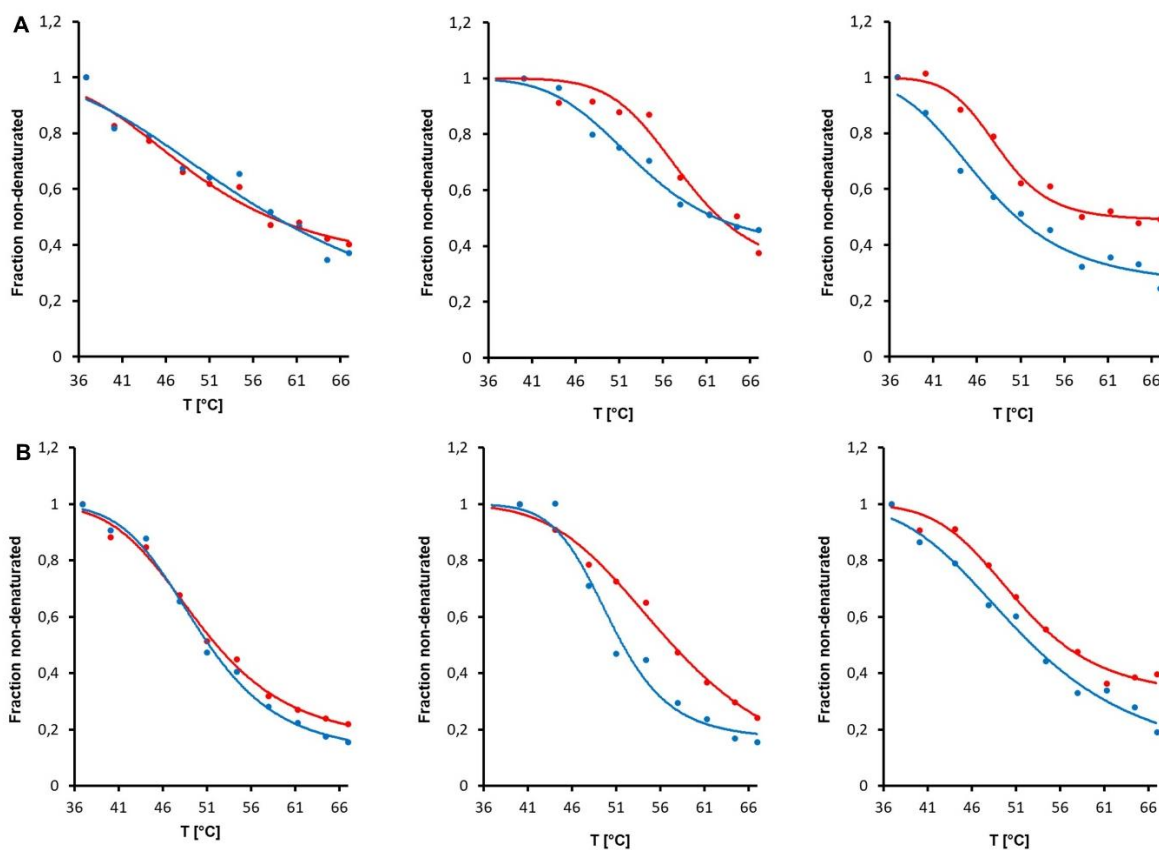


Figure 74: Thermal Proteome Profiling with Authipyrin **53**. MCF7/LC3 lysate was treated with 1 μ M Authipyrin **53** (red) or DMSO (blue). Samples were subjected to heat treatment and analyzed by mass spectrometry. **A:** Melting curves of NDUFB1. **B:** Melting curves of NDUFB2. $n = 3$, each graph represents one independent experiment.

Complex I consists of 45 different subunits. NDUFB1 and NDUFB2 are believed to be accessory subunits, which are not involved in catalysis.^[199] Nevertheless, compound binding could cause conformational changes that interfere with the catalytic function. In order to obtain further indication whether NDUFB1 and NDUFB2 should be considered as possible interaction partners of Authipyrin **53**, two more replicates of the TPP were prepared. However, neither NDUFB1 nor NDUFB2 were sufficiently identified in these replicates to calculate the shifts in melting temperature. In conclusion, the interaction of Authipyrin **53** with complex I could not be confirmed by TPP.

3.3.4.6. Complex I activity assay

A NADH-CoQ reductase activity assay was performed, to confirm whether the effect of Authipyrim **53** on complex I was direct or indirect (Figure 75). Complex I consumes NADH by transfer of electrons to coenzyme Q under generation of NAD^+ . An indirect effect of Authipyrim **53** on complex I could be caused by interference with the NADH supply chain. The *in vitro* assay was performed with isolated bovine heart mitochondria. NADH was added in excess to rule out the influence of the NADH supply chain. The mitochondrial respiration inhibitor rotenone is known to have a direct effect on complex I. Thus, it was employed as a positive control.

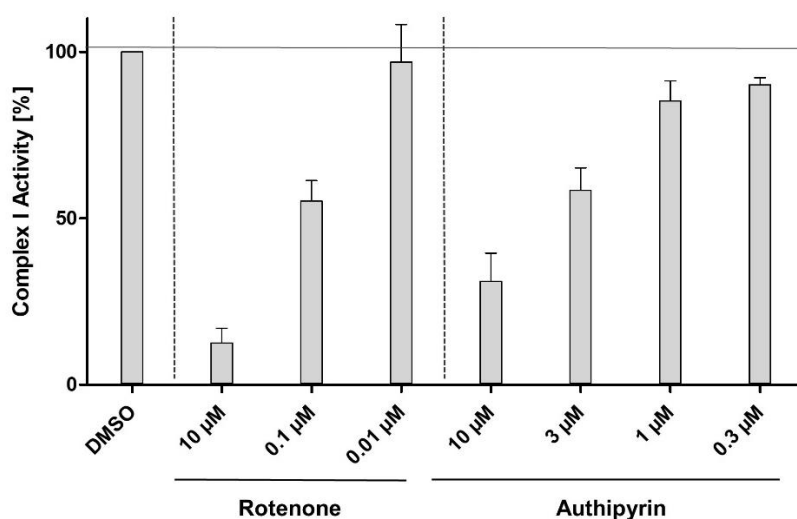


Figure 75: NADH-CoQ reductase activity assay with Authipyrim **53**. The known direct complex I inhibitor rotenone was employed as a positive control. Data shown is mean values \pm SD (n = 2, N=2).

Authipyrim **53** had a direct dose-dependent inhibitory effect on NADH-CoQ reductase activity. At a concentration of 10 μM Authipyrim **53** reduces complex I activity to about 30 %. Thus, it has the same mode of action as rotenone and the published autophagy inhibitor Aumitin **61**.^[160] Surprisingly, high compound concentrations were required in comparison to the Mito Stress Test and the semi-intact assay. However, in contrast to the Mito Stress Test and semi-intact assays, this experiment was not cell-based. Instead, isolated mitochondria were applied to examine the NADH-CoQ reductase activity. The comparably large number of mitochondria consequently resulted in a high concentration of the investigated protein. Thus, increased compound concentrations might be required to achieve the same inhibitory effect. This was

also observed for the complex I inhibitor Aumitin **61**.^[160] Conclusively, the direct inhibitory effect of Authipyrin **53** on complex I could be confirmed.

3.3.4.7. Cell painting assay

To gain further insight into the mode of action of Authipyrin **53**, the compound was analyzed by means of CPA (Figure 76). Authipyrin **53** had only a very low induction of 1.7% and 5.5%. An induction of more than 5% is considered sufficient to calculate biosimilarity to reference compounds. One reference compound, Beclomethasone dipropionate (BDP), with sufficient biological similarity of higher 65% could be determined.

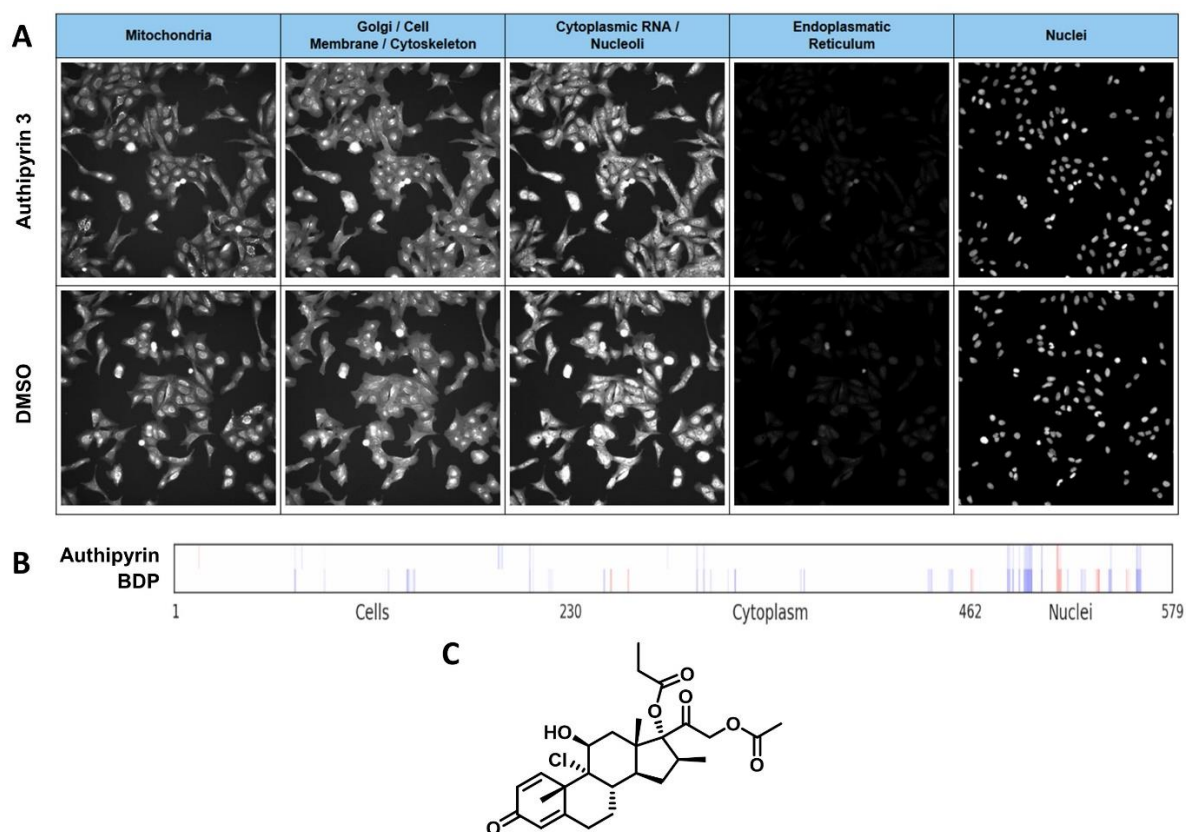


Figure 76: Results of the CPA with Authipyrin **53** performed at COMAS. **A:** Representative Fluorescence microscopy images. Five fluorescent dyes were employed to stain different cellular components and compartments. The upper row corresponds to Authipyrin **53** (10 μ M) treated samples and the lower row to the DMSO control. Representative images (n=3). **B:** Finger prints of Authipyrin **53** and the identified reference compound BDP. Data shown is mean values (n = 3). **C:** Structure of BDP **64**.

The reference compound BDP **64** had an induction of 10% and a biosimilarity to Authipyridin **53** of 71.9%. This corticosteroid is a ligand of the glucocorticoid receptor and reduces the expression of proinflammatory factors. BDP is applied in the treatment of asthma.^[200] No direct involvement of BDP in autophagy is known to date. However, at a concentration of 10 μM Authipyridin **53** causes only a minor induction of 1.7% and 5.5%. The compound does not seem to induce strong morphological changes. Thus, the identification of compounds with similar bioactivity by CPA is challenging. Conclusively, the CPA could not provide further insight into the mode of action of Authipyridin **53** or confirm complex I as a target.

3.3.4.8. Conclusion

Authipyridin **53** was validated as a highly potent inhibitor of autophagy with a starvation-induced IC_{50} of $0.02 \pm 0.01 \mu\text{M}$ and a rapamycin-induced IC_{50} of $0.18 \pm 0.07 \mu\text{M}$. Authipyridin **53** impairs mitochondrial respiration. Structurally similar thienopyrimidines **62** and **63**, which were inactive in the autophagy assay, had no influence on the OCR. Thus, the effect on respiration is directly connected to the modulation of autophagy. Similar to the known autophagy inhibitor Aumitin **61**, Authipyridin **53** targets the NADH-CoQ reductase complex by direct interaction. Furthermore, Authipyridin features selective toxicity under nutrition deprivation. Consequently, the effect of the compound is selective for autophagy.

Herein, a novel highly potent tool compound was discovered, which can be employed to investigate the interplay between mitochondrial respiration and autophagy. Up to date, this process is still poorly understood. However, altered mitochondria and impaired autophagy are both observed in patients suffering from Parkinson's disease. Furthermore, mitophagy is frequently dysregulated in Parkinson's disease, which prevents the turnover of damaged mitochondria.^[201] Thus, novel selective tool compounds, to elucidate the mechanism underlying this interdependency between mitochondria and autophagy are of utmost importance.

3.3.5. Summary

In the course of this project, three structurally different potential autophagy inhibitors were identified by means of medium throughput phenotypic screening (Figure 77). These compounds were evaluated regarding their effect on autophagy and characterized by target identification and validation to elucidate their mode of action. Autophagy is an essential catabolic process, which ensures cellular homeostasis and energy supply. This biological mechanism is highly involved in various pathological conditions. Even though the regulatory mechanisms of autophagic flux were intensely studied to date, this process is still not fully understood. Thus, these structurally novel autophagy modulators can expand the toolkit to further elucidate the autophagic machinery and unravel its function in disease.

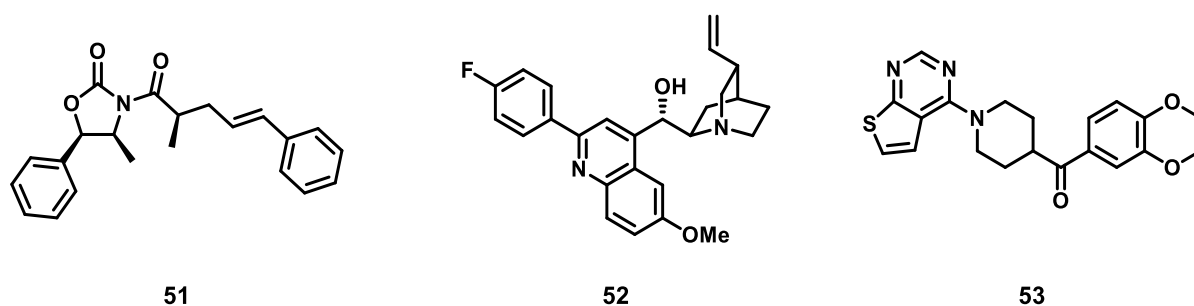


Figure 77: Structures of potential autophagy inhibitors Autoxain **51**, Autoquin **52** and Authipyrin **53** identified by phenotypic screening.

The first potential autophagy inhibitor is the oxazolidinone-based compound Autoxain **51**. The influence of Autoxain **51** on autophagy markers LC3 and p62 was determined. However, the results were inconclusive and could not confirm an inhibitory effect on autophagic flux. Furthermore, no selective toxicity under nutrient-deprivation was observed. This could be explained by the low potency of Autoxain **51**. Target identification initially attempted by means of CPA was unsuccessful. Autoxain **51** featured an induction of only 1%, which is considered not sufficient for calculation of a fingerprint. Thus, no biosimilarity to reference compounds could be determined. Subsequently, a TPP experiment was performed, which suggested an interaction of Autoxain **51** with the cytoplasmic and mitochondrial ribosome. Literature research revealed that the oxazolidinones tedizolid and linezolid are commercially available antibiotics. These compounds exert their antibacterial activity by inhibition of prokaryotic protein biosynthesis via the ribosome. Furthermore, linezolid was shown to inhibit

the mitochondrial ribosome, which is a possible cause of long-term side effects. Presumably, Autoxain **51** features a similar mode of action, but might not necessarily differentiate between the different ribosomes. However, TPP only indicates a possible interaction. Thus, Autoxain **51** does not necessarily have an influence on protein biosynthesis. Nevertheless, since Autoxain **51** could not be validated as an autophagy inhibitor and might target the ribosome, the project was not pursued further.

The second compound of interest was Autoquin **52**, which is derived from the known autophagy inhibitor Oxautin-1. Autoquin **52** is a potent autophagy inhibitor with a starvation-induced IC_{50} of $0.90 \pm 0.09 \mu\text{M}$. The compound is inactive in rapamycin-induced autophagy and thus probably acts upstream of mTOR. By TPP several mitochondrial proteins were identified as potential interactions partners. However, Autoquin **52** only slightly increased the ECAR and did not influence the OCR. The structural similarity to the lysosomotropic compound chloroquine suggested that Autoquin **52** has similar properties. As chloroquine, Autoquin **52** seems to impair autophagosome lysosome fusion and indirectly inhibits the lysosomal protein aCD. Lysosomotropic compounds frequently interfere with sphingolipid hydrolase activity. Sphingolipid metabolism and autophagic flux are highly interdependent. However, the exact mechanism underlying this interplay still remains to be elucidated. By affinity enrichment FECH was identified as a potential target of Autoquin **52**. However, the hit protein could not be confirmed by competitive pulldown. Nevertheless, FECH indicated a possible mode of action for Autoquin **52**. FECH catalyzes the production of Fe(III)PPIX. Autoquin **52** is based on the quinidine scaffold, which is known to complex Fe(III)PPIX. Thus, Autoquin **52** might also complex Fe(III)PPIX. Furthermore, Rodriguez and coworkers published the lysosomotropic autophagy inhibitors Salinomycin and Ionomycin. These compounds sequester iron in the lysosome and finally cause ferroptosis. Autoquin **52** might feature a similar mode of action. For this reason, the iron sequestering effect of Autoquin **52** is presently investigated in detail. Autophagy maintains the cellular iron balance and regulates iron recycling by degradation of iron-based proteins. However, little is known to date about the mechanism, which underlies the interplay of iron metabolism and autophagy.^[188] Thus, small molecules tool compounds to investigate this biological process are highly relevant.

The last potential autophagy inhibitor in this project was Authipyridin **53**. Authipyridin **53** affected starvation-induced autophagy with a starvation-induced IC_{50} of $0.02 \pm 0.01 \mu\text{M}$ and rapamycin-induced autophagy with an IC_{50} of $0.18 \pm 0.07 \mu\text{M}$. Authipyridin **53** features autophagy-

dependent toxicity under nutrition deprivation. Similar to the known autophagy inhibitor Aumitn **61**, the compound potentially impairs mitochondrial respiration. Structurally similar thienopyrimidines **62** and **63**, were tested regarding their effect on oxidative phosphorylation. These small molecules were inactive in the autophagy assay and had no influence on the OCR. Thus, the inhibition of mitochondrial respiration by Authipyrimin **53** is directly connected to the modulation of autophagy. Authipyrimin **53** has a direct effect on the mitochondrial complex I and does not affect it by interfering with the NADH supply chain. Misfunctional mitochondria and altered autophagic flux are both observed in Parkinson's disease. Furthermore, the turnover of damaged mitochondria is frequently impaired in this neurodegenerative disorder. Thus, novel tool compounds, to study the interplay between mitochondria and autophagy are of utmost importance.

Conclusively, three potential autophagy inhibitors were identified by a forward chemical genetic approach. While the influence of Autoxain **51** on autophagy could not be validated, the results obtained for Autoquin **52** and Authipyrimin **53** support their inhibitory effect on autophagic flux. These two compounds could extend the available toolkit to investigate the regulation of autophagic flux, as well as the interplay of autophagy with further biological processes and the involvement of this catabolic mechanism in disease.

4. EXPERIMENTAL PART

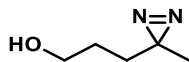
4.1 General chemical methods

Thin layer chromatography (TLC) was performed on Merck pre-coated Silica 60 plates, using anisaldehyde stain or UV for visualization. Column chromatography was carried out on Acros silica gel (35-70 μm , 60 \AA). Analytical HPLC-MS chromatograms were obtained from an Agilent HPLC (1100 series) using a reversed phase column (C4 or C18 – 5 μm , 250x4.6 mm) equipped with a Finnigan LCQ ESI spectrometer and an UV/VIS detector (flow rate: 1.0 ml/min; time: 15 min; using 0.1% HCOOH in H₂O, and 0.1% HCOOH in MeCN). Preparative HPLC runs were performed on an Agilent HPLC (1100 series) using a reversed-phase C4 or C18 column. NMR spectra were recorded on a Varian Mercury VX 400, Bruker Avance 500 or Bruker Avance 600 spectrometer. All recorded spectra were referenced to the solvent signal or TMS. High resolution mass spectra (HRMS) were measured on a Thermo Orbitrap coupled to a Thermo Accela HPLC system (HPLC column: Hypersyl GOLD, 50 mm x 1mm particle size 1.9 μm) using electrospray ionization (ESI). Solid phase peptide synthesis was performed in a CEM-Liberty Peptide Synthesizer equipped with a CEM-Discover Microwave.

4.1.1. Materials

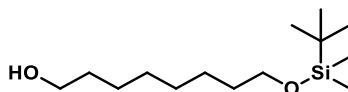
All chemicals and solvents were obtained from commercial sources (ABCR, Acros, Aldrich, Alfa Aesar, Fluka, Iris Biotech, Novabiochem or TCI) and used without further purification unless stated otherwise. Dry solvents were purchased from Acros or Aldrich or purified using published methods.^[202] GG1198 and Squarunkin A were kindly provided by Dr. Guillaume Garivet and Dr. Tom Mejuch. Autoxain was Synthesized by Dr. Christina Nöcker. Autoquin and the respective probes were kindly provided by Dr. Daniel Foley. Authipyrin was ordered from Enamine (Product ID: Z229457132).

4.2. Chemical synthesis



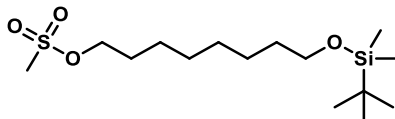
3-(3-Methyl-3H-diazirin-3-yl)propan-1-ol (5): In a 500 ml three-neck flask, equipped with magnetic stirrer, thermometer, dropping funnel, dry ice condenser and a rubber septum, 5-hydroxy-2-pentanone **4** (8.1 ml, 79.96 mmol) was dissolved in liquid NH₃ (42 ml). The reaction mixture was stirred for 5 h at -15 °C, cooled to -78 °C and a solution of hydroxyl-amine-*O*-sulfonic acid (10.4 g, 91.96 mmol) in methanol (71 ml) was added dropwise. After stirring for additional 1 h at -15 °C the flask was opened and the stirring was continued for 13 h to remove the excess of NH₃. The remaining precipitate was filtered and washed with methanol. The volume of the filtrate was reduced to 200 ml, it was cooled to 0 °C and Et₃N (10.0 ml, 71.75 mmol) was added dropwise. Iodine was subsequently added until the reaction mixture maintained its brown color. The mixture was diluted with saturated aqueous NaCl-solution and extracted with Et₂O (3 x 50 ml). The combined organic phases were dried over MgSO₄ and concentrated under reduced pressure. The product was obtained by vacuum distillation to give the product as yellow oil (3.42 g, 38%).

¹H NMR (500 MHz, CDCl₃) δ 3.43 (d, *J* = 5.5 Hz, 2H), 3.14 (d, *J* = 7.1 Hz, 1H), 1.30 (d, *J* = 3.3 Hz, 4H), 0.90 (s, 3H). ¹³C NMR (126 MHz, CDCl₃) δ 61.49, 30.54, 26.86, 25.58, 19.68. HRMS: [M+H]⁺ calc. 115.08659, found 115.08621.



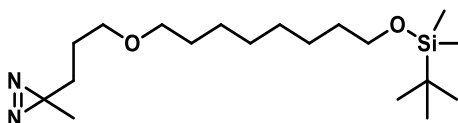
8-((*Tert*-butyldimethylsilyl)oxy)octan-1-ol (7): In a 1 l flask, equipped with a magnetic stirrer and rubber septum, 1,8-octanediol **6** (8.78 g, 60.0 mmol) was dissolved in dry THF (140 ml). NaH (1 g, 25.0 mmol, 60% in immersion oil) was added at 0 °C. The reaction mixture was stirred under argon atmosphere for 30 min at 0 °C and additionally 2.5 h at ambient temperature. TBDMSCl (3.01 g, 20.0 mmol) was dissolved in dry THF (100 ml) and added dropwise. The resulting solution was stirred at ambient temperature for 16 h, poured into water and extracted with Et₂O (4 x 80 ml). The combined organic phases were dried over MgSO₄ and concentrated under reduced pressure. The resulting oil was subjected to column chromatography on silica gel (eluent: cyclohexane/EtOAc 10:1) to give the product as colorless oil (4.42 g, 85 %).

^1H NMR (500 MHz, CDCl_3) δ 3.61 (dt, $J = 19.8, 6.6$ Hz, 4H), 1.60 – 1.47 (m, 4H), 1.40 – 1.28 (m, 10H), 0.89 (s, 9H), 0.04 (s, 6H). ^{13}C NMR (126 MHz, CDCl_3) δ 63.3, 63.1, 32.8, 32.8, 29.4, 29.4, 26.0, 25.7, 25.7, 18.4, -5.3. HRMS: $[\text{M}+\text{H}]^+$ calc. 261.22443, found 261.22473.



8-((*Tert*-butyldimethylsilyl)oxy)octyl methanesulfonate (8): In a 250 ml flask, equipped with a magnetic stirrer and a rubber septum, the monoprotected alcohol **7** (2.00 g, 7.68 mmol) was dissolved in dry DCM (50 ml) and dry Et_3N (3.0 ml, 21.44 mmol) was added. The reaction mixture was stirred for 20 min, methanesulfonyl chloride (1.5 ml, 19.43 mmol) was added and the stirring was continued for additional 2 h at 0 °C. The reaction was quenched by the addition of water and the reaction mixture was poured into water/ Et_2O (1:1, 60 ml). The phases were separated and the solvent of the organic phase was removed under reduced pressure. The residue was redissolved in Et_2O (40 ml) and washed with water (2 x 30 ml), saturated aqueous NaCl-solution (2 x 30 ml) and NaHCO_3 (5% aq. solution, 2 x 30 ml). The organic phase was dried over MgSO_4 and concentrated under reduced pressure. The product was obtained as colorless oil (2.52 g, 97 %).

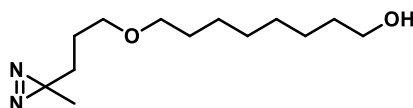
^1H NMR (500 MHz, CDCl_3) δ 4.21 (t, $J = 6.6$ Hz, 2H), 3.59 (t, $J = 6.6$ Hz, 2H), 2.99 (s, 3H), 1.78 – 1.70 (m, 2H), 1.49 (m, $J = 13.3, 6.6$ Hz, 2H), 1.38 (m, $J = 13.7, 6.3$ Hz, 2H), 1.31 (s, 6H), 0.88 (s, 9H), 0.04 (s, 6H). ^{13}C NMR (126 MHz, CDCl_3) δ 70.1, 63.2, 37.3, 32.8, 29.2, 29.1, 29.0, 26.0, 25.7, 25.3, 18.3, -5.3. HRMS: $[\text{M}+\text{H}]^+$ calc. 339.20198, found 339.20358.



3-(3-((8-((*Tert*-butyldimethylsilyl)oxy)octyl)oxy)propyl)-3-methyl-3H-diazirine (9): In a 100 ml flask, equipped with a magnetic stirrer and a reflux condenser, the alcohol **5** (675 mg, 5.91 mmol) was dissolved in dry 1,4-dioxane (25 ml) and KH in paraffin^[92] (616 mg, 7.68 mmol) was added to the ice-cold mixture. The resulting mixture was stirred for 60 min at 0 °C. The mesylated alcohol **8** (2.00 g, 5.91 mmol) was dissolved in dry 1,4-dioxane (5 ml) and added dropwise to the ice-cold mixture. The reaction mixture was refluxed for 1 h, cooled to 0 °C and then quenched by slow addition of methanol (5 ml) and ice. The product was extracted with Et_2O (3 x 30 ml). The combined organic phases were dried over MgSO_4 and

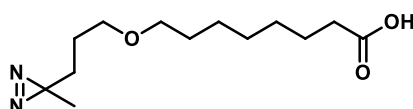
concentrated under reduced pressure. The residue was purified by column chromatography on silica gel (eluent: cyclohexane/EtOAc 80:1), to furnish a colorless oil (728 mg, 35 %).

^1H NMR (400 MHz, CDCl_3) δ 3.59 (t, J = 6.5 Hz, 2H), 3.39 – 3.31 (m, 4H), 1.62 – 1.46 (m, 4H), 1.46 – 1.37 (m, 4H), 1.30 (s, 8H), 1.01 (s, J = 0.5 Hz, 3H), 0.89 (s, 9H), 0.04 (s, 6H). ^{13}C NMR (101 MHz, CDCl_3) δ 71.0, 69.7, 63.3, 32.9, 31.1, 29.7, 29.5, 29.4, 26.1, 26.0, 25.8, 25.6, 24.3, 19.8, 18.4, -5.3. HRMS: $[\text{M}+\text{H}]^+$ calc. 357.29318, found 357.29405.



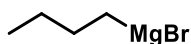
8-(3-(3-Methyl-3H-diazirin-3-yl)propoxy)octan-1-ol (10): In a 25 ml flask, equipped with a magnetic stirrer and a rubber septum, the TBDMS-protected alcohol **9** (220.0 mg, 0.62 mmol) was dissolved in dry THF (4 ml) and TBAF (0.74 ml, 0.74 mmol, 1 M in THF) was slowly added. The reaction mixture was stirred for 2 h at ambient temperature, poured into water (10 ml) and extracted with Et_2O (3 x 10 ml). The combined organic phase was dried over MgSO_4 and concentrated under reduced pressure. Column chromatography on silica gel (eluent: cyclohexane/EtOAc 8:1) furnished the product (117 mg, 78 %).

^1H NMR (400 MHz, CDCl_3) δ 3.64 (t, J = 6.6 Hz, 2H), 3.36 (td, J = 6.4, 4.3 Hz, 4H), 1.61 – 1.49 (m, 4H), 1.49 – 1.38 (m, 6H), 1.31 (s, 7H), 1.01 (d, J = 0.6 Hz, 3H). ^{13}C NMR (101 MHz, CDCl_3) δ 71.0, 69.7, 63.0, 32.8, 31.0, 29.7, 29.4, 29.3, 26.1, 25.7, 25.6, 24.3, 19.8. HRMS: $[\text{M}+\text{H}]^+$ calc. 243.2067, found 243.206.

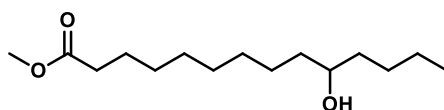


Pacman-1 (1): In a 100 ml flask, equipped with a magnetic stirrer and a rubber septum the alcohol **1** (175.0 mg, 0.72 mmol) was dissolved in DCM (15 ml). TEMPO (45 mg, 0.29 mmol) was added to the ice-cold reaction mixture, followed by a mixture of NaBr (11 mg, 0.11 mmol), TBAB (12 mg, 0.04 mmol), NaHCO_3 (sat. aq. solution, 4.7 ml), NaClO (2.7 ml, 2.16 mmol) and water (2.8 ml). The mixture was stirred at 0 °C for 2 h, quenched with MeOH (5 ml) and the pH was adjusted to 11 by addition of sat. aq. solution of NaHCO_3 . The reaction mixture was extracted with Et_2O (3 x 20 ml), the water phase was acidified to pH=1 with 1 M HCl (aq.) and again extracted with Et_2O (3 x 25 ml). The combined organic phases of the second extraction were dried over MgSO_4 and concentrated under reduced pressure. The product was obtained as colorless oil and used for the next step without further purification. (124 mg, 67%).

^1H NMR (400 MHz, CDCl_3) δ 3.36 (td, $J = 6.4, 4.4$ Hz, 4H), 2.34 (t, $J = 7.5$ Hz, 2H), 1.69 – 1.58 (m, 2H), 1.58 – 1.49 (m, 2H), 1.45 – 1.37 (m, 4H), 1.32 (s, 6H), 1.00 (s, 3H). ^{13}C NMR (101 MHz, CDCl_3) δ 179.62, 70.88, 69.75, 33.95, 31.01, 29.56, 29.02, 28.95, 25.92, 25.60, 24.58, 24.26, 19.80. HRMS: $[\text{M}+\text{H}]^+$ calc. 257.1860, found 257.1847.

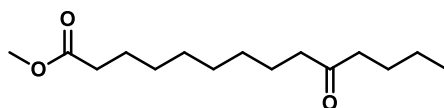


Butylmagnesium bromide (12): A two-neck flask, equipped with a condenser and addition funnel was charged with magnesium turnings (2.263 g, 93.13 mmol). The magnesium turnings were covered with THF. A mixture of 1-bromobutane **11** (5.000 ml, 46.56 mmol) in THF was placed in the addition funnel. Several drops of the mixture were added to the magnesium turnings and the mixture was gently heated with the fan until gentle reflux was achieved. The remaining amount of **11** was added at such a rate to maintain a gentle reflux. Subsequently the mixture was stirred for another 3.5 h. The total volume of THF was 20 ml. By titration of a solution of salicylaldehyde phenylhydrazone with the Grignard reagent, the concentration of butylmagnesium bromide (1.65 mM) was determined.



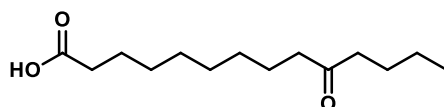
Methyl 10-hydroxytetradecanoate (14): A solution of methyl 9-formylnonanoate **13** (1.501 ml, 7.27 mmol) in THF (45 ml) was cooled to -78 °C and butylmagnesium bromide **12** in THF (0.45 M, 4.544 ml, 7.27 mmol) was added dropwise. The reaction mixture was stirred at -78 °C for 5 h, quenched with saturated NH_4Cl solution and extracted with Et_2O (3 x 50 ml). The combined organic phases were washed with saturated NH_4Cl solution and the solvent was removed under reduced pressure. The crude residue was redissolved in diethylether (20 ml) and an aqueous saturated NaHSO_3 -solution (20 ml) was added. The mixture was stirred at the ambient temperature for 18 h and the precipitate was removed by filtration. Subsequently the phases were separated and the organic phase was dried over MgSO_4 . The solvent was removed under reduced pressure and the product was obtained by column chromatography on silica gel (cyclohexane/ EtOAc) in 45% yield.

^1H NMR (400 MHz, CDCl_3) δ 3.66 (s, 2H), 3.61 – 3.49 (m, 1H), 2.29 (t, $J = 7.5$ Hz, 2H), 1.69 – 1.56 (m, 2H), 1.51 – 1.37 (m, 6H), 1.35 – 1.22 (m, 11H), 0.90 (t, $J = 7.0$ Hz, 3H). ^{13}C NMR (101 MHz, CDCl_3) δ 174.29, 71.96, 51.41, 37.45, 37.18, 34.09, 29.60, 29.38, 29.16, 29.10, 27.83, 25.59, 24.92, 22.75, 14.05. HRMS: $[\text{M}+\text{H}]^+$ calc. 259.22677, found 295.22701.



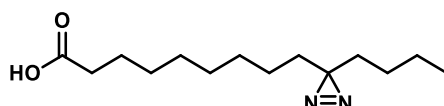
Methyl 10-oxotetradecanoate (15): Methyl 10-hydroxytetradecanoate **14** (1.00 g, 3.87 mmol) was dissolved in freshly distilled dry DCM (38 ml) and DMP (1.65 g, 3.95 mmol) was added. After 18 h stirring at the ambient temperature the reaction was quenched with saturated aqueous sodium thiosulfate solution and saturated aqueous sodium hydrogen carbonate solution. The reaction mixture was extracted with DCM, dried over MgSO₄ and the solvent was removed under reduced pressure. The pure product was obtained by column chromatography on silica gel (eluent: cyclohexane/EtOAc 10:1) in 97% yield (965.0 mg).

¹H NMR (400 MHz, CDCl₃) δ 3.66 (s, 3H), 2.38 (td, J = 7.5, 2.1 Hz, 4H), 2.29 (t, J = 7.5 Hz, 2H), 1.68 – 1.47 (m, 6H), 1.38 – 1.22 (m, 10H), 0.90 (t, J = 7.3 Hz, 3H). ¹³C NMR (101 MHz, CDCl₃) δ 211.57, 174.26, 51.42, 42.75, 42.52, 34.07, 29.19, 29.17, 29.05, 25.99, 24.90, 23.81, 22.37, 13.84. HRMS: [M+H]⁺ calc. 257.2111, found 257.2116.



10-oxotetradecanoic acid (16): Methyl 10-oxotetradecanoate **15** (500.0 mg, 1.95 mmol) was dissolved in 1,4-dioxane (3.3 ml) and LiOH (2 M, 1.1 ml, 2.24 mmol) was added. The reaction mixture was stirred at the ambient temperature for 3 h at 80 °C. The reaction was quenched with 0.5 M HCl and the mixture was extracted with EtOAc. Subsequently, the combined organic phases were dried over MgSO₄ and the solvent was removed under reduced pressure. The desired product was purified by column chromatography on silica and obtained in 97 % (457.0 mg) yield.

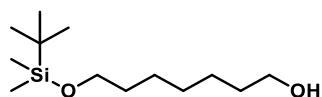
¹H NMR (400 MHz, CDCl₃) δ 2.44 – 2.29 (m, 6H), 1.68 – 1.50 (m, 6H), 1.39 – 1.24 (m, 10H), 0.90 (t, J = 7.3 Hz, 3H). ¹³C NMR (101 MHz, CDCl₃) δ 211.70, 179.47, 42.75, 42.53, 33.92, 29.16, 29.03, 28.96, 25.99, 24.62, 23.81, 22.37, 13.84.



Pacman-2 (2): To a solution of 10-oxotetradecanoic acid **16** (440.0 mg, 1.82 mmol) in methanol (1.3 ml) was added ammonia in methanol (7 N, 27.0 ml) at 0 °C under argon. The reaction mixture was stirred at 0 °C for 4 h and hydroxylamine-*O*-sulfonic acid (410.67 mg,

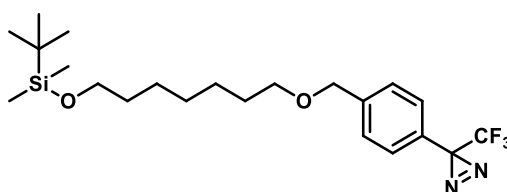
3.63 mmol) in methanol (6.5 ml) was added dropwise. The solution was allowed to warm up to the ambient temperature and stirred for 16 h. The white precipitate was removed by filtration and the solvent was removed under reduced pressure. The residue was re-dissolved in methanol and Et₃N (0.6 ml, 3.99 mmol) was added. A solution of iodine (506.9 mg, 2.00 mmol) in methanol (6.5 ml) was added dropwise until the reaction mixture maintained a red-brown color. The reaction was quenched with sat. sodium sulfite solution and extracted with DCM. The combined organic phases were dried over MgSO₄ and concentrated under reduced pressure. Purification by column chromatography on silica gel (DCM + 0.1% AcOH to DCM/EtOAc 15:1 + 0.1% AcOH) provided the desired product in 23% yield (109.0 mg).

¹H NMR (400 MHz, CDCl₃) δ 2.34 (t, *J* = 7.5 Hz, 2H), 1.62 (p, *J* = 7.4 Hz, 2H), 1.37 – 1.20 (m, 14H), 1.13 – 1.02 (m, 4H), 0.88 – 0.83 (m, 3H). ¹³C NMR (101 MHz, CDCl₃) δ 179.90, 33.98, 32.89, 32.63, 29.15, 29.12, 29.05, 28.95, 25.98, 24.61, 23.79, 22.32, 13.83. MS: [M-H]⁻: calc. 253.2, found 253.0.



7-((*Tert*-butyldimethylsilyl)oxy)heptan-1-ol (18): In a 500 ml flask, equipped with a magnetic stirrer and rubber septum, 1,7-heptanediol **17** (6.96 ml, 50 mmol) was dissolved in dry THF (120 ml). At 0 °C NaH (2 g, 50 mmol, 60% in immersion oil) was added. The reaction mixture was stirred under argon atmosphere for 30 min at 0 °C and additionally 2.5 h at ambient temperature. TBDMSCl (6.02 g, 40 mmol) was dissolved in dry THF (60 ml) and added dropwise to the reaction mixture. The solution was stirred at ambient temperature for 16 h, poured into water and extracted with Et₂O (4 x 75 ml). The combined organic phases were dried over MgSO₄ and concentrated under reduced pressure. The resulting oil was subjected to column chromatography on silica gel (eluent: cyclohexane/EtOAc 4:1) to give the product as colorless oil (4.63 g, 47%).

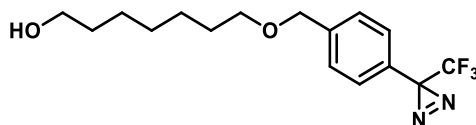
¹H NMR (400 MHz, CDCl₃) δ 3.61 (dt, *J* = 15.2, 6.6 Hz, 4H), 1.60 – 1.47 (m, 4H), 1.33 (s, 6H), 0.89 (s, 9H), 0.04 (s, 6H). ¹³C NMR (126 MHz, CDCl₃): δ 63.7, 63.5, 33.3, 33.2, 29.7, 26.5, 26.3, 26.2, 18.2, -4.8. HRMS: [M+H]⁺ calc. 247.20878, found 247.20983.



3-(4-(((7-((*Tert*-butyldimethylsilyl)oxy)heptyl)oxy)methyl)phenyl)-3-(trifluoromethyl)-

3H-diazirine (19): In a 100 ml flask, equipped with a magnetic stirrer and rubber septum alcohol **18** (471.0 mg, 1.91 mmol) was dissolved in dry THF (25 ml). At 0 °C NaH (114.8 mg, 2.87 mmol, 60% in immersion oil) was added. The reaction mixture was stirred at 0 °C for 30 min and 4-(3-(trifluoromethyl)-3H-diazirine-3-yl)benzyl bromide (800.0 mg, 2.87 mmol) was added. The resulting mixture was stirred at 35 °C for 16 h. The reaction mixture was diluted with water, extracted with EtOAc (3 x 25 ml) and dried over MgSO₄. The solvent was removed under reduced pressure and the resulting oil was subjected to column chromatography on silica gel (eluent: cyclohexane/EtOAc 8:1) to give the product as a yellow oil (602 mg, 71 %).

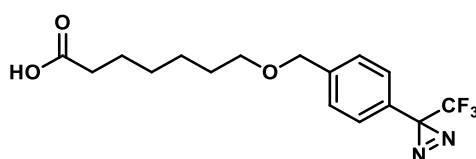
¹H NMR (500 MHz, CDCl₃) δ 7.37 (d, *J* = 8.4 Hz, 2H), 7.17 (d, *J* = 8.0 Hz, 2H), 4.50 (s, 2H), 3.59 (t, *J* = 6.6 Hz, 2H), 3.46 (t, *J* = 6.6 Hz, 2H), 1.65 – 1.56 (m, 2H), 1.54 – 1.46 (m, 2H), 1.40 – 1.29 (m, 6H), 0.89 (s, 9H), 0.04 (s, 6H). ¹³C NMR (126 MHz, CDCl₃) δ 140.8, 128.3, 127.9, 126.7, 72.2, 71.0, 63.4, 33.0, 29.8, 29.42, 26.3, 26.1, 25.9, -5.1. ¹⁹F NMR (282 MHz, CDCl₃) δ -64.46, HRMS: [M+H]⁺ calc. 445.24927, found 445.24949.



7-((4-(3-(Trifluoromethyl)-3H-diazirin-3-yl)benzyl)oxy)heptan-1-ol (20): In a 25 ml flask, equipped with a magnetic stirrer and rubber septum, the TBDMS-protected alcohol **19** (950.0 mg, 2.14 mmol) was dissolved in dry THF (10 ml) and TBAF (2.6 ml, 2.60 mmol, 1 M in THF) was added. The reaction mixture was stirred for 2 h at ambient temperature, poured into water and extracted with Et₂O (3 x 10 ml). The combined organic phases were dried over MgSO₄ and concentrated under reduced pressure. Crude product was purified by column chromatography on silica gel (eluent: cyclohexane/EtOAc 2:1) to yield the pure product as an oil (502 mg, 71%).

Optimized synthesis route: KH in paraffin (646 mg, 8.06 mmol) was slowly added to an ice-cold mixture of 1,7-heptanediol **17** (2.24 ml, 16.13 mmol) in dry 1,4-dioxane (70 ml). Subsequently the reaction mixture was stirred for 60 min at 0 °C. 4-[3-(Trifluoromethyl)-3H-diazirin-3-yl]benzyl bromide (1.50 g, 5.38 mmol) was dissolved in dry 1,4-dioxane (10 ml) and added dropwise to the ice-cold mixture. After 1 h at reflux the reaction mixture was cooled to 0 °C and then quenched by slow addition of methanol (10 ml) and ice. The product was

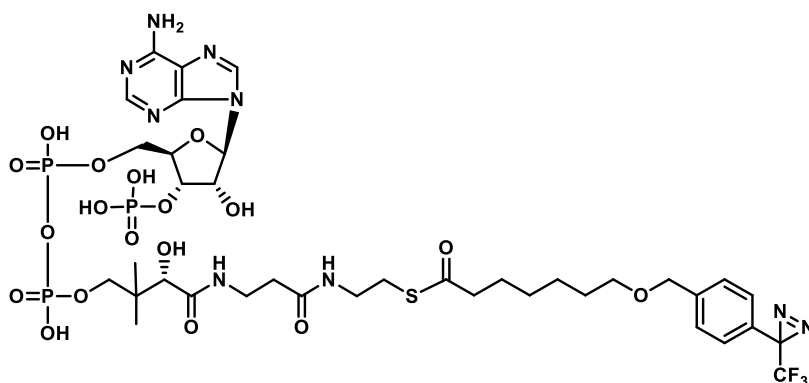
extracted with Et₂O (3 x 50 ml). The combined organic phases were dried over MgSO₄ and concentrated under reduced pressure. The desired product was obtained after purification by column chromatography on silica gel (eluent: cyclohexane/EtOAc 2:1) in 64% yield (1.17 g). ¹H NMR (500 MHz, CDCl₃) δ 7.36 (d, *J* = 8.5 Hz, 2H), 7.17 (d, *J* = 8.1 Hz, 2H), 4.50 (s, 2H), 3.63 (t, *J* = 6.6 Hz, 2H), 3.46 (t, *J* = 6.6 Hz, 2H), 1.66 – 1.52 (m, 4H), 1.42 – 1.30 (m, 7H). ¹³C NMR (126 MHz, CDCl₃) δ 140.8, 128.3, 127.9, 126.7, 72.2, 70.9, 63.2, 32.9, 29.8, 29.4, 26.3, 25.8. ¹⁹F NMR (282 MHz, CDCl₃) δ -64.46. HRMS: [M+H]⁺ calc. 331.16279, found 331.16323.



Pacman-3 (3): In a 250 ml flask, equipped with a magnetic stirrer and a rubber septum, the alcohol **20** (450.0 mg, 1.36 mmol) was dissolved in DCM (45 ml). TEMPO (85.0 mg, 0.54 mmol) was added to the ice-cold reaction mixture, followed by a mixture of NaBr (21.0 mg, 0.2 mmol), TBAB (21.9 mg, 0.07 mmol), NaHCO₃ (sat. aq, 9.2 ml), NaOCl (5.1 ml, 4.08 mmol) and water (4.5 ml). The resulting mixture was stirred at 0 °C for 4 h, quenched with MeOH (1 ml), acidified to pH=4 with 1 M HCl (aq) and extracted with EtOAc (3 x 50 ml). The combined organic phases were dried over MgSO₄ and concentrated under reduced pressure. The crude product was purified by column chromatography on silica gel (eluent: cyclohexane/EtOAc 1:1) to furnish a colorless oil (254 mg, 54 %).

Optimized synthesis route: 2,2,6,6-tetramethyl-1-piperidinyloxy (22.00 mg, 140,80 μmol) was added to a solution of 7-((4-(3-(trifluoromethyl)-3H-diazirin-3-yl)benzyl)oxy)heptan-1-ol **20** (1.100 g, 3.33 mmol) in DCM (110 ml) at 0 °C. Subsequently a mixture of sodium bromide (49.50 mg, 481,08 μmol), tetrabutylammonium bromide (55,000 mg, 170,61 μmol), NaHCO₃ sat. (aq, 24 ml), sodium hypochlorite (7.70 ml, 9.99 mmol) and water (12 ml) was prepared and added dropwise. The mixture was stirred at 0 °C for 4 h, quenched with MeOH (10 ml) and acidified to pH 4 with 1.0 M HCl (aq). The carboxylic acid was extracted with ethyl acetate (3x 80 ml), the combined organic phases were dried over MgSO₄ and concentrated under reduced pressure. The desired product (746.00 mg, 2,17 mmol) was obtained without further purification in 65 % yield.

^1H NMR (600 MHz, CDCl_3) δ 7.36 (d, $J = 8.2$ Hz, 2H), 7.17 (d, $J = 8.1$ Hz, 2H), 4.50 (s, 2H), 3.46 (t, $J = 6.5$ Hz, 2H), 2.35 (t, $J = 7.5$ Hz, 2H), 1.67 – 1.59 (m, 4H), 1.43 – 1.32 (m, 4H). ^{13}C NMR (151 MHz, CDCl_3) δ 180.0, 140.7, 128.3, 127.9, 126.7, 72.2, 70.7, 34.1, 29.6, 29.0, 26.0, 24.7. ^{19}F NMR (188 MHz, CDCl_3) δ -65.69. HRMS: $[\text{M}+\text{H}]^+$ calc. 345.14205, found 345.14230.



Pacman-3-Coenzyme A (40): Pacman-3 **3** (10,000 mg, 0,03 mmol) was dissolved in THF (2 ml) and a solution of PyBOP (44,582 mg, 0,06 mmol) and DIPEA (40,471 μl , 0,23 mmol) was added dropwise, followed by an aqueous solution of coenzyme A free acid trihydrate **39** (44,582 mg, 0,06 mmol, 2 ml). After stirring for 5 h at ambient temperature the reaction mixture was lyophilized and the crude product purified by reverse phase HPLC with a gradient of H_2O (10 mM NH_4OAc) and MeOH (10 mM NH_4OAc). The solvent was removed under reduced pressure. Traces of water were removed by lyophilization to provide Pacman-3-CoA (8,620 mg, 0,01 mmol) as a white solid in 27% yield.

HRMS: $[\text{M}+\text{H}]^+$ calc. 1094.24670, found 1094.24595.

4.2.1. General methods in solid phase peptide synthesis (SPPS)

Solid phase peptide synthesis was carried out on commercially available Rink-Amide-MBHA resin (resin loading 0.59 mmol/g) at 0.1 mmol or 0.25 mmol scale, using a CEM-Liberty peptide synthesizer equipped with a CEM-Discover microwave. Cleavage of the Fmoc-group was performed with piperidine in DMF (20% v/v) for 1 min at 30 °C (intensity = 40 W) and 5 min at 70 °C (intensity = 40 W). In between deprotection and the coupling the resin was washed with DMF and DCM (1 ml solvent per 100 mg resin). The amino acids (4 eq., 0.2 M) were coupled with a mixture of HCTU (4 eq.) and DIPEA (8 eq.) for 10 min at 80 °C (intensity = 20 W). For each amino acid the coupling step was performed twice. After completion of the

peptide sequence, the resin was washed with DCM (5 x 5 ml), DMF (5 x 5 ml) and again with DCM (5 x 5 ml).

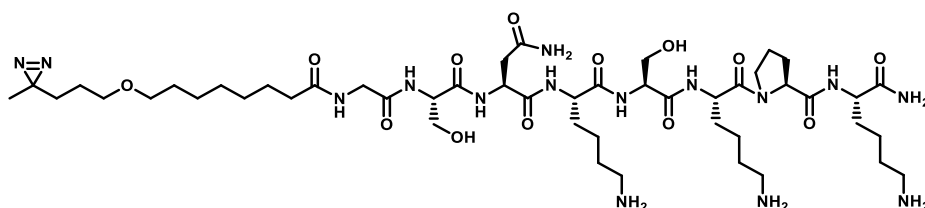
4.2.1.1. Test-cleavage

To confirm completion of the respective synthesis steps a small amount of the resin bound peptide was treated with a solution of TFA/H₂O/TES (95:2.5:2.5) (1 ml) for 1 h at ambient temperature. The solution was evaporated under a stream of argon and the resulting residue was analyzed by LC-MS.

4.2.1.2. N-terminal attachment of Pacman

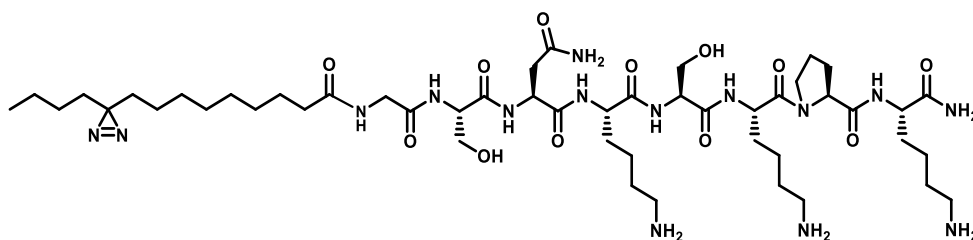
The resin-bound peptide was swollen in DMF (2 ml, over 30 min). The Fmoc-group was deprotected by the treatment of the resin with a solution of piperidine in DMF (20% v/v, 1 ml) for 30 min at ambient temperature. The resin was washed with DMF (5 x 2 ml) and the deprotection step was repeated. The resin was washed with DMF (5 x 2 ml). The myristoyl analogue **1**, **2** or **3** (3 eq), HCTU (3 eq) and DIPEA (6 eq) were dissolved in DMF (0.5 ml) and the resin was shaken with the resulting mixture in darkness for 16 h at ambient temperature. The resin was washed with DMF (5 x 1 ml), DCM (5 x 1 ml) and again with DMF (5 x 1 ml).

Pacman-1-Src (**21a**):



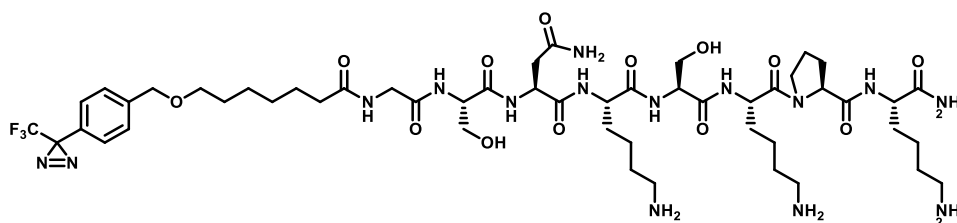
HRMS: [M+H]⁺ calc. 1082.666805, found 1082.67166.

Pacman-2-Src (**22a**):



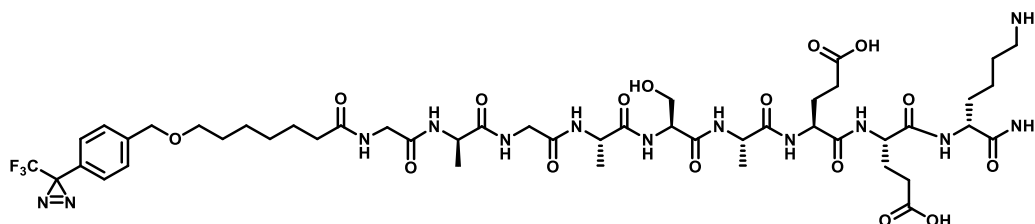
HRMS: $[M+H]^+$ calc. 1080.688879, found 1080.69307

Pacman-3-Src (**23a**):



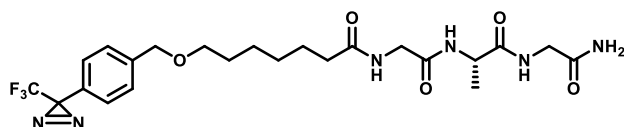
HRMS: $[M+H]^+$ calc. 1170.62414, found 1770.62627

Pacman-3-Gnat (**24a**):



HRMS: $[M+H]^+$ calc. 1144.52448, found 1144.51991

Pacman-3-shGnat (**25**):



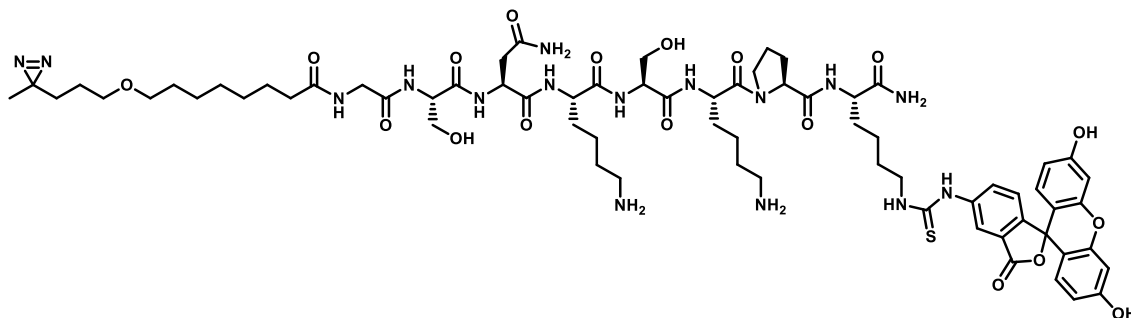
HRMS: $[M+H]^+$ calc. 529.2391, found 529.2379

4.2.1.3. FITC labeling

The Mtt-group was removed by treating the resin bound peptide with a solution of HFIP/DCM (1:4) (1 ml) for 20 min at ambient temperature. Mtt-deprotection was performed four times. The resin was washed with DCM (5 x 1 ml), DMF (5 x 1 ml) and DCM (5 x 1 ml).

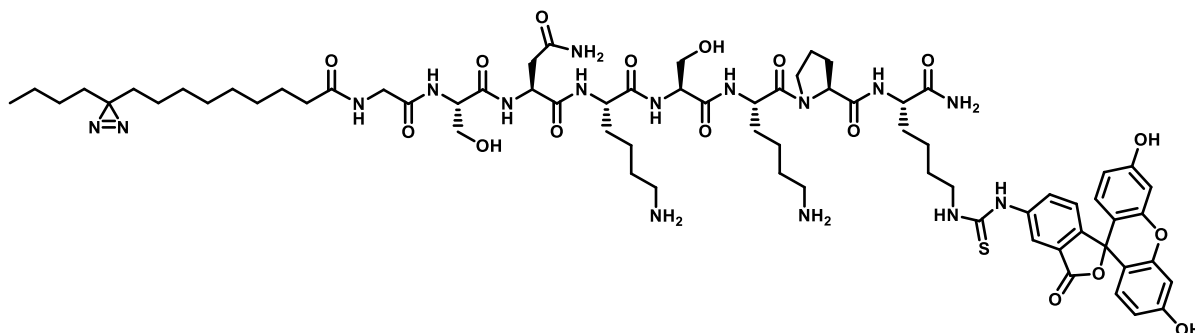
Subsequently, the resin was shaken with a solution of FITC (5 eq) and DIPEA (5 eq) in DMF (0.5 ml) for 4 h at ambient temperature. The resin was washed with DCM (5 x 1 ml), DMF (5 x 1 ml) and DCM (5 x 1 ml). The coupling step was performed an additional time over 16 h.

FITC labeled Pacman-1-Src (**21b**):



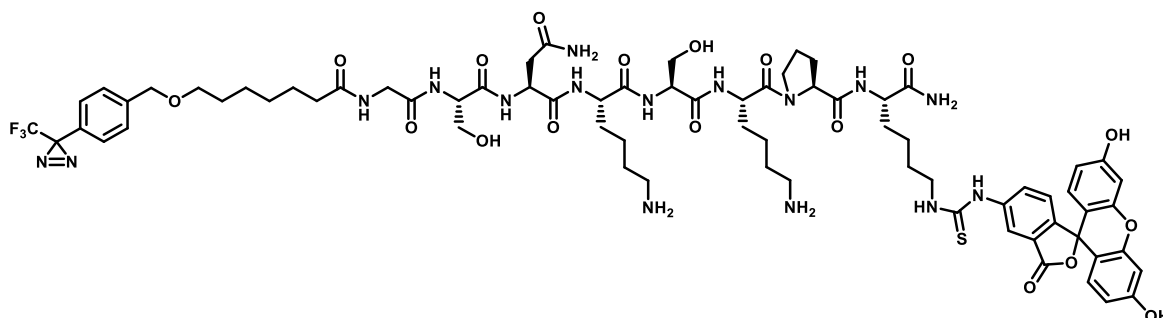
HRMS: $[M+2H]^{2+}$ calc. 736.35556, found 736.35738

FITC labeled Pacman-2-Src (**22b**):



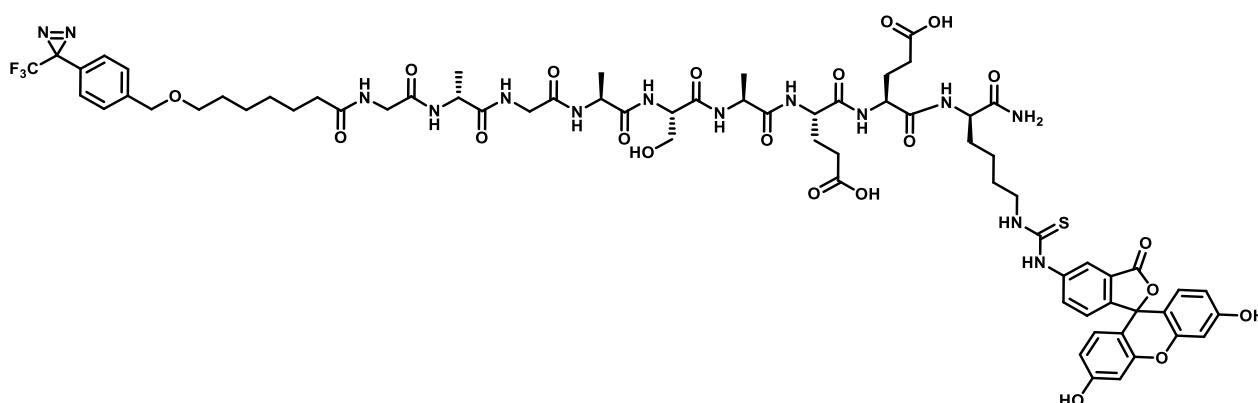
MS: $[M+H]^+$ calc.1470.73, found 1470.72

FITC labeled Pacman-3-Src (**23b**):



HRMS: $[M+H]^+$ calc.1559.6599, found 1559.6628

FITC labeled Pacman-3-Gnat (**24b**):



HRMS: $[M+H]^+$ calc.1533.56026, found 1533.55555

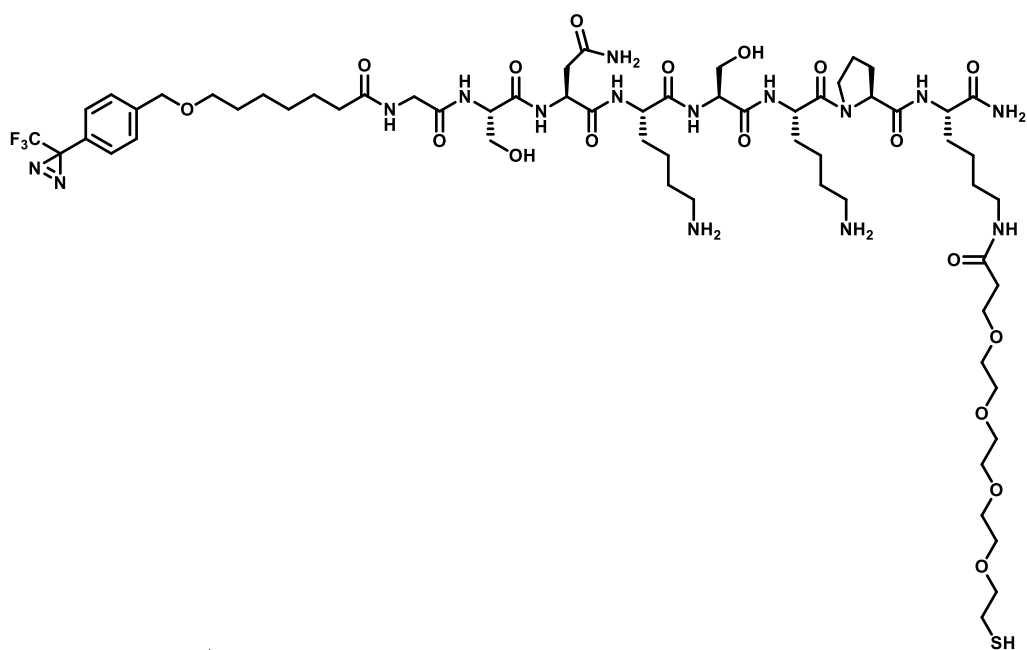
4.2.1.4. N-terminal acetylation of negative pulldown probes

The resin-bound peptide was swollen in DCM (1 ml, over 30 min). The Fmoc-group was removed by treatment of the resin with a solution of piperidine in DMF (20% v/v, 1 ml) for 30 min at ambient temperature. The resin was washed with DMF (5 x 2 ml), the deprotection step was repeated and the resin was washed with DMF (5 x 2 ml) again. Acetic anhydride (250 μ l) and DIPEA (250 μ l) were dissolved in DMF (2 ml) and the resin was shaken with the resulting mixture for 4 h at the ambient temperature. The resin was washed with DMF (5 x 1 ml), DCM (5 x 1 ml) and again with DMF (5 x 1 ml). The coupling step was carried out a second time over 16 h and the peptide was used for further ligation with the desired linker.

4.2.1.5. Linker coupling

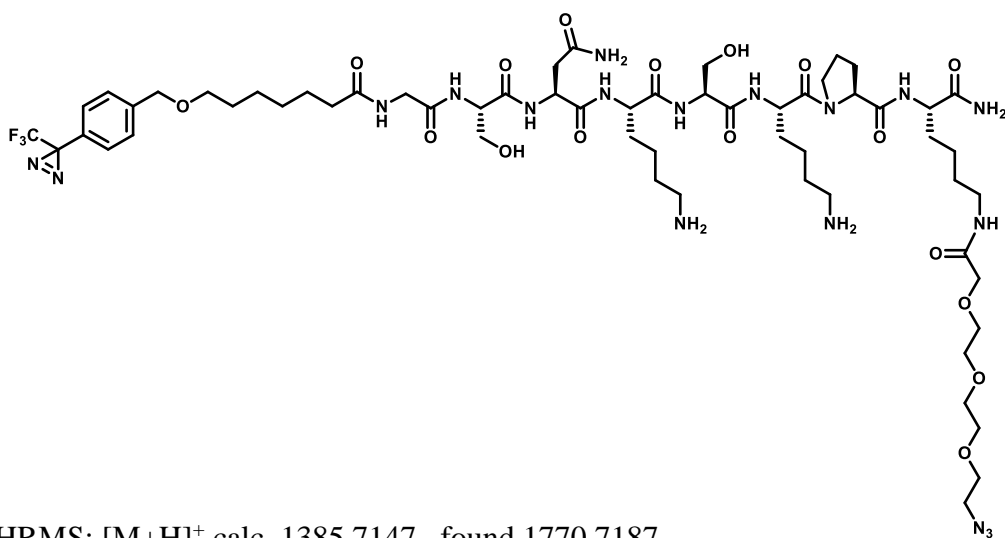
The Mtt-group was removed by treating the resin bound peptide with a solution of HFIP/DCM (1:4) (1 ml) for 20 min at ambient temperature. Mtt-deprotection was performed four times. The resin was washed with DCM (5 x 1 ml), DMF (5 x 1 ml) and DCM (5 x 1 ml). Subsequently, the resin was shaken with a solution of the respective linker (4 eq), COMU (4 eq), oxima (4 eq) and DIPEA (8 eq) in DMF (0.5 ml) for 4 h at ambient temperature. The resin was washed with DCM (5 x 1 ml), DMF (5 x 1 ml) and DCM (5 x 1 ml). The coupling step was performed an additional time over 16 h.

Affinity enrichment probe Pacman-3-Src (**30a**):



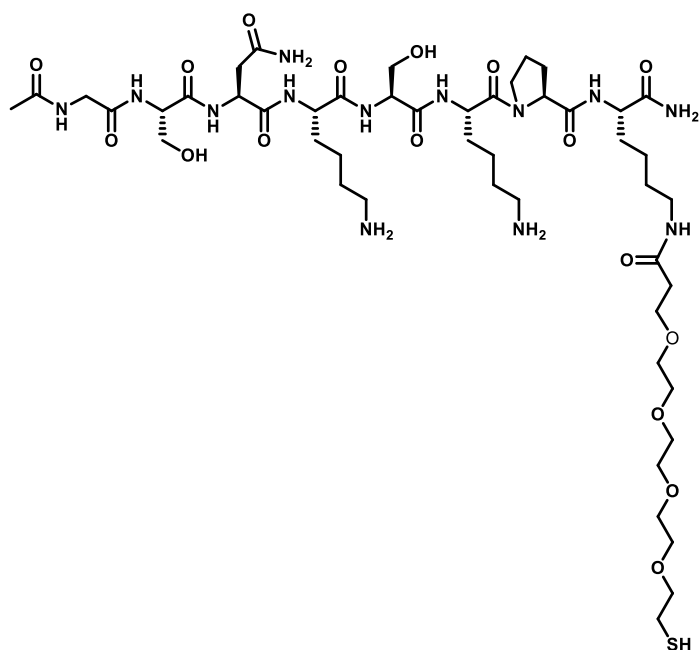
HRMS: $[M+H]^+$ calc. 1434.7273, found 1434.7289

Affinity enrichment probes Pacman-3-Src (**34a**):



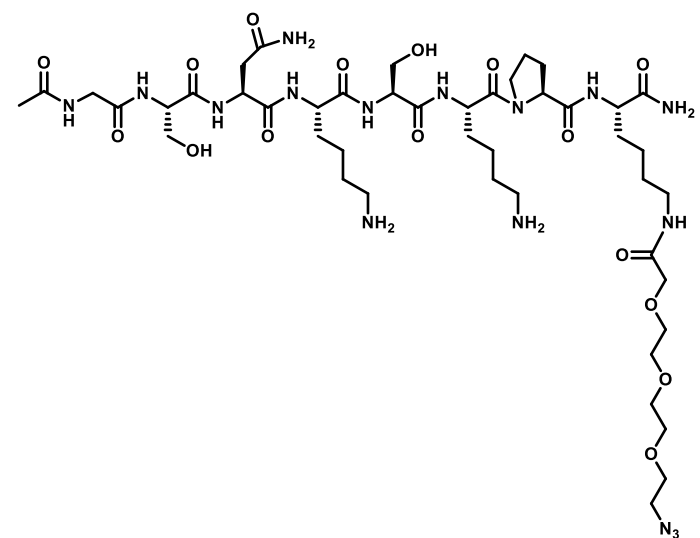
HRMS: $[M+H]^+$ calc. 1385.7147, found 1770.7187

Affinity enrichment probes acetylated Src (**30b**):



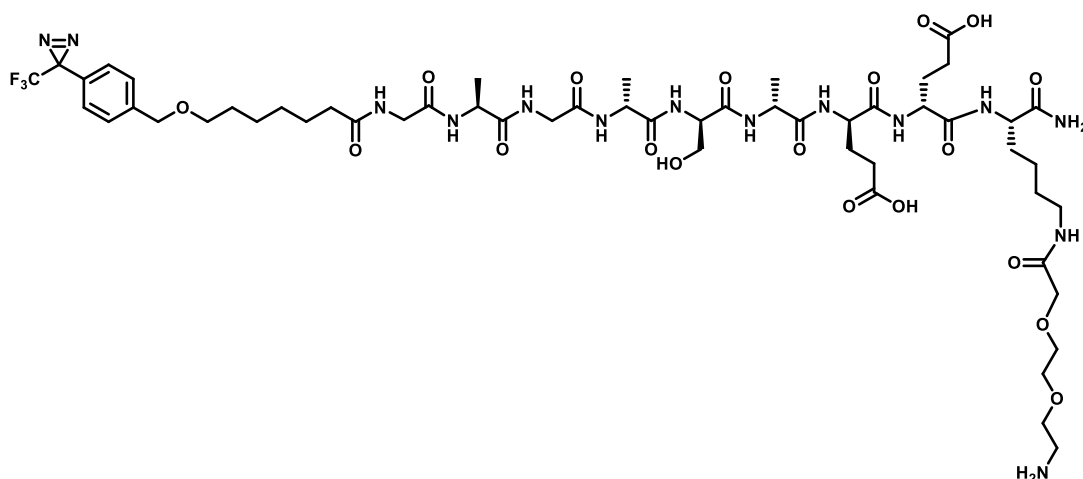
HRMS: $[M+H]^+$ calc. 1150.6146 , found 1150.6136

Affinity enrichment probes acetylated Src (**34b**):



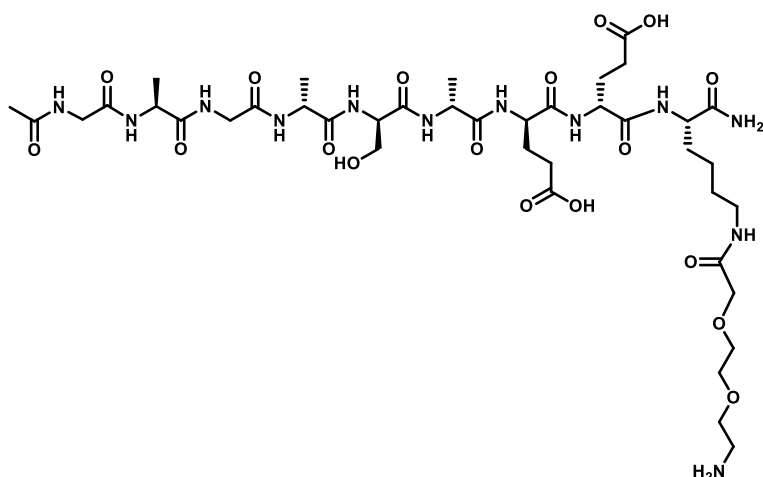
HRMS: $[M+H]^+$ calc. 1101.6011 , found 1101.5990

Affinity enrichment probe Pacman-3-Gnat (**38a**):



HRMS: [M+H]⁺ calc. 1289.5984 , found 1289.6002

Affinity enrichment probe acetylated Gnat (**38b**):



HRMS: [M+H]⁺ calc. 1005.4847 , found 1005.4861

4.2.1.6. Final deprotection and cleavage from the resin

The peptides were fully deprotected and cleaved from the resin by treating the resin with a solution of TFA/H₂O/TES (95:2.5:2.5) (3 ml) for 3 h at ambient temperature. The resin was washed with DCM (5 x 2 ml), DCM/MeOH (1:1, 5 x 2 ml) and MeOH (5 x 2 ml). To the combined filtrate toluene was added and the resulting solution was concentrated under reduced pressure. The resulting residue was co-evaporated with toluene (3 x 5 ml), purified by preparative HPLC and characterized by HRMS.

4.3. Materials for biological experiments

4.3.1. Buffers and Solutions

Name	Composition
Alkylation solution	50 mM chloracetamide in reducing buffer
CPM buffer A	2.5 mM potassium dihydrogen phosphate, 17.5 mM sodium hydrogen phosphate, 0.5 mM EDTA, 0.1% Triton X-100, 1% DMSO, pH 7.90-7.95
CPM buffer B	CPM buffer A with 5% DMSO
Crystallization buffer	25 mM Tris, 50 mM NaCl, 3 mM DTE
Fixation buffer	4% formaldehyde, 2 µg/ml Hoechst (Sigma Aldrich Cat. B2261-25mg) in PBS
PBS	137 mM NaCl, 2.7 mM KCl, 10 mM Na ₂ HPO ₄ , 2.0 mM KH ₂ PO ₄ , pH 7.4
LysC digestion solution	0.5 µg/µl in H ₂ O
Mapping buffer A	50 mM Tris (pH 7.5), 1 mM DTT, 10 µM Ammonium bicarbonate, 5.5 µg Trypsin in 10 mM HCl, 2.2 M Urea
Mapping buffer B	0.5 M Iodacetamide in H ₂ O
Mitochondrial Assay Solution	220 mM Mannitol, 70 mM Sucrose, 10 mM KH ₂ PO ₄ , 5 mM MgCl ₂ , 2 mM HEPES, 1 mM EGTA, pH 7.4 at 37 °C
NHS blocking buffer A	0.5 M Ethanolamine, 0.5 M NaCl, pH 8.3
NHS blocking buffer B	0.1 M Na-Acetate, 0.5 M NaCl
NHS coupling buffer	0.15 M Triethanolaminem, 0.5 M NaCl, pH 8.3
NHS equilibration buffer	1 mM HCl
NHS lysis buffer A	PBS

Name	Composition
NHS lysis buffer B	50 mM PIPES (pH 7.4), 50 mM NaCl, 5 mM MgCl ₂ , 5 mM EGTA, 0.1% (v/v) NP40, 0.1% (v/v) Triton, 0.1% (v/v) Tween
Protein expression buffer A	20 mM Tris (pH 7.5), 300 mM NaCl, 50% (v/v) glycerol, 3 mM βME, 0.25% (v/v) Triton X-100, 0.25% (v/v) NP40, 1 mM PMSF, DNase
Protein expression buffer B	20 mM Tris (pH 7.5), 300 mM NaCl, 50% (v/v) glycerol, 3 mM βME
Stage Tip buffer A	H ₂ O with 0.1% formic acid
Stage Tip buffer B	H ₂ O/ACN 2:8 with 0.1% formic acid
SDS lysis buffer	10% v/v Glycerol, 50 mM Tris (pH 6.8), 2% w/v SDS, 100 mM DTE
SDS loading buffer (5x)	50% v/v Glycerol, 250 mM Tris (pH 6.8), 10% w/v SDS, 500 mM DTE, 360 μM bromophenol blue
SulfoLink coupling buffer	50 mM Tris pH 8.5, 25 mM TCEP
SulfoLink blocking buffer	50 mM L-cystein-HCl in coupling buffer
SulfoLink wash solution	1 M NaCl in H ₂ O
SulfoLink elution buffer	0.15 M glycine, pH 2.5
TBS	150 mM NaCl, 50 mM Tris-Cl, pH 7.6
TBS-T	TBS with 0.1% Tween
TPP alkylation buffer	375 mM iodacetamide in water
TPP buffer A	100 mM TEAB
TPP buffer B	200 mM TCEP, 0.2 mM TEAB
TPP lysis buffer	PBS (with or without 0.4% NP40)

Name	Composition
Transfer buffer	14.41 g/l glycine, 3.03 g/l Tris, 20% v/v MeOH
Tris-buffer	50 mM Tris, pH 7.5
Trypsin digestion solution	0.4 µg/µl in 10 mM HCl
Reducing buffer	8 M urea, 1 mM DTT in Tris-buffer

4.3.2. Laboratory equipment

Name	Supplier
Analytical balance BP221S	Sartorius
Analytical balance MC210P	Sartorius
Analytical balance ED224S	Sartorius
AxioVert 200M fluorescence microscope	Carl Zeiss
Bio-Link BLX365 Crosslinker	Vilber
Centrifuge 5415R	Eppendorf
Centrifuge 5424R	Eppendorf
Centrifuge 5430	Eppendorf
Centrifuge 5810R	Eppendorf
Centrifuge, Minispin	Eppendorf
Concentrator Plus SpeedVac	Eppendorf
Countess™ II Automated Cell Counter	Thermo Fisher Scientific
IncuCyte® S3	Essen BioScience
Infinite M200 Plate Reader	Tecan
Leica DM IRB inverted research microscope	Leica
MALDI-TOF/TOF-System ultrafleXtreme	Bruker
MALDI MTP 384 target plate ground steel BC	Bruker

Name	Supplier
MagRack 6	GE Healthcare Life Sciences
Mastercycler ep gradient S	Eppendorf
Mini-PROTEAN® Tetracell Electrophoresis System	Bio-Rad
Nanodrop 2000c	Thermo Scientific
NuAire NU-437-400E biosafety cabinet	ibs tecnomara
NuAire NU-440-400E biosafety cabinet	ibs tecnomara
NuAire NU-5500E incubator	IBS integra biosciences
Odyssey® Fc imaging System	LI-COR Biosciences
Peltier-cooled incubator IPP-300	memmert
pH-Meter	Mettler Toledo
Reciprocating Motion Shaker 3006	GFL
Rotator SB3	Stuart
RS-TR 5 Analog tuberoller	Phonix Instrument
Safire ² ™ Plate Reader	Tecan
Spark multimode microplate reader	Tecan
Seahorse XFp Analyzer	Agilent
Sonation Tomy mini personal	Sonation lab solutions
Sonoplus ultrasound device	Bandelin
Sonorex Super ultrasound bath	Bandelin
Thermomixer comfort 5355	Eppendorf
Ultracentrifuge Optima™ MAX-XP	Beckman Coulter
Vortex-gene 2	Scientific Industries

4.4. General biological methods

4.4.1. Mammalian cell culture

Mammalian cells were cultured at 37 °C with 5% CO₂. Work with living mammalian cells was performed in cell culture-approved benches with sterile solutions and equipment. The produced waste was sterilized by autoclaving at 134 °C for 15 min.

Jurkat cells were cultivated in RPMI 1640 medium (PAN Biotech, Cat. No.: P04-18047), supplemented with 10% fetal bovine serum (Invitrogen, Cat. No.: 10500-084), 1% sodium pyruvate (PAN Biotech, Cat. No.: P04-43100), 1% non-essential amino acids (PAN Biotech Cat. No.: P08-32100) and 1% PenStrep (PAN Biotech, Cat. No.: P06-07100). HEK cells were cultivated in DMEM medium (PAN Biotech, Cat. No.: P04-03550) supplemented with 10% fetal bovine serum, 1% sodium pyruvate and 1% non-essential amino acids. MCF7 cells were cultivated in DMEM medium supplemented with 10% fetal bovine serum, 1% sodium pyruvate and 1% non-essential amino acids and 0.01 mg/ml human insulin (Sigma Aldrich, Cat. No.: I9278). MCF7 cells stably transfected with eGFP-LC3 (MCF7/LC3) were cultured in Eagle's MEM (PAN Biotech, Cat No.: P04-08500) containing 10% FBS, 1% sodium pyruvate, 1% non-essential amino acids, 0.01 mg/ml human insulin and 200 µg/ml G418 (Sigma Aldrich, Cat. No.: G8168). U2OS cells were cultivated in DMEM Medium containing 10% fetal calve serum (PAN Biotech, 131206), 1% L-Glutamine (PAN Biotech, P04-80100), 1% non-essential amino acids, (Gibco, 11140-035) and 1% sodium pyruvate (Gibco 11360-0930).

4.4.1.2. Thawing of cryo-conserved cells

Cryo-Conserved cells were thawed in a water bath at 37 °C. Afterwards the cells were transferred into 10 ml of the respective medium and centrifuged for 5 min at 350 g. The supernatant was removed and the cell pellet was resuspended in 10 ml of fresh medium. The cells were transferred into two 25 cm² tissue culture flasks.

4.4.1.2. Cryo-conservation of cells

Cells were grown in 175 cm² tissue culture flasks until they reached 80-90% confluence. The cells were detached by trypsinization and centrifuged for 5 min at 350 g. The cell pellet was resuspended in 6 ml of the respective culture medium supplemented with 5 % (v/v) DMSO and

distributed to cryo-conservation vials. The vials were transferred into a cell freezing container (CoolCell® LX) and kept at -80 °C overnight, facilitating a controlled temperature decrease of 1 °C/min. For long term the cells were stored in liquid nitrogen.

4.4.1.3. Passaging of mammalian cells

The cells were grown to 80-90 % confluence in 75 cm² or 175 cm² tissue culture flasks. In advance all required solutions were warmed to 37 °C. The old medium was removed and the cells were carefully washed with PBS (10 ml for 75 cm² and 20 ml 175 cm² tissue culture flasks). PBS was removed immediately and replaced with trypsin (2 ml for 75 cm² and 4 ml 175 cm² tissue culture flasks). The cells were incubated for 2 min at 37 °C with 5 % CO₂ and completely detached by carefully tapping against the tissue culture flask. Subsequently fresh medium were added, in order to inactivate trypsin and a desired amount of the cell suspension was transferred to a new tissue culture bottle containing fresh medium (8 ml for 75 cm² and 20 ml 175 cm² tissue culture flasks).

4.4.1.4. Cell counting

The cells were diluted with Trypan blue in a 1:1 ratio to distinguish between living and dead cells. Afterwards 5 µl of the mixture were transferred to a Countess® Cell Counting Chamber Slide (Thermo Fisher Scientific, Cat. No. C10228). The slide was inserted into the Countess™ II Automated Cell Counter. The cell count was performed according to the manufacturer's instructions.

4.4.1.5. Lysate preparation

Cells were cultivated according to previously described procedure. Adherent cells were washed with PBS and detached with trypsin/EDTA or cell dissociation solution (Sigma Aldrich, Cat. No. C5915) and resuspended in medium or PBS buffer respectively. Cells were harvested by centrifugation at 350 g for 5 min and washed twice with PBS buffer. Subsequently, the cell pellet was resuspended in the respective lysis buffer and lysed by the freeze and thaw method. For TPP experiments, the insoluble cell components were precipitated by centrifugation with an ultra-centrifuge at 100,000 g, for 20 min, at 4 °C using polycarbonate tubes. For all other

experiments, the insoluble cell components were precipitated by centrifugation at 14,000 g for 20 min, at 4 °C. Lysate concentration was determined by DC assay. The lysate was snap-frozen and stored at -80 °C until further use.

4.4.2. Thermal proteome profiling

4.4.2.1. Cell lysis

MCF7/LC3 cells were harvested by centrifugation at 350 g for 5 min and washed twice with PBS. Cells were re-suspended in TPP lysis buffer prior to lysis by freeze-thaw cycles. Insoluble cell components were precipitated by centrifugation at 100,000 g for 20 min at 4 °C in an ultracentrifuge. The lysate was snap-frozen and stored at -80 °C until further use.

4.4.2.2. Thermal denaturation

Lysate was diluted with lysis buffer to a protein concentration of 2 mg/ml and a total volume of 2.9 ml. The diluted lysate was split into two aliquots of 1.4 ml each. One part of the samples was treated with the compound and the other one with an equal amount of DMSO. Final compound concentrations were 1 µM for GG1198, Squarunkin A and Authipyrin **53**, 16 µM for Autoquin **52**, and 30 µM of Autoxain **51**. The compound and vehicle sample were incubated at ambient temperature for 10 min prior to splitting each into 10 aliquots of 120 µl. Aliquots were heated at a temperature gradient of 37 - 67 °C in a the PCR cycler for 3 min. One vehicle sample was always heated in parallel with one compound sample. Subsequently, samples were cooled to 4 °C and centrifuged at 100,000 g for 20 min at 4 °C in an ultracentrifuge. The supernatant (100 µl) was transferred into low binding Eppendorf tubes.

4.4.2.3. Trypsin digestion

Of each sample a 75 µl aliquot was treated with an equal volume of freshly prepared TPP buffer A (100 mM TEAB) and 7.5 µl of TPP buffer B (200 mM TCEP, 0.2 mM TEAB) and incubated for 1 h at 55°C. A freshly prepared solution of TPP alkylation buffer (375 mM iodacetamide in water) was added to each sample followed by incubation for 30 min in darkness. Subsequently, 900 µl of pre-cooled acetone were added to precipitate the proteins

overnight at -20 °C. Samples were centrifuged at 8000 g for 10 min at 4 °C, pellets were air-dried for 1.5 h and resuspended in 100 µl of freshly prepared TPP buffer A. Subsequently 7.5 µl of Trypsin digestion buffer were added to the samples and digestion was performed at 37 °C overnight.

4.4.2.4. TMT labeling

This part of the experiment was performed by Jens Warmers

The TMT10plex label reagents (Thermo Fisher Scientific, Cat. No. 90110) were equilibrated at room temperature and each label was dissolved in 82 µl anhydrous acetonitrile. Each DMSO- or compound-treated sample was then incubated with one of the TMT label reagents so that given TMT label codes for one temperature of the used temperature gradient. After incubation for 2 h at ambient temperature an aqueous hydroxylamine solution was added to each vial and incubation continued for another 15 min. All aliquots of the compound- or the DMSO-treated samples respectively were combined and evaporated to dryness in a centrifugal evaporator at 30 °C.

4.4.2.5. pH fractionation and nanoHPLC analysis

This part of the experiment was performed by the mass spectrometry group

Samples were dissolved in 120 µl ammonium formate (NH₄COO, 20 mM, pH 11), ultrasonified for 2 min at the ambient temperature and vortexed for 1 min, followed by centrifugation at 13000 rpm for 3 min at 20 °C. Subsequently, 110 µl of the supernatant were transferred into a polypropylene sample vial (250 µl, SUN-Sri 200046, 12x32 equipped with a 6820.0028 lid from Thermo Scientific). The peptides were fractionated using an XBridge C18 column (130 3.5 µm 1.0 × 150 mm) on a Thermo Scientific Ultimate 3000 (LPG-3400MB, TCC-3000SD, WPS-3000TBFC ANALYTICAL, VWD-3100). Solvent A (20 mM NH₄COO in water, pH 11) and solvent B (20 mM NH₄COO in water with 60 % acetonitrile). The gradient was adjusted in order to achieve ideal separation into 10 new fraction samples. Between the different runs the column was washed with blank runs to avoid carry over from vehicle to compound samples. After fractionation the samples were evaporated to dryness in a centrifugal evaporator at 30 °C. For nanoHPLC-MS/MS analysis the samples were dissolved in 20 µl of

0.1% TFA and 3 μ l were injected into the nanoHPLC-MS (Thermo Scientific Ultimate 3000 (SRD-3400, NCS-3500RS NANO, WPS-3000TPL-RS, VWD-3400RS, Thermo Scientific QExactive Plus mass spectrometer). The samples were injected onto a pre-column cartridge (5 μ m, 100 \AA , 300 μ m ID * 5 mm, Dionex, Germany). The eluent was 0.1 % TFA in water with a flow rate of 30 μ L/min. The precolumn was flushed with the eluent for 5 min, followed by transfer of the sample from the pre-column to the PepMap100 RSLC C18 nano-HPLC column (2 μ m, 100 \AA , 75 μ m ID \times 25 cm, nanoViper, Dionex, Germany) using a linear gradient starting with 95 % solvent A (water containing 0.1 % formic acid) / 5 % solvent B (acetonitrile containing 0.1 % formic acid). Over a time of 125 min with a flow rate of 300 nl/min, the gradient was increased to 60 % solvent A 0.1 % formic acid / 40 % solvent B.

The nano-HPLC was online coupled to the Quadrupole-Orbitrap Mass Spectrometer using a standard coated SilicaTip (ID 20 μ m, Tip-ID 10 μ m, New Objective, Woburn, MA, USA). Mass range of m/z 300 to 1650 was acquired with a resolution of 70000 for full scan, followed by up to ten high energy collision dissociation (HCD) MS / MS scans of the most intense at least doubly charged ions using a resolution of 35000 and a NCE energy of 35 %.

4.4.2.6. Data evaluation

This part of the experiment was performed by the mass spectrometry group

Data evaluation was carried out with MaxQuant software (v.1.5.3.30) including the Andromeda search algorithm, based on the Uniprot database as a reference for the human proteome.^[203] The search criteria was a full enzymatic trypsin cleavage with tolerance for two miscleavages. Carbamidomethylation was a fixed and oxidation of methionine and acetylation of the N-terminus as variable protein modifications. For relative quantification the type “reporter ion MS2” was chosen and for all lysines and peptide N-termini 10plex TMT labels were defined. The mass accuracy for full mass spectra was set to 20 ppm (first search) and 4.5 ppm (second search), respectively and for MS/MS spectra to 20 ppm. For peptide and protein identification a false discovery rate of 1 % was chosen. Only proteins for which at least two peptides were quantified were chosen for further validation. Relative quantification of proteins was performed using the reporter ion MS2 algorithm implemented in MaxQuant.

4.4.2.7. Calculation of protein melting curves

This part of the experiment was performed by the mass spectrometry group

The difference in melting point between compound and vehicle was determined based on an in-house developed Excel-Macro. Therefore, the amount of non-denaturated protein was determined by the reporter ion intensity and normalized to the lowest temperature, which was adjusted to 1.

The relative fold changes were calculated as a function of temperature. The measuring points were fitted according to the following equation using an iterative working macro for Microsoft Excel.

$$y = \text{bottom plateau} + \frac{(\text{top plateau} - \text{bottom plateau})}{1 + e^{-\left(\frac{a}{\text{Temp}}\right)^{-b}}$$

Top plateau is fixed to one, Temp is the temperature, bottom plateau is a protein specific constant that defines the maximal denaturation and a and b are constants which describe the curve progression.

The melting point of a protein is defined as the temperature at which half of the protein has been denaturated. This point aligns with the inflection point of the curve.

For hit identification following requirements were defined and had to be fulfilled for all replicates: (1) the protein has to be identified with at least two unique peptides, (2) the DMSO control has to melt nicely, i.e. the TMT labels of the two highest temperatures have to have a relative intensity of smaller or equal of 35 % of the label of the highest temperature, (3) the shifts of the melting points for the same protein have to exhibit a consistent stabilization or destabilization of at least 3°C.

4.5. Biological methods UNC119 project

4.5.1. Expression of human UNC119 protein constructs

This experiment was performed by Christine Nowak

BL21DE3RILK+ cells were transformed with the pGex4T3HRG4 plasmid, which contains the desired human UNC119A analogue. The bacteria were grown in a 10 L culture of TB medium

with Ampicillin and Chloramphenicol. UNC119A expression was induced by the addition of IPTG to a final concentration of 100 mM. The bacteria culture was incubated over night at 18 °C. The cells were separated by centrifugation and disrupted in protein expression buffer A (20 mM Tris (pH 7.5), 300 mM NaCl, 50% (v/v) glycerol, 3 mM β ME, 0.25% (v/v) Triton X-100, 0.25% (v/v) NP40, 1 mM PMSF, DNase) by sonication (3 times), fluidizer (2 times) and centrifugation. The supernatant was applied to a GSH-column, and washed with protein expression buffer B (20 mM Tris (pH 7.5), 300 mM NaCl, 50% (v/v) glycerol, 3 mM β ME) until the optical density decreased. The protein was digested over night with 3000 units of thrombin and eluted from the column. The concentration was determined according to Bradford and the obtained product was purified with a 16/60 G200 gel filtration column. The UNC119A containing fractions were combined and again the concentration was determined by a Bradford assay.

4.5.2. Fluorescence polarization measurement

Fluorescence polarization experiments were performed in black, non-binding 384-well plates (Coring, Cat. No. CLS3575). To each well fluorescein-labeled Pacman probe or myristoylated Src (200 nM) and decreasing concentrations of UNC119A or UNC119B (7000 to 0 nM) were added to reach a final volume of 20 μ L in PBS buffer. Each experiment was performed in triplicate. The plate was covered with foil and shaken in darkness for 1 h at 4 °C. Subsequently, fluorescence polarization was measured after 1 h at an excitation wavelength of 470 nm and an emission wavelength of 525 nm.

4.5.3. Photo-crosslinking of Pacman probes to UNC119 proteins

4.5.3.1. General procedure

Peptide stock solutions (20 mM) were prepared in DMSO. In glass vials, UNC119 protein (50 μ M) and the respective amount of Pacman probe were mixed in PBS (50-100 μ L). Irradiation of the solutions was performed over 20 min at 365 nm and the aliquots were taken after designated time points and stored on ice, in darkness.

4.5.3.2. MALDI measurement

For the preparation of the matrix, a saturated solution of sinapic acid in acetonitrile/aqueous 0.1% TFA was prepared. The aliquots from the photo-crosslinking experiments were diluted with matrix (1:10). The diluted sample (1 μ L) was deposited on the MALDI target plate and allowed to air dry. The samples were measured with linear positive mode, operating with the detection range of 0.7 - 2 kDa for peptide identification and 5 – 50 kDa for the protein detection.

4.5.4. Mapping of UNC119 binding pocket

In glass vials, Pacman probe was diluted with PBS (40 μ l) to a final concentration of 150 μ M. The respective UNC119 protein was added in a final concentration of 50 μ M. Irradiation of the solution was performed over 20 min at 350 nm. For Pacman-1-Src three cycles of peptide addition and irradiation were performed and for Pacman-1-Gnat two cycles. (Pacman-1-Gnat total: peptide: 6 equivalents (300 μ M), irradiation time: 40 min; Pacman-Src total: peptide: 6 equivalents 450 μ M, irradiation time: 60 min). The sample was diluted with 60 μ l PBS-buffer to a final protein concentration of 20 μ M. Subsequently, 100 μ l of mapping buffer A (50 mM Tris (pH 7.5), 1 mM DTT, 10 μ M ammonium bicarbonate, 5.5 μ g trypsin in 10 mM HCl, 2.2 M urea) were added to each sample. After 1 h incubation at 37 °C 100 μ l of mapping buffer B (0.5 M iodacetamide in H₂O) were added and incubation was continued over night at 37 °C. The samples were desalinated by Stop and Go Extraction (Stage) Tip purification and dried in a centrifugal evaporator at 30 °C for 3h.

4.5.4.1. Stop and go extraction tip-based peptide purification

C18 Stage tips (3M™ Empore™ C18 Extraction Disks, Mfr. No. 2215) were activated with 100 μ l methanol. Subsequently, the tips were washed once with 100 μ l buffer B (H₂O/ACN 2:8 with 0.1 % formic acid) and twice with 100 μ l Stage Tip buffer A (H₂O with 0.1 % formic acid). The samples were loaded and incubated for 1 min before washing with 100 μ l of Stage Tip buffer A. Afterwards the samples were eluted by incubating the samples for 1 min with 20 μ l of Stage Tip buffer B and subsequent centrifugation for 5 min at 8000 rpm. The elution step was repeated once more and the combined fractions were dried at 30 °C in a SpeedVac Concentrator.

4.5.4.2. Nano-HPLC-MS/MS

After tryptic digestion and purification, the protein fragments were analyzed by nano-HPLC-MS/MS using an UltimateTM 3000 RSLC nano-HPLC system and a Q ExactiveTM HF or a Q ExactiveTM Plus Hybrid Quadrupole-Orbitrap mass spectrometer equipped with a nano-spray source (all ThermoFisher Scientific). Briefly, the lyophilized tryptic peptides were dissolved in 20 μ l 0.1 % TFA and 3 μ l of these samples were injected and enriched onto a C18 PepMap 100 column (5 μ m, 100 \AA , 300 μ m ID * 5 mm, Dionex, Germany) using 0.1 % TFA and a flow rate of 30 μ l/min for 5 min. Subsequently, the peptides were separated on a C18 PepMap 100 column (3 μ m, 100 \AA , 75 μ m ID * 25 cm) using a linear gradient starting with 95 % solvent A/5 % solvent B and increasing to 40.0 % solvent B in 90 min with a flow rate of 300 nl/min, followed by a linear gradient up to 60 % solvent B in 5 min, a further increase to 95 % solvent B in 5 min, and washing of the column using 95 % solvent B for 5 min (solvent A: water containing 0.1 % formic acid, solvent B: acetonitril containing 0.1 % formic acid). The nano-HPLC was online coupled to a Q Exactive HF or Q Exactive Plus mass spectrometer using a standard coated Pico Tip emitter (ID 20 μ m, Tip-ID 10 μ M, New Objective, Woburn, MA, USA). Mass range of m/z 300 to 1650 was acquired with a resolution of 60000 (HF) or 70000 (Plus) for full scan, followed by up to 15 (HF) or 10 (Plus) high energy collision dissociation (HCD) MS/MS scans of the most intense at least doubly charged ions with a resolution of 15000 (HF) or 17500 (Plus).

4.5.5. Sequence alignment

For the sequence alignment of human UNC119A and UNC119B the Basic Local Alignment Search Tool (BLAST) for protein sequences was employed. As input files served the FASTA files provided by Uniprot.

4.5.6. Preparation of UNC119B model

The model of human UNC119B was prepared using SWISS-MODEL.^[86] The crystal structure of human UNC119A protein in complex with myristoylated NPHP3 peptide (PDB code: 5L7K) with the sequence identity of 72.6% was used as the template.^[62]

Molecular modelling experiments were performed with the Maestro 10.5 suite (Schrödinger). Both ligand and receptor flexibility were taken into account by using receptor docking (Glide) in combination with the protein structure prediction embedded in the program Prime. Protein Preparation Wizard (Schrödinger Maestro suite) was used to prepare the UNC119B protein for the calculations. Hydrogen atoms were added and resulting structure was refined by OPLS2005 force field. The minimization was ended when the RMSD reached 0.3 Å. Receptor Grid Preparation (Glide) was used to generate the protein grid that was subsequently utilized in docking experiments. The van der Waals radius scaling factor was set to 1 with a partial charge cutoff of 0.25. Ligand preparation for docking was carried out with LigPrep in Maestro 10.5 and the OPLS2005 force field. Epika was used to generate possible states at target pH 7.0 ± 2.0 . Ligand-docking options in Glide were used for the first round of docking experiments. Under Setting, SP (standard precision), Dock flexibly, sample nitrogen inversions, sample ring conformation and Epik state penalties to docking score were selected, amide bonds were penalized for nonplanar conformation. Under the Ligands section, the Van der Waals radius scaling factor was set to 0.8. Several high-score binding poses were generated and analyzed using Pymol (Molecular Graphics System, Version 1.7.4.1. Schrödinger, LLC).

4.5.7. Crystallization of shUNC119A and shUNC119B

For crystallization with Pacman-1-shGnat truncated versions of UNC119A and UNC119B (shUNC119A and shUNC119B) were used. Initially, the photocrosslink between probe and protein was established. Therefore, Pacman-1-shGnat (3 eq, 14.4 μ l) was added to 158 μ l of shUNC119A (AAs: 58-240; conc.: 1.52 mM) or shUNC119B (AAs: 42-251; conc.: 1.41 mM) in crystallization buffer (25 mM Tris, 50 mM NaCl, 3 mM DTE) and the solution was diluted with crystallization buffer to a final protein concentration of 500 μ M (total volume: 450 μ l). The sample was irradiated for 20 min at 350 nm and another 3 eq of Pacman-1-Gnat were added, followed by a second round of irradiation for 20 min. Subsequently, the sample was distributed equally on three different vials (150 μ l each). To one of the samples 1:1000 Trypsin (stock 5 mg/ml) was added and to the second one 1:1000 Trypsin and 1:1000 Chymotrypsin (stock 5 mg/ml). The last sample was not treated with protease. The samples were incubated for 1 h at 4 °C and subsequently centrifuged at 14,000 g for 15 min at 4 °C.

Suitable conditions for protein crystallization were screening with the mosquito LCP crystallization robot using sitting-drop vapor diffusion method. Sreened crystallization

conditions were Classics, CoreI, CoreII, CoreIII, CoreIV, PEGs, PEGsII and Protein Complex. The photolabelled protein (100 nL) was mixed 1:1 with the reservoir solution on IQ 3drops TTPlabtech plates. Crystallization was monitored for 90 days at rt. Optimization of crystallization conditions was performed with hanging-drop vapor diffusion in 24-well plates Linbro 24 Conical Flat Bottom Wells (MP Biomedicals, Santa Ana, US-CA). Therefore, the photolabelled protein (1 μ l) was diluted with reservoir solution (1 μ l) and incubated in presence of 500 μ l reservoir solution at the ambient temperature.

4.5.8. Affinity enrichment of UNC119 with Pacman probes

4.5.8.1. Affinity enrichment with SulfoLink Coupling Resin

SulfoLink Coupling Resin (ThermoFisher Scientific, Cat. No. 20401) and all other reagents were equilibrated to room temperature. The resin was suspended (100 μ l) and transferred to Pierce™ Spin Column (Nr. 69705). The resin was equilibrated with four resin-bed volumes of Coupling Buffer and the bottom column cap was replaced. The positive and negative probe were diluted in 100 μ l SulfoLink coupling buffer (50 mM Tris pH 8.5, 25 mM TCEP) to a final concentration of 100 μ M. The samples were inverted for 45 min at the ambient temperature. Sequentially the top and bottom caps were removed and the solution was removed by centrifugation. Afterwards the resin was washed with three resin-bed volumes of SulfoLink coupling buffer. Non-specific binding sites were blocked by adding 500 μ l SulfoLink blocking buffer (50 mM L-Cystein-HCl in coupling buffer) and inverted for 45 min at the ambient temperature. Sequentially top and bottom cap were removed and the liquid was removed by centrifugation. The column was washed with six resin-bed volumes of SulfoLink wash solution (1 M NaCl in H₂O) and afterwards equilibrated with four resin-bed volumes of PBS. The HEK293 cell lysate (100 μ l, 5.0 mg/ml) was added and carefully transferred to the resin-bed by centrifugation. The columns were incubated shaking for 1h and subsequently irradiated at 365 nm for another 30 min. Non-covalently bound components were removed by washing the columns with four resin-bed volumes of PBS (3x 5 min) and four resin-bed volumes of SulfoLink elution buffer (0.15 M glycine, pH 2.5; 3x 10 min). Afterwards the resin was equilibrated with nine resin-bed volumes of PBS. An on-bead tryptic digestion was performed, followed by a Stage Tip purification.

4.5.8.2. Affinity enrichment with DBCO agarose beads

DBCO Agarose (Jena Bioscience, Cat. No- CLK-1034-2) was equilibrated to rt, and the beads (100 μ L) were washed with PBS (3x 500 μ l) and the respective azide compound in PBS (60 μ M, 0.01 % DMSO) was added. The mixture was incubated rotating at 4 °C overnight and subsequently washed with PBS (3x 500 μ l, 10 min). HEK293 cell lysate (500 μ l, 5 mg/ml) was added to the beads and the samples were incubated rotating at 4 °C for 1.5 h. Afterwards, the samples were irradiated at 365 nm for 30 min (invert every 5 min). The supernatant was removed and the beads were washed with PBS (3x 500 μ l, 10 min). Finally, an in solution digestion was performed followed by a Stage Tip purification.

4.5.8.3. Affinity enrichment with NHS Activated Beads

The free amine compound was added to coupling buffer (500 μ l), resulting in a final concentration of 60 μ M. NHS Mag Sepharose beads (28951380, GE-Healthcare) were equilibrated to room temperature. For each positive and negative probe 100 μ l of bead slurry was washed with 500 μ l ice cold NHS equilibration buffer (1 mM HCl) and the respective free amine compound in NHS coupling buffer (0.15 M Triethanolaminem, 0.5 M NaCl, pH 8.3) was added. After 1h incubation rotating at the ambient temperature the beads were subsequently washed with 500 μ l NHS blocking buffer A (0.5 M Ethanolamine, 0.5 M NaCl, pH 8.3) and 500 μ l NHS blocking buffer B (0.1 M Na-Acetate, 0.5 M NaCl), followed by 15 min incubation with NHS blocking buffer A, rotating at the ambient temperature. The beads were washed with NHS blocking buffer B, NHS blocking buffer A and again with NHS blocking buffer B. HEK293 lysate was diluted with NHS lysis buffer A (PBS) to a final protein concentration of 5 mg/ml. The beads were equilibrated with 500 μ l PBS and incubated with cell lysate rotating for 1.5 h at 4 °C. Subsequently the beads were irradiated for 5 min at 365 nm, inverted and again irradiated for 5 min. This procedure was repeated until a total irradiation time of 25 min. The cycle of irradiation and inversion was afterwards repeated five more times with an irradiation time of 1 min. The beads were washed with 500 μ l PBS (3x3min). Finally a tryptic digestion and Stage Tip purification were performed.

4.5.8.4. On-bead digestion

As a control, the tryptic digestion was also performed with BSA in PBS (5 pM, 100 µl). The samples were incubated with 50 µl of reducing buffer (8 M urea, 1 mM DTT in Tris-buffer) shaking at 350 rpm for 30 min at the ambient temperature. Afterwards 5.5 µl of alkylation solution (50 mM chloroacetamide in reducing buffer) were added and incubation was continued for another 30 min. The beads were treated with 2 µl LysC digestion solution (0.5 µg/µl in H₂O) and after 1 h incubation at 37 °C the supernatant was transferred to a fresh Eppendorf tube. Afterwards 2.5 µl of Trypsin digestion solution (0.4 µg/µl in 10 mM HCl) in 165 µl Tris-buffer (50 mM Tris, pH 7.5) were added and the resin was incubated shaking for 1h at 37 °C. The supernatants of the respective LysC- and trypsin digestion steps were combined. Another 5 µl of trypsin digestion solution were added and the samples were incubated overnight at 37 °C shaking at 350 rpm. The next day the reaction was terminated by addition of 2 µl concentrated TFA followed by STAGE-based peptide purification (Chapter 4.5.4.1.)

4.5.8.5. Data evaluation by Nano-LC-MS/MS

This part of the experiment was performed by the MS-team

Protein identification and relative quantification were performed using MaxQuant v.1.5.6.5^[203] including the Andromeda search algorithm and searching the human reference proteome of the uniprot database and in parallel the contaminants database included in MaxQuant. Briefly, a MS/MS ion search was performed for full enzymatic trypsin cleavages allowing two miscleavages. For protein modifications carbamidomethylation was chosen as fixed and oxidation of methionine and acetylation of the N-terminus of the protein as variable modifications. The mass accuracy was set to 20 ppm for the first and 4.5 ppm for the second search. The false discovery rates for peptide and protein identification were set to 0.01. Only proteins for which at least two peptides were quantified were chosen for further validation.

Relative quantification of proteins was carried out using the label-free quantification algorithm implemented in MaxQuant.^[204] All experiments were performed in biological duplicates (technical triplicates, each). For further data mining the program Perseus^[205] was used and the biological duplicates were evaluated separately. In brief, label-free quantification (LFQ) intensities were logarithmized (log₂) and samples resulting from affinity purification using the

active molecule bound to solid support were grouped together and samples resulting from affinity purification using the inactive control molecule bound to solid support as well. Proteins that were not three times quantified in at least one of the groups were filtered off. Missing values were imputed using small normal distributed values and a t-test was performed. Proteins that were statistically significant outliers in both biological duplicates and enriched in the samples resulting from affinity enrichment using the active molecule bound to the solid support were considered as hits.

4.5.8.6. 7-Diethylamino-3-(4'-maleimidylphenyl)-4-methylcoumarin (CPM)-based assay

To decreasing concentrations of Pacman-CoA was added the respective NMT in CMP buffer A (2.5 mM potassium dihydrogen phosphate, 17.5 mM sodium hydrogen phosphate, 0.5 mM EDTA, 0.1 % Triton X-100, 1 % DMSO, pH 7.90-7.95) in a final concentration of 300 μ M. The highest final concentration of Pacman-CoA was 64 μ M (2x dilution series). The respective peptide substrate/CPM mixture (buffer A containing 5 % DMSO) was added, each with a final concentration of 16 μ M, to start the assay. The fluorescence intensity (excitation 380 nm and emission at 470 nm) was measured over a time of 2 h every minute.

Species	Peptide Substrate
<i>Homo sapiens</i>	GSNKSKPK-NH ₂
<i>Leishmania donovani</i> , <i>Leishmania major</i>	GSNKSKPKDASQRRR-NH ₂
<i>Trypanosoma brucei</i> , <i>Plasmodium falciparum</i>	GLYVSRLFNRLFQKK-NH ₂

4.6. Biological methods autophagy project

4.6.1. Medium throughput GFP-LC3 puncta formation assay

This screening was performed COMAS.

MCF7 cells stably expressing eGFP-LC3 were seeded in a 384-well Greiner μ clear plate (cat# 781080, lid cat# 656191) at a density of 400 cells/were in 25 μ l medium. The cells were

incubated overnight (37 °C, 5% CO₂). The cells were washed three times with PBS employing a plate washer (Biotek, ELx405), followed by aspiration of the washing buffer. Of the compound solution (10 mM stock solution in DMSO) 25 nl were added with an echo dispenser (Labcyte, Echo 520 dispenser). To induce autophagy 25 µl of the respective medium was added with a Multidrop Combi (Thermo Scientific). For rapamycin-induced autophagy standard medium containing 50 µM chloroquine and 100 nM rapamycin (Biomol, cat# Cay13346) were used and for starvation-induced autophagy EBSS supplemented with 50 µM chloroquine. Following another three hours of incubation (37 °C, 5% CO₂) the cells were fixed with 25 µl fixation solution (formaldehyde/PBS 1:4 with 1:500 Hoechst (stock: 1 mg/ml, Sigma Aldrich cat# B2261-25mg)), incubated at the ambient temperature for 20 min and washed three times with 1X PBS. With an ImageXpress Micro XL (Molecular Devices) four images were recorded per well at 20-fold magnification. The granularity setting of MetaXpress Software (Molecular Devices) was used for automated image analysis.

4.6.2. Determination of protein lysate concentration

Protein concentration was determined by means of DC Assay (Bio Rad) according to the “DC protein assay instruction manual”. Calculation of the protein concentration was performed with a BSA standard curve (0 mg/ml – 2.5 mg/ml). The absorbance was measured at 750 nm in a Teacan plate reader.

4.6.3 SDS-PAGE and western blotting

4.6.3.1. Sodium dodecyl sulfate–polyacrylamide gel electrophoresis (SDS-PAGE)

SDS-PAGE was carried out in a Mini-PROTEAN® Tetra Cell chamber (Bio Rad) according to standard procedure. The samples were diluted with fivefold SDS loading buffer (50% v/v Glycerol, 250 mM Tris (pH 6.8), 10% w/v SDS, 500 mM DTE, 360 µM bromophenol blue) to a final SDS concentration of 2 % (w/v). Subsequently the proteins samples were denatured by heating to 95 °C for 5 min and loaded onto the SDS-gel. As a size standard PageRuler™ Plus Prestained Protein Ladder (Thermo Fisher Scientific, Cat. No. 26619) was used. The gel was initially run at 80 V for 30 min and afterwards at 120 V until the marker reached sufficient separation.

4.6.3.2. Western blotting

After size dependent separation by SDS-PAGE the proteins were transferred to a polyvinylidene fluoride (PVDF) membrane. The PVDF membrane was shortly activated in MeOH and afterwards both, SDS-gel and PVDF membrane were equilibrated in transfer buffer. Also the filter paper was soaked in transfer buffer immediately before assembly of the Trans-Blot® SD Semi-Dry Transfer Cell (Bio-Rad) system. The transfer was performed at 25 V for 45 min according to the manufactures instructions.

4.6.3.3. Immunoblotting

All immunoblots were prepared according to standard semi-dry blotting procedure for 45 min at 25 V. Subsequently the membrane was stained with Ponceau S, washed with water and blocked with the respective blocking buffer for 1 h at the ambient temperature. Afterwards the membrane was incubated at 4 °C overnight with primary antibody in the respective blocking buffer. The primary antibody solution was discarded, the membrane washed with TBS-T (3x 10 min) and incubated with the secondary antibody for 1 h at the ambient temperature. Finally the membrane was washed again with TBS-T (3x 10 min) and visualized.

The HRP signal was induced with SuperSignal West Pico/Femto Chemiluminescent Substrate (Pierce) and detected with a capture time of 10 min in the Odyssey® Fc Imaging System (LI-COR® Bioscience).

antibody	host	dilution	blocking buffer	supplier	Cat. No.
LC3	rabbit	1:1,000	5 % w/v milk powder in TBS-T	Cell Signaling	2775
p62	rabbit	1:10,000	5 % w/v milk powder in TBS-T	MBL internatio nal	PM045
β-actin	rabbit	1:10,000	5 % w/v milk powder in TBS-T	Abcam	ab8227
FECH	rabbit	1:1000	5 % w/v milk powder in TBS-T	GeneTex	GTX113435
Anti-rabbit HRP	goat	1:10,000	Same as primary AB	Pierce	31460
IRDye® 800CW Donkey anti-Rabbit	donkey	1:10,000	Odyssey® Blocking Buffer (PBS)	LI-COR	P/N 925- 32213

4.6.3.4. Immunoblotting against autophagy markers LC3 and p62

MCF7/LC3 cells were seeded in 6-well plates (250,000 cells/2 ml medium) and incubated overnight. Subsequently the medium was removed and replaced by fresh medium or EBSS containing the respective compound in desired concentration. After another 3 h of incubation, the medium was removed and the cells were washed with 1 ml PBS. In order to lyse the cells, SDS lysis buffer (10% v/v Glycerol, 50 mM Tris (pH 6.8), 2% w/v SDS, 100 mM DTE) was added and the cells were collected with cells scrapers. Completion of cell lysis and solubilization was achieved by sonification. After determination of protein concentration by means of DC assay the samples were diluted with SDS loading buffer (5x) to a final SDS concentration of 2% (w/v). Proteins were denatured by heating to 95 °C for 5 min. The samples were stored at -80 °C until further use for SDS-PAGE separation and western blot preparation. As markers for autophagy p62 and LC3 were chosen and β-actin served as a loading control.

4.6.4. Selective viability assay

For fed and starved conditions 5000 MCF7 cells in 100 μ l were seeded in clear flat-bottom 96 well plates one day prior to the experiment. The next day the old medium was removed and 80 μ l of the respective fresh medium containing propidium iodide (1:60) were added. For fed conditions standard medium was used, for starved conditions medium without glucose. A threefold dilution series of compound in medium was prepared with a starting concentration of 50 μ M and a total number of nine different concentrations. Afterwards 20 μ l of the respective compound concentration was added to the cells. As a control DMSO (0.1 %) and Nocodazol (10 μ M) were used. The cells were incubated in the IncuCyte® ZOOM for 72 h. Two images per well were recorded at 10 fold magnification every 2 h in the red and phase channel. The images were analyzed using the IncuCyte® ZOOM software.

4.6.5. Kinase profiling and IC₅₀ determination

This part of the experiment was performed by SelectScreen Kinase Profiling Service of Life Technologies.

Kinase inhibition was determined with single point concentrations (1 μ M) for the whole panel of provided kinases. The IC₅₀ determination was carried out for a selected subset of six kinases as a ten-point measurement with a starting concentration of 10 μ M and a threefold dilution. Both screens were performed according to the “protocol and assay conditions” provided on the company’s website. (<https://www.thermofisher.com/us/en/home/products-and-services/services/custom-services/screening-and-profiling-services/selectscreen-profiling-service/selectscreen-kinase-profiling-service.html>)

4.6.6. Affinity-based proteomics

4.6.6.1. Affinity enrichment with NHS-activated beads

The free amine compound was added to 500 μ l NHS coupling buffer (0.15 M Triethanolaminem, 0.5 M NaCl, pH 8.3), resulting in a final concentration of 10 μ M. NHS Mag Sepharose beads (GE-Healthcare, Cat. No. 28951380) were equilibrated to room temperature. For each positive and negative probe 25 μ l of bead slurry was washed with 500 μ l ice cold NHS equilibration buffer (1 mM HCl) and the respective free amine compound in NHS

coupling buffer was added. After 1h incubation rotating at the ambient temperature the beads were subsequently washed with 500 μ l NHS blocking buffer A (0.5 M Ethanolamine, 0.5 M NaCl, pH 8.3) and 500 μ l NHS blocking buffer B (0.1 M Sodium acetate, 0.5 M NaCl), followed by 15 min incubation with NHS blocking buffer A, rotating at the ambient temperature. The beads were washed with NHS blocking buffer B, NHS blocking buffer A and again with NHS blocking buffer B. MCF7/LC3 lysate was diluted with NHS lysis buffer B (50 mM PIPES (pH 7.4), 50 mM NaCl, 5 mM MgCl₂, 5 Mm EGTA, 0.1% (v/v) NP40, 0.1% (v/v) Triton, 0.1% (v/v) Tween) to a final protein concentration of 4.5 mg/ml. The beads were equilibrated with 500 μ l NHS lysis buffer and incubated with cell lysate rotating for 2 h at 4 °C. The beads were washed with 500 μ l NHS lysis buffer B (2x 10 min) and 500 μ l PBS (2x 10 min). Finally an on-bead digestion (Chapter 4.5.8.4.) and a stage tip purification (Chapter 4.5.4.1.) were performed.

For the competitive pulldown the lysate was incubated for 1 h at 4 °C with varying amounts of the free active probe (1 μ M, 10 μ M and 100 μ M) before adding it to the beads. Instead of tryptic digestion and stage tip purification the samples were suspended in 40 μ l PBS and 10 μ l 5x SDS buffer and denaturated by heating to 95 °C for 5 min. Subsequently immunoblotting was performed employing an antibody against FECH.

4.6.6.2. Data evaluation by nano-LC-MS/MS

This part of the experiment was performed by the mass spectrometry group

For protein identification and relative quantification tryptic peptides were separated and analyzed by nano-HPLC/MS/MS. The separations were carried out on UltiMate™ 3000 RSLCnano system (Dionex, Germany). The MS and MS/MS experiments were carried out on a Q Exactive Hybrid Quadrupole-Orbitrap Plus™ or HF™ Mass Spectrometer equipped with a nano-spray source (Nanospray Flex Ion Source, Thermo Scientific). All solvents were LC-MS grade. The lyophilized tryptic peptides were dissolved in 20 μ l 0.1 % TFA in water. 3 l of sample were injected onto a pre-column cartridge (5 μ m, 100 Å, 300 μ m ID * 5 mM, Dionex, Germany) using 0.1 % TFA in water as eluent with a flow rate of 30 μ l/min. Desalting was performed for 5 min with eluent flow to waste followed by back-flushing of the sample during the whole analysis from the pre-column to the PepMap100 RSLC C18 nano-HPLC column (2 μ m, 100 Å, 75 μ m ID \times 50 cm, nanoViper, Dionex, Germany). Following linear gradient was used for peptide separation: starting conditions 95% solvent A / 5% solvent B, linear

increase to 30% B in 90 min, further linear increase to 60% B in 5 min, further linear increase to 95% B in 5 min, washing with these conditions for 5 min, and re-equilibration to starting conditions. Water containing 0.1% formic acid was used as solvent A, acetonitrile containing 0.1% formic acid as solvent B.

The nano-HPLC was coupled online to the Quadrupole-Orbitrap Mass Spectrometer using a standard coated SilicaTip (ID 20 μm , Tip-ID 10 μM , New Objective, Woburn, MA, USA). Mass range of m/z 300 to 1650 was acquired with a resolution of 70000 (Q-Exactive Plus) or 60000 (Q-Exactive HF) for full scan, followed by up to 10 (Q-Exactive Plus) or 15 (Q-Exactive HF) high energy collision dissociation (HCD) MS / MS scans of the most intense at least doubly charged ions.

Data evaluation was performed separately for both biological replicates using MaxQuant software (v.1.6.1.0) including the Andromeda search algorithm and searching the human reference proteome of the Uniprot database.^[203] The search was performed for full enzymatic trypsin cleavages allowing two miscleavages. For protein modifications carbamidomethylation was chosen as fixed and oxidation of methionine and acetylation of the N-terminus as variable modifications. The mass accuracy for full mass spectra was set to 4.5 ppm and for MS/MS spectra 20 ppm. The false discovery rates for peptide and protein identification were set to 1%. Only proteins for which at least two peptides were quantified were chosen for further validation. Relative quantification of proteins was carried out using the label-free quantification algorithm implemented in MaxQuant. Further data evaluation was performed using Perseus software (v. 1.6.1.1).^[206] Proteins not identified with at least two peptides in at least one of the samples and known contamination were filtered off. Samples resulting from pulldown using the active probe were grouped together and those from the pulldown using the inactive one as well. Label-free quantification (LFQ) intensities were logarithmized (\log_2) and proteins, which were not three times quantified in at least one of the groups, were filtered off. Missing values were imputed using small normal distributed values (width 0.3, down shift 1.8) and a two sided t-test ($s_0 = 1$, FDR 0.05) was performed. Proteins which were statistically significant enriched by the active probe compared to the inactive one were considered as hits.

4.6.7. Isothermal dose response fingerprint

MCF7/LC3 lysate (100 μl) was treated with decreasing concentrations of Autoquin (400 μM to 12.5 μM) or the respective amount of DMSO, incubated for 10 min at ambient temperature

and subjected to heat treatment at 56 °C. Subsequently, the samples were centrifuged at 100,000 g for 20 min and the supernatant was transferred into new Eppendorf tubes. The remaining amount of Ferrochelatase in each sample was detected by western blotting.

4.6.8. Seahorse XF Cell Mito Stress Test

MCF7/LC3 cells were seeded one day prior to the assay with a density of 20,000 cells/well in 100 µl medium. The moats around the wells were filled with PBS (400 µl). The XF cartridge was hydrated with XF Calibrant (200 µl/well) for approximately 24 h in a non-CO₂ incubator at 37 °C. In order to obtain the assay medium, XF base medium was supplemented with glucose (final concentration 10 mM), GlutaMax (final concentration 2 mM) and sodium pyruvate (final concentration 1 mM). Subsequently, the pH of the assay medium was adjusted to 7.4 at 37 °C.

On the day of the assay the medium was removed and replaced with 180 µl of assay medium. The cells were equilibrated for 45 min at 37°C without CO₂. Stocks from the Seahorse XF Cell Mito Stress Test Kit (Agilent Cat. No. 103015-100) were dissolved in assay buffer to final concentration of 50 mM for oligomycin and FCCP and 25 µM for rotenone/antimycin A. The compounds were diluted with assay buffer to the desired concentrations and were loaded into the respective injection ports. For the protocol template, each cycle was adjusted to 3 min mixing and 3 min measurement. The baseline was recorded over 5 cycles, followed by injection of the inhibitor or DMSO control recorded over 10 cycles. Injection of oligomycin, FCCP and rotenone/antimycin A was each detected over 3 cycles. Analysis of the results was performed with the Wave program.

4.6.9. Mitochondrial complex inhibition screening

MCF7/LC3 cells were seeded one day prior to the assay with a density of 20,000 cells/well in 100 µl medium. The moats around the wells were filled with PBS (400 µl). The XF cartridge was hydrated with XF Calibrant (200 µl/well) for approximately 24 h in a non-CO₂ incubator at 37 °C. For Complex I to III the mitochondrial assay solution (220 mM Mannitol, 70 mM Sucrose, 10 mM KH₂PO₄, 5 mM MgCl₂, 2 mM HEPES, 1 mM EGTA, pH 7.4 at 37 °C) was supplemented with 0.2 % (w/v) fatty acid free BSA. Oligomycin, antimycin A and sodium azide were diluted with mitochondrial assay solution to tenfold of their final concentration. For the assay each inhibitor was injected with ADP (final concentration 1 mM) and substrates of

the respective complex. Subsequently, oligomycin (final concentration 1 μM) was injected followed by antimycin A (final concentration 1 μM) for complex I and II and sodium azide (final concentration 20 mM) for complex III and IV. For each of the complexes a known inhibitor was tested as a positive control. For the protocol template, each cycle was adjusted to 2 min mixing, 2 min waiting and 3 min measurement. The baseline was recorded over 3 cycles, followed by injection of the respective reagents, ADP and inhibitor or DMSO control recorded over 5 cycles. Injection of oligomycin and antimycin A or sodium azide was each detected over 3 cycles. Analysis of the results was performed with the Wave program.

Mitochondrial Complex	Reagents	Control Inhibitor
Complex I	Pyruvate (10 mM) Malate (1 mM)	Rotenone (1 μM)
Complex II	Succinate (10 mM) Rotenone (1 μM)	Malonate (4 mM)
Complex III	Duroquinol (0.5 mM)	Antimycin A (30 μM)
Complex IV	TMPD (0.5 mM) Ascrobate (2 mM)	KCN (20 mM)

4.6.10. Direct mitochondrial complex I activity test

The direct influence of Authipyrin on complex I was investigated with the MitoCheck® Complex I Activity Assay Kit (Caymen Chemical, Cat. No. 700930) according to the manufacturer's instructions.

4.6.11. Cell painting assay

Initially, 5 μl U2OS medium were added to each well of a 384-well plate (PerkinElmer CellCarrier-384 Ultra). Subsequently, U2OS cell were seeded with a density of 1600 cells per well in 20 μl medium. The plate was incubated for 5 min at the ambient temperature, followed by an additional 4 h incubation (37 $^{\circ}\text{C}$, 5% CO_2). Compound treatment was performed with the Echo 520 acoustic dispenser (Labcyte) at final concentrations of 10 μM , 3 μM or 1 μM .

Incubation with compound was performed for 20 h (37 °C, 5% CO₂). Subsequently, mitochondria were stained with Mito Tracker Deep Red (Thermo Fisher Scientific, Cat. No. M22426). The Mito Tracker Deep Red stock solution (1 mM) was diluted to a final concentration of 100 nM in prewarmed medium. The medium was removed from the plate leaving 10 µl residual volume and 25 µl of the Mito Tracker solution were added to each well. The plate was incubated for 30 min in darkness (37 °C, 5% CO₂). To fix the cells 7 µl of 18.5 % formaldehyde in PBS were added, resulting in a final formaldehyde concentration of 3.7 %. Subsequently, the plate was incubated for another 20 min in darkness (37 °C, 5% CO₂) and washed three times with 70 µl of PBS. (Biotek Washer Elx405). Cells were permeabilized by addition of 25 µl 0.1% Triton X-100 to each well, followed by 15 min incubation (37 °C, 5% CO₂) in darkness. The cells were washed three times with PBS leaving a final volume of 70 µl. To each well 25 µl of a staining solution were added, which contains 1% BSA, 50 µl Phalloidin (Thermo Fisher Scientific, A12381), 25 µg/ml Concanavalin A (Thermo Fisher Scientific, Cat. No. C11252), 50 µl/ml Hoechst 33342 (Sigma, Cat. No. B2261-25mg), 15 µl/ml WGA-Alexa594 conjugate (Thermo Fisher Scientific, Cat. No. W11262) and 0.3 µl/ml SYTO 14 solution (Thermo Fisher Scientific, Cat. No. S7576). The plate is incubated for 30 min (37 °C, 5% CO₂) in darkness and washed three times with 70 µl PBS. After the final washing step the PBS was not aspirated. The plates were sealed and centrifuged for 1 min at 500 rpm.

The plates were prepared in triplicates and imaged using a Micro XL High-Content Screening System (Molecular Devices, 5 channels, 9 sites per well, 20x magnification, binning 2). The generated images were processed with the CellProfiler package (<https://cellprofiler.org/>) on a computing cluster of the Max Planck Society. Further analysis was performed with custom Python (<https://www.python.org/>) scripts using the Pandas (<https://pandas.pydata.org/>) and Dask (<https://dask.org/>) data processing libraries. Data was aggregated per well and a subset of 579 parameters calculated by CellProfiler that had a high reproducibility between biological repeats was used to determine morphological fingerprint profiles. These profiles were calculated from log₂-fold changes of the parameters to the median values and the median absolute deviations (MAD) of the DMSO controls. Similarities of these morphological profiles were calculated from the correlation distances between two profiles (<https://docs.scipy.org/doc/scipy-0.14.0/reference/generated/scipy.spatial.distance.correlation.html>) and the most similar profiles were determined from a set of 3000 reference compounds that was also measured in the assay.

5. APPENDIX

Table 7: Kinase inhibition by Authipyrin. The inhibitory effect of Authipyrin on 458 kinases was determined by SelectScreen Kinase Profiling (Thermo Fisher Scientific). Three different assay formats were employed: Z-Lyte (activity based), Adapta (activity based) and Lantha (binding based). The six kinases with strongest inhibition were analyzed in dose-response.

Method	cATP [μ M]	Kinase	Inhibition [%]		Inhibition [%] mean
			Point 1	Point 2	
Z-Lyte	Km app	AMPK (A1/B2/G2)	14	8	11
Z-Lyte	Km app	AMPK (A1/B2/G3)	10	3	6
Z-Lyte	Km app	AMPK (A2/B1/G2)	3	8	6
Z-Lyte	Km app	AMPK (A2/B1/G3)	4	9	7
Z-Lyte	Km app	AMPK (A2/B2/G3)	6	3	4
Z-Lyte	Km app	AMPK A1/B1/G1	3	3	3
Z-Lyte	Km app	AMPK A2/B1/G1	5	3	4
Z-Lyte	Km app	AURKA (Aurora A)	15	14	14
Z-Lyte	Km app	AURKB (Aurora B)	12	10	11
Z-Lyte	Km app	AURKC (Aurora C)	6	7	6
Z-Lyte	Km app	AXL	3	2	3
Z-Lyte	Km app	BLK	51	42	47
Z-Lyte	Km app	BMX	9	8	9
Z-Lyte	100	BRAF V599E	17	17	17
Z-Lyte	100	BRAF	23	19	21
Z-Lyte	Km app	BRSK1 (SAD1)	2	14	8
Z-Lyte	Km app	BTK	18	16	17
Z-Lyte	Km app	CAMK1D (CaMKI delta)	2	-1	0
Z-Lyte	Km app	CAMK1G (CaMKI gamma)	-2	-4	-3
Z-Lyte	Km app	CAMK2A (CaMKII alpha)	8	21	14
Z-Lyte	Km app	CAMK2B (CaMKII beta)	1	5	3
Z-Lyte	Km app	CAMK2D (CaMKII delta)	-4	-5	-4
Z-Lyte	Km app	CAMK4 (CaMKIV)	-4	1	-2
Z-Lyte	Km app	CDC42 BPA (MRCKA)	23	20	22
Z-Lyte	Km app	CDC42 BPB (MRCKB)	0	-5	-3
Z-Lyte	Km app	CDC42 BPG (MRCKG)	-5	-5	-5
Z-Lyte	Km app	CDK1/cyclin B	19	6	13
Z-Lyte	Km app	CDK17/cyclin Y	5	21	13
Z-Lyte	Km app	CDK18/cyclin Y	8	11	9
Z-Lyte	Km app	CDK2/cyclin A	5	4	5
Z-Lyte	Km app	CDK5/p25	2	9	5
Z-Lyte	Km app	CDK5/p35	1	3	2
Z-Lyte	Km app	CDKL5	13	13	13
Z-Lyte	Km app	CHEK1 (CHK1)	9	16	12
Z-Lyte	Km app	CHEK2 (CHK2)	2	1	2
Z-Lyte	Km app	CLK1	7	6	6
Z-Lyte	Km app	CLK2	21	16	19

Z-Lyte	Km app	CLK3	4	6	5
Z-Lyte	Km app	CSF1R (FMS)	19	16	17
Z-Lyte	Km app	CSK	11	7	9
Z-Lyte	Km app	CSNK1A1 (CK1 alpha 1)	8	8	8
Z-Lyte	Km app	CSNK1A1L	10	9	9
Z-Lyte	Km app	CSNK1D (CK1 delta)	5	5	5
Z-Lyte	Km app	CSNK1E (CK1 epsilon) R178C	14	10	12
Z-Lyte	Km app	CSNK1E (CK1 epsilon)	21	26	23
Z-Lyte	Km app	CSNK1G1 (CK1 gamma 1)	0	3	1
Z-Lyte	Km app	CSNK1G2 (CK1 gamma 2)	6	5	6
Z-Lyte	Km app	CSNK1G3 (CK1 gamma 3)	5	9	7
Z-Lyte	Km app	CSNK2A1 (CK2 alpha 1)	1	5	3
Z-Lyte	Km app	CSNK2A2 (CK2 alpha 2)	7	2	5
Z-Lyte	Km app	DAPK3 (ZIPK)	0	12	6
Z-Lyte	Km app	DCAMKL1 (DCLK1)	7	6	6
Z-Lyte	Km app	DCAMKL2 (DCK2)	6	7	6
Z-Lyte	Km app	DNA-PK	-3	0	-2
Z-Lyte	Km app	DYRK1A	5	3	4
Z-Lyte	Km app	DYRK1B	-1	0	-1
Z-Lyte	Km app	DYRK3	9	10	9
Z-Lyte	Km app	DYRK4	2	3	3
Z-Lyte	Km app	EEF2K	6	4	5
Z-Lyte	Km app	EGFR (ErbB1) C797S	5	-3	1
Z-Lyte	Km app	EGFR (ErbB1) G719C	11	7	9
Z-Lyte	Km app	EGFR (ErbB1) G719S	6	7	6
Z-Lyte	Km app	EGFR (ErbB1) L858R	12	-4	4
Z-Lyte	Km app	EGFR (ErbB1) L861Q	6	7	6
Z-Lyte	Km app	EGFR (ErbB1) T790M C797S L858R	-1	8	3
Z-Lyte	Km app	EGFR (ErbB1) T790M L858R	0	-4	-2
Z-Lyte	Km app	EGFR (ErbB1) T790M	2	9	5
Z-Lyte	Km app	EGFR (ErbB1)	1	-2	0
Z-Lyte	Km app	EPHA1	12	5	8
Z-Lyte	Km app	EPHA2	4	5	4
Z-Lyte	Km app	EPHA4	4	7	5
Z-Lyte	Km app	EPHA5	7	0	4
Z-Lyte	Km app	EPHA8	17	18	17
Z-Lyte	Km app	EPHB1	5	4	4
Z-Lyte	Km app	EPHB2	9	6	7
Z-Lyte	Km app	EPHB3	8	8	8
Z-Lyte	Km app	EPHB4	3	7	5
Z-Lyte	Km app	ERBB2 (HER2)	1	-1	0
Z-Lyte	Km app	ERBB4 (HER4)	4	2	3
Z-Lyte	Km app	FER	9	4	7
Z-Lyte	Km app	FES (FPS)	-2	1	0
Z-Lyte	Km app	FGFR1	3	6	4

Z-Lyte	Km app	FGFR2 N549H	4	7	5
Z-Lyte	Km app	FGFR2	1	3	2
Z-Lyte	Km app	FGFR3 K650E	6	6	6
Z-Lyte	Km app	FGFR3 V555M	-1	0	0
Z-Lyte	Km app	FGFR3	-6	-2	-4
Z-Lyte	Km app	FGFR4	4	5	5
Z-Lyte	Km app	FGR	13	20	17
Z-Lyte	Km app	FLT1 (VEGFR1)	3	0	2
Z-Lyte	Km app	FLT3 D835Y	25	23	24
Z-Lyte	Km app	FLT3	4	5	5
Z-Lyte	Km app	FLT4 (VEGFR3)	10	9	10
Z-Lyte	Km app	FRAP1 (mTOR)	-15	-7	-11
Z-Lyte	Km app	FRK (PTK5)	35	31	33
Z-Lyte	Km app	FYN	12	13	13
Z-Lyte	Km app	GRK4	7	8	8
Z-Lyte	Km app	GRK5	1	2	1
Z-Lyte	Km app	GRK6	11	10	11
Z-Lyte	Km app	GRK7	3	11	7
Z-Lyte	Km app	GSK3A (GSK3 alpha)	5	4	4
Z-Lyte	Km app	GSK3B (GSK3 beta)	3	3	3
Z-Lyte	Km app	HCK	44	42	43
Z-Lyte	Km app	HIPK1 (Myak)	0	1	0
Z-Lyte	Km app	HIPK2	8	2	5
Z-Lyte	Km app	HIPK3 (YAK1)	-3	2	-1
Z-Lyte	Km app	HIPK4	10	4	7
Z-Lyte	Km app	IGF1R	-5	4	-1
Z-Lyte	Km app	IKBKB (IKK beta)	-17	5	-6
Z-Lyte	Km app	IKBKE (IKK epsilon)	20	11	15
Z-Lyte	Km app	INSR	5	0	2
Z-Lyte	Km app	INSRR (IRR)	2	4	3
Z-Lyte	Km app	IRAK4	-9	5	-2
Z-Lyte	Km app	ITK	1	-2	0
Z-Lyte	Km app	JAK1	2	2	2
Z-Lyte	Km app	JAK2 JH1 JH2 V617F	-1	-10	-5
Z-Lyte	Km app	JAK2 JH1 JH2	-5	-5	-5
Z-Lyte	Km app	JAK2	-13	-7	-10
Z-Lyte	Km app	JAK3	-2	0	-1
Z-Lyte	Km app	KDR (VEGFR2)	5	2	4
Z-Lyte	Km app	KIT T670I	-4	1	-2
Z-Lyte	Km app	KIT V559D V654A	1	2	2
Z-Lyte	Km app	KIT V559D	-2	5	1
Z-Lyte	Km app	KIT V560G	18	11	15
Z-Lyte	Km app	KIT	5	8	6
Z-Lyte	Km app	KSR2	11	3	7
Z-Lyte	Km app	LCK	8	10	9

Z-Lyte	Km app	LTK (TYK1)	4	2	3
Z-Lyte	Km app	LYN A	22	24	23
Z-Lyte	Km app	LYN B	23	25	24
Z-Lyte	100	MAP2K1 (MEK1)	14	16	15
Z-Lyte	100	MAP2K2 (MEK2)	-2	-3	-3
Z-Lyte	100	MAP2K6 (MKK6)	11	9	10
Z-Lyte	Km app	MAP3K19 (YSK4)	-15	-12	-13
Z-Lyte	100	MAP3K8 (COT)	13	9	11
Z-Lyte	Km app	MAP3K9 (MLK1)	9	14	12
Z-Lyte	Km app	MAP4K2 (GCK)	9	12	10
Z-Lyte	Km app	MAP4K4 (HGK)	12	10	11
Z-Lyte	Km app	MAP4K5 (KHS1)	21	16	18
Z-Lyte	Km app	MAPK1 (ERK2)	2	-7	-3
Z-Lyte	100	MAPK10 (JNK3)	2	0	1
Z-Lyte	Km app	MAPK11 (p38 beta)	6	8	7
Z-Lyte	Km app	MAPK12 (p38 gamma)	12	5	8
Z-Lyte	Km app	MAPK13 (p38 delta)	1	0	1
Z-Lyte	Km app	MAPK14 (p38 alpha) Direct	4	2	3
Z-Lyte	100	MAPK14 (p38 alpha)	3	13	8
Z-Lyte	Km app	MAPK3 (ERK1)	7	4	5
Z-Lyte	Km app	MAPK7 (ERK5)	11	10	11
Z-Lyte	100	MAPK8 (JNK1)	-2	2	0
Z-Lyte	100	MAPK9 (JNK2)	2	0	1
Z-Lyte	Km app	MAPKAPK2	3	5	4
Z-Lyte	Km app	MAPKAPK3	-4	-2	-3
Z-Lyte	Km app	MAPKAPK5 (PRAK)	4	13	8
Z-Lyte	Km app	MARK1 (MARK)	9	3	6
Z-Lyte	Km app	MARK2	2	10	6
Z-Lyte	Km app	MARK3	7	3	5
Z-Lyte	Km app	MARK4	2	4	3
Z-Lyte	Km app	MATK (HYL)	15	4	9
Z-Lyte	Km app	MELK	19	11	15
Z-Lyte	Km app	MERTK (cMER)	6	7	6
Z-Lyte	Km app	MET (cMet) Y1235D	17	14	15
Z-Lyte	Km app	MET (cMet)	5	5	5
Z-Lyte	Km app	MET M1250T	13	16	15
Z-Lyte	Km app	MINK1	6	5	6
Z-Lyte	Km app	MKNK1 (MNK1)	-8	13	3
Z-Lyte	Km app	MST1R (RON)	-6	-1	-3
Z-Lyte	Km app	MST4	8	8	8
Z-Lyte	Km app	MUSK	18	18	18
Z-Lyte	Km app	MYLK2 (skMLCK)	0	1	0
Z-Lyte	Km app	NEK1	5	3	4
Z-Lyte	Km app	NEK2	6	5	5
Z-Lyte	Km app	NEK4	-1	1	0

Z-Lyte	Km app	NEK6	5	5	5
Z-Lyte	Km app	NEK9	-2	-3	-2
Z-Lyte	Km app	NIM1K	10	13	12
Z-Lyte	Km app	NTRK1 (TRKA)	10	14	12
Z-Lyte	Km app	NTRK2 (TRKB)	3	4	4
Z-Lyte	Km app	NTRK3 (TRKC)	5	8	7
Z-Lyte	Km app	PAK1	9	9	9
Z-Lyte	Km app	PAK2 (PAK65)	11	-6	2
Z-Lyte	Km app	PAK3	-14	8	-3
Z-Lyte	Km app	PAK4	13	13	13
Z-Lyte	Km app	PAK6	-1	4	1
Z-Lyte	Km app	PAK7 (KIAA1264)	3	-1	1
Z-Lyte	Km app	PASK	8	8	8
Z-Lyte	Km app	PDGFRA (PDGFR alpha)	0	4	2
Z-Lyte	Km app	PDGFRA D842V	5	11	8
Z-Lyte	Km app	PDGFRA T674I	8	5	7
Z-Lyte	Km app	PDGFRA V561D	19	6	13
Z-Lyte	Km app	PDGFRB (PDGFR beta)	3	-3	0
Z-Lyte	Km app	PDK1 Direct	6	3	4
Z-Lyte	100	PDK1	9	5	7
Z-Lyte	Km app	PEAK1	82	84	83
Z-Lyte	Km app	PHKG1	-5	-10	-8
Z-Lyte	Km app	PHKG2	-6	-4	-5
Z-Lyte	Km app	PIM1	11	6	8
Z-Lyte	Km app	PIM2	-2	-5	-3
Z-Lyte	Km app	PIM3	-1	-4	-3
Z-Lyte	Km app	PKN1 (PRK1)	-25	-18	-22
Z-Lyte	Km app	PLK1	9	6	8
Z-Lyte	Km app	PLK2	1	3	2
Z-Lyte	Km app	PLK3	-2	2	0
Z-Lyte	Km app	PRKACA (PKA)	-5	-1	-3
Z-Lyte	Km app	PRKCA (PKC alpha)	13	18	15
Z-Lyte	Km app	PRKCB1 (PKC beta I)	-5	-1	-3
Z-Lyte	Km app	PRKCB2 (PKC beta II)	9	-1	4
Z-Lyte	Km app	PRKCD (PKC delta)	-2	-3	-2
Z-Lyte	Km app	PRKCE (PKC epsilon)	14	2	8
Z-Lyte	Km app	PRKCG (PKC gamma)	25	29	27
Z-Lyte	Km app	PRKCH (PKC eta)	20	16	18
Z-Lyte	Km app	PRKCI (PKC iota)	4	1	2
Z-Lyte	Km app	PRKCN (PKD3)	6	9	8
Z-Lyte	Km app	PRKCQ (PKC theta)	-15	-18	-16
Z-Lyte	Km app	PRKCZ (PKC zeta)	-10	-3	-7
Z-Lyte	Km app	PRKD1 (PKC mu)	11	14	13
Z-Lyte	Km app	PRKD2 (PKD2)	4	7	5
Z-Lyte	Km app	PRKG1	8	3	6

Z-Lyte	Km app	PRKG2 (PKG2)	6	4	5
Z-Lyte	Km app	PRKX	-1	-13	-7
Z-Lyte	Km app	PTK2 (FAK)	7	7	7
Z-Lyte	Km app	PTK2B (FAK2)	8	6	7
Z-Lyte	Km app	PTK6 (Brk)	1	1	1
Z-Lyte	100	RAF1 (cRAF) Y340D Y341D	28	23	25
Z-Lyte	Km app	RET A883F	7	-2	3
Z-Lyte	Km app	RET S891A	-7	6	-1
Z-Lyte	Km app	RET V804E	12	7	9
Z-Lyte	Km app	RET V804L	1	3	2
Z-Lyte	Km app	RET Y791F	7	6	6
Z-Lyte	Km app	RET	2	6	4
Z-Lyte	Km app	ROCK1	-6	6	0
Z-Lyte	Km app	ROCK2	0	23	12
Z-Lyte	Km app	ROS1	5	1	3
Z-Lyte	Km app	RPS6KA1 (RSK1)	7	6	6
Z-Lyte	Km app	RPS6KA2 (RSK3)	9	8	9
Z-Lyte	Km app	RPS6KA3 (RSK2)	6	8	7
Z-Lyte	Km app	RPS6KA4 (MSK2)	3	9	6
Z-Lyte	Km app	RPS6KA5 (MSK1)	4	-2	1
Z-Lyte	Km app	RPS6KA6 (RSK4)	-4	11	4
Z-Lyte	Km app	RPS6KB1 (p70S6K)	-1	-20	-11
Z-Lyte	Km app	RPS6KB2 (p70S6Kb)	-7	0	-4
Z-Lyte	Km app	SBK1	-10	-9	-9
Z-Lyte	Km app	SGK (SGK1)	2	0	1
Z-Lyte	Km app	SGK2	2	6	4
Z-Lyte	Km app	SGKL (SGK3)	-8	4	-2
Z-Lyte	Km app	SNF1LK2	15	1	8
Z-Lyte	Km app	SRC N1	6	8	7
Z-Lyte	Km app	SRC	21	22	22
Z-Lyte	Km app	SRMS (Srm)	7	6	7
Z-Lyte	Km app	SRPK1	0	1	0
Z-Lyte	Km app	SRPK2	1	1	1
Z-Lyte	Km app	STK22B (TSSK2)	14	5	10
Z-Lyte	Km app	STK22D (TSSK1)	12	14	13
Z-Lyte	Km app	STK23 (MSSK1)	3	3	3
Z-Lyte	Km app	STK24 (MST3)	17	13	15
Z-Lyte	Km app	STK25 (YSK1)	4	6	5
Z-Lyte	Km app	STK3 (MST2)	5	2	3
Z-Lyte	Km app	STK4 (MST1)	-1	14	6
Z-Lyte	Km app	SYK	3	6	4
Z-Lyte	Km app	TAOK2 (TAO1)	4	-3	1
Z-Lyte	Km app	TBK1	8	3	5
Z-Lyte	Km app	TEK (TIE2) Y897S	0	2	1
Z-Lyte	Km app	TEK (Tie2)	8	17	12

Z-Lyte	Km app	TNK1	-3	15	6
Z-Lyte	Km app	TXK	-3	6	1
Z-Lyte	Km app	TYK2	7	8	8
Z-Lyte	Km app	TYRO3 (RSE)	6	6	6
Z-Lyte	Km app	YES1	14	16	15
Z-Lyte	Km app	ZAP70	4	4	4
Adapta	10	CAMK1 (CaMK1)	9	14	11
Adapta	10	CDK4/cyclin D1	10	5	7
Adapta	10	CDK4/cyclin D3	8	-1	3
Adapta	10	CDK6/cyclin D1	-7	2	-3
Adapta	Km app	CDK7/cyclin H/MNAT1	7	3	5
Adapta	Km app	CDK9/cyclin T1	14	2	8
Adapta	Km app	CHUK (IKK alpha)	5	-2	1
Adapta	Km app	DAPK1	11	11	11
Adapta	Km app	GSG2 (Haspin)	56	47	51
Adapta	Km app	IRAK1	4	7	6
Adapta	Km app	LRRK2 FL	-2	9	3
Adapta	Km app	LRRK2 G2019S FL	-5	3	-1
Adapta	Km app	LRRK2 G2019S	3	7	5
Adapta	Km app	LRRK2 I2020T	1	6	4
Adapta	Km app	LRRK2 R1441C	14	5	9
Adapta	Km app	LRRK2	11	8	10
Adapta	Km app	NUAK1 (ARK5)	17	26	21
Adapta	Km app	PI4K2A (PI4K2 alpha)	4	3	4
Adapta	Km app	PI4K2B (PI4K2 beta)	5	6	5
Adapta	10	PI4KA (PI4K alpha)	-4	-1	-3
Adapta	Km app	PI4KB (PI4K beta)	9	11	10
Adapta	Km app	PIK3C2A (PI3K-C2 alpha)	17	14	16
Adapta	10	PIK3C2B (PI3K-C2 beta)	17	15	16
Adapta	Km app	PIK3C2G (PI3K-C2 gamma)	32	35	34
Adapta	Km app	PIK3C3 (hVPS34)	9	17	13
Adapta	10	PIK3CA E542K/PIK3R1 (p110 alpha E542K/p85 alpha)	18	11	15
Adapta	Km app	PIK3CA E545K/PIK3R1 (p110 alpha E545K/p85 alpha)	12	9	11
Adapta	Km app	PIK3CA/PIK3R1 (p110 alpha/p85 alpha)	18	34	26
Adapta	Km app	PIK3CA/PIK3R3 (p110 alpha/p55 gamma)	5	4	4
Adapta	Km app	PIK3CB/PIK3R1 (p110 beta/p85 alpha)	6	1	3
Adapta	Km app	PIK3CB/PIK3R2 (p110 beta/p85 beta)	11	11	11
Adapta	Km app	PIK3CD/PIK3R1 (p110 delta/p85 alpha)	15	9	12
Adapta	Km app	PIK3CG (p110 gamma)	9	15	12
Adapta	10	PIP4K2A	11	12	11
Adapta	10	PIP5K1A	0	2	1

Adapta	10	PIP5K1B	9	-2	4
Adapta	10	PIP5K1C	5	1	3
Adapta	Km app	SPHK1	18	9	13
Adapta	10	SPHK2	-1	1	0
Lantha	1000	AAK1	5	4	5
Lantha	1000	ABL1 H396P	8	11	9
Lantha	1000	ABL1 M351T	27	29	28
Lantha	1000	ABL1 Q252H	21	18	19
Lantha	1000	ACVR1 (ALK2) R206H	11	9	10
Lantha	1000	ACVR1 (ALK2)	2	-4	-1
Lantha	1000	ACVR2A	18	13	16
Lantha	1000	ACVR2B	-9	-4	-7
Lantha	1000	ACVRL1 (ALK1)	-8	-6	-7
Lantha	1000	ADCK3	18	-2	8
Lantha	1000	ALK C1156Y	9	15	12
Lantha	1000	ALK F1174L	3	15	9
Lantha	1000	ALK L1196M	3	6	5
Lantha	1000	ALK R1275Q	11	3	7
Lantha	1000	ALK T1151_L1152insT	12	8	10
Lantha	1000	AMPK (A1/B1/G2)	3	2	3
Lantha	1000	AMPK (A1/B1/G3)	6	4	5
Lantha	1000	AMPK (A1/B2/G1)	-1	-6	-3
Lantha	1000	AMPK (A2/B2/G1)	7	1	4
Lantha	1000	AMPK (A2/B2/G2)	2	12	7
Lantha	1000	ANKK1	-8	7	-1
Lantha	1000	AXL R499C	10	8	9
Lantha	1000	BMPR1A (ALK3)	6	8	7
Lantha	1000	BMPR1B (ALK6)	14	18	16
Lantha	1000	BMPR2	16	23	20
Lantha	1000	BRAF V599E	5	6	6
Lantha	1000	BRAF	6	21	13
Lantha	1000	BRSK2	4	7	6
Lantha	1000	CAMK2G (CaMKII gamma)	3	-5	-1
Lantha	1000	CAMKK1 (CAMKKA)	1	-5	-2
Lantha	1000	CAMKK2 (CaMKK beta)	0	1	0
Lantha	1000	CASK	-1	8	3
Lantha	1000	CDC7/DBF4	24	33	29
Lantha	1000	CDK11 (Inactive)	69	71	70
Lantha	1000	CDK11/cyclin C	37	40	38
Lantha	1000	CDK13/cyclin K	5	2	4
Lantha	1000	CDK14 (PFTK1)/cyclin Y	5	16	11
Lantha	1000	CDK16 (PCTK1)/cyclin Y	5	-1	2
Lantha	1000	CDK2/cyclin A1	5	2	3
Lantha	1000	CDK2/cyclin E1	15	18	17
Lantha	1000	CDK2/cyclin O	16	24	20

Lantha	1000	CDK3/cyclin E1	28	20	24
Lantha	1000	CDK5 (Inactive)	-2	-10	-6
Lantha	1000	CDK8/cyclin C	37	35	36
Lantha	1000	CDK9 (Inactive)	-4	2	-1
Lantha	1000	CDK9/cyclin K	6	8	7
Lantha	1000	CLK4	46	44	45
Lantha	1000	DAPK2	8	-3	3
Lantha	1000	DDR1	6	-3	2
Lantha	1000	DDR2 N456S	56	60	58
Lantha	1000	DDR2 T654M	5	8	7
Lantha	1000	DDR2	14	14	14
Lantha	1000	DMPK	-5	3	-1
Lantha	1000	DYRK2	31	31	31
Lantha	1000	EGFR (ErbB1) d746-750	9	8	8
Lantha	1000	EGFR (ErbB1) d747-749 A750P	4	9	6
Lantha	1000	EIF2AK2 (PKR)	7	7	7
Lantha	1000	EPHA3	14	15	14
Lantha	1000	EPHA6	2	3	3
Lantha	1000	EPHA7	2	4	3
Lantha	1000	ERN1	14	19	17
Lantha	1000	ERN2	17	-2	8
Lantha	1000	FGFR1 V561M	3	6	4
Lantha	1000	FGFR3 G697C	18	18	18
Lantha	1000	FGFR3 K650M	17	29	23
Lantha	1000	FLT3 ITD	-2	7	2
Lantha	1000	FYN A	18	21	20
Lantha	1000	GAK	26	38	32
Lantha	1000	GRK1	-5	-1	-3
Lantha	1000	HUNK	3	-5	-1
Lantha	1000	ICK	26	21	23
Lantha	1000	IRAK3	30	42	36
Lantha	1000	KIT A829P	5	6	6
Lantha	1000	KIT D816H	17	10	13
Lantha	1000	KIT D816V	22	10	16
Lantha	1000	KIT D820E	8	6	7
Lantha	1000	KIT N822K	16	11	13
Lantha	1000	KIT T670E	5	5	5
Lantha	1000	KIT V559D T670I	5	7	6
Lantha	1000	KIT V654A	-4	-1	-3
Lantha	1000	KIT Y823D	-3	6	2
Lantha	1000	LATS2	6	-3	2
Lantha	1000	LIMK1	3	-4	-1
Lantha	1000	LIMK2	3	0	2
Lantha	1000	MAP2K1 (MEK1) S218D S222D	0	4	2
Lantha	1000	MAP2K1 (MEK1)	2	3	2

Lantha	1000	MAP2K2 (MEK2)	-2	3	1
Lantha	1000	MAP2K4 (MEK4)	-1	-1	-1
Lantha	1000	MAP2K5 (MEK5)	5	13	9
Lantha	1000	MAP2K6 (MKK6) S207E T211E	0	4	2
Lantha	1000	MAP2K6 (MKK6)	1	0	0
Lantha	1000	MAP3K10 (MLK2)	-2	-13	-8
Lantha	1000	MAP3K11 (MLK3)	5	13	9
Lantha	1000	MAP3K14 (NIK)	7	-4	2
Lantha	1000	MAP3K2 (MEKK2)	42	51	46
Lantha	1000	MAP3K3 (MEKK3)	-15	-7	-11
Lantha	1000	MAP3K5 (ASK1)	6	-6	0
Lantha	1000	MAP3K7/MAP3K7IP1 (TAK1-TAB1)	9	14	11
Lantha	1000	MAP4K1 (HPK1)	22	27	24
Lantha	1000	MAP4K3 (GLK)	2	5	4
Lantha	1000	MAPK10 (JNK3)	3	7	5
Lantha	1000	MAPK15 (ERK7)	13	6	10
Lantha	1000	MAPK8 (JNK1)	-5	6	1
Lantha	1000	MAPK9 (JNK2)	-1	2	1
Lantha	1000	MASTL	21	5	13
Lantha	1000	MERTK (cMER) A708S	11	4	8
Lantha	1000	MET D1228H	5	4	4
Lantha	1000	MKNK2 (MNK2)	29	27	28
Lantha	1000	MLCK (MLCK2)	-18	-15	-17
Lantha	1000	MLK4	9	-5	2
Lantha	1000	MYLK (MLCK)	2	3	2
Lantha	1000	MYLK4	0	6	3
Lantha	1000	MYO3A (MYO3 alpha)	9	-7	1
Lantha	1000	MYO3B (MYO3 beta)	4	2	3
Lantha	1000	NEK8	-1	-5	-3
Lantha	1000	NLK	4	5	4
Lantha	1000	NUAK2	18	17	17
Lantha	1000	PKMYT1	4	-5	-1
Lantha	1000	PKN2 (PRK2)	8	8	8
Lantha	1000	PLK4	8	19	14
Lantha	1000	PRKACB (PRKAC beta)	16	8	12
Lantha	1000	PRKACG (PRKAC gamma)	2	11	6
Lantha	1000	RAF1 (cRAF) Y340D Y341D	3	13	8
Lantha	1000	RET G691S	8	4	6
Lantha	1000	RET M918T	-2	14	6
Lantha	1000	RET V804M	-5	-7	-6
Lantha	1000	RIPK2	-4	-7	-6
Lantha	1000	RIPK3	28	5	16
Lantha	1000	SIK1	2	7	4
Lantha	1000	SIK3	0	2	1
Lantha	1000	SLK	5	7	6

Lantha	1000	STK16 (PKL12)	2	6	4
Lantha	1000	STK17A (DRAK1)	6	5	5
Lantha	1000	STK17B (DRAK2)	19	6	13
Lantha	1000	STK32B (YANK2)	-2	16	7
Lantha	1000	STK32C (YANK3)	15	0	7
Lantha	1000	STK33	17	3	10
Lantha	1000	STK38 (NDR)	17	18	17
Lantha	1000	STK38L (NDR2)	21	9	15
Lantha	1000	STK39 (STLK3)	7	2	4
Lantha	1000	TAOK1	31	8	20
Lantha	1000	TAOK3 (JIK)	5	16	10
Lantha	1000	TEC	2	7	4
Lantha	1000	TEK (TIE2) R849W	7	16	11
Lantha	1000	TEK (TIE2) Y1108F	-6	-4	-5
Lantha	1000	TESK1	-1	6	2
Lantha	1000	TESK2	5	7	6
Lantha	1000	TGFBR1 (ALK5)	-3	-5	-4
Lantha	1000	TGFBR2	14	21	18
Lantha	1000	TLK1	11	0	6
Lantha	1000	TLK2	-3	-7	-5
Lantha	1000	TNIK	6	12	9
Lantha	1000	TNK2 (ACK)	1	10	6
Lantha	1000	TTK	-5	10	3
Lantha	1000	ULK1	2	3	2
Lantha	1000	ULK2	-1	2	1
Lantha	1000	ULK3	-11	2	-4
Lantha	1000	VRK2	10	0	5
Lantha	1000	WEE1	12	17	14
Lantha	1000	WNK1	0	1	0
Lantha	1000	WNK2	16	4	10
Lantha	1000	WNK3	5	3	4
Lantha	1000	ZAK	9	10	10

Table 8: List of proteins identified as hits in a TPP experiment performed with Authipyrin, including gene name, protein name, dT_m [°C] and the shift in intensity at 67 °C ($dI_{67\text{ °C}}$). Data is shown as mean \pm SD (n = 3).

Entry	Gene name	Protein name	dT_m [°C]	$dI_{67\text{ °C}}$
1	MYO1E	Unconventional myosin-Ie	5.8 \pm 4.3	0.07 \pm 0.05
2	IMPA1	Inositol mono+B4:B32phosphatase 1	4.8 \pm 4.8	0.09 \pm 0.05
3	KIF16B	Kinesin-like protein KIF16B	4.4 \pm 0.9	0.08 \pm 0.02
4	STK32C	Serine/threonine-protein kinase 32C	4.2 \pm 4.5	0.13 \pm 0.15
5	GPATCH4	G patch domain-containing protein 4	3.4 \pm 2.8	0.14 \pm 0.01
6	SIRT3	NAD-dependent protein deacetylase sirtuin-3, mitochondrial	3.4 \pm 3.4	0.11 \pm 0.05
7	SLC25A13	Calcium-binding mitochondrial carrier protein Aralar2	3.3 \pm 2.8	0.10 \pm 0.12
8	BSCL2	Seipin	3.1 \pm 2.0	0.02 \pm 0.06
9	SPG20	Spartin	2.9 \pm 1.8	0.16 \pm 0.04
10	PTP4A2	Protein tyrosine phosphatase type IVA 2	2.9 \pm 0.7	0.02 \pm 0.05
11	MRPL40	39S ribosomal protein L40, mitochondrial	2.7 \pm 1.4	0.03 \pm 0.05
12	PHAX	Phosphorylated adapter RNA export protein	2.7 \pm 0.7	0.14 \pm 0.04
13	ITCH	E3 ubiquitin-protein ligase Itchy homolog	2.7 \pm 0.7	0.05 \pm 0.04
14	ARSB	Arylsulfatase B	2.3 \pm 0.6	0.00 \pm 0.01
15	WDR47	WD repeat-containing protein 47	1.8 \pm 0.4	0.02 \pm 0.02
16	MLYCD	Malonyl-CoA decarboxylase, mitochondrial	1.8 \pm 0.5	0.04 \pm 0.03
17	COQ9	Ubiquinone biosynthesis protein COQ9, mitochondrial	1.7 \pm 0.7	0.07 \pm 0.05
18	FAM195A	Protein FAM195A	1.7 \pm 2.7	0.16 \pm 0.02
19	GIT2	ARF GTPase-activating protein GIT2	1.6 \pm 3.7	0.20 \pm 0.04
20	BET1	BET1 homolog	1.3 \pm 2.0	0.16 \pm 0.07
21	POLR2A	DNA-directed RNA polymerase II subunit RPB1	1.2 \pm 1.1	0.18 \pm 0.01
22	PTK2	Focal adhesion kinase 1	1.2 \pm 2.1	0.17 \pm 0.01
23	CLASP2	CLIP-associating protein 2	0.3 \pm 1.9	0.13 \pm 0.02
24	PPP1R37	Protein phosphatase 1 regulatory subunit 37	0.1 \pm 2.9	0.15 \pm 0.01
25	SPINT1	Kunitz-type protease inhibitor 1	0.0 \pm 0.5	0.19 \pm 0.09

26	NFIA	Nuclear factor 1;Nuclear factor 1 A-type	-0.1 ± 0.4	0.24 ± 0.08
27	CEBPZ	CCAAT/enhancer-binding protein zeta	-1.6 ± 0.4	-0.02 ± 0.04
28	CTR9	RNA polymerase-associated protein CTR9 homolog	-2.3 ± 0.8	0.00 ± 0.06
29	CCDC97	Coiled-coil domain-containing protein 97	-2.7 ± 1.5	-0.04 ± 0.03
30	PNSR	Arginine/serine-rich protein PNISR	-4.91 ± 4.1	0.26 ± 0.14

6. LIST OF ABBREVIATIONS

AB	antibody
Abl1	Abelson tyrosine-protein kinase 1
AC	adenylyl cyclase
aCD	acid ceramidase
ACN	acetonitrile
AMBRA1	Activating molecule in BECN1-regulated autophagy protein 1
AMP	Adenosine monophosphate
AMPK	AMP-activated protein kinase
Arl	Arf-like proteins
Atg	autophagy-related
aSM	acid sphingomyelinase
ATP	adenosine triphosphate
BDP	beclomethasone dipropionate
BIOS	biology-oriented synthesis
BLK	B-lymphoid tyrosine kinase
Boc	<i>tert</i> -butyloxycarbonyl
BSA	bovine serum albumin
cAMP	cyclic adenosine monophosphate
CD	circular dichroism
CD4	cluster of differentiation 4
CDK11	cyclin-dependent kinase 11
CETSA	cellular thermal shift assay
CMA	chaperone-mediated autophagy
COMAS	compound management and screening center
CoA	Coenzyme A
COMU	1-cyano-2-ethoxy-2-oxoethylideneaminoxy)dimethylamino morpholino-carbenium hexafluorophosphate
CPA	cell painting assay
CPM	7-diethylamino-3-(4'-maleimidylphenyl)-4-methyl-coumarin

CPT2	carnitine O-palmitoyltransferase 2
CQ	chloroquine
CSE1L	exportin 2
CytC	cytochrome C
DBCO	dibenzocyclooctyne
DCM	dichloromethane
DDR2	discoidin domain-containing receptor 2
DIC	<i>N,N'</i> -diisopropylcarbodiimide
DIPEA	<i>N,N</i> -diisopropylethylamine
DMF	dimethylformamid
DMSO	dimethyl sulfoxide
DNA	deoxyribonucleic acid
DSF	differential scanning fluorimetry
DTE	dithioerythritol
dT _m	shift in melting temperature
DTT	dithiothreitol
EBSS	Earle's balanced salt solution
ECAR	extracellular acidification rate
ECH1	eelta(3,5)-eelta(2,4)-dienoyl-CoA isomerase
ECI2	enoyl-CoA delta isomerase 2
EDTA	ethylenediaminetetraacetic acid
eGFP	enhanced green fluorescent protein
EGTA	ethylene glycol-bis(β-aminoethyl ether)- <i>N,N,N',N'</i> -tetraacetic acid
ER	endoplasmic reticulum
EXOC6B	exocyst complex component 6B
FAD	flavin adenine dinucleotide
FBL	rRNA 2-O-methyltransferase fibrillar
FBS	fetal bovine serum
FCCP	carbonyl cyanide 4-(trifluoromethoxy)phenylhydrazone

FDA	Food and Drug Administration
Fe(III)PPIX	iron(III) protoporphyrin IX
FECH	ferrochelatase
FSCN1	Fascin
FIP200	family-interacting protein of 200kD
FITC	fluorescein isothiocyanate
Fmoc	Fluorenylmethyloxycarbonyl chloride
FP	fluorescence polarization
GAP	GTPase-activating protein
GCN1L1	translational activator GCN1
Gnat	G protein subunit alpha transducin
GPR	golgi pH regulator
G protein	guanine nucleotide binding protein
GSK	glycogen synthase kinase 3
HCTU	O-(1H-6-chlorobenzotriazole-1-yl)-1,1,3,3-tetramethyluronium Hexafluorophosphate
HEPES	4-(2-hydroxyethyl)-1-piperazineethanesulfonic acid)
HFIP	hexafluoroisopropanol
HNRNPR	Heterogeneous nuclear ribonucleoprotein R
HPLC	high performance liquid chromatography
HRG4	human retina gene 4
HRMS	high-resolution mass spectrometry
HRP	horse radish peroxidase
HSD17B4	Peroxisomal multifunctional enzyme type 2
HSDL2	hydroxysteroid dehydrogenase-like protein 2
HTS	high-throughput screenin
HUS1	Checkpoint protein HUS1
IC ₅₀	half maximal inhibitory concentration
IDH3G	isocitrate dehydrogenase [NAD] subunit

IMPase	inositol monophosphatase
Ins	inositol
IP	inositol monophosphate
IP ₂	inositol bisphosphate
IP ₃	inositol trisphosphate
IPO5	importin-5
IPTG	isopropyl β-D-1-thiogalactopyranoside
ITC	isothermal titration calorimetry
ITDRF	isothermal dose-response fingerprint
KNTC1	kinetochore-associated protein 1
LARS	leucine--tRNA ligase
LC3	microtubule-associated protein 1 light chain
Lck	lymphocyte-specific protein tyrosine kinase
LFQ	label-free quantification
MALDI	matrix assisted laser desorption ionization
MAKSU1	mitochondrial assembly of ribosomal large subunit protein 1
MBHA	4-methylbenzhydramine hydrochloride
MC	mitochondrial carrier
MEM	minimum Essential Medium
MNK1	mitogen-activated protein kinase-interacting kinase 1
MPRL	39S ribosomal protein L
MPRS	28S ribosomal protein S
MS	mass spectrometry
mTOR	mammalian target of rapamycin
Mtt	4-methyltrityl
MUT	methylmalonyl-CoA mutase
MVK	mevalonate kinase
Myr-Src	myristoylated Src
NAD	Nicotinamide adenine dinucleotide

NDUF	NADH dehydrogenase [ubiquinone] 1 alpha subcomplex subunit
NHS	<i>N</i> -hydroxysuccinimide
NLS	nuclear localization sequence
NMT	<i>N</i> -myristoyl transferase
NO66	Bifunctional lysine-specific demethylase and histidyl-hydroxylase NO66
NP-40	4-nonylphenyl-polyethylene glycol
NPHP3	nephrocystin-3
NQO2	ribosyldihyronicotinamide dehydrogenase
OCR	oxygen consumption rate
Oxyrna	ethyl cyanohydroxyiminoacetate
PAGE	polyacrylamide gel electrophoresis
PBS	phosphate-buffered saline
PCA	principal-component-analysis
PCR	polymerase chain reaction
PDB	protein databank
PDE δ	Photoreceptor cGMP phosphodiesterase δ subunit
PDK1	[Pyruvate dehydrogenase (acetyl-transferring)] kinase isozyme 1
PDK1	pleckstrin homology domain containing proteins phosphoinositide dependent kinase 1
PE	Phosphatidyl ethanolamine
PEG	polyethylene glycol
PEAK1	pseudopodium-enriched atypical kinase 1
PFKM	ATP-dependent 6-phosphofructokinase, mitochondria
PFKL	ATP-dependent 6-phosphofructokinase, liver
PI3P	phosphatidylinositol 3-phosphate
PIP ₂	Phosphatidylinositol-4,5-bisphosphate
PIP ₃	Phosphatidylinositol (3,4,5)-trisphosphate
PIPES	piperazine- <i>N,N'</i> -bis(2-ethanesulfonic acid)

PLC ϵ	Phospholipase C ϵ
PMFS	phenylmethylsulfonyl fluoride
PMP	plasma membrane permeabilizer
POC	percent-of-control
POLR3C	DNA-directed RNA polymerase III subunit RPC3
PPI	protein-protein interactions
PVDF	polyvinylidene fluoride
PyBOP	(benzotriazol-1-yloxy)tripyrrolidinophosphonium hexafluorophosphate
PTM	posttranslational modifications
Rag	Ras-related GTP-binding protein
Rap2B	Ras-related protein Rap-2B
RE	recycling endosome
RIPA	radioimmunoprecipitation assay
RNA	ribonucleic acid
ROS	reactive oxygen species
RPL	60S ribosomal protein L
RPMI	Roswell Park Memorial Institute
RPS	40S ribosomal protein S
RZZ	ROD–Zwilch–ZW10
SAR	structure activity relationship
SCP2	sterol carrier protein-2
SD	standard deviation
SDS	sodium dodecyl sulfate
SFK	Src family kinases
sh	short
SLC	solute carrier family
SNX7	sorting nexin-7
SPPS	solid phase peptide synthesis

STAGE	Stop and Go Extraction
STT3A	dolichyl-diphosphooligosaccharide--protein glycosyltransferase subunit STT3A
SURF4	surfeit locus protein 4
TBAB	tetrabutylammonium bromide
TBAF	tetrabutylammonium fluoride
TBDMSCl	<i>tert</i> -Butyldimethylsilyl chloride
TBS	tris-buffered saline
TCEP	tris(2-carboxyethyl)phosphine
TCR	T-cell receptor
TEAB	triethylammonium bicarbonate
TEMPO	2,2,6,6-tetramethylpiperidin-1-yl)oxyl
TFA	trifluoroacetic acid
THF	terahydrofuran
TIS	triisopropylsilane
TLC	thin layer chromatography
T _m	melting temperature
TMEM	transmembrane protein 128
TMPD	<i>N,N,N',N'</i> -Tetramethyl- <i>p</i> -phenylenediamine
TMT10	neutron-encoded isobaric mass tagging reagents
TOF	time of flight
TPP	thermal proteome profiling
TSC	tuberous sclerosis complex
TUBA	Tubulin alpha chain
ULK	Unc51-like kinase
UNC119	uncoordinated 119
UV	ultraviolet
VPS34	Vacuolar protein sorting-associated protein 34
WIPI2	WD repeat domain phosphoinositide-interacting protein 2
ZW10	Centromere/kinetochore protein zw10 homolog

ZWILCH

Protein zwilch homolog

β ME

β -mercaptoethanol

7. REFERENCES

- [1] M. Kostic, *Cell Chem. Biol.* **2017**, *24*, 427.
- [2] E. L. Ostler, *Chem. Cent. J.* **2007**, *1*.
- [3] H. v. Hattum, H. Waldmann, *J.Am.Chem.Soc.* **2014**, *136*, 11853-11859.
- [4] S. Wetzel, R. S. Bon, K. Kumar, H. Waldmann, *Angew. Chem. Int. Ed.* **2011**, *50*, 10800-10826.
- [5] G. Karageorgis, E. S. Reckzeh, J. Ceballos, M. Schwalfenberg, S. Sievers, C. Ostermann, A. Pahl, S. Ziegler, H. Waldmann, *Nat. Chem.* **2018**, *10*, 1103-1111.
- [6] D. R. Spring, *Chem. Soc. Rev.* **2005**, *34*, 472-482.
- [7] R. S. Lokey, *Curr. Opin. Chem. Biol.* **2003**, *7*, 91-96.
- [8] C. J. O. Connor, L. Laraia, D. R. Spring, *Chem. Soc. Rev.* **2011**, *40*, 4332-4345.
- [9] W. Zheng, N. Thorne, J. C. McKew, *Drug Discov. Today* **2013**, *18*, 1067-1073.
- [10] K. Wrobel, E. Claudia, F. Segade, S. Ramos, P. S. Laze, *J. Immunol. Methods* **1996**, *189*, 243-249.
- [11] R. Pepperkok, J. Ellenberg, *Nat. Rev. Mol. Cell Biol.* **2006**, *7*, 690-696
- [12] J. Lippincott-Schwartz, G. H. Patterson, *Science* **2003**, *300*, 87-91.
- [13] J. Inglese, R. L. Johnson, A. Simeonov, M. Xia, W. Zheng, C. P. Austin, D. S. Auld, *Nat. Chem. Biol.* **2007**, *3*, 466-479.
- [14] E. Michelini, L. Cevenini, L. Mezzanotte, A. C. Roda, *Anal. Bioanal. Chem.* **2010**, *398*, 227-238.
- [15] B. K. Wagner, S. L. Schreiber, *Cell Chem. Biol.* **2016**, *23*, 3-9.
- [16] A. Ursu, H. Waldmann, *Bioorganic Med. Chem. Lett.* **2015**, *25*, 3079-3086.
- [17] G. C. Terstappen, C. Schlüpen, R. Raggiaschi, G. Gaviraghi, *Nat. Rev. Drug Discov.* **2007**, *6*, 891-903.
- [18] J. Li, H. Xu, G. M. West, L. H. Jones, *MedChemCom* **2016**, *7*, 769-777.
- [19] D. M. Molina, R. Jafari, M. Ignatushchenko, T. Seki, E. A. Larsson, C. Dan, L. Sreekumar, Y. Cao, P. Nordlund, *Science* **2013**, *341*, 84-87.
- [20] R. Jafari, H. Almqvist, H. Axelsson, M. Ignatushchenko, T. Lundbäck, P. Nordlund, D. M. Molina, *Nat. Protoc.* **2014**, *9*, 2100-2122.
- [21] H. Franken, T. Mathieson, D. Childs, G. M. A. Sweetman, T. Werner, I. Tögel, C. Doce, S. Gade, M. Bantscheff, G. Drewes, F. B. M. Reinhard, W. Huber, M. M. Savitski, *Nat. Protoc.* **2015**, *10*, 1567-1593.

- [22] F. B. M. Reinhard, D. Eberhard, T. Werner, H. Franken, D. Childs, C. Doce, M. F. Savitski, W. Huber, M. Bantscheff, M. M. Savitski, G. Drewes, *Nat. Methods* **2015**, *12*, 1129-1131.
- [23] M. M. Savitski, F. B. M. Reinhard, H. Franken, T. Werner, M. F. Savitski, D. Eberhard, D. M. Molina, R. Jafari, R. B. Dovega, S. Klaeger, B. Kuster, P. Nordlund, M. Bantscheff, G. Drewes, *Science* **2014**, *346*.
- [24] M. Bray, S. Singh, H. Han, C. T. Davis, B. Borgeson, C. Hartland, M. Kost-Alimova, S. M. Gustafsdottir, C. C. Gibson, A. E. Carpenter, *Nat. Protoc.* **2016**, *11*, 1757-1774.
- [25] S. Ziegler, V. Pries, C. Hedberg, H. Waldmann, *Angew. Chem. Int. Ed.* **2013**, *52*, 2744-2792.
- [26] N. J. Moerke, *Curr. Protoc. Chem. Biol.* **2009**, *1*, 1-15.
- [27] D. M. Molina, P. Nordlund, *Annu. Rev. Pharmacol. Toxicol.* **2016**, *56*, 30.31–30.21.
- [28] F. H. Niesen, H. Berglund, M. Vedadi, *Nat. Protoc.* **2007**, *2*, 2212-2221.
- [29] M. W. Freyer, E. A. Lewis, *Methods Cell Biol.* **2008**, *84*, 79-113.
- [30] N. J. Greenfield, *Nat. Protoc.* **2006**, *1*, 2527-2535.
- [31] A. M. Hassell, G. An, R. K. Bledsoe, J. M. Bynum, H. L. Carter, S. J. Deng, R. T. Gampe, T. E. Grisard, K. P. Madauss, R. T. Nolte, W. J. Rocque, L. Wang, K. L. Weaver, S. P. Williams, G. B. Wisely, R. Xua, L. M. Shewchuka, *Acta Crystallogr. D* **2006**, *63*, 72-79.
- [32] D. E. Danley, *Acta Crystallogr. D* **2006**, *62*, 569-575.
- [33] A. I. Archakov, V. M. Govorun, A. V. Dubanov, Y. D. Ivanov, A. V. Veselovsky, P. Lewi, P. Janssen, *Proteomics* **2003**, *3*, 380-391.
- [34] I. S. Moreira, P. A. Fernandes, M. J. Ramos, *Proteins* **2007**, *68*, 803-812.
- [35] T. Rolland, M. Taşan, B. Charlotiaux, S. J. Pevzner, Q. Zhong, N. Sahni, S. Yi, I. Lemmens, C. Fontanillo, R. Mosca, A. Kamburov, S. D. Ghiassian, X. Yang, L. Ghamsari, D. Balcha, B. E. Begg, P. Braun, M. B. e. al., *Cell* **2014**, *159*, 1212-1226.
- [36] M. Pellegrini, D. Haynor, J. M. Johnso, *Expert Rev. Proteomics* **2004**, *1*, 239–249.
- [37] G. Walsh, R. Jefferis, *Nat. Biotechnol.* **2006**, *24*, 1241-1252.
- [38] M. Mann, O. N. Jensen, *Nat. Biotechnol.* **2003**, *21*, 255-261.
- [39] O. N. Jensen, *Curr. Opin. Chem. Biol.* **2004**, *8*, 33-41.
- [40] C. T. Walsh, S. Garneau-Tsodikova, G. J. Gatto, *Angew. Chem. Int. Ed.* **2005**, *44*, 7342-7372.
- [41] B. T. Seet, I. Dikic, M. Zhou, T. Pawson, *Nat. Rev. Mol. Cell Biol.* **2006**, *7*, 473-483.

- [42] G. Triola, H. Waldmann, C. Hedberg, *ACS Chem. Biol.* **2012**, *7*, 87-99.
- [43] R. Roskoski, *Biochem. Biophys. Res. Commun.* **2003**, *303*, 1-7.
- [44] H. C. Hang, M. E. Linder, *Chem. Rev.* **2011**, *111*, 6341-6358.
- [45] M. E. Linder, R. J. Deschenes, *Nat. Rev. Mol. Cell Biol.* **2007**, *8*, 74-84.
- [46] J. E. Smotrys, M. E. Linder, *Annu. Rev. Biochem.* **2004**, *73*, 559-587.
- [47] L. E. P. Dietrich, C. Ungermann, *EMBO Rep.* **2004**, *5*, 1053-1057.
- [48] M. J. Nadolski, M. E. Linder, *FEBS Journal* **2007**, *274*, 5202-5210.
- [49] M. D. Resh, *Curr. Biol.* **2013**, *23*, R431-R435.
- [50] J. A. Boutin, *Cell Signal.* **1997**, *9*, 15-35.
- [51] J. H. C. Wilcox, E. N. Olson, *Science* **1987**, *238*, 1275-1278.
- [52] H. P. Price, M. R. Meno, C. Panethymitaki, D. Goulding, P. G. McKean, D. F. Smith, *J. Biol. Chem.* **2003**, *278*, 7206-7214.
- [53] D. A. Rudnick, C. A. McWherterll, W. J. Rocquell, P. J. Lennonll, D. P. Getmanll, J. I. Gordon, *J. Biol. Chem.* **1991**, *266*, 9732-9973.
- [54] M. D. Resh, *Biochim. Biophys. Acta* **1999**, *1451*, 1-16.
- [55] M. H. Wright, W. P. Heal, D. J. Mann, E. W. Tate, *J. Chem. Biol.* **2010**, *3*, 19-35.
- [56] J. Goldberg, *Cell Signal.* **1998**, *95*, 237-248.
- [57] C. Spilker, K. Braunewell, *Mol. Cell. Neurosci.* **2003**, *24*, 766-778.
- [58] H. Zhang, R. Constantine, S. Vorobiev, Y. Chen, J. Seetharaman, Y. J. Huang, R. Xiao, G. T. Montelione, C. D. Gerstner, M. W. Davis, G. Inana, F. G. Whitby, E. M. Jorgensen, C. P. Hill, L. Tong, W. Baehr, *Nat. Neurosci.* **2011**, *14*, 874-880.
- [59] M. Maduro, D. Pilgrim, *Genetics* **1995**, 977-988.
- [60] R. Constantine, H. Zhang, C. D. Gerstner, J. M. Frederick, W. Baehr, *Vision Res.* **2012**, *75*, 26-32.
- [61] S. A. Ismail, Y. Chen, M. Miertschke, I. R. Vetter, C. Koerner, A. Wittinghofer, *EMBO J.* **2012**, *21*, 4085-4094.
- [62] M. Jaiswal, E. K. Fansa, S. K. Kosling, T. Mejuch, H. Waldmann, A. Wittinghofer, *J. Biol. Chem.* **2016**, *291*, 20766-20778.
- [63] K. J. Wright, L. M. Baye, A. Olivier-Mason, S. Mukhopadhyay, L. Sang, M. Kwong, W. Wang, P. R. Pretorius, V. C. Sheffield, P. Sengupta, D. C. Slusarski, P. K. Jackson, *Genes Dev.* **2011**, *25*, 2347-2360.

- [64] K. N. Gopalakrishna, K. Doddapunen, K. K. Boyd, I. Masuho, K. A. Martemyanov, N. O. Artemyev, *J. Biol. Chem.* **2011**, *286*, 28954-28962.
- [65] T. Mejuch, H. v. Hattum, G. Triola, M. Jaiswal, H. Waldmann, *ChemBioChem* **2015**, *16*, 2460-2465.
- [66] A. D. Konitsiotis, L. Roßmannek, A. Stanoev, M. Schmick, P. I. H. Bastiaens, *Nat. Commun.* **2017**, *8*.
- [67] O. Cen, M. M. Gorska, S. J. Stafford, S. Sur, R. Alam, *J. Biol. Chem.* **2003**, *278*, 8837–8845.
- [68] M. M. Gorska, S. J. Stafford, O. Cen, S. Sur, R. Alam, *J. Exp. Med.* **2004**, *199*, 369-379.
- [69] L. C. Kim, L. Song, E. B. Haura, *Nat. Rev. Clin. Oncol.* **2009**, *6*, 587–595.
- [70] A. Kobayashi, T. Higashide, D. Hamasaki, S. Kubota, H. Sakuma, W. An, T. Fujimaki, M. J. McLaren, R. G. Weleber, G. Inana, *Invest. Ophthalmol. Vis. Sci.* **2000**, *41*.
- [71] M. M. Gorska, R. Alam, *Blood* **2012**, *119*, 1399-1406.
- [72] T. Mejuch, G. Garivet, W. Hofer, N. Kaiser, E. K. Fansa, C. Ehrt, O. Koch, M. Baumann, S. Ziegler, A. Wittinghofer, H. Waldmann, *Angew. Chem. Int. Ed.* **2017**, *129*, 6277-6282.
- [73] G. Garivet, W. Hofer, A. Konitsiotis, C. Klein, N. Kaiser, T. Mejuch, E. Fansa, A. Wittinghofer, P. I. H. Bastiaens, H. Waldmann, *Cell Chem. Biol.* , *Manscript accepted*.
- [74] T. Cierpicki, J. Grembecka, *Immunol. Rev.* **2015**, *263*, 279-301.
- [75] B. J. Leslie, P. J. Hergenrother, *Chem. Soc. Rev.* **2008**, *37*, 1347-1360.
- [76] D. J. Lapinsky, *Bioorg. Med. Chem.* **2012**, *20*, 6237-6242.
- [77] G. Dormán, G. D. Prestwich, *Tibtech.* **2000**, *18*, 64-77.
- [78] G. W. Preston, A. J. Wilson, *Chem. Soc. Rev.* **2013**, *42*, 3289-3301.
- [79] E. Smith, I. Collins, *Future Med. Chem.* **2015**, *7*, 159-183.
- [80] L. Dubinsky, B. P. Krom, M. M. Meijler, *Bioorg. Med. Chem.* **2012**, *20*, 554–570.
- [81] M. Hashimoto, Y. Hatanaka, *Eur. J. Org. Chem.* **2008**, *2008*, 2513-2523.
- [82] J. Das, *Chem. Rev.* **2011**, *111*, 405-4417.
- [83] H. Zhang, Y. Song, Y. Zou, Y. Ge, Y. An, Y. i. Ma, Z. Zhu, C. J. Yan, *Chem. Commun.* **2014**, *50*, 4891-4894.
- [84] A. L. MacKinnon, J. Taunton, *Curr Protoc Chem Biol.* **2009**, *1*, 55-73.
- [85] D. A. Modarelli, S. Morgan, M. S. Platz, *J. Am. Chem. Soc.* **1992**, *114*, 7034-7041.

- [86] L. Bordoli, F. Kiefer, K. Arnold, P. Benkert, J. Battey, T. Schwede, *Nat. Protoc.* **2009**, *4*, 1/13.
- [87] N. Kaiser, T. Mejuch, R. Fedoryshchak, P. Janning, E. W. Tate, H. Waldmann, *ChemBioChem* **2019**, *20*, 134-139.
- [88] C. S. McKay, M. G. Finn, *Chem. Biol.* **2014**, *21*, 1075-1101.
- [89] E. J. Murphy, *Mol. Cell. Biochem.* **2002**, *239*, 87-93.
- [90] D. Kowalik, F. Haller, J. Adamski, G. Moeller, *J. Steroid Biochem. Mol. Biol.* **2009**, *117*, 117-124.
- [91] F. D. Ledley, M. R. Lumetta, H. Y. Zoghbi, P. VanTuinen, S. A. Ledbetter, D. H. Ledbetter, *Am. J. Genet.* **1988**, *42*, 839-846.
- [92] S. Mosalaganti, J. Keller, A. Altenfeld, M. Winzker, P. Rombaut, M. Saur, A. Petrovic, A. Wehenkel, S. Wohlgemuth, F. Müller, S. Maffini, T. Bange, F. Herzog, H. Waldmann, S. Raunser, A. Musacchio, *J. Cell Biol.* **2017**, *216*, 961-981.
- [93] S. Kosugi, M. Hasebe, N. Matsumura, H. Takashima, E. Miyamoto-Sato, M. Tomita, H. Yanagawa, *J. Biol. Chem.* **2009**, *284*, 478-485.
- [94] V. Goncalves, J. A. Brannigan, E. Thinon, T. O. Olaleye, R. Serwa, S. Lanzarone, A. J. Wilkinson, E. W. Tate, R. J. Leatherbarrow, *Anal Biochem.* **2012**, *421*.
- [95] S. Ohshima, M. Ohashi-Suzuki, Y. Miura, Y. Yabu, N. Okada, N. Ohta, T. Suzuki, *PLOS one* **2012**, *5*, e15577.
- [96] S. W. Ryter, S. M. Cloonan, A. M. K. Choi, *Mol. Cells* **2013**, *36*, 7-16.
- [97] Y. Feng, D. He, Z. Yao, D. J. Klionsky, *Cell Res.* **2014**, *24*, 24-41.
- [98] J. F. Dice, *Autophagy* **2007**, *3*, 295-299.
- [99] D. Mijaljica, M. Prescott, R. J. Devenish, *Autophagy* **2011**, *7*, 673-682.
- [100] B. Bissa, V. Deretic, *Curr. Biol.* **2018**, *12*, R347-R349.
- [101] M. Hamasaki, N. Furuta, A. Matsuda, A. Nezu, A. Yamamoto, N. Fujita, H. Oomori, T. Noda, T. Haraguchi, Y. Hiraoka, A. Amano, T. Yoshimori, *Nature Communications* **2013**, *495*, 389-393.
- [102] A. C. Nascimbeni, F. Giordano, N. Dupont, D. Grasso, M. I. Vaccaro, P. Codogno, E. Morel, *EMBO J.* **2017**, *36*, 2018-2033.
- [103] Z. Xie, D. J. Klionsky, *Nat. Cell. Biol.* **2007**, *9*, 1102-1109.
- [104] D. J. Klionsky, J. M. Cregg, W. A. Dunn, S. D. Emr, Y. Sakai, I. V. Sandoval, A. Sibirny, S. Subramani, M. Thumm, M. Veenhuis, Y. Ohsumi, *Dev. Cell* **2003**, *5*, 539-545.
- [105] N. Mizushima, *Curr. Opin. Cell Biol.* **2010**, *22*, 132-139.

- [106] F. M. Menzies, A. Fleming, D. C. Rubinsztein, *Nat. Rev. Neurosci.* **2015**, *16*, 345-357.
- [107] R. C. Russell, Y. Tian, H. Yuan, H. W. Park, Y. Chang, J. Kim, H. Kim, T. P. Neufeld, A. Dillin, K. Guan, *Nat. Cell. Biol.* **2013**, *15*, 741-750.
- [108] E. Karanasios, E. Stapleton, M. Manifava, T. Kaizuka, N. Mizushima, S. A. Walker, N. T. Ktistakis, *J. Cell Sci.* **2013**, *126*, 5224-5238.
- [109] H. E. J. Polson, J. de Lartigue, D. J. Rigden, M. Reedijk, S. Urbé, M. J. Clague, S. A. Tooze, *Autophagy* **2010**, *6*, 506-522.
- [110] D. C. Rubinsztein, T. Shpilka, Z. Elazar, *Curr. Biol.* **2012**, *22*, R29-R34.
- [111] C. Puri, M. Renna, C. F. Bento, K. Moreau, D. C. Rubinsztein, *Cell* **2013**, *154*, 1285-1299.
- [112] S. T. Shibutani, T. Yoshimori, *Cell Res.* **2014**, *24*, 56-68.
- [113] C. H. Jung, S. Ro, J. Cao, N. M. Ott, D. Kim, *FEBS Lett.* **2010**, *584*, 1287-1295.
- [114] Y. Sancak, T. R. Peterson, Y. D. Shaul, R. A. Lindquist, C. C. Thoreen, L. Bar-Peled, D. M. Sabatini, *Science* **2008**, *320*, 1496-1501.
- [115] L. C. Cantley, *Science* **2002**, *296*, 1655-1657.
- [116] K. Inoki, T. Zhu, K. Guan, *Cell* **2003**, *115*, 577-590.
- [117] K. Inoki, H. Ouyang, T. Zhu, C. Lindvall, Y. Wang, X. Zhang, Q. Yang, C. Bennett, Y. Harada, K. Stankunas, C. Wang, X. He, O. A. MacDougald, M. You, B. O. Williams, K. Guan, *Cell* **2006**, *126*, 955-968.
- [118] S. Sarkar, *Biochem. Soc. Trans.* **2013**, *41*, 1103-1130.
- [119] K. Sato-Kusubata, Y. Yajima, S. Kawashima, *Biochem J.* **2000**, *347*, 33-40.
- [120] M. B. Mestre, M. I. Colombo, *PLoS Pathog.* **2012**, *8*, e1002664.
- [121] M. Gloerich, J. L. Bos, *Annu. Rev. Pharmacol. Toxicol.* **2010**, *50*, 355-357.
- [122] J. Di, J. Tang, H. Qian, D. A. Franklin, C. Deisenroth, Y. Itahana, J. Zheng, Y. Zhang, *Oncotarget.* **2017**, *8*, 64657-64669.
- [123] T. Shintani, D. J. Klionsky, *Science* **2004**, *306*, 990-995.
- [124] T. Hara, K. Nakamura, M. Matsui, A. Yamamoto, Y. Nakahara, R. Suzuki-Migishima, M. Yokoyama, K. Mishima, I. Saito, H. Okano, N. Mizushima, *Nature Communications* **2006**, *441*, 885-889.
- [125] D. D.O.Martin, S.Ladha, D. E.Ehrhoefer, M. R.Hayden, *Trends Neurosci.* **2015**, *38*, 26-35.
- [126] M. G. Spillantini, M. L. Schmidt, V. M. Y. Lee, J. Q. Trojanowski, R. Jakes, M. Goedert, *Nature Communications* **1997**, *388*, 839-940.

- [127] S. C. Correia, R. Resende, P. I. Moreira, C. M. Pereira, *DNA Cell Biol.* **2015**, *34*, 261-273.
- [128] T. E. Moors, J. J. M. Hoozemans, A. Ingrassia, T. Beccari, L. Parnetti, M. Chartier-Harlin, W. D. J. v. d. Berg, *Mol. Neurodegener.* **2017**, *12*.
- [129] B. Levine, *Nature Communications* **2007**, *446*, 745-747.
- [130] E. White, *Nat. Rev. Cancer* **2012**, *12*, 401-410.
- [131] Y. Kondo, T. Kanzawa, R. Sawaya, S. Kondo, *Nat. Rev. Cancer* **2005**, *5*, 726-734.
- [132] L. Galluzzi, J. M. B.-S. Pedro, B. Levine, D. R. Green, G. Kroemer, *Nat. Rev. Drug Discov.* **2017**, *16*, 487-511.
- [133] P. Spilman, N. Podlutskaya, M. J. Hart, J. Debnath, O. Gorostiza, D. Bredesen, A. Richardson, R. Strong, V. Galvan, *PLoS one* **2010**, *5*, e9979.
- [134] V. Vingtdeux, L. Giliberto, H. Zhao, P. Chandakkar, Q. Wu, J. E. Simon, E. M. Janle, J. Lobo, M. G. Ferruzzi, P. Davies, P. Marambaud, *J. Biol. Chem.* **2010**, *285*, 9100-9013.
- [135] S. He, Q. Li, X. Jiang, X. Lu, F. Feng, W. Qu, Y. Chen, H. Sun, *J. Med. Chem.* **2018**, *16*, 4656-4687.
- [136] C. I. Chude, R. K. Amaravadi, *Int. J. Mol. Sci.* **2017**, *18*, 1279.
- [137] P. Wipf, R. J. Halter, *Org. Biomol. Chem.* **2005**, *3*, 2053-2061.
- [138] B. Ronan, O. Flamand, L. Vescovi, C. Dureuil, L. Durand, F. Fassy, M. Bachelot, A. Lambertson, M. Mathieu, T. Bertrand, J. Marquette, Y. El-Ahmad, B. Filoche-Romme, L. Schio, C. Garcia-Echeverria, H. Goulaouic, P. B, *Nat. Chem. Biol.* **2014**, *10*, 1013–1019.
- [139] W. E. Dowdle, B. Nyfeler, J. Nagel, R. A. Elling, S. Liu, E. Triantafellow, S. Menon, Z. Wang, A. Honda, G. Pardee, J. Cantwell, C. Luu, I. Cornella-Taracido, E. Harrington, P. Fekkes, H. Lei, Q. Fang, M. E. Digan, D. Burdick, A. F. Powers, S. B. Helliwell, S. D'Aquin, J. Bastien, H. Wang, D. Wiederschain, J. Kuerth, P. Bergman, D. Schwalb, J. Thomas, S. Ugwonal, F. Harbinski, J. Tallarico, C. J. Wilson, V. E. Myer, J. A. Porter, D. E. Bussiere, P. M. Finan, M. A. Labow, X. Mao, L. G. Hamann, B. D. Manning, R. A. Valdez, T. Nicholson, M. Schirle, M. S. Knapp, E. P. Keaney, L. O. Murphy, *Nat. Cell. Biol.* **2014**, *16*, 1069–1079.
- [140] R. Bago, N. Malik, J. M. M, A. R. Prescott, P. Davies, E. Sommer, N. Shpiro, R. Ward, D. Cross, I. G. Ganley, D. R. Alessi, *Biochem J.* **2014**, *463*, 413-427.
- [141] L. Robke, L. Laraia, M. A. C. Corrales, G. Konstantinidis, M. Muroi, A. Richters, M. Winzker, T. Engbring, S. Tomassi, N. Watanabe, H. Osada, D. Rauh, H. Waldmann, Y. Wu, J. Engel, *Angew. Chem. Int. Ed.* **2017**, *56*, 8153-8157.
- [142] M. Mauthe, I. Orhon, C. Rocchi, X. Zhou, M. Luhr, K. J. Hijlkema, R. P. Coppes, N. Engedal, M. Mari, F. Reggiori, *Autophagy* **2018**, *14*, 1435-1455.

- [143] K. M. Kacprzak, in *Natural Products: Phytochemistry, Botany and Metabolism of Alkaloids, Phenolics and Terpenes* (Eds.: K. G. Ramawat, J.-M. Mérillon), Springer Berlin Heidelberg, Berlin, Heidelberg, **2013**, pp. 605-641.
- [144] T. J. Egan, D. C. Ross, P. A. Adams, *FEBS Lett.* **1994**, *352*, 54-57.
- [145] S. Kumar, M. Guha, V. Choubey, P. Maity, U. Bandyopadhyay, *Life Sci.* **2007**, *80*, 913-828.
- [146] K. A. d. Villiers, J. Gildenhuis, T. I. Roex, *ACS Chem. Biol.* **2012**, *7*, 666-671.
- [147] J. Gildenhuis, C. J. Sammy, R. Müller, V. A. Streltsov, T. I. Roex, D. Kuter, K. A. d. Villiers, *Dalton Trans.* **2015**, *44*, 16767-16777.
- [148] S. Nadanaciva, S. L. David, F. Gebhard, B. A. Jessen, W. D. Pennie, Y. Will, *Toxicol. Vitro* **2011**, *25*, 715-723.
- [149] R. Thomé, S. C. P. Lopes, F. T. M. Costa, L. Verinauda, *Immunol. Lett.* **2013**, *153*, 50-57.
- [150] L. Zhang, J. Yu, H. Pan, P. Hu, Y. Hao, W. Cai, H. Zhu, A. D. Yu, X. Xie, D. Ma, J. Yuan, *PNAS* **2007**, *104*, 19023-19028.
- [151] A. D. Balgi, B. D. Fonseca, E. Donohue, T. C. F. Tsang, P. Lajoie, C. G. Proud, I. R. Nabi, M. Roberge, *PLoS one* **2009**, *4*, e7124.
- [152] N. Mizushima, A. Yamamoto, M. Matsui, T. Yoshimori, Y. Ohsumi, *Mol. Biol. Cell* **2004**, *15*, 1101-1111.
- [153] T. E. Rusten, K. Lindmo, G. Juhász, M. Sass, P. O. Seglen, A. Brech, H. Stenmark, *Dev. Cell* **2004**, *7*, 179-192.
- [154] C. He, C. R. Bartholomew, W. Zhou, D. J. Klionsky, *Autophagy* **2009**, *5*, 520-526.
- [155] H. Zhu, P. Tannous, J. L. Johnstone, Y. Kong, J. M. Shelton, J. A. Richardson, V. Le, B. Levine, B. A. Rothermel, J. A. Hill, *J. Clin. Invest* **2007**, *117*, 1782-1793.
- [156] E. Iwai-Kanai, H. Yuan, C. Huang, M. R. Sayen, C. N. Perry-Garza, L. Kim, R. A. Gottlieb, *Autophagy* **2008**, *4*, 322-329.
- [157] N. Mizushima, T. Yoshimori, B. Levine, *Cell* **2010**, *140*, 313-326.
- [158] J. Liu, H. Xia, M. Kim, L. Xu, Y. Li, L. Zhang, Y. Cai, H. V. Norberg, T. Zhang, T. Furuya, M. Jin, Z. Zhu, H. Wang, J. Yu, Y. Li, Y. Hao, A. Choi, H. Ke, D. Ma, J. Yuan, *Cell* **2011**, *147*, 223-234.
- [159] J. V. Peppard, C. Rugg, M. Smicker, C. Dureuil, B. Ronan, O. Flamand, L. Durand, B. Pasquier, *Curr. Chem. Genom. Transl. Med.* **2014**, *8*, 3-15.
- [160] L. Robke, Y. Futamura, G. Konstantinidis, J. Wilke, H. Aono, Z. Mahmoud, N. Watanabe, Y. Wu, H. Osada, L. Laraia, H. Waldmann, *Chem. Sci.* **2018**, *9*, 3014-3022.

- [161] D. C. Rubinsztein, P. Codogno, B. Levine, *Nat. Rev. Drug Discov.* **2012**, *11*, 709-730.
- [162] L. Laraia, K. Ohsawa, G. Konstantinidis, L. Robke, Y. Wu, K. Kumar, H. Waldmann, *Angew. Chem. Int. Ed.* **2017**, *56*, 2145-2150.
- [163] W. Zhu, H. Qu, K. Xu, B. Jia, H. Li, Y. Du, G. Liu, H. Wei, H. Zhao, *Anim. Cells Syst.* **2017**, *21*, 190-198.
- [164] B. Ravikumar, C. Vacher, Z. Berger, J. E. Davies, S. Luo, L. G. Oroz, F. Scaravilli, D. F. Easton, R. Duden, C. J. O'Kane, D. C. Rubinsztein, *Nat. Genet.* **2004**, *36*, 585-595.
- [165] P. Jiang, N. Mizushima, *Methods Cell Biol.* **2015**, *75*, 13-18.
- [166] M. Komatsu, S. Kageyama, Y. Ichimura, *Pharmac. Res.* **2012**, *66*, 457-462.
- [167] D. N. Wilson, F. Schluenzen, J. M. Harms, A. L. Starosta, S. R. Connell, P. Fucini, *PNAS* **2008**, *105*, 13339–11334.
- [168] K. L. Leach, S. M. Swaney, J. R. Colca, W. G. McDonald, J. R. Blinn, L. M. Thomasco, R. C. Gadwood, D. Shinabarger, L. Xiong, A. S. Mankin, *Mol. Cell* **2007**, *26*, 393-402.
- [169] E. E. Nagiec, L. Wu, S. M. Swaney, J. G. Chosay, D. E. Ross, J. K. Brieland, K. L. Leach, *Antimicrob. Agents Chemother.* **2005**, *49*, 3896-3902.
- [170] S. Lu, T. Sung, N. Lin, R. T. Abraham, B. A. Jessen, *PLOS one* **2017**, *12*, e0173771.
- [171] B. Levine, G. Kroemer, *Cell* **2008**, *132*, 27-42.
- [172] J. Kornhuber, P. Tripal, M. Reichel, L. Terfloth, S. Bleich, J. Wiltfang, E. Gulbins, *J. Med. Chem.* **2008**, *51*, 219-237.
- [173] A. G. Roth, S. Redmer, C. Arenz, *ChemBioChem* **2009**, *10*, 2367-2374.
- [174] J. Kornhuber, M. Muehlbacher, S. Trapp, S. Pechmann, A. Friedl, M. Reichel, C. Mühle, L. Terfloth, T. W. Groemer, G. M. Spitzer, K. R. Liedl, E. Gulbins, P. Tripal, *PLOS one* **2011**, *6*, e23852.
- [175] K. P. Bhabak, A. Hauser, S. Redmer, S. Banhart, D. Heuer, C. Arenz, *ChemBioChem* **2013**, *14*, 1049-1052.
- [176] M. M. Young, M. Kester, H. G. Wang, *J. Lipid. Res.* **2013**, *54*, 5-19.
- [177] D. A. Stroud, L. E. Formosa, X. W. Wijeyeratne, T. N. Nguyen, M. T. Ryan, *J. Biol. Chem.* **2013**, *288*, 1685–1690.
- [178] F. Palmieri, *Mol. Aspects Med.* **2012**, *34*, 465-484.
- [179] D. A. Kubli, Å. B. Gustafsson, *Cric. Res.* **2012**, *111*, 1208-1221.
- [180] M. Greaf, J. Nunnari, *EMBO J.* **2011**, *30*, 2101-2114.
- [181] M. D. Brand, D. G. Nicholls, *Biochem J.* **2011**, *435*, 297-312.

- [182] G. A. Hunter, S. Al-Karadaghi, G. C. Ferreira, *J. Porphyr. Phthalocyanines*. **2011**, *15*, 350-356.
- [183] H. A. Dailey, T. A. Dailey, C. K. Wu, A. E. Medlock, K. F. Wang, J. P. Rose, B. C. Wang, *Cell. Mol. Life Sci.* **2000**, *57*, 1909–1926.
- [184] A. P. Asuru, M. An, L. S. Busenlehner, *Biochemistry* **2012**, *51*.
- [185] A. Djimdé, O. K. Doumbo, J. F. Cortese, K. Kayentao, S. Doumbo, Y. Diourté, D. Coulibaly, A. Dicko, X. Su, T. Nomura, D. A. Fidock, T. E. Wellems, C. V. Plowe, *N. Engl. J. Med.* **2001**, *344*, 257-263.
- [186] K. Y. Fong, D. W. Wright, *Future Med. Chem.* **2013**, *5*, 1437-1450.
- [187] T. T. Mai, A. Hamäi, A. Hienzschi, T. Cañeque, S. Müller, J. Wicinski, O. Cabaud, C. Leroy, A. David, V. Acevedo, A. Ryo, C. Ginestier, D. Birnbaum, E. e. Charafe-Jauffret, P. Codogno, M. Mehrpour, R. Rodriguez, *Nat. Chem.* **2017**, *9*, 1025-1033.
- [188] T. Horie, T. Kawamata, M. Matsunami, Y. Ohsumi, *J. Biol. Chem.* **2017**, *292*, 8533-8543.
- [189] A. Gopalsamy, M. Shi, Y. Hua, F. Lee, L. Feldberg, E. Frommer, S. Kim, K. Collins, D. Wojciechowicz, R. Mallon, *Bioorganic Med. Chem. Lett.* **2010**, *20*, 2431-2434.
- [190] A. Zhao, X. Gao, Y. Wang, J. Ai, Y. Wang, Y. Chen, M. Geng, A. Zhang, *Bioorg. Med. Chem.* **2011**, *19*, 3906-3918.
- [191] T. Horiuchi, J. Chiba, K. Uoto, T. Soga, *Bioorganic Med. Chem. Lett.* **2009**, *19*, 305-308.
- [192] T. P. Heffron, M. Berry, G. Castanedo, C. Chang, I. Chuckowree, J. Dotson, A. Folkes, J. Gunzner, J. D. Lesnick, C. Lewis, S. Mathieu, J. Nonomiya, A. Olivero, J. Pang, D. Peterson, L. Salphati, D. Sampath, S. Sideris, D. P. Sutherlin, V. Tsui, N. C. Wand, S. Wang, S. Wonge, B. Zhu, *Bioorganic Med. Chem. Lett.* **2010**, *20*, 2408-2411.
- [193] I. Choi, Y. S. Cho, H. J. Jung, H. J. Kwon, *Biochem. Biophys. Res. Commun.* **2010**, *393*, 849-854.
- [194] Y. Wang, J. A. Kelber, H. S. T. Cao, G. T. Cantin, R. Lin, W. Wang, S. Kaushal, J. M. Bristow, T. S. Edgington, R. M. Hoffman, M. Bouvet, J. R. Yates, R. L. Klemke, *PNAS* **2010**, *107*, 10920-10925.
- [195] Y. Zhou, J. K. Shen, F. J. Hornicek, Q. Kan, Z. Duan, *Oncotarget*. **2016**, *7*, 40846-40859.
- [196] I. Kawai, T. Hisaki, K. Sugiura, K. Naito, K. Kano, *Biochem. Biophys. Res. Commun.* **2012**, *427*, 611-617.
- [197] B. J. Mader, V. N. Pivtoraiko, H. M. Flippo, B. J. Klocke, K. A. Roth, L. R. Mangieri, J. J. Shacka, *ACS Chem. Neurosci.* **2012**, *3*, 1063-1072.
- [198] J. K. Salabei, A. A. Gibb, B. G. Hill, *Nat. Protoc.* **2014**, *9*, 421-438.

- [199] L. Sánchez-Caballero, S. Guerrero-Castillo, L. Nijtmans, *Biochim. Biophys. Acta* **2016**, *1857*, 980-990.
- [200] N. Mygind, L. P. Nielsen, H. Hoffmann, A. Shukla, G. Blumberga, R. Dahl, H. Jacobi, *J. Allergy Clin. Immunol.* **2001**, *108*, 16-25.
- [201] J. Zhang, M. L. Culp, J. G. Craver, V. Darley-USmar, *J. Neurochem.* **2018**, *144*, 691-709.
- [202] W. L. F. Armarego, C. L. L. Chai, *Purification of Laboratory Chemicals* **2003**, *5th ed.*
- [203] J. Cox, M. Mann, *Nat. Biotechnol.* **2008**, *26*, 1367-1372.
- [204] J. Cox, M. Y. Hein, C. A. Lubner, I. Paron, N. Nagaraj, M. Mann, *Mol. Cell. Proteomics* **2014**, *13*, 2513-2526.
- [205] S. Tyanova, T. Temu, P. Sinitcyn, A. Carlson, M. Y. Hein, T. Geiger, M. Mann, J. Cox, *Nat. Methods* **2016**, *13*, 731-740.
- [206] S. Tyanova, J. Cox, *Methods. Mol. Biol.* **2018**, *1711*, 133-148.

CURRICULUM VITA

Personal Information

Surname: Kaiser

Name: Nadine

Date of Birth: 02.04.1991

Place of Birth: Arnsberg, NRW, Germany

Citizenship: German

Education

09/2015 – 01/2019: PhD student at Max Planck Institute of Molecular Physiology

Research topic: Design and synthesis of photoactivatable myristic acid analogues for UNC119 cargo interactions and target identification of autophagy inhibitors.

Advisor: Prof. Dr. Dr. h.c. Herbert Waldmann

10/2013 – 09/2015: Master's at Technical University Dortmund in Chemical Biology

Master thesis:

Research topic: Syntheses and Evaluation of Myristoyl Analogues for Affinity Enrichment with UNC119.

Advisor: Prof. Dr. Dr. h.c. Herbert Waldmann

10/2010 – 09/2013: Bachelor's at Technical University Dortmund in Chemical Biology

Bachelor thesis:

Research topic: Synthese eines Indol-basierten Scaffolds für DNA-kodierte Molekülbibliotheken.

Advisor: Dr. Andreas Brunschweiger,